

**Energy Spectra Informed Performance of Clocked  
Quantum-dot Cellular Automata**

by

Jacob Retallick

B.A.Sc., The University of British Columbia, 2014

A THESIS SUBMITTED IN PARTIAL FULFILLMENT OF  
THE REQUIREMENTS FOR THE DEGREE OF

**Doctor of Philosophy**

in

THE FACULTY OF GRADUATE AND POSTDOCTORAL STUDIES  
(Electrical and Computer Engineering)

THE UNIVERSITY OF BRITISH COLUMBIA  
(Vancouver)

December 2020

© Jacob Retallick, 2020

The following individuals certify that they have read, and recommend to the Faculty of Graduate and Postdoctoral Studies for acceptance, the thesis entitled:

**Energy Spectra Informed Performance of Clocked Quantum-dot Cellular Automata**

submitted by Jacob Retallick in partial fulfillment of the requirements for  
the degree of Doctor of Philosophy  
in Electrical and Computer Engineering

**Examining Committee:**

Konrad Walus, Electrical and Computer Engineering, UBC  
*Supervisor*

Steve Wilton, Electrical and Computer Engineering, UBC  
*Supervisory Committee Member*

Lukas Chrostowski, Electrical and Computer Engineering, UBC  
*University Examiner*

Robert Raussendorf, Physics and Astronomy, UBC  
*University Examiner*

**Additional Supervisory Committee Members:**

John Madden, Electrical and Computer Engineering, UBC  
*Supervisory Committee Member*

# Abstract

Understanding the dynamic behaviour of nanoscale quantum-dot cellular automata (QCA) networks involves the simulation of large numbers of QCA devices, with the complexity of the full quantum treatment exponential in the network size. Previous attempts to limit this complexity introduce simplifying assumptions with known inaccuracies. In this thesis we investigate an alternate approach, extracting performance metrics through analysing the low energy eigenspectrum of a clocked network. We make two major contributions.

In the first part of this thesis, we study the use of silicon dangling bonds (SiDBs) as a platform for combinatorial logic, and ultimately nanoscale QCA. We present models for understanding the preferred configurations and dynamics of charges in these structures. We consider the clocking of SiDB-based QCA wires, and reveal a complicated trajectory of charge states that serve as a challenge for QCA operation. By studying SiDB-based QCA from the framework of the familiar 3-state model, in which these preferred charge states translate to eigenstates of a system Hamiltonian, we determine conditions for which SiDB-QCA wires can correctly operate when clocked. These conditions are potentially impractical unless net-neutral SiDB arrangements can be achieved.

The remaining bulk of the thesis revolves around the link between QCA clocking and quantum annealing. We first investigate the adiabaticity of simple 2-state QCA networks under zone clocking. We present upper bounds on the clocking frequency beyond which adiabaticity falls below a 99% threshold, and demonstrate how we can efficiently estimate clocking performance using only a few of the energy eigenstates. Due to a natural mapping between QCA cells and superconducting flux qubits, the potential for investigating performance using a physical quan-

tum annealer is explored. Methods for embedding QCA networks onto the annealer are discussed and a selection of annealing results are analyzed. Finally, we establish a method for decomposing the system Hamiltonian into contributions from given components, and a means to identify meaningful components which critically affect clocking performance. This framework reveals a heuristic algorithm for approximating the low energy eigenspectra of large QCA networks, enabling future investigations into the performance of networks well beyond previous size limitations.

# Lay Summary

There is increasing interest in technologies which extend beyond the expected scaling limitations of silicon transistors. Quantum-dot cellular automata (QCA) is a potential approach which can represent binary information by the arrangements of electrons among a collections of atoms or within single molecules. At this small scale, understanding the behaviour of QCA circuits requires modelling large numbers of devices as they are being clocked. This requires an exponential amount of computational resources.

In this work, we make two major contributions. First, we assess one potential architecture for implementing nanoscale QCA using silicon dangling bonds. Second, we develop an approach to understanding the behaviour of QCA arrangements by looking at the rate of transitions between a few of the lowest energy states of the system, and present an efficient method for finding these low energy states even for large QCA circuits.

# Preface

This work was supervised by Dr. Konrad Walus and is focused around two related research efforts. First, a collaboration with the research group of Dr. Robert A. Wolkow at the University of Alberta to understand and model the behaviour of networks of silicon dangling bonds (SiDBs) on hydrogen passivated silicon. The second effort is the main contribution of my research, a study of the behaviour of quantum-dot cellular automata (QCA) networks near the adiabatic limit employing knowledge of the low energy eigenspectrum. Several parts of this thesis contain content which has previously been published or is currently in submission.

The first three chapters present a review of models and simulation techniques for QCA devices and performance, including a discussion on quantum annealing and its link to QCA clocking. **Chapter 4** presents an overview of published work regarding SiDB structures with content from the following:

- [1] M. Rashidi, W. Vine, T. Dienel, L. Livaderu, **J. Retallick**, T. Huff, K. Walus, and R. A. Wolkow, “Initiating and monitoring the evolution of single electrons within atom-defined structures,” *Phys. Rev. Lett.*, vol. 121, no. 16, p. 166801, Oct. 2018.
- [2] S. S. H. Ng, **J. Retallick**, H. N. Chiu, R. Lupoiu, L. Livadaru, T. Huff, M. Rashidi, W. Vine, T. Dienel, R. A. Wolkow, and K. Walus, “SiQAD: A design and simulation tool for atomic silicon quantum dot circuits,” *IEEE Transactions on Nanotechnology*, vol. 19, pp. 137-146, 2020.

- [3] H. N. Chiu, S. S. H. Ng, **J. Retallick**, and K. Walus, “PoisSolver: a tool for modelling silicon dangling bond clocking networks,” in *2020 IEEE 20th International Conference on Nanotechnology (IEEE-NANO)*. IEEE, Jul. 2020, pp. 134-139

The experimental work by Wolkow’s group discussed in [1] was the motivating for the models and tools in [2–4] that followed. My main contribution to the manuscript for [1] was in discussion of interpreting the experimentally observed slow dynamics, the potential influence of the tip on charge transitions, and heuristic models which would be used in later work. An effort in implementing SiQAD, a CAD tool for designing and simulating SiDB structures is discussed in [2]. I developed the initial version of the graphical interface, as well as much of the low level code for design definitions and tools. In addition, I was responsible for the models used both for defining low energy metastable charge configurations in SiDB arrangements as well as the hopping model and its Python implementation. The solver for the general Poisson equation and the resulting manuscript [3] was primarily the work of Nathan Chiu. My main contribution was in early discussion on scalable strategies for solving arbitrary electrode arrangements as well as commenting the manuscript.

For all remaining content, I was the lead researcher, prepared the manuscripts, and produced all code, data, and figures. Dr. Walus provided insight for directing the investigations and advice for manuscript development. A version of **Chapter 5** has been published in [4]. The discussion has been slightly expanded to better integrate with the rest of this thesis.

- [4] **J. Retallick** and K. Walus, “Population congestion in 3-state quantum-dot cellular automata,” *Journal of Applied Physics*, vol. 127, no. 24, p. 244301, 2020.

**Chapter 6** has been published in [5]. New results regarding better estimates of performance using the low energy spectrum have been added.

- [5] **J. Retallick** and K. Walus, “Limits of adiabatic clocking in quantum-dot cellular automata,” *Journal of Applied Physics*, vol. 127, no. 5, p. 054502, 2020.

**Chapter 7** contains work published in a number of forms. The embedding algorithm was based on earlier work by Michael Babcock, Miguel Aroca-Ouellette, and Shane McNamara; however, the more recent implementation and its improvements were my work, as well as all results discussed in the manuscript [6]. An unpublished expanded discussion can be found on the arXiv [7]. Annealing results using the quantum annealer developed by D-Wave Systems Inc. were done with the assistance of Aidan Roy, and a sample of these results previously presented at the ACS Spring Meeting in 2017 [8].

[6] **J. Retallick**, M. Babcock, M. Aroca-Ouellette, S. McNamara, S. Wilton, A. Roy, M. Johnson, and K. Walus, “Embedding of quantum-dot cellular automata circuits onto a quantum annealing processor,” in *2014 Conference of Optoelectronic and Microelectronic Materials & Devices*. IEEE, Dec. 2014.

[8] **J. Retallick** and K. Walus, “Investigation of quantum-dot cellular automata networks using a quantum annealing processor,” Presented at the 253rd ACS National Meeting, San Francisco, USA, Apr. 2017

A version of **Chapter 8** has been submitted and conditionally accepted by IEEE Transactions on Nanotechnology. Code for extracting performance metrics from the heuristic estimate of the low energy spectra has since been implemented. Appropriate results are included in Section 8.4 which are not currently included in the submitted work.

[9] **J. Retallick** and K. Walus, “Low-energy eigenspectrum decomposition (LEED) of quantum-dot cellular automata networks,” submitted for publication, June 2020

# Table of Contents

<b>Abstract</b> . . . . .	<b>iii</b>
<b>Lay Summary</b> . . . . .	<b>v</b>
<b>Preface</b> . . . . .	<b>vi</b>
<b>Table of Contents</b> . . . . .	<b>ix</b>
<b>List of Tables</b> . . . . .	<b>xii</b>
<b>List of Figures</b> . . . . .	<b>xiii</b>
<b>List of Abbreviations</b> . . . . .	<b>xviii</b>
<b>Acknowledgments</b> . . . . .	<b>xx</b>
<b>1 Introduction</b> . . . . .	<b>1</b>
1.1 Background and Motivation . . . . .	1
1.2 Thesis Overview . . . . .	5
<b>2 Modelling and Simulation of QCA Devices</b> . . . . .	<b>6</b>
2.1 Reduced Basis Representations . . . . .	7
2.2 Dynamics Using Reduced Correlation Models . . . . .	11
<b>3 QCA Clocking as Quantum Annealing</b> . . . . .	<b>20</b>
3.1 Quantum Annealing . . . . .	21
3.2 QCA Clocking . . . . .	25

<b>4</b>	<b>Dangling Bonds on Hydrogen Passivated Silicon . . . . .</b>	<b>26</b>
4.1	Charge States of SiDB Arrangements . . . . .	27
4.2	Clocking SiDB Structures . . . . .	34
4.3	Dynamic Behaviour . . . . .	34
4.4	SiQAD: Simulation and Design of SiDB Structures . . . . .	39
4.5	SiDB Implementations of QCA . . . . .	40
4.6	Summary . . . . .	45
<b>5</b>	<b>Population Congestion in 3-State QCA . . . . .</b>	<b>46</b>
5.1	Full 3-State Hamiltonian . . . . .	47
5.2	Considered Devices . . . . .	48
5.3	Ground State Characterisation . . . . .	53
5.4	Wave Clocking of Wires . . . . .	65
5.5	Summary . . . . .	69
<b>6</b>	<b>Limits of Adiabatic Clocking for 2-State QCA Networks . . . . .</b>	<b>71</b>
6.1	Choosing a Clocking Schedule . . . . .	72
6.2	Coherent Behaviour of QCA Components . . . . .	82
6.3	Dissipative Behaviour . . . . .	91
6.4	Summary . . . . .	102
<b>7</b>	<b>Simulating 2-State QCA on Quantum Annealing Hardware . . . . .</b>	<b>103</b>
7.1	Embedding Problems on the QPU . . . . .	105
7.2	Annealing Results . . . . .	114
7.3	Summary . . . . .	121
<b>8</b>	<b>Eigenspectrum Decomposition of QCA Networks . . . . .</b>	<b>122</b>
8.1	Decomposing the QCA Network Hamiltonian . . . . .	123
8.2	System Energy-Based Decomposition . . . . .	126
8.3	Heuristic Solver for Large Networks . . . . .	132
8.4	Estimating Transitions in the Component Mode Basis . . . . .	137
8.5	Component Substitution . . . . .	140
8.6	Application to Alternate QCA Models . . . . .	140
8.7	Summary . . . . .	143

<b>9 Conclusion and Future Work . . . . .</b>	<b>144</b>
9.1 SiDBs as a Platform for Nanoscale QCA . . . . .	144
9.2 Estimating QCA Performance using the Low Energy Spectrum . .	145
<b>Bibliography . . . . .</b>	<b>148</b>
<b>A Algorithm Details . . . . .</b>	<b>161</b>
A.1 SiDB HoppingDynamics Engine . . . . .	161
A.2 Dense Placement Algorithm . . . . .	164
A.3 Component Mode Solver . . . . .	169
<b>B Additional Derivations . . . . .</b>	<b>172</b>
B.1 Analytical Estimate of the 3-State QCA Cell Ground State Energy	172
B.2 Clocking Field Range for 3-State QCA Wires . . . . .	173
B.3 Y Spin Invariance in the 2-State Approximation . . . . .	174
<b>C Supplemental Details . . . . .</b>	<b>175</b>
C.1 Pegasus Topology . . . . .	175
C.2 Additional Embedding Results . . . . .	175
<b>D Equations . . . . .</b>	<b>180</b>
D.1 Gell-Mann Matrices . . . . .	180
D.2 Equations for All Single and Two Point Correlations . . . . .	180

# List of Tables

Table 5.1	Worst-case errors over all $(h, \mathcal{C})$ for different $u$ parameter approximations. . . . .	55
Table 5.2	Upper limits on $\xi$ for in-order population of a wire in the weak tunneling limit. . . . .	58
Table 6.1	F-parameters in Eq. (6.4) from Eq. (6.5) for the simulated devices.	74
Table 6.2	Fit parameters for the hyperbolic approximation of the minimum gap of the inverter for the different clocking schedules. . .	77
Table 6.3	Comparison of fit and analytical estimates of the Landau-Zener $v$ parameter for wires. . . . .	85
Table 6.4	Maximum clocking frequencies relative to $f_0$ , for our basic QCA circuits based on different metrics. . . . .	88
Table 6.5	Maximum clocking frequencies computed using different adiabaticity estimation methods. . . . .	90
Table 6.6	Threshold $\beta$ value for high performance in the relaxed regime.	95
Table 6.7	Comparison of $\beta^*$ values for the two temperature dependent steady states. . . . .	100
Table 7.1	Benchmark circuits and the number of non-driver cells . . . . .	111
Table C.1	Power law fit parameters for the characteristic circuit size, $\mu$ , and run time $t(\mu)$ . . . . .	178

# List of Figures

Figure 1.1	Schematics and polarizations for common QCA devices . . .	2
Figure 1.2	Common QCA building blocks used in larger QCA circuits. . .	2
Figure 1.3	Schematic of 4-phase clocking . . . . .	3
Figure 1.4	Schematic for zone and dynamic wave clocking protocols. . .	4
Figure 1.5	Example electrode arrangements for 4-phase clocking. . . . .	4
Figure 2.1	2-state QCA device configuration states . . . . .	7
Figure 2.2	3-state QCA device configuration states . . . . .	9
Figure 2.3	Majority gate with uneven inputs under the ICHA. . . . .	11
Figure 2.4	Conversion rules for generating 2-state CVF equations. . . . .	14
Figure 2.5	Graph representations of the interdependence of correlation tensors. . . . .	15
Figure 2.6	Simulation of a five cell QCA wire using a few correlation models excluding any dissipation. . . . .	16
Figure 2.7	Majority gate using a single multi-cell Hamiltonian. . . . .	18
Figure 2.8	Two majority gates in series with potential multi-cell groups. .	19
Figure 3.1	Schematic avoided level crossing described in the Landau-Zener approximation. . . . .	23
Figure 4.1	Schematic of the H-Si(100)-2×1 surface. . . . .	27
Figure 4.2	Schematic of the SiDB charge states and the band structure of the silicon substrate. . . . .	28
Figure 4.3	Experimentally observed charge configurations for an SiDB OR gate . . . . .	30

Figure 4.4	Simulated charge configurations of the OR gate . . . . .	33
Figure 4.5	Demonstration of hopping behaviour in a symmetric structure studied in Ref. [1] . . . . .	35
Figure 4.6	Schematic of hopping rates in the hopping model. . . . .	36
Figure 4.7	Dynamics simulation of the system in Fig. 4.5 . . . . .	38
Figure 4.8	Experimental demonstration of a 4-dot SiDB cell. . . . .	40
Figure 4.9	SiDB implementation of an inverting chain and the equivalent 2-dot QCA representation. . . . .	41
Figure 4.10	Sequence of lowest energy metastable configurations of the SiDB inverting chain. . . . .	41
Figure 4.11	SiDB implementation of a non-inverting wire and the equiva- lent 4-dot QCA representation. . . . .	42
Figure 4.12	Sequence of lowest energy metastable configurations of the SiDB wire. . . . .	42
Figure 4.13	Dynamics simulation of an SiDB inverting chain under 4-phase wave clocking. . . . .	44
Figure 5.1	Schematics for 3-state $\text{Fc}^+\text{FcC}_2\text{B}_9^-$ devices. . . . .	49
Figure 5.2	Kink and congestion energies for both $\text{Fc}^+\text{FcC}_2\text{B}_9^-$ device con- figurations. . . . .	50
Figure 5.3	SiDB device geometries and interaction energies. . . . .	51
Figure 5.4	Normalized clocking wave profiles. . . . .	52
Figure 5.5	Spectra of the 3-state Cell Hamiltonian . . . . .	54
Figure 5.6	3-state cell responses in the two limiting cases of polarization bias . . . . .	55
Figure 5.7	Arrangements for driven 3-state wires. . . . .	56
Figure 5.8	Driven inverting wire in the weak tunneling limit after success- fully populating the first $n$ cells. . . . .	57
Figure 5.9	Ground state polarizations and populations of biased 3 cell wires	59
Figure 5.10	Ground state polarizations and populations of a biased 3-dot inverting wire with $\gamma = E_0^k/10$ . . . . .	60
Figure 5.11	Maximum congestion ratios for 3 cell wires using devices for varying tunneling rates. . . . .	61

Figure 5.12	Ground states of Maj-101 using different congestion ratios. . .	62
Figure 5.13	Ground states, energy gaps, and transition parameters for Maj-101 with non-zero tunneling. . . . .	64
Figure 5.14	Increases in the maximum congestion ratios of 3 cell wires for wave clocking at various tunneling rates . . . . .	66
Figure 5.15	Dependence of the minimum required clocking fields on the null site depth for a 3-dot wire using a 200 nm trapezoidal wave	68
Figure 6.1	QCA device dimensions and computed kink energies relative to $\mathcal{E}$ . . . . .	74
Figure 6.2	Schedule energies for the Linear, Quasilinear, and Sinusoidal clocking schedules. . . . .	76
Figure 6.3	Comparison of classical performances for the different clocking schedules. . . . .	78
Figure 6.4	Initial coherent oscillations in a simulation of Maj-101 using the Quasilinear schedule. . . . .	79
Figure 6.5	Classical performance of Maj-101 for different $\alpha_0$ values before and after smoothing. . . . .	79
Figure 6.6	Classical performance of a wire and inverter for different $\alpha_0$ values. . . . .	80
Figure 6.7	Low energy spectra of the simulated devices. . . . .	81
Figure 6.8	Landau-Zener parameters as a function of the wire length. . .	83
Figure 6.9	Performance and maximum characteristic rates of wires of different lengths. . . . .	84
Figure 6.10	Performance metrics for the QCA building blocks. . . . .	86
Figure 6.11	Low energy spectrum and performance metrics of Maj-110. . .	87
Figure 6.12	Transition parameters for the QCA devices . . . . .	89
Figure 6.13	Logical performance of Maj-101 for different spectral steady states. . . . .	93
Figure 6.14	Three operational regimes for steady state relaxation models. .	94
Figure 6.15	Logical performance in the relaxed regime for QCA components with the Boltzmann distribution steady state. . . . .	94

Figure 6.16	Maximum clocking frequencies relative to $f_0$ for different spectral steady states. . . . .	96
Figure 6.17	ICHA: Maximum clocking frequencies relative to $f_0$ for the different spectral steady states. . . . .	97
Figure 6.18	Oscillations in the ICHA simulation of Wire-5. . . . .	98
Figure 6.19	Logical performance in the relaxed regime for the mean field relaxation with the ICHA. . . . .	100
Figure 6.20	Maximum clocking frequencies relative to $f_0$ for mean field relaxation using the ICHA. . . . .	101
Figure 7.1	Qubit layout for one tile of the QPU . . . . .	104
Figure 7.2	Additional couplers in the Pegasus topology. . . . .	104
Figure 7.3	Minimal embeddings for $K_4$ on the Chimera and Pegasus topologies. . . . .	105
Figure 7.4	Schematic of 4-dot QCA device connectivity. . . . .	107
Figure 7.5	Schematic of 2-dot QCA device connectivity. . . . .	107
Figure 7.6	Connectivity graph representations for a selection of simple QCA components. . . . .	108
Figure 7.7	Minimal embeddings for the 4-dot majority gate. . . . .	109
Figure 7.8	Minimal embeddings for the 4-dot inverter. . . . .	109
Figure 7.9	Number of physical qubits used for benchmark circuits . . . . .	111
Figure 7.10	Comparison of physical qubit usage and vertex model sizes for both algorithms and adjacencies . . . . .	112
Figure 7.11	Average number of physical qubits needed to embed generated QCA circuits of different sizes . . . . .	113
Figure 7.12	Average single trial embedding success probabilities . . . . .	113
Figure 7.13	Annealing schedule for the D-Wave 2X . . . . .	114
Figure 7.14	Annealing results for wires of different lengths with various annealing times. . . . .	115
Figure 7.15	Change in the spectra of embedded QCA networks . . . . .	117
Figure 7.16	Comparison of transition parameters before and after embedding	118
Figure 7.17	Proportion of annealing results which produce the ground state as a function of the annealing time . . . . .	120

Figure 8.1	Sample decomposition of the 2-dot majority gate with binary inputs 101. . . . .	130
Figure 8.2	Example decomposition tree of a large QCA network. . . . .	134
Figure 8.3	Circuit diagram and the equivalent 4-dot QCA network for the considered 49 cell XOR gate, not counting fixed input cells. . . . .	135
Figure 8.4	Sample decompositions of the XOR gate. . . . .	136
Figure 8.5	Estimates of the transition parameters for the 49 cell XOR gate. . . . .	139
Figure 8.6	Change in the spectra and transition parameters associated with substituting the inverting element in the XOR gate. . . . .	141
Figure A.1	Cohopping schematic . . . . .	163
Figure A.2	Example embedding of a serial adder QCA circuit . . . . .	166
Figure A.3	Occurrence probability of qubit chain lengths and vertex-model sizes for the Dense Placement and Minorminer algorithms . . . . .	167
Figure A.4	Schematic of a chain between two end nodes . . . . .	168
Figure C.1	Tile connectivity of the Pegasus topology. . . . .	176
Figure C.2	Connectivity between qubits in different Chimera sub-graphs. . . . .	176
Figure C.3	Average run times for generated circuits on the 512 qubit processor for both algorithms with best fits. . . . .	177
Figure C.4	Metrics for the 50% circuit size and characteristic run time for both embedding algorithms. . . . .	178
Figure C.5	Relative decrease in the embeddable circuit size as a function of the proportion of qubits disabled. . . . .	179

# List of Abbreviations

**AFM** atomic force microscope.

**AQC** adiabatic quantum computing.

**CAD** computer-aided design.

**CM** Component Mode solver.

**CMOS** complementary metal-oxide semiconductor.

**CVF** coherence vector formalism.

**DMRG** density matrix renormalization groups.

**DP** Dense Placement embedding algorithm.

**FEM** finite element method.

**FPGA** field-programmable gate array.

**ICHA** Intercellular Hartree-Fock Approximation.

**LES** low energy eigenspectrum.

**MVM** mixed valence molecule.

**ODE** ordinary differential equation.

**QA** quantum annealing.

**QCA** quantum-dot cellular automata.

**QPU** quantum processing unit.

**QUBO** quadratic unconstrained binary optimization.

**SA** simulated annealing.

**SiDB** silicon dangling bond.

**SiQAD** Silicon Quantum Atomic Designer.

**STM** scanning tunneling microscope.

**TISG** transverse Ising spin glass.

**USE** Universal, Scalable, and Efficient clocking scheme.

**VRH** variable range hopping.

# Acknowledgments

I would like to thank my graduate supervisor, Dr. Konrad Walus, for his guidance, support, and the many insightful discussions around campus. I would also like to thank my lab mates, Samuel Ng and Nathan Chiu, for their camaraderie and for bringing humour and compelling discourse to what might otherwise have been long hours in the lab. Finally, I would like to thank my family for their years of support throughout my education.

This work was supported by the Natural Sciences and Engineering Research Council of Canada under Grant STPGP 478838-15.

# Chapter 1

## Introduction

### 1.1 Background and Motivation

In recent years, there has been great interest in technologies that extend beyond the projected scale limits of conventional CMOS, ranging from new transistor designs with alternate channels [10, 11] to entirely novel computational architectures [12–14]. Quantum-dot cellular automata (QCA) encodes binary information in the distribution of charges in devices or *cells* composed of arrays of quantum dots [15, 16]. Schematics of some common QCA devices are shown in Fig. 1.1. Coulombic interactions between occupying charges facilitate coupling between the charge states of neighbouring cells. Arrangements of these cells can be designed with ground states that encode familiar logic gates [17]. Inverters and majority gates form the fundamental basis of logic functions for the vast majority of QCA designs. Suitable arrangements for these functions are shown in Fig. 1.2. Early proof-of-concept implementations have been fabricated and tested using metallic island devices [17–21], and nanomagnetics [22–24]. More recent efforts have focused on the potential for nanoscale implementations of QCA. Among the most promising candidates are mixed-valence molecular devices [25, 26] and patterned dangling bonds on hydrogen passivated silicon [14, 27, 28]. Each QCA cell occupies only a few nm<sup>2</sup> in area, potentially offering high device densities of 10<sup>14</sup> cm<sup>-2</sup>. Significant challenges must be solved for any realistic QCA implementation, such as limiting device power at high density using reversible gates [29, 30], designing

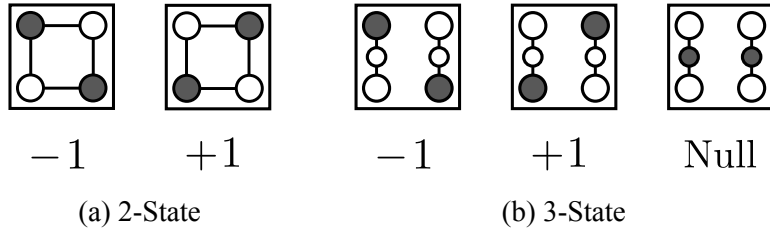


**Figure 1.1:** Schematics and polarizations for common QCA devices. The shaded quantum dots show the locations of mobile charges. Inter-dot tunneling paths are indicated by the lines.

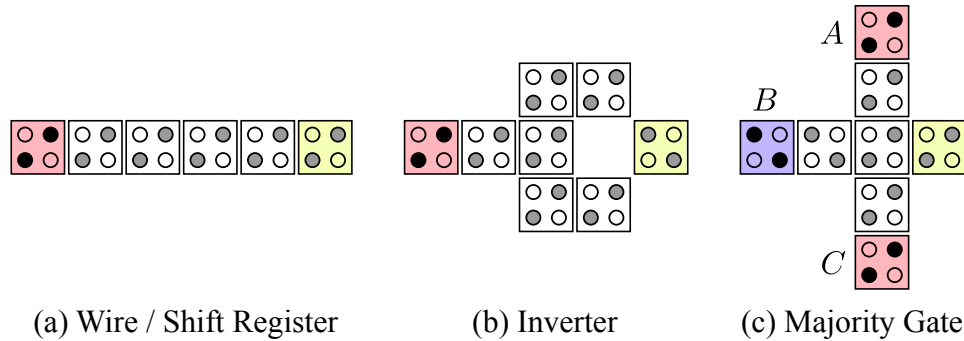


**Figure 1.2:** Common QCA building blocks used in larger QCA circuits. Red and blue shaded cells indicate inputs with +1 or -1 polarization respectively. The rightmost yellow cells produce the logical output. In this work, we will denote by “Wire- $N$ ” a wire of  $N$  cells and “Maj-ABC” a majority gate with binary inputs as indicate: ex Maj-101 shown.

robust wire crossings [31] and clocking networks [32, 33], and interfacing with the existing CMOS architecture.

The operation of QCA networks requires the generation of multi-phase *clocking fields* which control information flow by sequentially activating QCA devices [20]. One common approach is to segment the network into *clock zones*, regions which each share a clocking phase. Fig. 1.3 shows a schematic of this clocking protocol. This approach is used in QCADesigner [34], a popular QCA design and simulation tool, and is ubiquitous in the design literature. The complexity of computing the ground state of a clock zone is exponential in the number of cells. Mean

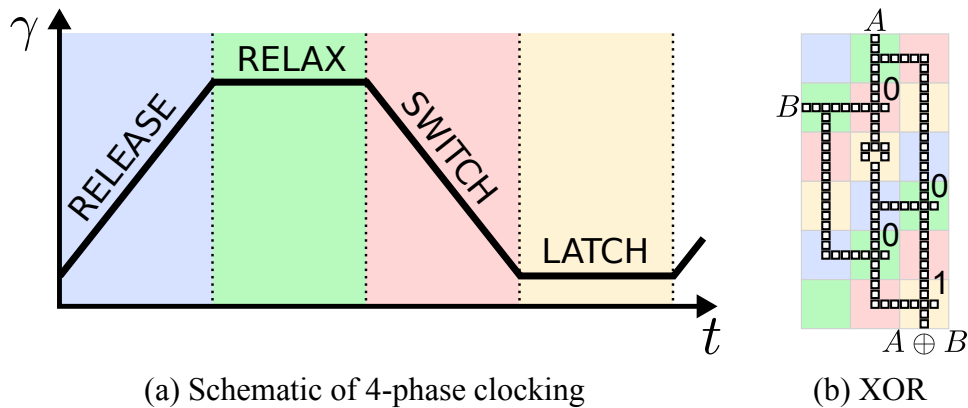


**Figure 1.3:** (a) Schematic of the 4-phase clocking protocol. Regions of QCA devices are driven between unpolarized *relaxed* and polarized *latched* states: eg. by modulating their inter-dot tunneling energies,  $\gamma$ . Adjacent clock zones are  $\pi/2$  phase shifted to enforce directional information flow. (b) An example XOR gate with suitable clock zones phases indicated by the colours. We are primarily interested in the *switching* phase, in which the polarization ground state needs to be achieved.

field methods are often employed to approximate the ground state using manageable resources [15, 35]. These methods are known to produce incorrect ground states for certain QCA arrangements [36]. QCA designs and selections of clock zones are often influenced by what these approximation methods can reliably handle rather than any expectation of real behaviour. An alternative approach is to employ electrodes, each addressed with one of the clock phases, to generate a dynamic clocking wave which can be swept over the network [30, 37]. Instead of clock zones being activated in sequence, devices are then activated within the rising edge of the travelling clocking wave. A schematic comparison of zone and wave clocking is shown in Fig. 1.4. Example electrode arrangements appropriate for either zone or wave clocking are shown in Fig. 1.5. Columnar or 2DWave [38] floor plans are suitable for feed-forward combinatorial networks but cannot implement feedback. A scheme like the USE floor plan proposed in [32], or similar [33], can be used for more general QCA networks.

Current nanofabrication limitations constrain the minimum separation for clocking electrodes to tens of nm [39]. Not only does this restrict possible electrode ge-

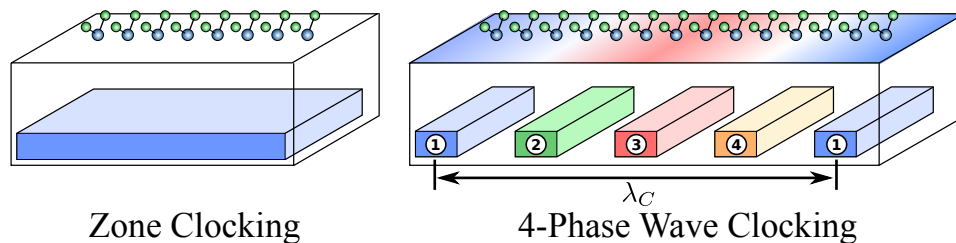


**Figure 1.4:** Schematics of both clocking protocols. For zone clocking, all devices see the same clocking field. By using 4-phase buried electrodes, we generate a travelling wave where computation is done within the rising edge.

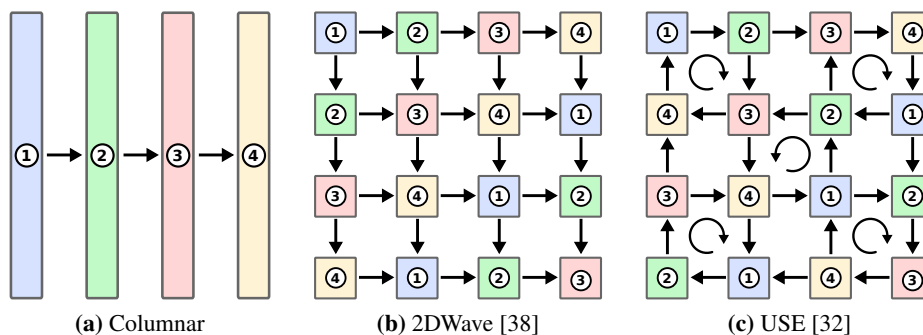


**Figure 1.5:** Example electrode arrangements for 4-phase clocking. The phase of each electrode is indicated. Arrows show the direction of information flow. All are infinitely tileable.

ometries, but it results in a lower bound on the size of a region of a QCA network that has non-trivial dynamics. In zone clocking, our clock zones have minimum dimensions and cannot be arbitrarily assigned based on simulation requirements; for wave clocking, we must expect multiple QCA devices to occupy the region of the rising edge. It is not yet clear how much computation can be reliably achieved within a single clock zone at some desired operational frequency. Such a question requires a greater capacity for estimating the behaviour of larger QCA networks.

Work by Tóth and Lent demonstrated that the inaccuracies in the mean field models resulted from missing inter-cell correlations [36, 40]. Their proposed intermediate model which incorporates a subset of these correlations has proven suc-

cessful at producing more accurate results; however, there remain challenges in applying this approach to general arrangements of QCA cells [41, 42]. In this thesis, we consider an alternate approach to studying the dynamic behaviour of QCA networks in the fully coherent regime. We will investigate QCA clocking from within the framework of quantum annealing, in which performance is governed by particular details of the low energy spectrum.

## **1.2 Thesis Overview**

This thesis is organized as follows. In Chapter 2, a brief overview of the various models and simulation methods used in the study of QCA devices is given, with emphasis on reduced basis approximations of the system Hamiltonian and dynamics. In Chapter 3, we discuss quantum annealing, adiabatic evolution, and present the link to QCA clocking. Chapters 4 and 5 contain a study of silicon dangling bonds and their potential applications for combinatorial logic and nanoscale QCA. In Chapter 6, we perform a detailed investigation of the performance of small 2-state QCA networks under zone clocking, extracting meaningful metrics from the low energy spectrum. In Chapter 7, we discuss one potential approach to studying larger QCA networks: direct hardware simulation on a quantum annealing processor. Finally, in Chapter 8, we develop a methodology for understanding the spectra of QCA networks in terms of contributions from network components, and present a novel method for approximating the low energy spectrum of large QCA networks.

## Chapter 2

# Modelling and Simulation of QCA Devices

For an arrangement of  $N$  devices, each composed of some number of quantum dots with a finite set of possible charge and spin states, the Hamiltonian can be expressed as a Hubbard model in second quantization [43]:

$$\hat{H} = \sum_{m,i} E_0 \hat{n}_{mi,\sigma} - \sum_{m,i \neq j} t_{ij} \hat{a}_{mi,\sigma}^\dagger \hat{a}_{mj,\sigma} + \sum_{m,i} E_Q \hat{n}_{mi,\uparrow} \hat{n}_{mi,\downarrow} + K_c \sum_{m,\langle ij \rangle} \frac{\hat{n}_{mi,\sigma} \hat{n}_{mj,\sigma'}}{|\vec{r}_{mi} - \vec{r}_{mj}|} + K_c \sum_{\langle mk \rangle, i,j} \frac{\hat{n}_{mi,\sigma} \hat{n}_{kj,\sigma'}}{|\vec{r}_{mi} - \vec{r}_{kj}|}, \quad (2.1)$$

where  $\hat{a}_{mi,\sigma}^\dagger$  and  $\hat{a}_{mi,\sigma}$  are the creation and annihilation operators for a spin state  $\sigma$  at the  $i$ 'th dot of the  $m$ 'th device,  $\hat{n}_{mi,\sigma} = \hat{a}_{mi,\sigma}^\dagger \hat{a}_{mi,\sigma}$  is the corresponding number operator, and the  $\vec{r}_{mi}$  give the positions of each dot. The first term accounts for the *on-site* energy of a charge occupying a given dot. The second term represents the energy associated with *tunneling* between two dots within a device. Intuitively, a particle with a given  $\sigma$  is first annihilated at one dot and then created at the other. The third term represents the energy of two charges with differing  $\sigma$  occupying the same dot. Finally, the remaining two terms define the Coulombic interactions of charges respectively within and between devices, where  $K_c = q_e^2/4\pi\epsilon$  for electron charge  $q_e$  and electrical permittivity  $\epsilon$ . Einstein summation is employed over the

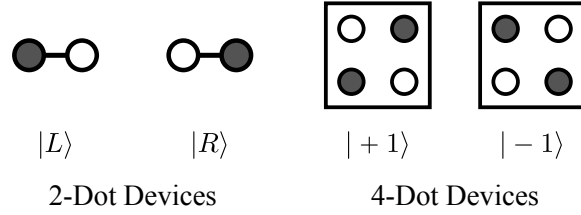


**Figure 2.1:** Example polarization configurations for 2-state QCA devices.

spin states  $\sigma, \sigma'$  for conciseness. This model excludes terms associated with charge hopping between devices.

## 2.1 Reduced Basis Representations

The Hubbard model produces a Hilbert space which is impractically large in dimension for most QCA networks of interest. For example, among the most common model devices considered in QCA is a 4 dot cell containing two charges of opposite spin [43]. In this case, there are 16 possible charge configurations in the single cell Hamiltonian. For  $N$  cells, the full Hilbert space is then  $16^N$  in size. Even finding the ground state of such a system is computationally intractable beyond a handful of devices. Using Lanczos iteration [44], which can make use of the sparsity and Hermitian structure of the Hamiltonian, eigenvalue decomposition is at least as complex as matrix-vector multiplication. In the basis of charge states, the Hamiltonian contains  $16^N$  diagonal elements, and each row of the matrix contains  $6N$  off-diagonal non-zero elements. The off-diagonal elements correspond to states that can be reached by hopping one charge to one of its potential alternate sites in a cell:  $2N$  charges, 3 locations per charge. In total then, matrix-vector multiplication requires  $16^N(1 + 6N)$  multiplications. At 5 devices, we already have about 32.5 million operations per Lanczos iteration. In practice, we assume each device can be modelled using a subset of the full set of charge states.

### 2.1.1 Two-State Approximation

For the 4-dot devices discussed, it has been shown that the ground state can be approximately described within a subspace of the 16 dimension Hilbert space given by the 2 polarization states shown in Fig. 2.1 [43]. The projection of the system

Hamiltonian into this reduced basis is known as the *two-state approximation*. We can express the Hamiltonian of a single 2-state QCA device in the  $\{|+1\rangle, |-1\rangle\}$  basis as

$$\hat{H}_i(t) = -\frac{1}{2}\gamma_i(t)\hat{\sigma}_x + \frac{1}{2}h_i\hat{\sigma}_z = \frac{1}{2} \begin{bmatrix} h_i & -\gamma_i(t) \\ -\gamma_i(t) & -h_i \end{bmatrix}, \quad (2.2)$$

where  $\gamma_i(t)$  is the tunneling energy with  $\gamma_i/\hbar$  a measure of the rate of tunneling between the two polarization states,  $h_i$  is some polarization bias, and the  $\hat{\sigma}_\mu$  for  $\mu \in \{x, y, z\}$  are the Pauli matrices, included for convenience:

$$\hat{\sigma}_x = \begin{pmatrix} 0 & 1 \\ 1 & 0 \end{pmatrix}, \quad \hat{\sigma}_y = \begin{pmatrix} 0 & -i \\ i & 0 \end{pmatrix}, \quad \hat{\sigma}_z = \begin{pmatrix} 1 & 0 \\ 0 & -1 \end{pmatrix}.$$

Devices in this model are clocked by manipulating the tunneling rates  $\gamma_i$ . In the case of metal island QCA, tunneling barriers between the sites could be directly controlled, thereby enabling a simple mechanism for clocking [18, 20]; however, it is not yet clear if this model of clocking is appropriate for nanoscale QCA. For  $N$  cells, we incorporate coupling between polarization states of neighbouring devices via the so-called *kink energy*,  $E_{ij}^k$ , the cost of two cells having opposite polarizations. The Hamiltonian takes the form

$$\hat{H}(t) = -\frac{1}{2} \sum_i \gamma_i(t) \hat{\sigma}_x^i + \frac{1}{2} \left[ \sum_i h_i \hat{\sigma}_z^i - \sum_{\langle ij \rangle} E_{ij}^k \hat{\sigma}_z^i \hat{\sigma}_z^j \right], \quad (2.3)$$

where here  $h_i = \sum_D E_{iD}^k \mathcal{P}_D$  is understood to arise from interactions with fixed-polarization *driver* or input cells, and the  $\hat{\sigma}_\mu^i$  operate on device  $i$ . These Pauli operators are constructed by replacing the  $i$ 'th of  $N$  identity operators in a Kronecker product with the corresponding Pauli matrix:

$$\hat{\sigma}_\mu^i = \hat{I} \otimes \cdots \otimes \hat{\sigma}_\mu \otimes \cdots \otimes \hat{I}.$$

In this form, the polarization of cell  $i$  in the ground state is given as  $\mathcal{P}_i = \langle \hat{\sigma}_z^i \rangle$ . Matrix-vector multiplication in this approximation involves a somewhat more manageable  $2^N(1+N)$  terms. This allows us to handle networks approximately 4 times larger using the same computational resources. In practice, simulations without

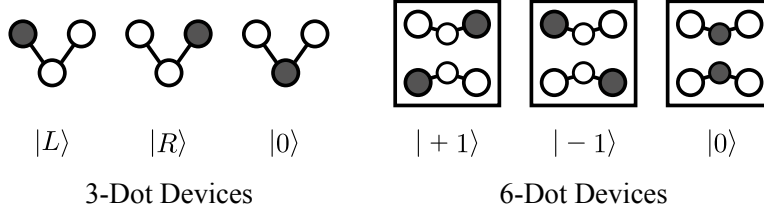


**Figure 2.2:** Example polarization configurations for 3-state QCA devices.

further approximation are feasible for networks of at most 20 or so devices. Note that while Tougaw and Lent also demonstrated that the dynamical behaviour of a driven 3 cell QCA wire in this approximation shows close similarity to results obtained using the full basis [43], the general robustness of the two-state approximation is likely strongly dependent on the particular QCA implementation.

### 2.1.2 Three-State Approximation

Another important model for QCA devices is the *three-state approximation*. In this case, we consider devices which accommodate both two polarization states as well as a third *null* or inactive state. This null state produces no polarization-like interaction with neighbouring devices. An example of such a device and its configurations are shown in Fig. 2.2. It is common to exclude tunneling between polarization states, in which case the Hamiltonian of a 3-state cell can be expressed in the  $\{|+1\rangle, |-1\rangle, |0\rangle\}$  basis as

$$\hat{H}_i(t) = -\gamma_i \hat{\Gamma} + h_i \hat{\mathcal{P}} - \mathcal{C}_i(t) (\hat{\mathcal{N}} - \hat{I}) = \begin{bmatrix} h_i & 0 & -\gamma_i \\ 0 & -h_i & -\gamma_i \\ -\gamma_i & -\gamma_i & \mathcal{C}_i(t) \end{bmatrix}. \quad (2.4)$$

Here  $\gamma_i$  defines the tunneling between the polarized and null states,  $h_i$  is again a polarization bias, and  $\mathcal{C}_i$  describes a modulated clocking field controlling the energy of the null state. The appropriate operators can be expressed as

$$\hat{\Gamma} = \begin{pmatrix} 0 & 0 & 1 \\ 0 & 0 & 1 \\ 1 & 1 & 0 \end{pmatrix}, \quad \hat{\mathcal{P}} = \begin{pmatrix} 1 & 0 & 0 \\ 0 & -1 & 0 \\ 0 & 0 & 0 \end{pmatrix}, \quad \hat{\mathcal{N}} = \begin{pmatrix} 1 & 0 & 0 \\ 0 & 1 & 0 \\ 0 & 0 & 0 \end{pmatrix}.$$

It is clear that  $\hat{\Gamma}$  takes the role of  $\hat{\sigma}_x$  from Eq. (2.2) and  $\hat{\mathcal{P}}$  the role of  $\hat{\sigma}_z$ . The polarization is similarly defined as  $\mathcal{P} = \langle \hat{\mathcal{P}} \rangle$ . Another useful quantity is the *activation* or *population*,  $\mathcal{N} = \langle \hat{\mathcal{N}} \rangle$ . For theoretical manipulations, it can be useful to express these operators in terms of the Gell-Mann matrices:  $\hat{\Gamma} = \hat{\lambda}_4 + \hat{\lambda}_6$ ,  $\hat{\mathcal{P}} = \hat{\lambda}_3$ , and  $\hat{\mathcal{N}} = \frac{1}{3} \left( 2\hat{I} + \sqrt{3}\hat{\lambda}_8 \right)$ . The Gell-Mann matrices are included in Appendix D.1. Details of this method, including considerations for the  $N$  cell Hamiltonian, will be discussed later in Chapter 5. For completeness, the number of non-zero elements in the 3-state Hamiltonian is  $3^N \left( 1 + \frac{4}{3}N \right)$ .

### 2.1.3 Intercellular Hartree-Fock Approximation

While the reduced basis approximations somewhat limit the computational complexity when compared to the full Hubbard model, the space of states remains exponential. There are a number of strategies we might employ to further reduce complexity. Perhaps the most extreme is the Intercellular Hartree-Fock Approximation (ICHA), a ground state approximation method employing the Hartree-Fock method on the  $N$  cell Hamiltonian [15, 35]. It attempts to find the lowest energy state which can be expressed as a product state:  $|\psi_0\rangle = \bigotimes_{i=1}^N |\varphi_i\rangle$ . For the 2-state Hamiltonian, Eq. (2.3), the  $|\varphi_i\rangle$  end up being the ground states of effective cell Hamiltonians

$$\hat{H}_i = -\frac{1}{2}\gamma_i\hat{\sigma}_x^i + \frac{1}{2}\tilde{h}_i\hat{\sigma}_z^i, \quad (2.5)$$

where  $\tilde{h}_i = h_i - \sum_{j \neq i} E_{ij}^k \mathcal{P}_j$  is the effective polarization bias for the current cell polarizations,  $\mathcal{P}_j = \langle \varphi_j | \hat{\sigma}_z | \varphi_j \rangle$ . These polarizations must be computed self-consistently. For these simple  $2 \times 2$  cell Hamiltonians, the ground state can be computed analytically and an expression for  $\mathcal{P}_i$  found:

$$\mathcal{P}_i = \frac{-\tilde{h}_i}{\sqrt{\gamma_i^2 + \tilde{h}_i^2}}. \quad (2.6)$$

The ICHA is known to be highly susceptible to being trapped in higher energy metastable configurations [36], the most well-known of which being a majority gate with uneven input wire lengths. An example of this scenario is shown in Fig. 2.3. If we initially assume all cells to be unpolarized, the polarization of the

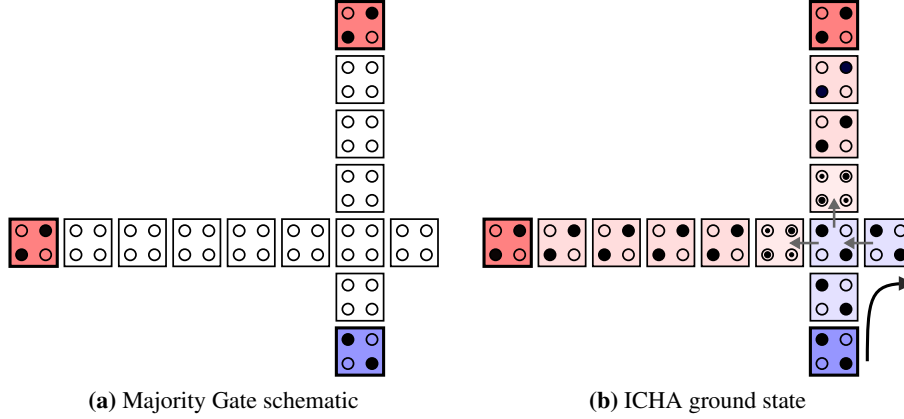


**Figure 2.3:** A majority gate with uneven input lengths exhibits incorrect behaviour using the ICHA. If we start with all cells unpolarized, the shortest input reaches the output cell in fewer iterations of the self-consistency method. The output cell then in turn biases the center cell which blocks the other inputs from contributing. The darker shaded cells here are fixed polarization inputs with  $P = +1$  (red) or  $P = -1$  (blue). In **(b)**, a typical ground state produced with the ICHA is shown. The lighter shading is mainly to help with interpreting the cell polarizations. The two cells adjacent to the cross from the longer inputs tend to be weaker in polarization due to backpressure.

shortest input will reach and polarize the output cell in fewer iterations. From that point, the center cell will always see two equally polarized neighbours and be resistant to flipping polarization, even when the other inputs eventually arrive. A common but non-ideal solution to this is to define clock zones such that, for example, all majority gates have inputs of the same length. This imposes rules on QCA design which have nothing to do with performance but instead merely limitations in the simulation tools.

## 2.2 Dynamics Using Reduced Correlation Models

If we ignore any decoherence mechanism, the dynamics of a network are given by the Schrödinger equation:

$$i\hbar \frac{d}{dt} |\psi\rangle = \hat{H}(t) |\psi\rangle.$$

It is useful to express the dynamics in dimensionless form

$$\tilde{f} \frac{d}{ds} |\psi\rangle = -i\hat{\mathcal{H}}(s)|\psi\rangle, \quad (2.7)$$

where  $s = ft$  for some frequency scale  $f$ ,  $\hat{H}(ft) = \mathcal{E}\hat{\mathcal{H}}(s)$  for energy scale  $\mathcal{E}$ , and  $\tilde{f}$  is a dimensionless characteristic rate defined by  $2\pi\tilde{f} = f/f_0$  with  $f_0 = \mathcal{E}/\hbar = \mathcal{E} \times 241.8\text{THz}/\text{eV}$ . The relevant energy scale is defined by the kink energies of the particular QCA implementation, on the order of tens to hundreds of meV for nanoscale QCA. Regardless of our choice in ordinary differential equation (ODE) solver, we are limited again by the matrix-vector product complexity of a Hamiltonian which is exponential in the QCA network size. When including decoherence effects, it is common to apply the Liouville-von Neumann equation with a relaxation term [29]. It can be expressed in dimensionless form as

$$\tilde{f} \frac{d}{ds} \hat{\rho}(s) = -i[\hat{\mathcal{H}}(s), \hat{\rho}(s)] - \tilde{\xi}[\hat{\rho}(s) - \hat{\rho}_{ss}(s, \hat{\rho})] \quad (2.8)$$

where  $\hat{\rho}_{ss}$  is the steady state density operator and  $2\pi\tilde{\xi} = 1/\tau f_0$  defines the dimensionless relaxation rate for some characteristic time  $\tau$  that it takes the system to relax to its steady state. In general, we allow  $\hat{\rho}_{ss}$  to be a function of both time and the current system state.

### 2.2.1 Coherence Vector Formalism

Due to suspected limited correlations in QCA networks, it has been proposed to express the dynamics in terms of the coherence vector formalism (CVF) [36, 42]. The density operator can be expressed in the basis of the generators of  $\text{SU}(2^N)$ :

$$\hat{\rho}(s) = \frac{1}{2^N} \left[ \hat{I} + \sum_i \lambda_a^i \hat{\sigma}_a^i + \sum_{\langle ij \rangle} K_{ab}^{ij} \hat{\sigma}_a^i \hat{\sigma}_b^j + \dots \right], \quad (2.9)$$

where we employ Einstein summation for the subscripts over the set  $\{x, y, z\}$ . The dynamics of  $\hat{\rho}$  are equivalent to those of the real-valued coefficients:  $\lambda_a^i = \langle \hat{\sigma}_a^i \rangle$ ,  $K_{ab}^{ij} = \langle \hat{\sigma}_a^i \hat{\sigma}_b^j \rangle$ , etc. These coefficients are classified by the number of cells they consider: each cell is assigned a *coherence vector*  $\boldsymbol{\lambda}_i$  containing the 3 single-point

expectation values  $\lambda_a^i$ ; each pair of cells gets a *two-point correlation tensor*  $\mathbf{K}_{ij}$  containing the  $3^2$  two-point correlations  $K_{ab}^{ij}$ ; and so on. The power of this formalism comes in the capacity to limit the number of terms used to approximate  $\hat{\rho}$ . The dynamics of any one of these terms can be computed as

$$\tilde{f} \frac{d}{ds} \Lambda_k(s) = i \langle [\hat{\mathcal{H}}(s), \hat{\Lambda}_k] \rangle - \tilde{\xi} [\Lambda_k(s) - \Lambda_k^{\text{ss}}(s, \hat{\rho})], \quad (2.10)$$

with  $\hat{\Lambda}_k$  any of the operators in Eq. (2.9),  $\Lambda_k$  its expected value, and  $\Lambda_k^{\text{ss}} = \text{Tr} \hat{\rho}_{ss} \hat{\Lambda}_k$ . Only the lowest order approximation of the dynamics is usually considered. This produces a dynamic equivalent of the ICHA, including only the coherence vectors, and excluding two-point and higher correlations. The resulting system of equations is given by

$$\tilde{f} \frac{d}{ds} \boldsymbol{\lambda}_i = \boldsymbol{\Gamma}_i \times \boldsymbol{\lambda}_i - \tilde{\xi} (\boldsymbol{\lambda}_i - \boldsymbol{\eta}_i), \quad (2.11)$$

with  $\boldsymbol{\Gamma}_i = \left[ -\gamma_i, \quad 0, \quad \frac{1}{2} (h_i - \sum_{n \neq i} E_{ni}^k \lambda_z^n) \right]$  and  $\boldsymbol{\eta}_i$  the local dissipation vector. Absent dissipation, this has the nice property that each cell can be seen to evolve under an instantaneous Hamiltonian dependent on the  $\lambda_z^i$  values of neighbouring cells. These are precisely our ICHA single-cell Hamiltonians:

$$\hat{\mathcal{H}}_i = -\frac{1}{2} \gamma_i \hat{\sigma}_x + \frac{1}{2} \left( h_i - \sum_{j \neq i} E_{ij}^k \lambda_z^j \right) \hat{\sigma}_z, \quad (2.12)$$

where we note  $\mathcal{P}_i = \lambda_z^i$  by definition. This guarantees unitary evolution of the system state.

### 2.2.2 Higher Order Models

By excluding all higher order correlations, the coherence vector formalism suffers all the same issues as the self-consistent ICHA approach for the ground state. As an attempt to resolve this issue, Tóth *et al.* detail an approach employing a restricted set of the correlation tensors [40]. There are two main concepts to apply. First, we consider the equations obtained from Eq. (2.10) for higher order correlation tensors. Expressions of  $i \langle [\hat{\mathcal{H}}, \hat{\Lambda}] \rangle$  can be found for any given  $K_{ab}^{ij}$ ,  $K_{abc}^{ijk}$ , etc. by applying a set of rules summarized in Fig. 2.4. These rules translate patterns in

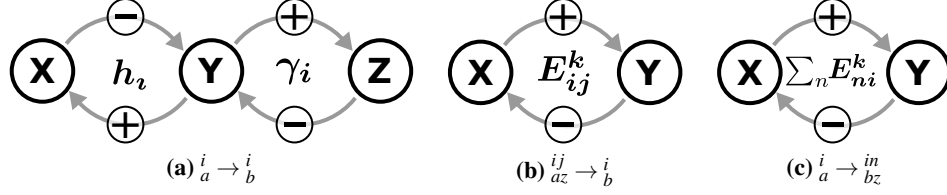


**Figure 2.4:** Super and subscript pattern conversion rules for generating equations for Eq. (2.10). Each matching pattern in a given  $K_{ab}^{ij}$ ,  $K_{abc}^{ijk}$ , etc. produces a single term in  $i\langle[\hat{\mathcal{H}}, \hat{\Lambda}]\rangle$ . The order of superscript-subscript pairs is arbitrary. Each arrow describes a conversion of a subscript  $a \rightarrow b$  which produces a term with a given signed weight. In (c), the sum is over all cells which are not in the original term.

the super-subscript pairs of  $K_{abc\dots}^{ijk\dots}$  into corresponding terms in Eq. (2.10). Take  $K_{xz}^{ij}$  as an example, which includes components from all rule-sets. From Fig. 2.4(a), we have  $K_{xz}^{ij} \rightarrow -h_i K_{yz}^{ij}$  and  $K_{xz}^{ij} \rightarrow -\gamma_i K_{xy}^{ij}$ ; from (b), we have  $K_{xz}^{ij} \rightarrow E_{ij}^k \lambda_y^i$ ; finally, from (c) we get the sum,  $K_{xz}^{ij} \rightarrow \sum_{n \notin \{ij\}} E_{ni}^k K_{yz}^{ijn}$ . We arrive at the dynamic equation

$$\tilde{f} \frac{d}{ds} K_{xz}^{ij} = -\gamma_i K_{xy}^{ij} - h_i K_{yz}^{ij} + E_{ij}^k \lambda_y^i + \sum_{n \notin \{ij\}} E_{ni}^k K_{yz}^{ijn} - \tilde{\xi} (K_{xz}^{ij} - K_{xz}^{ij}|_{ss}).$$

Appropriate definitions for the steady state term  $K_{xz}^{ij}|_{ss}$  and similar can be found in Ref. [45]. The equations for all the two-point correlations are summarized in Appendix D.2. These rules make it trivial to automatically generate the relevant equations for any order of included correlations. The second important concept lies in assessing the so-called *correlation tensor propers*:

$$M_{ab}^{ij} = \langle (\hat{\sigma}_a^i - \lambda_a^i)(\hat{\sigma}_b^j - \lambda_b^j) \rangle = K_{ab}^{ij} - \lambda_a^i \lambda_b^j, \quad (2.13a)$$

$$\begin{aligned} M_{abc}^{ijk} &= \langle (\hat{\sigma}_a^i - \lambda_a^i)(\hat{\sigma}_b^j - \lambda_b^j)(\hat{\sigma}_c^k - \lambda_c^k) \rangle \\ &= K_{abc}^{ijk} - \left( K_{ab}^{ij} \lambda_c^k + K_{ac}^{ik} \lambda_b^j + K_{bc}^{jk} \lambda_a^i \right) + 2\lambda_a^i \lambda_b^j \lambda_c^k, \end{aligned} \quad (2.13b)$$

and so on. These terms relate to the strength of specific correlations. If we either set or assume these terms to be zero, we can approximate higher order correlations as combinations of lower order terms: e.g.  $K_{ab}^{ij} = M_{ab}^{ij} + \lambda_a^i \lambda_b^j \approx \lambda_a^i \lambda_b^j$ . In Fig. 2.5, we see the dependence of the tensors for two-point interactions, before and after

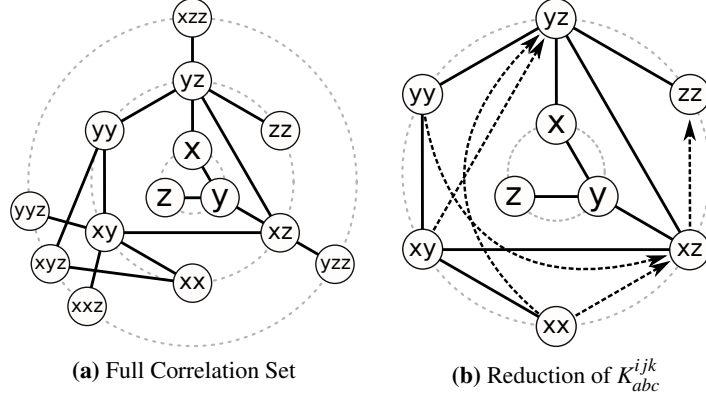


**Figure 2.5:** Graph representations of the interdependence of correlation tensors. All terms related to two-point correlations are shown in (a). Edges indicate a dependence of the dynamics of one node on the current values of the other. The structure of the conversion rules makes all dependencies symmetric. If three-point correlations are neglected, additional dependencies are introduced. Each arrow in (b) represents a new direct dependence of the root node: e.g.  $xz$  is now dependent on  $zz$ . These dependencies tend not to be symmetric. The new single-point correlation dependences are not shown.

applying Eq. (2.13) to approximate  $K_{abc}^{ijk}$ . Similar constructions can be made for correlations in 3-state QCA.

Tóth demonstrated that the difficulties experienced with the ICHA are primarily due to missing correlations in critical circuit components such as majority gates [36]. By reintroducing even just the two-point correlations, much of these issues are resolved. There are, however, caveats when attempting to apply this method.

### 2.2.3 Challenges with the CVF

It has previously been noted that calculated values of  $M_{xy}$  and  $M_{yz}$  during simulations of 2-state dynamics tend to be much smaller than other two-point correlations [36, 41, 42]. It was argued by Karim that  $K_{xy}$  and  $K_{yz}$  are therefore good candidates for approximation with  $\lambda_a$  values. We need to be careful making such arguments, for reasons that follow. From Eq. (2.11), we see that the cell polarizations,  $\lambda_z^i$ , are essentially just the integrals of  $\gamma_i(s)\lambda_y^i(s)$ . As the values of  $\gamma_i$  are independent

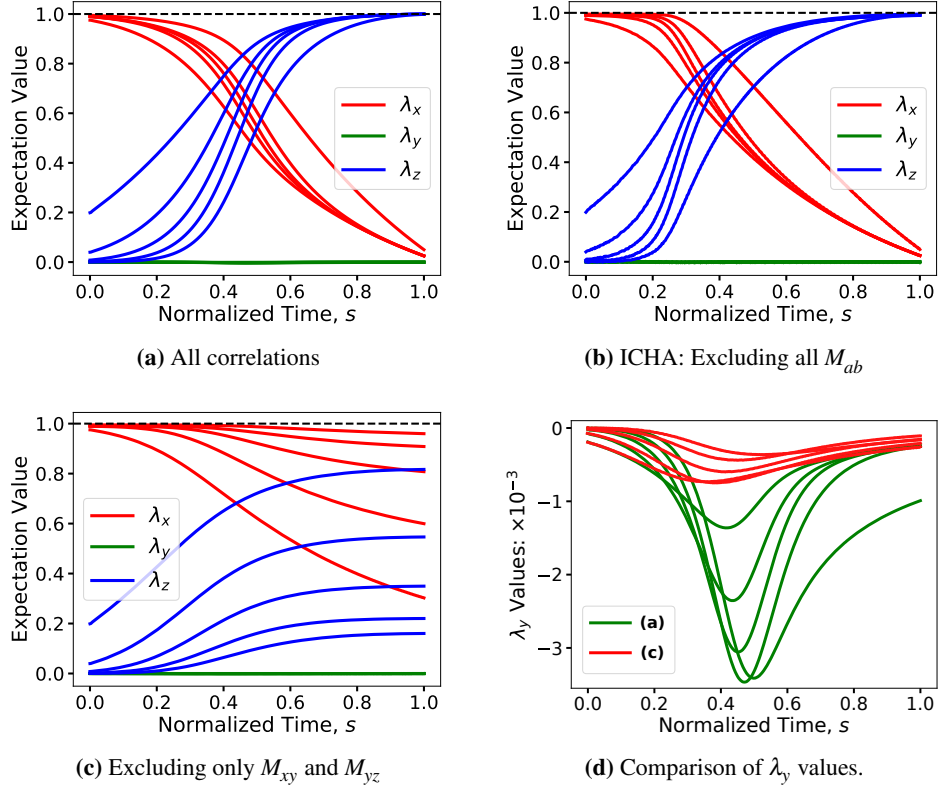


**Figure 2.6:** Simulation of a five cell QCA wire using a few correlation models excluding any dissipation. Each of (a-c) gives the coherence vector values for each cell in the wire throughout a clocking protocol discussed in Chapter 6; the details are otherwise unimportant here. In (d), we show that the arbitrary exclusion of  $M_{xy}$  and  $M_{yz}$  results in smaller amplitude  $\lambda_y$ , and thus a failure of the wire to fully polarize. Including all two-point correlations produces a result similar to (a). The value of  $\tilde{f}$  in these results is set at  $1 \times 10^{-3}$ , slow enough to be approximately adiabatic.

of  $\tilde{f}$ , we see that for a cell to go from unpolarized to fully polarized over a clock cycle, the scale of the  $\lambda_y$  values must be effectively proportional to  $\tilde{f}$ : i.e. if the clock takes twice as long, the values of  $\lambda_y^i$  must be roughly half as large. In fact, it is trivial to show (see Appendix B.3) that for any energy eigenstate of a 2-state Hamiltonian, the expected value of any product of Pauli operators with an odd number of  $\hat{\sigma}_y$  terms is exactly zero. It follows that any  $M_{abc\dots}$  term with an odd number of  $y$  subscripts will be small for a sufficiently slowly clocked system. The values of  $\lambda_y^i$ ,  $M_{xy}^{ij}$ , and  $M_{yz}^{ij}$  are all small for precisely the same reasons and under the same circumstances. The same argument that leads to negating  $M_{xy}$  would also justify setting  $\lambda_y^i$  to zero, neglecting all dynamics entirely. The same discussion applies to the 3-state Hamiltonian where  $\hat{\sigma}_y$  is replaced by any linear combination of  $\{\hat{\lambda}_2, \hat{\lambda}_5, \hat{\lambda}_7\}$  with real coefficients. In Fig. 2.6, simulations for a 5-cell wire using different included correlations demonstrate this result.

There is a more general issue when identifying correlations which may be excluded. As  $K_{abc\dots}^{ijk\dots}$  is the expected value of a product of Pauli operators, the values must satisfy certain constraints. For example, as each of the Pauli operators have eigenvalues of  $\pm 1$ , it follows that for any properly normalized state,  $-1 \leq K_{abc\dots}^{ijk\dots} \leq 1$ . More complicated relationships are satisfied by groups of the  $K_{abc\dots}^{ijk\dots}$ . The simplest relates the  $\lambda_a^i$  for any given device:  $(\lambda_x^i)^2 + (\lambda_y^i)^2 + (\lambda_z^i)^2 \leq 1$ . Whatever the values of  $M_{abc\dots}^{ijk\dots}$ , they must satisfy such normalization constraints. Arbitrarily assigning values without additional considerations can easily lead to physically non-viable states.

## 2.2.4 Multicellular ICHA Approach

One well behaved approach to incorporating additional necessary correlations which maintains all normalisation constraints is to use a generalized variation of the ICHA employing multi-cell Hamiltonians [36, 41]. A general interpretation of the ICHA can be seen as two approximations: (1) the system Hamiltonian is a sum, in particular a Kronecker sum, of cell Hamiltonians; and (2), the system state is a product state of individual cell states. These approximations can be summarized by the

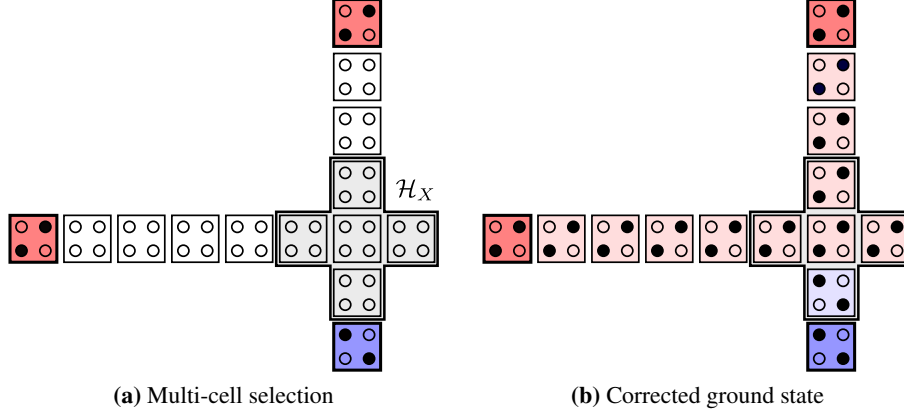


**Figure 2.7:** Describing the entire 5-cell cross using a single multi-cell Hamiltonian, the errors observed using the ICHA can be avoided.

following equations:

$$\hat{\mathcal{H}} = \bigoplus_{m=1}^M \hat{\mathcal{H}}_m, \quad |\Psi\rangle = \bigotimes_{m=1}^M |\varphi_m\rangle, \quad \tilde{f} \frac{d}{ds} |\varphi_m\rangle = -i \hat{\mathcal{H}}_m |\varphi_m\rangle, \quad (2.14)$$

where, for example,  $\bigoplus_{m=1}^3 \hat{\mathcal{H}}_m = \hat{\mathcal{H}}_1 \otimes \hat{I} \otimes \hat{I} + \hat{I} \otimes \hat{\mathcal{H}}_2 \otimes \hat{I} + \hat{I} \otimes \hat{I} \otimes \hat{\mathcal{H}}_3$  denotes the multi-term Kronecker sum, and  $\bigotimes_{m=1}^3 |\varphi_m\rangle = |\varphi_1\rangle \otimes |\varphi_2\rangle \otimes |\varphi_3\rangle$  is the Kronecker product. For the traditional ICHA, each  $\hat{\mathcal{H}}_m$  is a single cell Hamiltonian given by Eq. (2.5) and  $M = N$  is the number of non-fixed-polarization cells. In general,  $\hat{\mathcal{H}}_m$  can describe any group of cells rather than a single cell. In Fig. 2.7, we show one multi-cell choice which solves the issues observed in the majority gate with uneven input lengths. Each group Hamiltonian is treated as a normal multi-cell QCA network where, as with the ICHA, instantaneous cell polarizations produce additional contributions to the effective  $h$  biases in neighbouring  $\hat{\mathcal{H}}_m$ . More detail on a conceptually similar approach will be seen in Chapter 8. In the language of the previous discussion, this multi-cell ICHA neglects all  $M_{abc\dots}^{ijk\dots}$  involving cells in different groups; all correlations within groups are maintained. In addition, as each  $|\varphi_m\rangle$  simply evolves under a Schrödinger equation for an effective Hamiltonian, the evolution is unitary and all normalisation-like constraints are satisfied automatically.

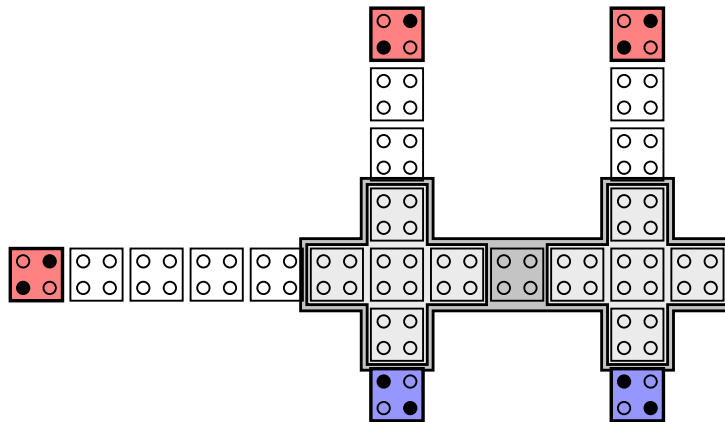


**Figure 2.8:** Two majority gates in series with potential multi-cell groups shown. Here it is necessary to combine the two majority gates into a single multi-cell group in order to avoid incorrect behaviour.

This approach is effective at resolving issues with individual majority gates, and similar cases such as certain inverters and fan-outs; however, there are known problems. As an example, Karim describes two majority gates in series [41]. A similar arrangement is depicted in Fig. 2.8. If the multi-cell groups are chosen simply to be the two majority gates, then for certain input lengths and polarizations we arrive at a similar problem to that of the ICHA. The order of events is roughly as follows. The rightmost negative input initially polarizes the second gate before its corresponding positive input arrives. The now negative second gate biases the output of the first gate. If this bias arrives before both of the positive inputs, the first gate will eventually remain in a situation where it sees two negative and two positive inputs. The output of the first gate remains negative, as will then be the output of the second gate. This can be corrected by increasing the distance between the majority gates, but we then again would be constraining our design choices to what a solver can handle. Alternatively, if both majority gates, as well as the connecting wire, are included in a single multi-cell group, then the correct behaviour is achieved. There remain two issues here: (1) it is not necessarily trivial to identify the set of groups which *avoid all problems*; and (2), these larger combined groups are constrained in size by the largest Hamiltonian size we can handle for matrix-vector multiplication. These issues are partially addressed in Chapter 8.

## Chapter 3

# QCA Clocking as Quantum Annealing

Adiabatic quantum computing (AQC) describes an approach to finding the ground state of a complicated system by slowly evolving an initially simple Hamiltonian into one of interest [46, 47]. In practice, the system of interest is typically constructed so that its ground state encodes the solution to some NP problem. In theory, the ground state of any such system is guaranteed to be found if the system is isolated from its environment and the evolution is sufficiently slow [48]; however, the exact meaning of *sufficiently slow* relates to details of the low energy eigenspectrum (LES): see Section 3.1.1. Quantum annealing (QA) is a heuristic approach which employs quantum evolution to attempt to find the lowest energy configuration of a given energy function, without strictly adhering to the conditions required for AQC [49]. QA can be implemented numerically as in simulated quantum annealing [50–52], or in hardware [53, 54]. It can be interpreted as an attempt to realise the ideal of AQC with the understanding that real systems cannot always be completely isolated, that the strict constraints on annealing speed demanded by AQC are not necessarily practical for all problems, and that often a sufficiently low energy approximation of the true optimum is good enough. In this chapter, a brief overview of the QA protocol is presented, and the link between QA and QCA clocking is demonstrated.

### 3.1 Quantum Annealing

Our goal is to find the ground state of a Hamiltonian of interest,  $\hat{\mathcal{H}}_P$ . We begin with some simple initial Hamiltonian,  $\hat{\mathcal{H}}_I$ , with an easy to achieve ground state. Often, this ground state is an equal superposition of all the eigenstates of  $\hat{\mathcal{H}}_P$ . The time-dependent Hamiltonian of the system can be expressed as

$$\hat{\mathcal{H}}(s) = A(s)\hat{\mathcal{H}}_I + B(s)\hat{\mathcal{H}}_P, \quad (3.1)$$

where  $A(s)$  and  $B(s)$  define the *annealing schedule* satisfying  $A(0)/B(0) \gg 1$  and  $B(1)/A(1) \gg 1$ . The quantity  $A(s)/B(s)$  plays a similar role in QA to the temperature in simulated annealing (SA).

#### 3.1.1 The Adiabatic Theorem

The *guarantee* of finding the ground state is provided by the quantum adiabatic theorem. A complete proof is not presented here, but it is informative to see the main idea. Following the approach of Born and Fock [48], we express the quantum state of the system in the basis of instantaneous eigenstates of  $\hat{\mathcal{H}}(s)$ :

$$|\psi(s)\rangle = \sum_n c_n(s) |\varphi_n(s)\rangle e^{-i\theta_n(s)/\tilde{f}}, \quad (3.2)$$

where  $\hat{\mathcal{H}}(s)|\varphi_n(s)\rangle = E_n(s)|\varphi_n(s)\rangle$  and  $\theta_n(s) = \int_0^s E_n(s') ds'$ . The dynamics of the coefficients  $c_n$  can be found by differentiating Eq. (3.2):

$$\frac{d}{ds}c_n = -c_n \langle \varphi_n | \frac{d}{ds} \hat{\mathcal{H}} | \varphi_n \rangle - \sum_{m \neq n} c_m \frac{\langle \varphi_n | \frac{d}{ds} \hat{\mathcal{H}} | \varphi_m \rangle}{E_m - E_n} e^{-i(\theta_m - \theta_n)/\tilde{f}}. \quad (3.3)$$

The first term can be set to zero by adding an arbitrary phase  $e^{i\phi_n(s)}$  to each eigenstate: see Ref. [55]. If we assume that we start in the ground state,  $c_0(0) = 1, c_{n \neq 0}(0) = 0$ , and integrate in the limit of small  $\tilde{f}$ , we eventually obtain

$$c_{n \neq 0}(s) = i\tilde{f} \left[ T_n(0) - e^{-i(\theta_n(s) - \theta_0(s))/\tilde{f}} T_n(s) \right] + O(\tilde{f}^2) \quad (3.4)$$

where we define the *transition parameters*

$$T_n(s) = \frac{\langle \varphi_n | \frac{d}{ds} \hat{\mathcal{H}} | \varphi_0 \rangle}{(E_n - E_0)^2}. \quad (3.5)$$

Here the  $\hat{\mathcal{H}}$ ,  $E_n$ , and hence also  $T_n$  are assumed to be dimensionless. In full units, the  $T_n$  are scaled by the ratio  $f/\mathcal{E}$  of the frequency and energy scales. In Eq. (3.4), these scale factors are ultimately absorbed into  $\tilde{f}$ . Though not strictly necessary for this discussion, it is useful to note

$$|c_{n \neq 0}(s)| = \tilde{f} |T_n(s)| [1 + O(|T_n(0)|/|T_n(s)|)] + O(\tilde{f}^2) \quad (3.6)$$

and that typically either  $T_n(0)$  is small as a result of the choice in annealing schedule, or at least  $T_n(0)/T_n(s)$  is small when  $c_n(s)$  is significant. The probability of being in the ground state is simply  $P_0(s) = |c_0(s)|^2 = 1 - \sum_{n \neq 0} |c_n(s)|^2$ , and the evolution is adiabatic if  $P_0(s)$  remains sufficiently close to 1. That is, the  $|c_n(s)|$  are all sufficiently small. We then arrive at the usual condition for adiabaticity:

$$\max_{s, n \neq 0} |c_n(s)| \propto \tilde{f} \max_{s, n \neq 0} \frac{|\langle \varphi_n | \frac{d}{ds} \hat{\mathcal{H}} | \varphi_0 \rangle|}{(E_n - E_0)^2} < \delta \quad (3.7)$$

For some small  $\delta \ll 1$ . This in turn can be reinterpreted as an upper bound on the characteristic rate:

$$\tilde{f} < \tilde{f}_{max} \sim \min_{s, n \neq 0} \frac{(E_n - E_0)^2}{|\langle \varphi_n | \frac{d}{ds} \hat{\mathcal{H}} | \varphi_0 \rangle|}. \quad (3.8)$$

This condition is often simplified to the softer bound  $\tilde{f}_{max} = O(\Delta_0^2/\sigma_{max})$  where  $\Delta_0 = \min_s (E_1 - E_0)$  is the smallest energy gap between the ground and first excited state and  $\sigma_{max} = \max_s \|\frac{d}{ds} \hat{\mathcal{H}}\|_2$  is the largest  $L_2$  matrix norm of  $\frac{d}{ds} \hat{\mathcal{H}}(s)$  [56].

### 3.1.2 Landau-Zener Approximation for Diabatic Transitions

Determining a specific value for  $\tilde{f}_{max}$  requires additional information about the particular eigenspectrum. The simplest model with an analytic solution was separately presented by Landau [57] and Zener [58]. The Landau-Zener approximation is a simplification of a two state avoided level crossing, shown in Fig. 3.1, with two assumptions: (1) the energy difference between the two states is a linear function

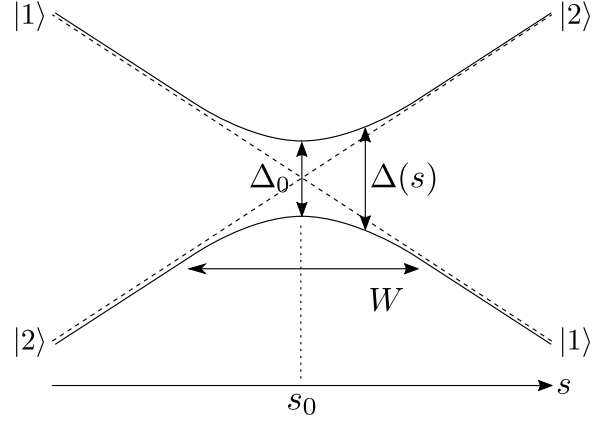


**Figure 3.1:** Schematic avoided level crossing described in the Landau-Zener approximation. It is assumed that the ground and excited states swap during the crossing. The dashed lines show the energies of  $|1\rangle$  and  $|2\rangle$ . The coupling term opens a gap at the point of crossing, producing a hyperbolic energy gap in the eigenenergies, shown with the solid lines.

of time:  $\langle 2|\hat{\mathcal{H}}|2\rangle - \langle 1|\hat{\mathcal{H}}|1\rangle = \alpha \cdot (s - s_0)$ ; and (2), the coupling term is a non-zero constant determined by the minimum gap:  $\langle 1|\hat{\mathcal{H}}|2\rangle = \pm \frac{1}{2}\Delta_0$ . Under these assumptions, the energy gap between the two eigenstates takes the form of a hyperbola:

$$\Delta(s) = \Delta_0 \sqrt{1 + \frac{1}{W^2}(s - s_0)^2}, \quad (3.9)$$

where  $W$  is a measure of the width of the crossing. The probability of a *diabatic* transition out of the ground state can be expressed analytically as

$$P_{g \rightarrow e} = e^{-2\pi\Delta_0 W / 4\tilde{f}}, \quad (3.10)$$

and the appropriate bound on the annealing rate for a defined adiabaticity,  $P_A$ , is

$$\tilde{f}_{max} = \frac{\pi\Delta_0 W}{-2\ln(1 - P_A)} \quad (3.11)$$

### 3.1.3 Special Case of Quadratic Optimization

One important class of NP problems are those that can be expressed in terms of quadratic unconstrained binary optimization (QUBO). A large set of challenging and important problems can be mapped, either exactly or as an approximation, to QUBO problems: graph partitioning and colouring [59], Hamiltonian cycles and travelling salesman [60], protein folding [61], boolean satisfiability (k-SAT) [62], integer factorization [63], and more [62, 64, 65]. In general, QUBO involves the minimization of a quadratic energy function

$$E(\mathbf{x}) = \sum_i b_i x_i + \sum_{\langle ij \rangle} Q_{ij} x_i x_j \quad (3.12)$$

with variables  $x_i$  in either  $\{0, 1\}$  or  $\{\pm 1\}$ , exchangeable under a linear transformation, and  $b_i$  and  $Q_{ij}$  some real-valued weights. The optimal solution exactly corresponds to the ground state of an Ising model, with Hamiltonian

$$\hat{\mathcal{H}}_{\text{Ising}} = \sum_i h_i \hat{\sigma}_z^i + \sum_{\langle ij \rangle} J_{ij} \hat{\sigma}_z^i \hat{\sigma}_z^j. \quad (3.13)$$

If the QUBO problem is expressed in the  $\{\pm 1\}$  basis, then  $h_i = b_i$  and  $J_{ij} = Q_{ij}$  up to some positive scaling factor. As a QA problem, it is practical to begin in a superposition of all possible solutions of Eq. (3.12):  $|\psi(0)\rangle = \sum_n |\mathbf{x}_n\rangle / 2^{N/2}$ , summed over all  $2^N$  possible binary vectors. This corresponds to the ground state of  $\hat{\mathcal{H}}_I = -\sum_i \hat{\sigma}_x^i$ , which defines a suitable initial Hamiltonian. The full time-dependent Hamiltonian can be expressed as

$$\begin{aligned} \hat{\mathcal{H}} &= \frac{1}{2}A(s)\hat{\mathcal{H}}_I + \frac{1}{2}B(s)\hat{\mathcal{H}}_{\text{Ising}} \\ &= -\frac{1}{2}A(s)\sum_i \hat{\sigma}_x^i + \frac{1}{2}B(s)\left[\sum_i h_i \hat{\sigma}_z^i + \sum_{\langle ij \rangle} J_{ij} \hat{\sigma}_z^i \hat{\sigma}_z^j\right], \end{aligned} \quad (3.14)$$

with the factors of  $1/2$  added for convention. This is the so-called transverse Ising spin glass (TISG) or sometimes transverse field Ising model: see for example Ref. [66]. This model is, by far, the most widely studied application of QA. It is simultaneously simple to implement as well as powerful due to its link to QUBO. It also describes the operational Hamiltonian provided by the quantum processing

unit (QPU) developed by D-Wave Systems Inc. [54, 67].

## 3.2 QCA Clocking

As discussed in Chapter 1, there are two main approaches considered for clocking QCA networks: zone clocking, and dynamic wave clocking. The relevant terms for clocking are the tunneling rates  $\gamma_i(s)$  and null state energies  $\mathcal{C}_i(s)$  for 2 and 3-state QCA respectively. The distinction between zone and wave clocking is fundamentally the same in both models; we consider 2-state clocking for simplicity.

### 3.2.1 Zone Clocking

In zone clocking, all cells within a single clock zone satisfy  $\gamma_i(s) = \gamma_\phi(s)$  for one of the clock phases. By comparing Eq. (2.3) and Eq. (3.14), we see that zone clocking in the 2-state approximation exactly corresponds to QA with a TISG model. A suitable mapping is given by

$$A(s) = \gamma_\phi(s), \quad B(s) = 1, \quad h_i = h_i^{QCA}, \quad J_{ij} = -E_{ij}^k. \quad (3.15)$$

3-state QCA zone clocking is somewhat different and will be discussed in more detail in Chapter 5. It can, however, still be understood as a QA problem, where the system is initialized with all cells in the null state,  $|\psi(0)\rangle = \otimes_i |0\rangle$ , and slowly transitioned towards a fully polarized final state.

### 3.2.2 Wave Clocking

For wave clocking, each cell experiences a clock dependent on its position:  $\gamma_i(s) = \gamma(s, \vec{r}_i)$ . The exact dependence is determined by the floor-plan of the clocking electrodes: see Fig. 1.5. In general, wave clocking cannot be expressed in the form of Eq. (3.1); however, the adiabatic theorem, as well as the concepts of avoided level crossings and diabatic transitions, still apply.

## Chapter 4

# Dangling Bonds on Hydrogen Passivated Silicon

So far, we have left ambiguous the actual structure of any physical QCA implementation. In this chapter we discuss a recent and promising candidate architecture for nanoscale QCA. Work by Wolkow *et al.* has made possible the precise fabrication of arrangements of silicon dangling bonds (SiDBs) on hydrogen passivated silicon substrate: H-Si(100)- $2\times 1$  [68–70]. A schematic of the relevant surface structure is shown in Fig. 4.1. Each SiDB is constructed by applying a voltage pulse through a scanning tunneling microscope (STM) tip positioned over a surface hydrogen, desorbing the hydrogen and leaving exposed a dangling bond [70–73]. The possible locations of SiDBs are constrained by the lattice geometry. The case for H-Si(100)- $2\times 1$  is shown in Fig. 4.1(b); however, alternate geometries such as the hexagonal lattice of H-Si(111) and its surface reconstructions could be of potential interest [74]. It has been demonstrated that particular patterns of SiDBs are capable of reproducing logic functions, such as the binary wires and OR gate described and investigated by Huff *et al.* [28]. The potential application of SiDBs as an architecture for nanoscale QCA has also been previously proposed [14, 27], with a simple biased QCA cell comprised of 4 SiDBs studied. Further details on fabrication can be found in the literature [68, 70, 75]. This chapter is structured in order to highlight both the properties of the SiDB architecture as well the capabilities of the simulation methods developed by members of Walus Lab. These methods

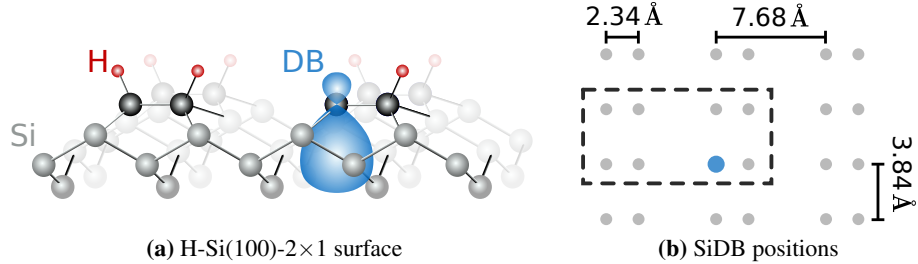


**Figure 4.1:** Hydrogen atoms cap the top-most layer in  $2 \times 1$  reconstructed Si(100). By applying a current through STM tip, surface hydrogen is desorbed exposing a dangling bond with charge states in the band gap. The dimensions and possible positions for created SiDBs are indicated in (b).

are included in the design tool discussed in Ref. [2]. Wherever appropriate, the models and simulated results are presented immediately following the theoretical discussion and experimental results.

## 4.1 Charge States of SiDB Arrangements

The core idea behind implementing logic using arrangements of the SiDB structures is relatively simple. Each SiDB can contain some number of electrons and take an appropriate charge state. The electrons in neighbouring SiDBs experience Coulombic repulsion, coupling the charge states and making certain charge configurations more favourable than others. Tunneling between the SiDBs as well as transport between the surface and available states in the bulk result in a capacity for the system to tend towards a low energy configuration. Here we discuss the nature of the SiDB charge states, experimental observations of the charge configurations of multi-SiDB arrangements, as well as a simple model for predicting these configurations.

### 4.1.1 The Preferred Population of an SiDB

Depending on the doping of the substrate, the distribution of charge in the nearby surface, and any applied bias in an STM or atomic force microscope (AFM) tip, SiDBs have been demonstrated to take on one of three charge states [27, 75]: an

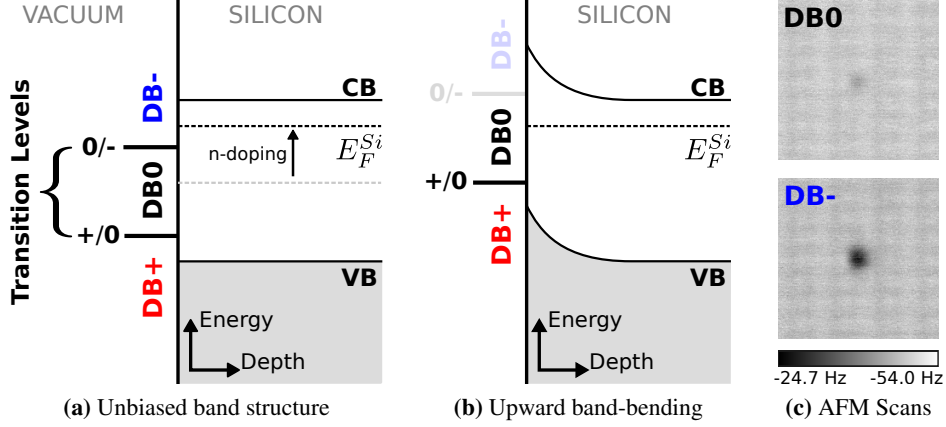


**Figure 4.2:** Schematic of the SiDB charge configurations and the band structure of the silicon substrate. The charge transition levels are known to lie in the gap between the valence and conduction bands. The bulk Fermi level,  $E_F^{Si}$  is a function of the doping and establishes the charge state of an isolated SiDB absent other effects. Additional interactions at the surface are taken both to shift the transition levels relative to  $E_F^{Si}$  as well as induce band-bending, shown in (b). In (c), we show AFM scans of an isolate SiDB at different surface-tip biases.

unoccupied positive state (DB+), singly occupied neutral state (DB0), and a doubly occupied negative state (DB-). We use *population* to describe the number of charges in an arrangement of SiDBs. The charge transition levels between these states are known to lie in the band gap of the bulk silicon [27]. It is argued that this isolates the surface charge states from the bulk, allowing for discrete and stable charge population in the surface [76]. A schematic of the band structure of the silicon bulk with the appropriate charge transition levels can be seen in Fig. 4.2.

Absent all other influences, a single isolated SiDB takes on a charge state determined by the position of the Fermi energy of the doped silicon bulk with respect to the transition levels [28]. For example, if the Fermi energy lies between the two transition levels, than a double occupied DB- SiDB should eventually lose one electron to the bulk, and any unoccupied DB+ SiDB should eventually take on an electron from the bulk. In this way, the “default” charge state is tunable by controlling the doping during fabrication. Further band-bending can result in a shift of these transition levels with respect to the Fermi energy, and thereby change the

preferred charge state. A number of factors can contribute to band-bending near the surface, such as tip induced effects [1, 77] or charge interactions at the surface [78]. Understanding how these interactions adjust the energy landscape of the surface is essentially to predicting the behaviour of these devices.

#### 4.1.2 Stable Configurations of Interacting SiDBs

The experimental results of Huff *et al.* regarding their OR gate implementation are included in Fig. 4.3. In these, and all other experimental results, the doping of the substrate produces a Fermi level above the (0/-) transition level, resulting in a preferred DB- charge state. Constant current STM is employed to visualize the locations of created SiDBs, whereas non-contact AFM is suitable for distinguishing between DB0 and DB- states. See Ref. [1] for a discussion on the conditions under which AFM imaging can be expected to influence the surface configuration. There are two qualitative observations that can be made: (1) not all SiDBs are doubly occupied; and (2), those that are seem to be fairly spread out.

Non-neutral SiDBs interact through Coulombic repulsion. These interactions result in shifts in the transition levels of each SiDB with DB- or DB+ neighbours. In Ref. [28], measurements were made of the shift in the (0/-) transition level in a test SiDB at various distances from a nearby DB- SiDB. The amount of shift was found to be consistent with a screened Coulomb potential of the form

$$\Delta E(r) \equiv q_e V = \frac{K_c}{r} e^{-r/\lambda_{TF}}, \quad (4.1)$$

with  $K_c \cdot \epsilon_r = 1.44 \text{ eV nm}$ ,  $r_{ij}$  the SiDB separation, and both the relative permittivity  $\epsilon_r$  and Thomas-Fermi screening wavelength  $\lambda_{TF}$  fit to experimental data. Values of  $\epsilon_r = 5.6$  and  $\lambda_{TF} = 5 \text{ nm}$  were reported. In Ref. [78], Huff *et al.* measured this shift in the presence of various surface defects, each having its own fit parameters. For SiDB-SiDB interactions, the appropriate values were  $\epsilon_r = 4.1 \pm 0.2$  and  $\lambda_{TF} = 1.8 \pm 0.1$ . These two sets of values were extracted from experiments on different regions of the H-Si(100)- $2 \times 1$  surface and are significantly different. We must allow then that for different samples, and potentially different locations on each sample, the physical parameters necessary for modelling may vary.

If we approximate a DB- state as a single electron at the center of a host silicon

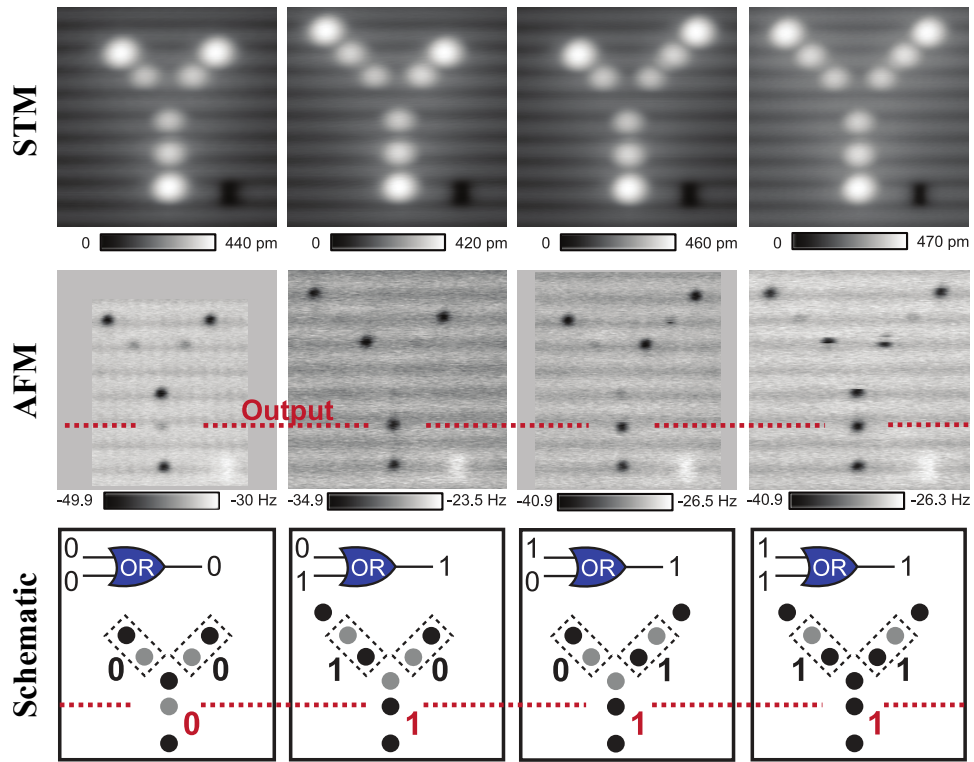


**Figure 4.3:** Experimentally observed charge configurations for the OR gate designs by Huff *et al.* [28]. In the **top** row, constant current STM scans reveal the locations of the exposed dangling bonds. The inputs of the gate are defined by the presence or absence of perturber SiDBs at the top: see the schematic representations on the **bottom** row for clarity. In the **middle** row, non-contact AFM reveal the individual charge states. Adapted with permission from Springer Nature Customer Service Center GmbH: Springer Nature, Nature Electronics, [28] (Huff *et al.* , Binary atomic silicon logic), ©2018.

atom, then we can associate the level shift with an electric potential  $V_{ij} = \Delta E_{ij}/q_e$ . A DB- SiDB raises the transition levels of its neighbours, potentially raising the (0/-) level above the Fermi energy. As two DB- SiDBs are placed closer together, their mutual repulsion raises their transition levels until they pass the Fermi energy. At this point, only one additional charge can exist between them. The number of charges in the surface is not simply a function of the number of SiDBs, but depends significantly on the particular arrangement and spacing of those SiDBs.

### 4.1.3 Predicting Stable Configuration

Using this observation of screened charge interactions, we can understand the task of finding stable charge configurations of any arrangement of SiDBs as a constrained energy optimisation problem. We assume the total energy of an arrangement of charged SiDBs can be expressed as

$$E(\mathbf{n}) = \sum_i V_i^{\text{ext}} n_i + \sum_{\langle ij \rangle} V_{ij} n_i n_j, \quad (4.2)$$

where  $n_i \in \{-1, 0, +1\}$  is the net charge at each SiDB,  $V_{ij}$  is the Coulombic interaction energy given by Eq. (4.1), and  $V_i^{\text{ext}}$  is the local potential at each site arising from any external sources such as electrodes or nearby impurities or surface inhomogeneities. Each SiDB experiences a local potential arising from both the external sources as well as the instantaneous population of all other sites:

$$V_i^{\text{loc}}(\mathbf{n}) = V_i^{\text{ext}} + \sum_{j \neq i} V_{ij} n_j. \quad (4.3)$$

The amount of upward band-bending experienced by a given SiDB is  $-V_i^{\text{loc}}$ . We impose two metastability criteria. Any electron in a DB- site should prefer to tunnel or hop to a nearby DB0 site if doing so reduces the total energy. We refer to this as *configuration stability*. This can be understood from the perspective of the local potentials. The change in energy associated with a charge  $n_i$  at site  $i$  moving to a previously uncharged site  $j$  can be found to be

$$\Delta E_{ij} = -[V_i^{\text{loc}} - (V_j^{\text{loc}} - V_{ij} n_i)] n_i, \quad (4.4)$$

where the  $V^{\text{loc}}$  are computed prior to the change. In the case of a DB- site, we have  $n_i = -1$ , and thus the energy decreases if  $V_j^{\text{loc}} - V_{ij}n_i > V_i^{\text{loc}}$ . Our configuration stability criterion is equivalent to the statement that all DB- SiDBs, after subtracting off their own influences  $V_{ij}n_i$  from all DB0 sites, should not see a higher  $V_j^{\text{loc}}$ .

As discussed, a stable charge configuration requires that the transition levels be appropriately positioned with respect to the Fermi energy. We define  $\mu_- = E_{TL} - E_F$  to be the energy difference between the (0/-) transition level and the Fermi energy for an isolated SiDB without any external bias. After band-bending, the (0/-) transition levels of every DB0 and DB- state must be above and below the Fermi energy respectively. We then require  $V_i^{\text{loc}} \geq \mu_-$  for all DB- sites and  $V_i^{\text{loc}} \leq \mu_-$  for DB0 sites. This we refer to as *population stability*. Note that we impose configuration stability even if the resulting change in state would violate population stability. Based on expected in-surface [79, 80] and bulk-surface [81] tunneling rates, it is assumed that the in-surface dynamics are much faster than the bulk-surface ones. A simulated annealing algorithm was implemented by Samuel Ng to find solutions to this problem [2, 82]. It makes use of a number of physically inspired heuristics to both efficiently explore the space of possible charge states and enforce metastability. Discussion on the criteria for DB+ states can be in [2].

In Fig. 4.4, we show simulated results for the OR gate from Fig. 4.3. As discussed in Ref. [2, 82], the particular physical parameters relevant to the original OR gate presented by Huff *et al.* are uncertain. Further, there is strong evidence of tip influence in the AFM scans, particularly in the case of the 11 input with 5 DB- sites in close proximity. Using the values of  $\epsilon_r$  and  $\lambda_{TF}$  reported in Ref. [28], we fail to produce either the experimental results or even suitable OR gate outputs; however, there exists a small range of parameters which produce the correct behaviour. An example set is shown in the middle row of Fig. 4.4. In Ref. [2], we demonstrated that a slight modification of the original design, simply moving the bottom-most SiDB to the lower site of the dimer, produces a much more robust OR gate with a large range of operating parameters.

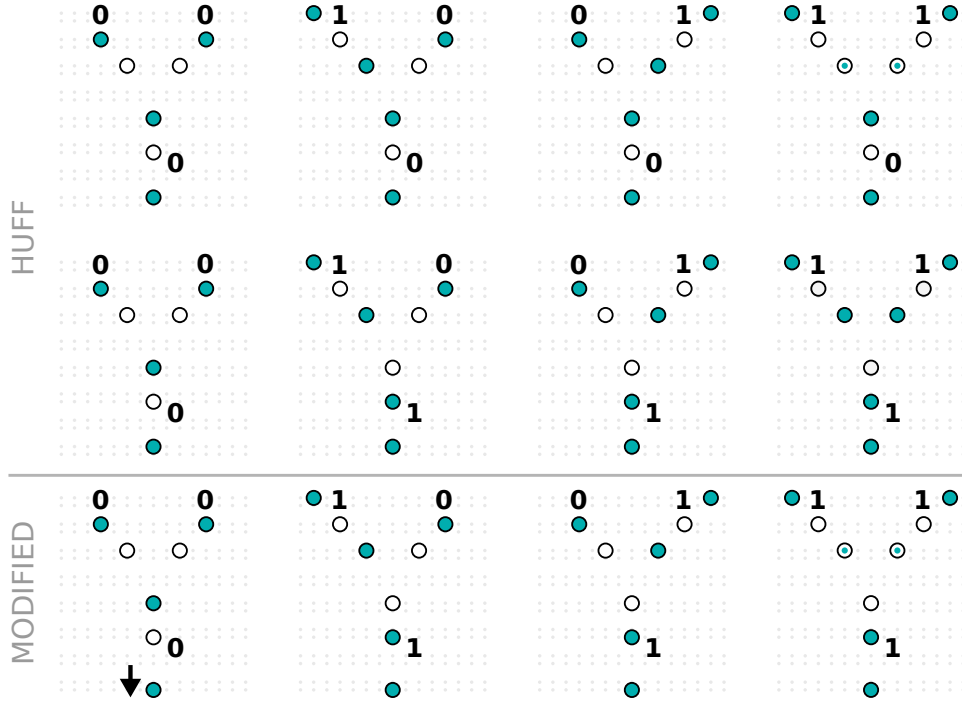


**Figure 4.4:** Simulated charge configurations of SiDB OR gates, showing the lowest energy metastable configurations for all inputs. The **top** row shows the results for the OR gate in Fig. 4.3, using the reported  $\epsilon_r = 5.6$ ,  $\lambda_{TF} = 5$  nm, and choosing  $\mu_- = -280$  meV. The **middle** row uses a parameter set which reproduces the correct OR gate behaviour:  $\epsilon_r = 10$ ,  $\lambda_{TF} = 10$  nm,  $\mu_- = -250$  meV. In the **bottom** row, we shift the perturber on the output down from the upper to the lower site of the dimer, weakening the repulsion on the output SiDB. This modification functions using the experimental parameters:  $\epsilon_r = 5.6$ ,  $\lambda_{TF} = 5$  nm, and  $\mu_- = -280$  meV. Filled circles indicate DB- sites. Half-filled circles indicate SiDB pairs with a charge degeneracy: a single electron occupying either site without any difference in energy.

## 4.2 Clocking SiDB Structures

The dopant concentration establishes the default charge state through setting the Fermi energy; however, we now understand that band-bending at the surface can result in a shift in the preferred charge states of SiDBs. This observation leads to a potential scheme for clocking SiDB arrangements by manipulating the band-bending through an externally controlled surface potential, thereby populating and depopulating the SiDBs. This effect was experimentally verified through use of a titanium silicide “island” created on the silicon surface with an array of SiDBs placed in proximity [83]. The island behaves like a Schottky contact. When applying an electrical bias to the silicide, STM measurements of the surface revealed upward band-bending. This allowed the controllable depopulation of all SiDBs near the island. In [2], we proposed a more general approach to clocking using either buried or suspended electrodes. These electrodes would be used to controllably induce band-bending at the surface, allowing the activation and deactivation of regions of the surface by raising or lowering the effective local ( $0/-$ ) transition levels relative to the Fermi energy.

## 4.3 Dynamic Behaviour

Pairs of SiDBs have been investigated as a potential candidate for charge qubits [79, 80]. The tunneling and decoherence rates of a shared charge were estimated to be on the order of terahertz, with the precise value rapidly decaying with the separation: from  $10^3$  THz at  $3.84 \text{ \AA}$ , to  $10^1$  THz at  $3 \times 3.84 \text{ \AA}$ . We should expect any observations of dynamics at this scale to be limited to very specific methods of investigation, such as time-resolved pump-probe scanning tunneling microscopy [81]. Observations of actual charge states of SiDB arrangements have thus far been limited to relatively slow AFM scans. However, recent results demonstrate that in certain circumstance much slower dynamics can be observed [1, 28].

### 4.3.1 Degenerate Hopping

In Fig. 4.5, one of the results of Rashidi *et al.* is reproduced [1]. An arrangement of six SiDBs was designed such that the two innermost sites share a single electron. Due to the symmetry of the arrangement, there is no preferred location absent

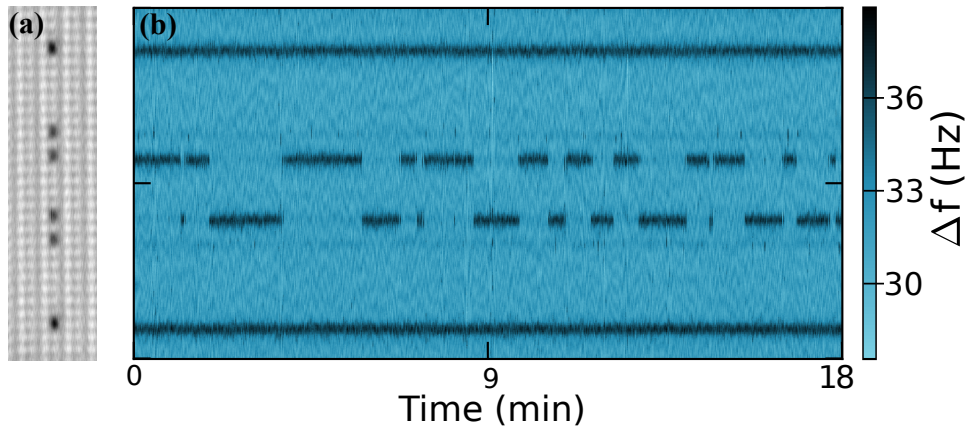


**Figure 4.5:** Symmetric structure studied in Ref. [1], with six SiDBs and a charge degeneracy between the two inner sites: **(a)** AFM scan at low tip-surface separation, revealing all SiDBs as DB- sites; **(b)** 800 AFM line scans, back and forth over the structure over about 18 minutes with a large tip-surface separation to prevent tip-induced band-bending. Adapted from [1] with permission, copyright from the American Physical Society.

additional bias. Repeated AFM scans were made, passing the tip back and forth over all SiDBs, observing the evolution of the charge state over a period of about 18 minutes. If the electron were distributed between the two degenerate sites, and assuming the interaction with the tip to be non-perturbative, we might expect to see both SiDBs as partially charged with  $\Delta f$  between the DB0 and DB- values. Alternatively, we might expect that, as the tip approaches, the charge is fixed to one side or the other. In that case the location would be randomized between scans due to the expected fast tunneling. Instead, we see that the charge state persists over multiple scans. This stabilization is attributed to lattice relaxation [1, 28], which serves as an additional energy barrier to charge dynamics that becomes significant in the cases of degeneracy. This barrier is potentially overcome in these experiments through a combination of thermal fluctuations and tip influence.

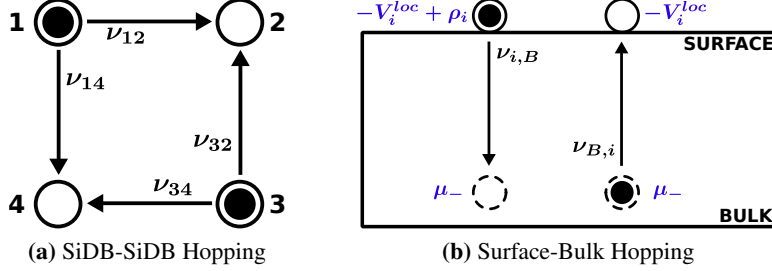


**Figure 4.6:** Schematic of hopping rates in the hopping model. For surface reconfigurations, rates are computed only from DB- to DB0 sites using Eq. (4.6). Population/depopulation is modelled by surface-bulk hopping, where each SiDB is paired with a state in the reservoir with an energy of  $\mu_-$ . The appropriate energies are shown in blue.

### 4.3.2 Hopping Rate Model for Charge Dynamics

A number of models were considered for approximating charge dynamics. An important qualifier for any chosen model should be that the metastable configurations defined in Section 4.1.3 be stable under the dynamics. One simple approach is to interpret all charge reconfigurations as sequences of hopping events. In particular, over some small time step  $dt$ , we allow some probability of a charge at a DB- site to *hop* to a DB0 site:  $p_{i \rightarrow j}(t; dt) = v_{ij}(t)dt$  where  $v_{ij}$  is the *hopping rate*. In this discussion, we will address our two metastability criteria separately.

#### Configuration Stability

If a hop is associated with a decrease in Eq. (4.2) we should require a large  $v_{ij}$ ; an increase in energy should be heavily penalized. A schematic of this scenario is shown in Fig. 4.6(a). Two suitable models for the hopping rate were implemented: Mott or Miller-Abrahams variable range hopping (VRH) [84], and Marcus Hopping [85]. The hopping rate between a DB- and DB0 site is expressed as

$$v_{ij} \propto e^{-2\alpha r_{ij}} \eta(\Delta G_{ij}) \quad (4.5)$$

where  $r_{ij}$  is the distance between the SiDBs,  $\alpha$  is the spatial decay of the hopping rate,  $\Delta G_{ij}$  is the change in Gibbs free energy associated with the hop, and  $\eta$  is

some function of  $\Delta G_{ij}$  which depends on the choice of hopping model. In the current implementation, we equate  $\Delta G_{ij}$  to the change in electrostatic energy,  $\Delta E_{ij}$  from Eq. (4.2), associated with the hop, plus an optional self-trapping energy,  $\rho_i$ , intended to approximate any expected effect of lattice relaxation. It is convenient to use a calibrated form for  $v_{ij}$ :

$$\text{VRH} : v_{ij} = v_0 e^{-2\alpha(r_{ij}-r_0)} e^{-\Delta E_{ij}/k_B T} \quad (4.6a)$$

$$\text{Marcus} : v_{ij} = v_0 e^{-2\alpha(r_{ij}-r_0)} e^{-\Delta E_{ij}[\Delta E_{ij}+2(\rho_i-\lambda_0)]/4\lambda_0 k_B T} \quad (4.6b)$$

where here  $v_0$  is the experimentally observed hopping rate between two degenerate ( $\Delta E_{ij} = 0$ ) SiDBs at a separation of  $r_0$ ,  $\lambda_0$  is the reorganization energy in Marcus theory, and  $k_B T$  is the thermal energy. Note that for VRH, assuming the same self-trapping energy for all DB- sites,  $\rho_i$  is absorbed into  $v_0$ . For the results in Fig. 4.5, we have at least 23 hops over 18 minutes and a separation of 5 dimers:  $v_0 \approx 21$  mHz,  $r_0 = 19.2\text{\AA}$ . In all results, a spatial decay of  $\alpha = 1\text{ nm}^{-1}$  and a thermal energy of  $k_B T = 0.36$  meV at 4.2 K is assumed. Note that for non-degenerate hopping, the  $\Delta E_{ij}$  are typically on the order of tens of meV. In this case, even though  $v_0$  is slow, the  $v_{ij}$  may be on the order of GHz or faster.

### Population Stability

For each SiDB, we require that its local potential from Eq. (4.3) be compatible with its charge state: including the self-trapping energy, a DB- site should depopulate if  $V_i^{\text{loc}} + \mu_- \leq \rho_i$ , and a DB0 site should populate if  $V_i^{\text{loc}} + \mu_- \leq 0$ . For DB- states, we define a *depopulation rate*  $v_{i,B}$ , associated with a hop between the surface SiDB and some charge reservoir, here understood to be the valence band of the bulk. We can define a similar *population rate*,  $v_{B,i}$ , between the reservoir and each DB0 site. We set the energy of charges in the reservoir to be at  $\mu_-$ . A schematic of surface-bulk hopping is shown in Fig. 4.6(b) with the appropriate energies. We assume self-trapping is present only for DB- sites and thus it is ignored for  $v_{B,i}$ . It is not clear that the form of these rates should be anything like those of surface hopping. We anticipate that there is some maximum surface-bulk tunneling rate  $v_B$  and invent some function  $f : \Delta E \rightarrow [0, 1]$ , which translates an energy difference

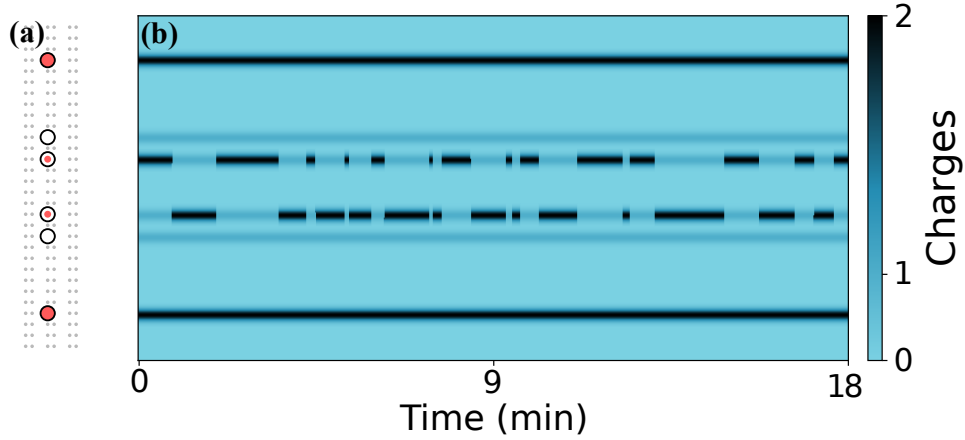


**Figure 4.7:** Simulation of the system in Fig. 4.5: **(a)** lowest energy metastable configuration, including the observed degenerate pair; **(b)** simulated degenerate hopping using calibrated VRH. The same tip trajectory used in [1] is simulated: 800 line scans over 18 minutes. This figure first appeared in [2].

between the surface-bulk states into a scaled hopping rate. We can write

$$v_{i,B} = v_B f(-V_i^{\text{loc}} + \rho_i - \mu_-), \quad (4.7a)$$

$$v_{B,i} = v_B f(\mu_- + V_i^{\text{loc}}). \quad (4.7b)$$

The function  $f$  should increase from  $f(-\infty) = 0$  to  $f(\infty) = 1$ . In this work, we opted to use a sigmoid of the form  $f(\Delta E) = 1/(1 + \exp(-\Delta E/k_B T))$ , consistent with a state of thermal equilibrium between the surface and bulk sites. In Ref. [81], expected values for bulk to surface tunneling rates were measured. At a temperature of 4K, values range from a few kHz to MHz. In our results we use  $v_B = 1$  MHz. In Fig. 4.7, we show a simulation of the same system studied in Ref. [1]. In these results, the trajectory of a tip was simulated travelling at 8.9 nm/s in order to achieve 800 line scans over 18 minutes to match the AFM scan. The charge of each SiDB was recorded as the “tip” passed over. No tip-induced band-bending or other interactions were considered. Further results using the hopping model will be presented in Section 4.5. Details on the implementation hopping model can be found in Appendix A.1.

## 4.4 SiQAD: Simulation and Design of SiDB Structures

Silicon dangling bonds show promise as a platform for nanoscale computing; however, exploration of this design space requires tools for the rapid design and simulation of arbitrary SiDB arrangements. To this end, a computer-aided design (CAD) tool was developed, with the code base and simulation tools developed by members of Walus Lab, and experimental calibration and additional theoretical discussion from members of Wolkow’s group.

**Silicon Quantum Atomic Designer (SiQAD)** is an open source CAD tool that provides both functionality for the rapid design of arrangements of SiDBs as well as a number of simulation suites to approximate the behaviour of those arrangements [2]. The graphical user interface (GUI) is designed using the Qt C++ framework [86]. A custom application programming interface (API) is provided for the modular integration of any simulation tools. This API also offers limited capacity for future efforts in design automation; an external tool can provide a list of commands to, for example, create or remove SiDBs, or specify electrode placement based on the current design. There are currently three simulation engines included with SiQAD:

**SimAnneal:** a simulated annealing algorithm implemented by Samuel Ng which attempts to efficiently find the lowest energy metastable configurations as defined in Section 4.1.3. For a detailed discussion on the implementation of SimAnneal, as well as a comparison against other potential solvers, see Refs. [2, 82].

**HoppingDynamics:** a graphical tool which allows users to run the hopping-based dynamics model in Section 4.3.2 and Appendix A.1 on designs made in SiQAD. Dynamics can be computed and observed in “real-time”, up to a time-scaling factor, with model and clocking parameters adjustable without interrupting or resetting the simulation. In the current implementation, it is not possible to add or remove SiDBs during the simulation, except perturbers with fixed charge.

**PoisSolver:** a finite element method (FEM) solver for the generalized Poisson equation developed by Nathan Chiu allowing for arbitrary arrangements of buried or suspended electrodes. Details of this method can be found in Ref. [3].

For an expanded discussion on the design and capabilities of SiQAD, see Refs. [2, 82].

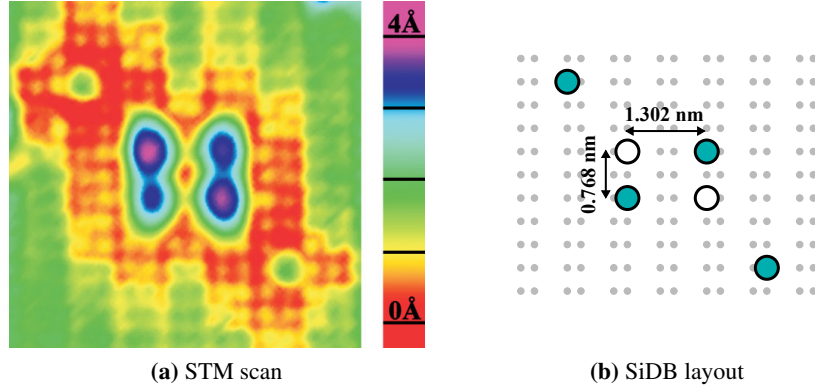


**Figure 4.8:** Constant current STM scan of a biased 4-dot QCA cell composed of 4 SiDBs designed by Haider *et al.* [27]. Adapted with permission from Ref. [27]. Copyrighted by the American Physical Society.

## 4.5 SiDB Implementations of QCA

Haider *et al.* demonstrated a simple 4 SiDB design which, when biased by two additional DB- sites, behaved like a 4-dot QCA cell. The relevant STM scan and SiDB layout are reproduced in Fig. 4.8. Beyond this result, there have been no further experimental investigations into the behaviour of larger arrays of SiDB-QCA cells. In his thesis, Ng presented a design for a 4-dot QCA cell made using SiDBs in a slightly different geometry. Calculations using SimAnneal were presented for some simple components: a wire, an inverter, a  $90^\circ$  wire bend, and a majority gate [82]. Ng demonstrated that, at a certain value of  $\mu_-$ , these arrangements have the correct metastable configurations. While an important result, this leaves open the question of whether they would operate correctly when clocked. SimAnneal cannot directly tell us anything about clocking performance; however, we can attempt to use it to find the sequence of lowest energy metastable configurations as the applied clocking field is swept. If we assume the physical system evolves to track these configurations, this sequence gives us an idea of the trajectory of charge states a clocked arrangement must go through.

In Fig. 4.9, we present an SiDB-based inverting chain with dimensions consistent with Ng's design. Each vertical pair of SiDBs can be understood as a 2-dot QCA cell. We add an input perturber to the left with the same separation as the

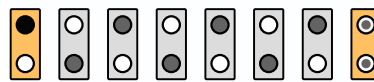
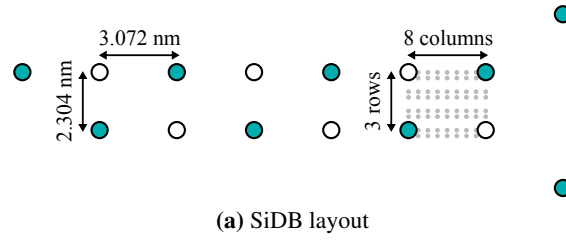


**Figure 4.9:** SiDB implementation of an inverting chain and its equivalent QCA representation. The leftmost SiDB serves as the input, and the rightmost SiDBs apply back-pressure without any polarisation bias. This emulates the effect of the rest of the circuit. The orange cells in (b) represent cells with fixed charge distribution. Important dimensions and a sub-region of the lattice are shown.

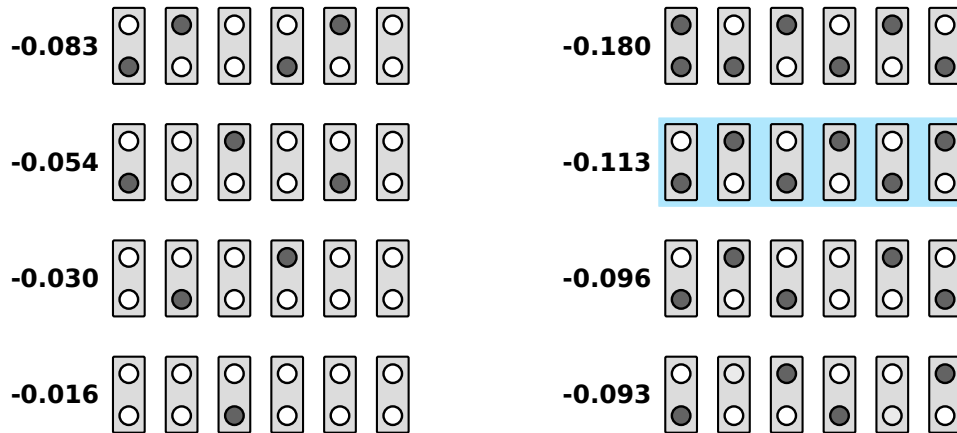


**Figure 4.10:** Sequence of lowest energy metastable configurations of the inverting chain as the value of  $\mu_-$  is swept. Perturber sites are excluded for simplicity. The numbers indicate the smallest magnitude  $\mu_-$ , in eV, necessary for the shown configuration. The intended final state is highlighted. Values shown are for  $\epsilon_r = 5.6$ ,  $\lambda_{TF} = 5$  nm.

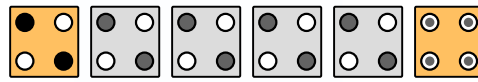
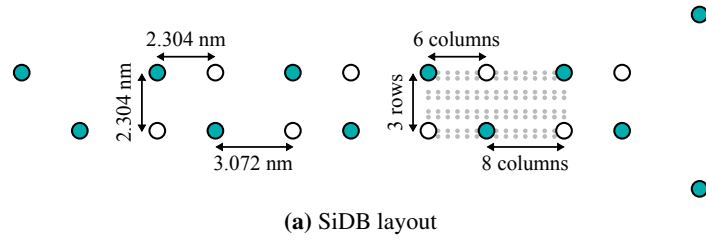
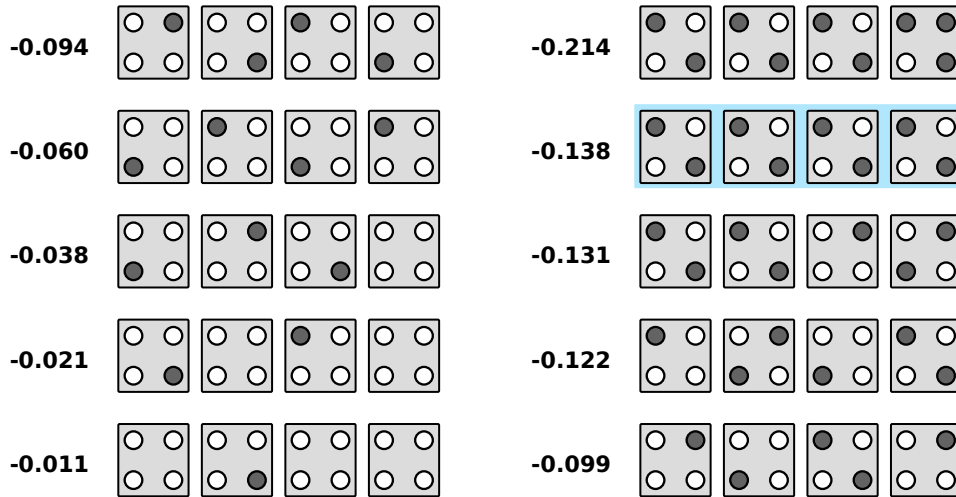


**Figure 4.11:** SiDB implementation of a non-inverting wire and its equivalent QCA representation. Note here that without drawing in the boundaries of each QCA cell, the distinction between four 4-dot QCA cells forming a wire, and eight 2-dot QCA cells forming an inverting chain is made non-arbitrary only by the differences in inter- and intra-cell distances.



cell-cell spacing. The two SiDBs at the right are there to apply back-pressure to the chain without adding any polarization bias. These make up for the missing band-bending due to truncating the chain. In Fig. 4.10, we sweep the value of  $\mu_-$  from slightly below zero<sup>1</sup> down until we first observe a lowest energy metastable state with one too many charges. The first value of  $\mu_-$  at which each state is observed was recorded. When clocking a QCA wire, the idea is to propagate the input polarization from cell to cell. This is not what we see here. The charge repulsion means that the wire populates effectively from the middle outwards. We will study this sort of population order more in the next chapter. We show very similar behaviour for a non-inverting wire of 4-SiDB cells in Fig. 4.11 and Fig. 4.12.

This picture of clocking, where we sweep the value of  $\mu_-$  shared by all SiDBs, is consistent with applying a uniform external voltage at the surface. This could be achieved over a finite region using an electrode like the zone clocking arrangement shown in Fig. 1.4. It is clear that some of the issues might be reduced by using wave clocking, which in this case would afford better control over where population/depopulation events occur. In Fig. 4.13, we show a simulation of an inverting wire under wave clocking using HoppingDynamics. An important quantity here is the ratio between the clocking wavelength,  $\lambda$ , and the inter-cell separation. We used a wavelength of 48 nm in order to demonstrate that, in principle, with a small enough wavelength these population order issues can be resolved; however, current limitations in nanofabrication techniques constrain the minimum electrode pitch, and hence also the clocking wavelength. A wavelength on the order of 200 nm is more realisable, four times the contacted gate pitch in current FinFET fabrication processes [39]. If we used a 200 nm clocking wave, we would require cell separations of about 12 nm in order to produce similarly well behaved clocking. This is roughly twice the Thomas-Fermi screening distance at 5.6 nm, significantly weakening the cell interactions. We will see in the next chapter that the inclusion of a tunneling energy within the SiDB-QCA cell model further helps here, potentially making wires practical; however, higher density regions like the center of a majority gate would still be a challenge.

---

<sup>1</sup>If we start at zero, the perturbers themselves are unpopulated. We start the sweep at the weakest  $\mu_-$  needed to populate the perturbers.

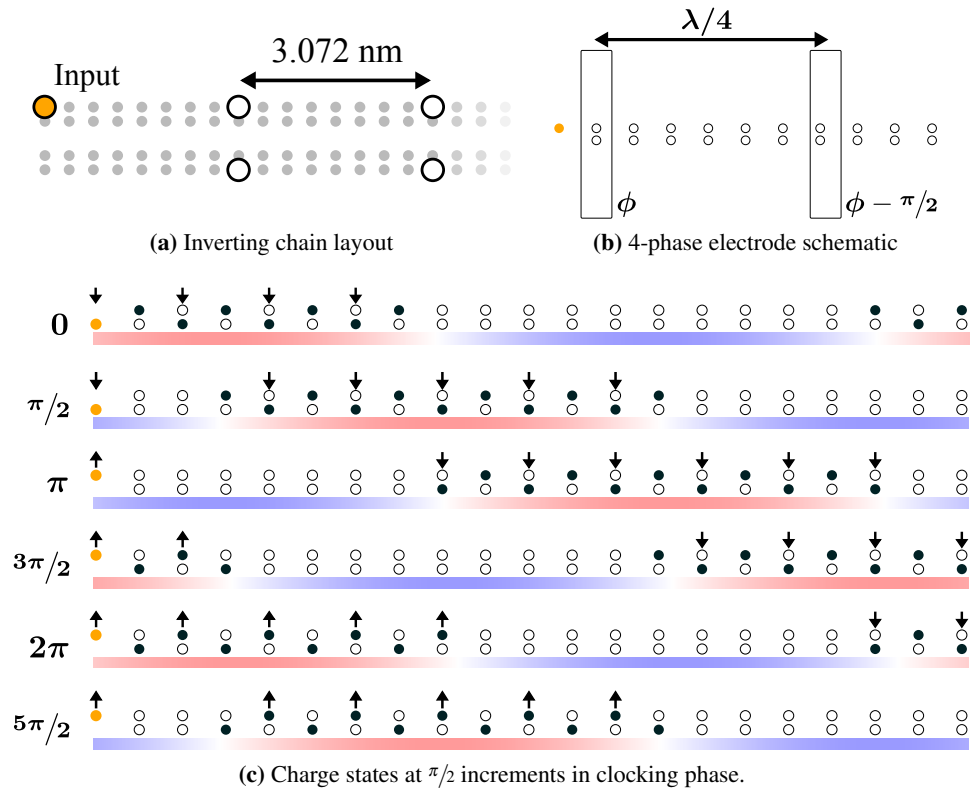


**Figure 4.13:** HoppingDynamics simulation of an SiDB inverting chain under 4-phase wave clocking. Clocking was implemented using buried electrodes, 100 nm below the surface with a clocking wavelength of  $\lambda = 48$  nm. At that depth the field at the surface is approximately a travelling sinusoid, chosen to have a peak-to-peak amplitude of 200 mV. Values of  $V^{\text{ext}}(x, t)$  are indicated by the colorbar. In (c), we show the charge states in a dynamic simulation at time slices corresponding to  $\pi/2$  phase shifts. With such a small clocking wavelength, the bit-packet propagation behaves as expected. Between  $\phi = \pi/2$  and  $\phi = \pi$ , we changed the input state in order to demonstrate that multiple wave packets can be propagated independently. The colorbars show  $V^{\text{ext}}(x, t)$ . A version of this figure first appeared in [2].

## 4.6 Summary

This chapter gave an overview of the potential of silicon dangling bond structures as a platform for binary logic, and in particular, their candidacy as a means of implementing nanoscale QCA. We demonstrated that experimentally observed charge states of arrangements of SiDBs can be understood as a constrained energy minimization problem. A simulated annealing solver, SimAnneal, was developed by Samuel Ng for the purpose of efficiently solving this problem. Despite expected rapid tunneling between neighbouring SiDBs, experimental results suggest significant lattice relaxation in H-Si(100)- $2\times 1$  which enforces charge localisation among degenerate SiDBs pairs over time scales on the order of seconds to minutes. This behaviour motivated a hopping model for the dynamics and ultimately a simulation tool, HoppingDynamics. We briefly introduced SiQAD, a CAD tool for developing and simulating SiDBs arrangements which makes use of SimAnneal, HoppingDynamics, and PoisSolver, our in-house FEM solver for finding the time-dependent electric potential at the surface due to any arbitrary arrangements of clocking electrodes. Finally, while it is possible to design SiDBs arrangements which reproduce the functionality of simple QCA networks, we discussed the potential challenge to clocking that arises due to the complex charge state trajectories that result from out-of-order population of even simple wires. In the next chapter, we will raise this issue of population order from the perspective of conventional QCA analysis.

## Chapter 5

# Population Congestion in 3-State QCA

When designing QCA networks, the predominant focus is on the coupling between polarized states, arising from the energy cost of neighbouring cells having the same or opposite polarizations. For 3-state mixed valence molecule (MVM) devices, it is known that additional interactions between the null and polarized states of neighbouring devices lead to an increase in the required clocking field needed to activate a cell [87, 88]. It has been proposed that complexities arising from these interactions can be mitigated by employing a dynamic clocking wave with a sufficiently large maximum field strength. In the previous chapter, we observed that for SiDB-based QCA implementations, the order of cell activations, in this case SiDB population events, can be complicated. We will use the term *congestion* to refer to this effect of strong population repulsion. SiDB devices pose an additional challenge in that a large applied clocking field can easily produce too large of a surface population. It is therefore unclear whether SiDB based QCA devices could be operated in a regime of clocking parameters for which this congestion is mitigated.

In this chapter, we investigate the conditions under which these congestion interactions contribute significantly to 3-state QCA devices and the behaviour of these devices in the regime of strong congestion. In Section 5.1, we discuss the  $N$  cell 3-state QCA Hamiltonian including congestion and polarization interactions. In Section 5.2, we consider two potential MVM and SiDB-QCA devices and ap-

proximate the dependence of the interaction energies on the device geometries. In Section 5.3, we study the ground states of simple QCA networks. We present an analytical estimate of the single cell ground state and calculate the maximum congestion interaction strength beyond which a QCA network displays irregular ground states. Finally, in Section 5.4, we discuss the extent to which dynamic wave clocking addresses these challenges for SiDB-QCA devices.

## 5.1 Full 3-State Hamiltonian

The Hamiltonian of a single 3-state QCA device in the presence of some clocking field was given in Eq. (2.4), repeated here for convenience:

$$\hat{H}_i(t) = -\gamma_i \hat{\Gamma}_i + h_i \hat{\mathcal{P}}_i - \mathcal{C}_i(t) (\hat{\mathcal{N}}_i - \hat{I})$$

The cell population/activation,  $\mathcal{N}_i = \langle \hat{\mathcal{N}}_i \rangle$ , is the probability of a device being in either of the polarized states, or equivalently, *not* in the null state. For multiple devices, the full Hamiltonian will take the form

$$\begin{aligned} \hat{H}(t) = & -\sum_i \gamma_i \hat{\Gamma}_i + \sum_i h_i \hat{\mathcal{P}}_i - \sum_i (\mathcal{C}_i(t) - \mu_i) (\hat{\mathcal{N}}_i - \hat{I}) \\ & - \frac{1}{2} \sum_{\langle ij \rangle} E_{ij}^k \hat{\mathcal{P}}_i \hat{\mathcal{P}}_j + \sum_{\langle ij \rangle} \mathcal{D}_{ij} \hat{\mathcal{N}}_i \hat{\mathcal{N}}_j \end{aligned} \quad (5.1)$$

where charges in the upper sites both interact via their polarizations through  $E_{ij}^k$  and inhibit population of neighbouring devices with *congestion energy*  $\mathcal{D}_{ij}$ . We also introduce a term  $\mu_i$  which represents a population/congestion bias. Individual effective device Hamiltonians from the 3-state ICHA are given by

$$\hat{H}_i = -\gamma_i \hat{\Gamma}_i + \tilde{h}_i \hat{\mathcal{P}}_i - (\mathcal{C}_i - \tilde{\mu}_i) (\hat{\mathcal{N}}_i - \hat{I}), \quad (5.2)$$

with  $\tilde{h}_i = h_i - \frac{1}{2} \sum_{j \neq i} E_{ij}^k \mathcal{P}_j$  as with the 2-state ICHA and instantaneous effective congestion biases  $\tilde{\mu}_i = \mu_i + \sum_{j \neq i} \mathcal{D}_{ij} \mathcal{N}_j$  for current populations  $\mathcal{N}_j$ . We can argue for a suitable value of  $\mathcal{D}_{ij}$  in the same way we define  $E_{ij}^k$ . Suppose we had a pair of 3-state devices with  $\gamma_i = h_i = \mu_i = \mathcal{C}_i = 0$ . The pair then has a Hamiltonian

$$\hat{H}_{ij} = -\frac{1}{2} E_{ij}^k \hat{\mathcal{P}}_1 \hat{\mathcal{P}}_2 + \mathcal{D}_{ij} \hat{\mathcal{N}}_1 \hat{\mathcal{N}}_2. \quad (5.3)$$

The eigenstates with non-zero energy are those with both devices in a polarization state. They have energies

$$\begin{aligned} |-1, -1\rangle &: -\frac{1}{2}E_{ij}^k + \mathcal{D}_{ij} & |-1, +1\rangle &: \frac{1}{2}E_{ij}^k + \mathcal{D}_{ij} \\ |+1, -1\rangle &: \frac{1}{2}E_{ij}^k + \mathcal{D}_{ij} & |+1, +1\rangle &: -\frac{1}{2}E_{ij}^k + \mathcal{D}_{ij} \end{aligned}$$

The kink energy is then the change in energy when one of the polarizations is switched, and the congestion energy is the average. That is, if  $E_{+-}$  and  $E_{++}$  are the energies of  $|+1, +1\rangle$  and  $|+1, -1\rangle$  absent all other devices and biases, then

$$E_{ij}^k = E_{+-} - E_{++}, \quad \mathcal{D}_{ij} = \frac{1}{2}(E_{+-} + E_{++}). \quad (5.4)$$

## 5.2 Considered Devices

We consider two interesting candidates for atomic scale QCA: zwitterionic nido carborane ( $\text{Fc}^+\text{FcC}_2\text{B}_9^-$ ) [26] and the discussed SiDBs [14, 28]. We assume  $E_{+-}$  and  $E_{++}$  can be expressed as a sum of point charge interactions between devices:

$$E(\mathbf{n}) = \sum_{i \in \Omega_1} \sum_{j \in \Omega_2} V(|\vec{r}_i - \vec{r}_j|) n_i n_j \quad (5.5)$$

where  $n_i$  is the number of electrons at site  $i$  located at  $\vec{r}_i$ ,  $V$  gives the distance dependence of the charge interaction, and  $\Omega_i$  is the set of sites in the  $i$ 'th device.

### 5.2.1 Zwitterionic Nido Carborane

A number of mixed-valence species have been considered as candidates for molecular QCA. Of particular interest in recent studies are diferrocenyl acetylene, having two Fe centers serving as quantum dots, and self-doping zwitterionic nido carborane. The latter contains two Fe centers as well as a carborane cage, providing three quantum dots, one fixed electron and a mobile hole [89]. The schematics of the appropriate 3-dot and 6-dot devices using  $\text{Fc}^+\text{FcC}_2\text{B}_9^-$  are shown in Fig. 5.1. We will focus on wire arrangements with device centers separated by some distance  $s \geq d$ . If the device separation is sufficiently large, we can find approximate

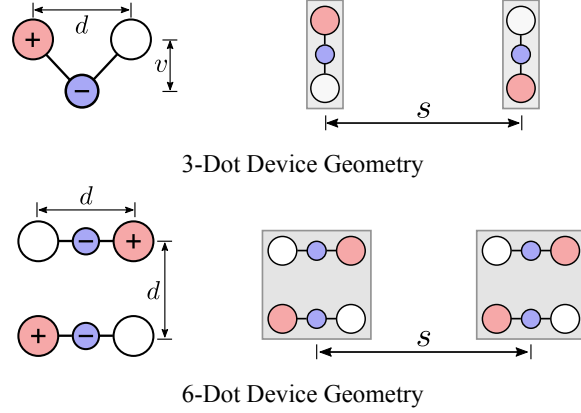


**Figure 5.1:** Schematics for 3-state  $\text{Fc}^+\text{FcC}_2\text{B}_9^-$  devices. Devices always remain net neutral. Parallel 3-dot devices produce inverting wire chains. 6-dot devices are made from pairs of 3-dot devices with upper sites forming a square.

expressions for our devices. Assuming no screening,  $V(r) = K_c/r$ , we arrive at

$$E_{3\text{-dot}}^k \approx -\frac{K_c}{2d} (d/s)^3 \left[ 1 - \frac{3}{8} (d/s)^2 \right], \quad (5.6a)$$

$$\mathcal{D}_{3\text{-dot}} \approx \frac{K_c}{v} (v/s)^3, \quad (5.6b)$$

for the 3-dot devices. Both parameters are cubic in inverse distance indicative of a dipole-dipole interaction between devices. For the 6-dot device, we get

$$E_{6\text{-dot}}^k \approx \frac{6K_c}{d} (d/s)^5, \quad (5.7a)$$

$$\mathcal{D}_{6\text{-dot}} \approx \frac{4K_c}{v} (v/s)^3 \left[ 1 + \frac{3}{2} (d/s)^2 \right]. \quad (5.7b)$$

Interestingly, while the kink energies fall off as  $(1/s)^5$ , the congestion energy decay remains cubic. From the point of view of congestion, there is no distinction between the two polarized states. In this view, both the 3-dot and 6-dot devices are effectively dipoles with some positive charge in the upper sites, negative charge in the lower site(s), and a length scale of  $v$ . For the 6-dot device this has the unfortunate outcome that the congestion persists between devices at separations well beyond the kink energies. Fig. 5.2 compares the exact  $E^k$  and  $\mathcal{D}$  values computed

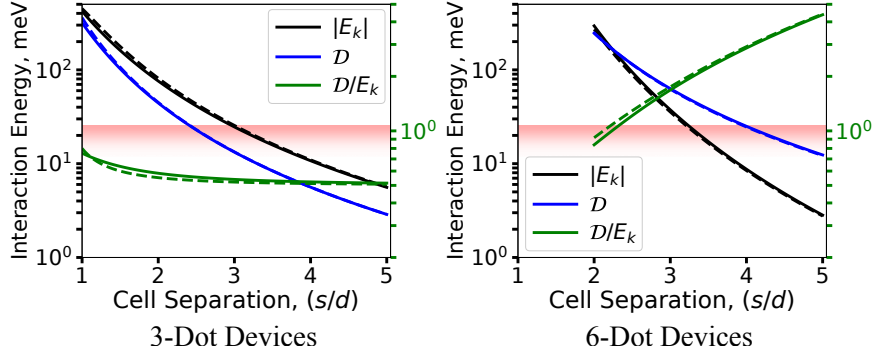


**Figure 5.2:** Kink and congestion energies for both  $\text{Fc}^+\text{FcC}_2\text{B}_9^-$  device configurations. Dashed lines show the values computed from Eqs. (5.6) and (5.7). The right axis gives values for the  $D/E^k$  ratio. For the 6-dot device,  $s < 2d$  is excluded as it has dot-dot separations between cells which are smaller than intra-cell separations. Values are shown for  $d = 1 \text{ nm}$ ,  $h = 0.5 \text{ nm}$ ,  $\epsilon_r = 1$ . The red gradient indicates the thermal energy at 300K for reference.

from Eq. (5.5) to the approximations. Device separations must be kept small to keep the kink energies above the thermal energy; however, at these separations the congestion energy is also significant. A higher clocking field must be applied in order to guarantee the eventual population of all devices.

## 5.2.2 Silicon Dangling Bonds

Dimensions for SiDB devices are shown in Fig. 5.3(a-b). We use the screened potential discussed in Section 4.1.2:  $V(r) = K_c \exp(-r/\lambda_{TF})/r$ , and opt to use the fit values given in Ref. [78]:  $\epsilon_r = 4.1$ ,  $\lambda_{TF} = 1.8 \text{ nm}$ . These values are more favourable for the  $D/E^k$  ratio. Absent evidence that doubly occupied and unoccupied states can be present at the same dopant concentration, we should expect QCA devices made of SiDBs to be either net negative or net positive. This hints at the susceptibility to congestion observed in employing them for logic gates. For the 2-dot device, we approximate the interaction strengths as

$$E_{2\text{-dot}}^k \approx -\frac{K_c}{2d} e^{-s/\lambda_{TF}} F_1(s/\lambda_{TF})(d/s)^3, \quad (5.8a)$$

$$D_{2\text{-dot}} \approx \frac{K_c}{s} e^{-s/\lambda_{TF}} \left[ 1 - \frac{1}{4} F_1(s/\lambda_{TF})(d/s)^2 \right], \quad (5.8b)$$

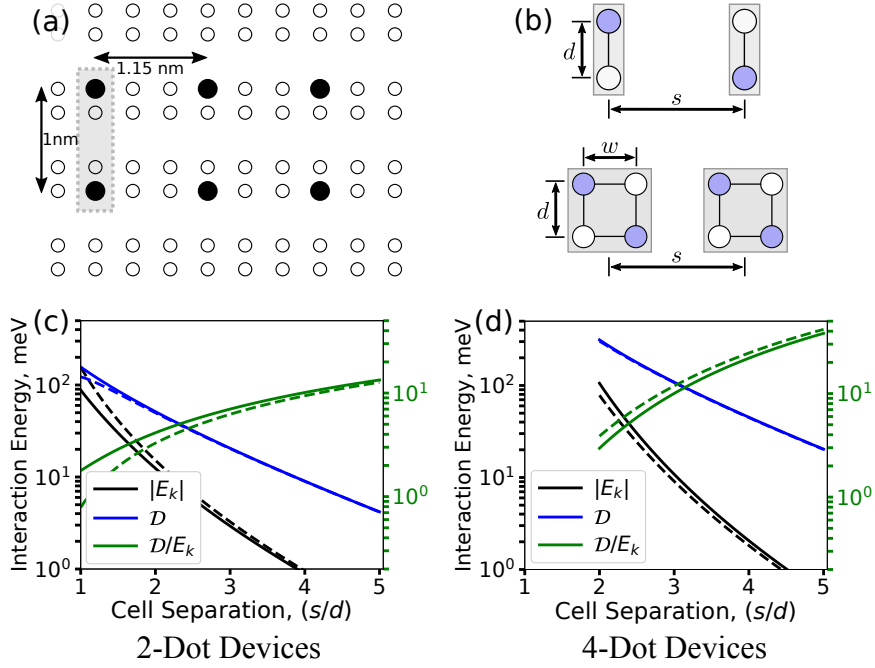


**Figure 5.3:** SiDB device geometries and separations are constrained by the H-Si(100)- $2\times 1$  surface lattice shown in (a). In (b) we define the relevant dimensions for 2-dot and 4-dot SiDB devices. The corresponding interaction energies are shown in (c) and (d) with  $d = 1$  nm and  $w = 1.15$  nm. At 4.2 K, the thermal energy is only about 0.36 meV.

where  $F_1(x) = 1 + x$  is the first of a set of polynomials which describe the screening dependence of the dominant terms in the expansion. Similarly, for the 4-dot devices:

$$E_{4\text{-dot}}^k \approx \frac{K_c}{2s} e^{-s/\lambda_{TF}} F_3(s/\lambda_{TF}) (d/s)^2 (w/s)^2, \quad (5.9a)$$

$$\mathcal{D}_{4\text{-dot}} \approx \frac{K_c}{s} e^{-s/\lambda_{TF}} \left[ 4 - F_1(s/\lambda_{TF}) (d/s)^2 + F_2(s/\lambda_{TF}) (w/s)^2 \right], \quad (5.9b)$$

with  $F_2(x) = 2F_1(x) + x^2$  and  $F_3(x) = 5F_2(x) + 2F_1(x) + x^3$ . The calculated interaction energies are shown in Fig. 5.3(c) and (d). Even with screening, we see that congestion dominates. We will see that for such large congestion energies 3-state QCA operation is a potential challenge. We conclude with a summary of our

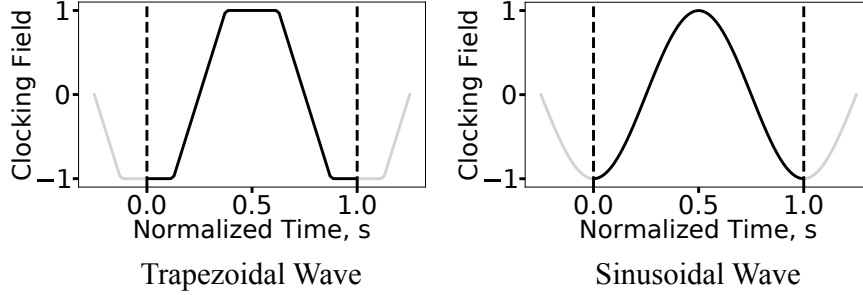


**Figure 5.4:** Simple normalised wave profiles. In our case, observe that the maximum clock occurs as  $s = 1/2$ .

approximations of the  $\xi = \mathcal{D}_0/E_0^k$  ratios, keeping only the most dominant term:

$$\begin{aligned} \xi_3 &\approx 2(v/d)^2, & \xi_6 &\approx \frac{2}{3}(v/d)^2(d/s)^{-2}, \\ \xi_2 &\approx \frac{2}{F_1(s/\lambda_{TF})}(d/s)^{-2}, & \xi_4 &\approx \frac{2}{3F_1(s/\lambda_{TF})}(d/s)^{-2}(w/s)^{-2}. \end{aligned} \quad (5.10)$$

### 5.2.3 Clocking

We will consider both zone and wave clocking: refer to Fig. 1.4. We write the clocking field in either case in the form

$$\textbf{Zone Clocking : } C_i(t) = C_0 + \frac{\Delta C}{2} \times \bar{C}(ft), \quad (5.11a)$$

$$\textbf{Wave Clocking : } C_i(t) = C_0 + \frac{\Delta C}{2} \times \bar{C}(ft - x_i/\lambda_c). \quad (5.11b)$$

where  $C_0$  and  $\Delta C$  define the average and peak-to-peak amplitude of the clocking field at the surface,  $f$  is the frequency of one of the clocking phases,  $x_i$  are the devices locations,  $\lambda_x$  is the wavelength of the clocking field, and  $\bar{C}$  is some function with a period of 1 satisfying  $-1 \leq \bar{C}(s) \leq 1$  which defines the clocking profile. For wave clocking, we disregard any complexities of the generated field and merely assume it to be some wave translated in  $\hat{x}$ . For the clocking profiles,  $\bar{C}$ , we consider only trapezoidal and sinusoidal waveforms, shown in Fig. 5.4 for completeness. We note also that the interpretation of the clocking field is slightly different between MVM and SiDB devices. For the 3-dot and 6-dot devices, we are interested

in the difference in electrical potential between the null and upper sites. This is approximately determined by the  $\hat{z}$  component of the electric field and the null site depth,  $v$ :  $C_i(t) \approx \vec{E}(x_i, t) \cdot v\hat{z}$ . For the 2-dot and 4-dot devices, the clocking field is just the applied electrical potential at each site associated with the clocking electrodes:  $C_i(t) = V_i^{\text{ext}}(t)$  [2].

There are two main constraints we need to impose on our clocking fields. First, we set a minimum clocking wavelength of 200 nm consistent with current nanofabrication limitations: see Section 4.5. Second, we must consider practical upper bounds on the clocking fields for our two architectures. For MVM devices, the combinations of large kink energies and small  $v$  gives rise to large electric fields. A required clocking field equal to  $E^k$  necessitates an electric field on the order of  $10^2$  or  $10^3$  meV/nm. While a few V/nm is realisable [88], larger electric fields are potentially a challenge. For SiDB devices, it is relatively easy to populate both of the SiDBs in a 2-dot device [2]. The population of one of the SiDBs raises the transition level of the other by an amount equal to  $V(d)$ , approximately 200 meV for our chosen parameters. The difference between a sufficiently large clocking field for full population and the case of over-population is then only about 200 meV. We will see that this constraint limits the benefits of wave clocking for SiDB devices.

### 5.3 Ground State Characterisation

Here we investigate the ground states of 3-state QCA devices. First, we look in detail at how a single device responds to all our parameters. Then we consider the conditions for which the ground state of simple QCA components indicate correct device operation.

#### 5.3.1 Single Device Analysis

It will be useful to fully understand the ground state of a single 3-state device under different parameters. We take the single-cell Hamiltonian given in Eq. (2.4) where we understand  $\mu$  to merely act as a shift in the clock  $\mathcal{C}$ . The population  $\mathcal{N}$  and polarization  $\mathcal{P}$  can be expressed in terms of the ground state energy,  $E_0$ :

$$\mathcal{N} = \frac{\mathcal{C} - E_0}{(\mathcal{C} + h\tilde{\mathcal{P}}) - 2E_0}, \quad \tilde{\mathcal{P}} = \frac{\mathcal{P}}{\mathcal{N}} = \frac{2E_0h}{E_0^2 + h^2}; \quad (5.12)$$

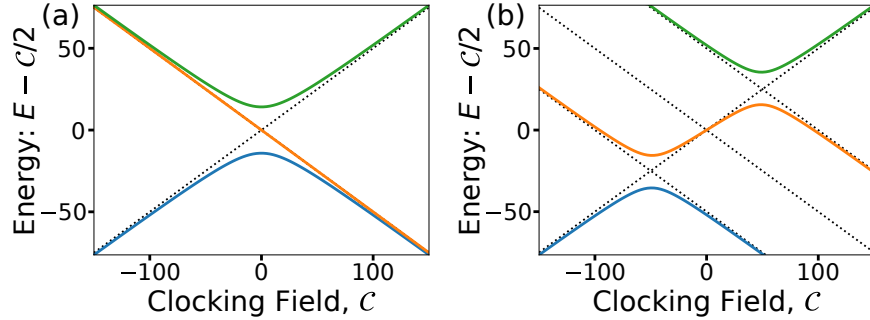


**Figure 5.5:** Spectra of the 3-State Cell Hamiltonian: (a)  $\gamma = 10$  meV,  $h = 0$  meV; (b)  $\gamma = 10$  meV,  $h = 50$  meV. Dotted lines indicate  $E = C, 0, \pm h$ . We subtract  $C/2$  from the energies to highlight symmetries in the spectrum. Energies are in meV.

however,  $E_0$  is non-trivial to express analytically. In Fig. 5.5, we show spectra for the two limiting cases of  $|h|$ : small and large with respect to  $\gamma$ . In both of these cases, the ground state energy is approximately the lower half of a hyperbola with center  $(C, E - C/2) = (-|h|, -|h|/2)$ . It is natural then to assume a general form of

$$E_0 = \frac{1}{2}(C - |h|) - \frac{1}{2}\sqrt{\alpha^2 + (C + |h|)^2}. \quad (5.13)$$

This is exact up to some parameter  $\alpha(\gamma, h, C)$ . In Appendix B.1, we discuss our approach to estimating  $\alpha^2$ . Here, it is sufficient to note that  $4\gamma^2 \leq \alpha^2 \leq 8\gamma^2$  with the minimum and maximum values achieved at  $\lim_{|h| \rightarrow \infty}$  and  $h = 0$ . The assumption of a hyperbolic form for  $E_0$  is equivalent to assuming  $\alpha$  is independent of  $C$ . We use a general approximation

$$\alpha^2(\gamma, h, C) = 4\gamma^2 \left[ 2 + u^2 - u\sqrt{2 + u^2} \right], \quad (5.14)$$

with a parameter  $u$  that depends on the desired accuracy. In Table 5.1, we give numerically achieved upper bounds on the errors relating to different forms of  $u$ . These bounds are independent of  $\gamma$ , justified as follows. From Eq. (5.12), we see that if  $E_0/\gamma$  is a function only of  $(h/\gamma, C/\gamma)$  then so are  $\mathcal{N}$  and  $\tilde{\mathcal{P}}$ . We can also rewrite Eq. (2.4) in the form  $\hat{H}(\gamma, h, C) = \gamma\bar{H}(h/\gamma, C/\gamma)$ . It follows that

$$E_0(\gamma, h, C) = \gamma\bar{E}_0(h/\gamma, C/\gamma). \quad (5.15)$$

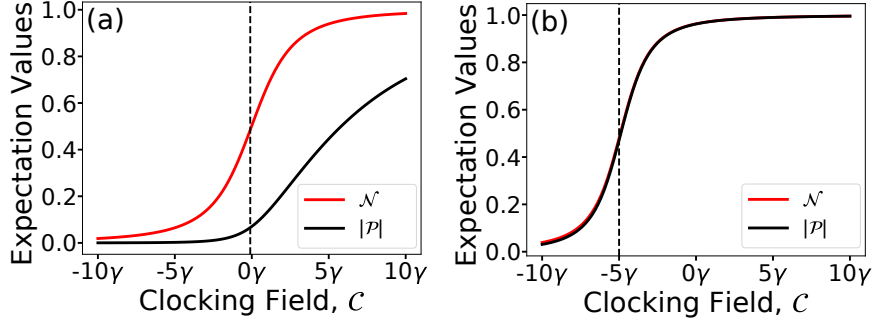


**Figure 5.6:** Polarization and population responses for the two limiting cases of biases: **(a)**  $h = \gamma/10$ ; **(b)**  $h = 5\gamma$ . The population is approximately a sigmoid with center  $C = -|h|$  (indicated) and a width of  $\alpha \propto \gamma$ .

**Table 5.1:** Worst-case errors over all  $(h, C)$  for different  $u$  parameter approximations.

Approximation	$\Delta E_0/(E_0 - C/2)$	$\Delta \tilde{\mathcal{P}}$	$\Delta \mathcal{N}$
$u = 1/2 \Leftrightarrow \alpha^2 = 6\gamma^2$	13.4%	0.037	0.039
$u =  h /\gamma$	4.7%	0.106 <sup>1</sup>	0.019
$u = 3 h /(\sqrt{9\gamma^2 + C^2} - C)$	1.1%	0.006	0.013

This form also holds for Eq. (5.13) if the  $u$  parameter depends only on  $(h/\gamma, C/\gamma)$ , as is the case for our approximations. The worst cases for the absolute errors of  $\mathcal{N}$  and  $\tilde{\mathcal{P}}$  and the relative error of any linear combination of  $(E_0, h, C)$  then occur at specific  $(h/\gamma, C/\gamma)$  pairs and are otherwise independent of the choice in  $\gamma$ . In Fig. 5.6, we show the typical cell response for low and high  $|h|/\gamma$ . A fair approximation of the population is the sigmoid

$$\mathcal{N} \approx \left[ 1 + e^{-\frac{2(C+|h|)}{\alpha(\gamma, h, -|h|)}} \right]^{-1} \quad (5.16)$$

obtained by expanding Eqs. (5.12) and (5.13) about  $C = -|h|$ . This sigmoid approximation gives a maximum error of  $\Delta \mathcal{N} \lesssim 0.06$  for  $u = 1/2$ . If the polarization bias is strong, the degree of polarization,  $|\mathcal{P}|$ , is essentially given by the population;

<sup>1</sup>In the case of  $u = |h|/\gamma$ , the large error in  $\tilde{\mathcal{P}}$  occurs in the regime where both  $C$  is large and  $|h| \ll \gamma$ . This corresponds to the presence of some kink at a populated cell. For  $C < 0$ , the error in  $\tilde{\mathcal{P}}$  is less than 0.014.

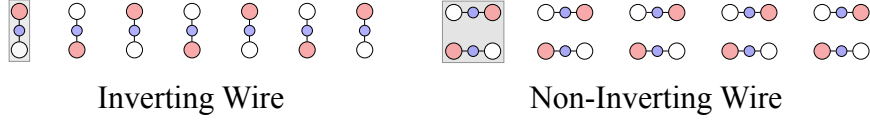


**Figure 5.7:** Wire arrangements with a driver cell to the left with fixed polarization and population of 1. Wires shown in their ideal fully populated configuration.

otherwise, the polarization will tend to lag behind the population as the clocking field is increased.

### 5.3.2 Populating a Wire near the Classical Limit

The influence of the congestion energy comes into effect only when multiple devices are being considered. In the ICHA picture the situation is intuitive: the instantaneous polarizations act to shift the biases,  $h_i$ , of each of the devices, and the populations shift the effective clocking fields,  $C_i$ . The net effect is to shift the population sigmoid to a new center, which we will refer to as the *activation energy*:

$$C_i^a = \mu_i + \sum_{j \neq i} \mathcal{D}_{ij} \mathcal{N}_j - \left| h_i - \frac{1}{2} \sum_{j \neq i} E_{ij}^k \mathcal{P}_j \right| = \tilde{\mu}_i - |\tilde{h}_i|, \quad (5.17)$$

neatly expressed in terms of the instantaneous effective biases from the ICHA Hamiltonian. We should expect a device to have a population of about  $1/2$  when the local clocking field is equal to the instantaneous activation energy. Using this idea, we can estimate bounds on the minimum clocking field needed to operate a functioning biased QCA wire as shown in Fig. 5.7. In Appendix B.2, we discuss bounds on the smallest and largest expected activation energies,  $C_{lo}^a$  and  $C_{hi}^a$ , during wire clocking. Note that for wires which populate out-of-order a larger range of activation energies may be possible. Using  $u = 1/2$  in Eq. (5.16), we expect that with a clocking field  $5\gamma$  above  $C_i^a$  we get a population of  $\mathcal{N}_i \approx 0.98$ . We extend our expected lower and upper bounds on the activation energy by this  $5\gamma$  factor to guarantee sufficient population and depopulation during clocking. We then obtain values for the average clock and clock swing:

$$C_0 = \frac{1}{2}(C_{lo}^a + C_{hi}^a), \quad \Delta C = C_{hi}^a - C_{lo}^a + 10\gamma. \quad (5.18)$$

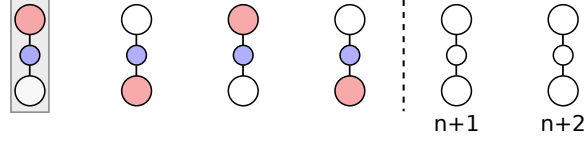


**Figure 5.8:** Driven inverting wire in the weak tunneling limit after successfully populating the first  $n$  cells. In-order population would be violated if cell  $n + 2$  has a lower activation energy than  $n + 1$ .

In the absence of congestion, wires tend to populate in-order. For zone clocking, this simply means  $\mathcal{N}_{n+1} \leq \mathcal{N}_n$  for all devices,  $n$ . In wave clocking, we are only concerned with the devices within the rising edge. We will consider the constraints on  $\xi$  which produce in-order population. The result is simple if we can ignore tunneling:  $\gamma = 0$ . We suppose that some number of the cells have populated in-order. This scenario is depicted in Fig. 5.8. The wire will continue to populate in order if  $\mathcal{C}_{n+2}^a \geq \mathcal{C}_{n+1}^a$ . From Eq. (5.17), this corresponds to the constraint

$$\xi \leq \frac{(|\tilde{h}_{n+1}| - |\tilde{h}_{n+2}|)/E_0^k}{(\tilde{\mu}_{n+1} - \tilde{\mu}_{n+2})/\mathcal{D}_0}. \quad (5.19)$$

In our case, the contributions to  $\mathcal{C}^a$  from congestion fall-off more slowly than from polarization. As a wire populates, we should then expect this bound to decrease. We assume then that there are only two cases of interest: (1) the first cell to populate in an unpopulated wire; and (2), the next cell to populate in an infinite wire. If we consider only the dominant term in our estimates of the kink and congestion energies, we can make a useful approximation of the cell interaction in a wire:

$$|E_{ij}^k| \approx E_0^k |i - j|^{-p}, \quad \mathcal{D}_{ij} \approx \mathcal{D}_0 \alpha_s^{|i-j|^{-1}} |i - j|^{-q}, \quad (5.20)$$

where  $\alpha_s = e^{-s_0/\lambda_{TF}}$  is the Thomas-Fermi screening factor for nearest neighbour cell-separation  $s_0$ , and  $p$  and  $q$  are some powers determined by the dependence on  $s$  in our interaction energy estimates. Note that we keep  $\alpha_s$  only in the case of the congestion energies in SiDBs as all of our other energies decay at least as fast as  $s^{-3}$ . Contributions from next-nearest neighbours are effectively negligible. As an

**Table 5.2:** Upper limits on  $\xi$  for in-order population of a wire in the weak tunneling limit. Values for  $\alpha_s$  correspond to device separations of 1.15 nm and 2.30 nm.

Device Geometry	$p$	$q$	$\alpha_s$	Eq. (5.22)	Eq. (5.23)
3-dot	3	3	1	0.500	0.402
6-dot	5	3	1	0.554	0.500
2-dot	3	1	0.527	0.594	0.402
4-dot	5	1	0.278	0.563	0.500

example, for a wire of 3-dot devices, we get

$$E_{ij}^k \approx -\frac{K_c}{2d}(d/s_{ij})^3 = -\frac{K_c}{2d}(d/s_0)^3|i-j|^{-3}. \quad (5.21)$$

We would then have  $E_{ij}^k \approx -E_0^k|i-j|^{-3}$ . Assuming interactions of the form given by Eq. (5.20), the first populated cell in a wire gives the constraint

$$\xi \leq \left(\frac{2^p - 1}{2^q - \alpha_s}\right)2^{q-p-1}. \quad (5.22)$$

For the case of the infinite wire, it depends on whether the wire is inverting or non-inverting:

$$\xi \leq \begin{cases} (1 - 1/2^{p-1})\zeta(p) - \frac{1}{2}, & \text{Inverting} \\ \frac{1}{2}, & \text{Non-Inverting} \end{cases} \quad (5.23)$$

where  $\zeta$  is the Riemann zeta function. The resulting constraints on  $\xi$  are summarized in Table 5.2. We can combine these constraints with our ratio estimates in Eq. (5.10) to obtain approximate requirements on our device geometries. For example, for a 3-dot device of the form presented in Fig. 5.1(a) to achieve in-order population of a wire using zone clocking with  $\gamma = 0$ , the device height must satisfy  $v \leq 0.45d$ . In Fig. 5.9, we show the polarizations and populations given by the ground states of biased 3 cell wires using zone clocking in the weak tunneling limit. We see that in this limit even the 3-dot and 6-dot wires would show out-of-order population for  $v = 0.5d$ . Similar ideas about out-of-order wire population have been seen in work by Karim *et al.*, although their focus was on identifying maximum required clocking fields [90]. Note that out-of-order population of non-

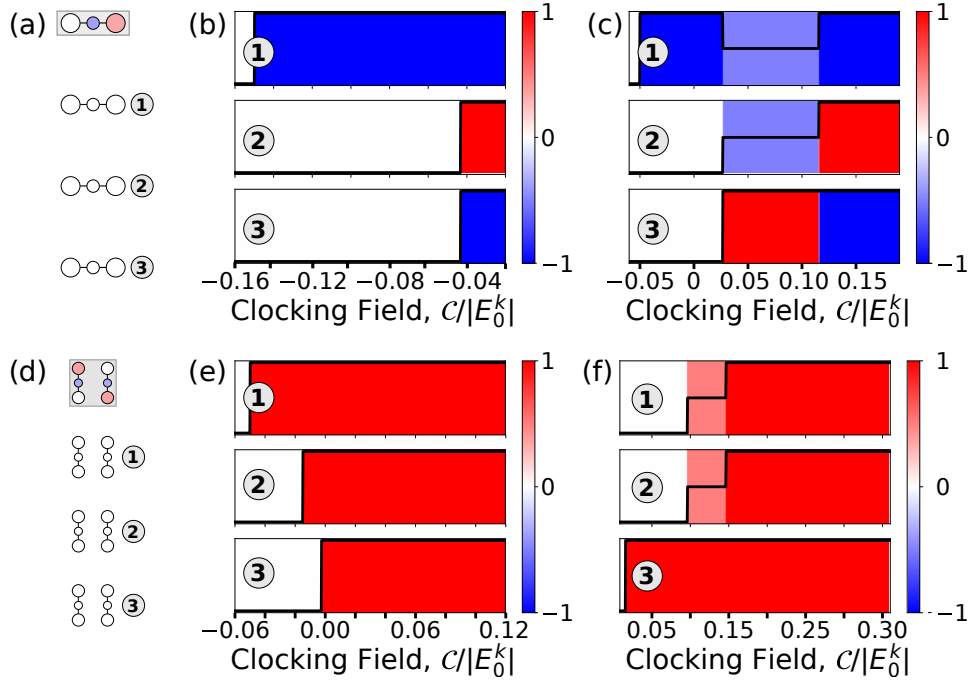


**Figure 5.9:** Ground state polarizations and populations of biased 3 cell wires: **(a-c)** show an inverting 3-dot wire with cells labelled and congestion ratios of **(b)** 0.35 and **(c)** 0.45; **(d-f)** show a non-inverting 6-dot wire with ratios **(e)** 0.45 and **(f)** 0.55. The polarizations for the indicated cells are shown by the bar color with the solid black line showing the population. The half-populated regimes in **(c)** and **(f)** indicate a degeneracy between populating cells 1 and 2.

inverting wires will not result in incorrect polarizations and thus presents less of an obstacle for properly functioning QCA networks. While this may be the case for wires, this argument will not apply in general as we will see in Section 5.3.4. For a 2-dot SiDB device, the appropriate constraint is  $(s/d)^2 \leq 0.201[1 + (d/\lambda_{TF})(s/d)]$ . In order to find a solution with  $s \geq d$ , we require that  $d$  be at least  $2.5\lambda_{TF}$ . The regime in which SiDB-based QCA wires operate in the classical limit using zone clocking corresponds to a case where the SiDBs barely interact at all.

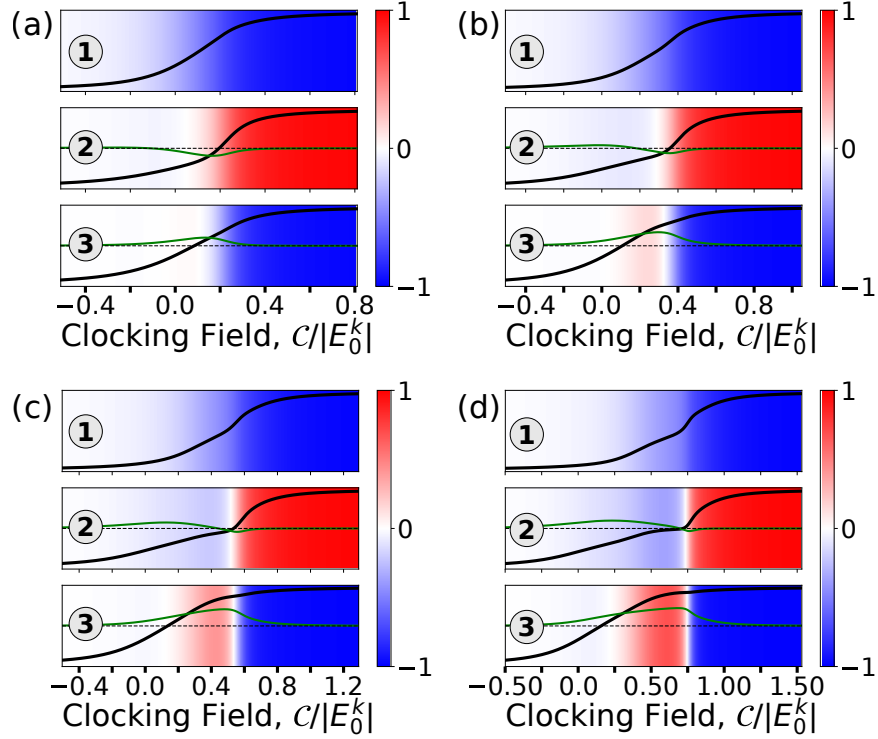


**Figure 5.10:** Ground state polarizations and populations of a biased 3-dot inverting wire with  $\gamma = E_0^k/10$  and congestion ratios of (a) 0.5, (b) 0.6, (c) 0.7, and (d) 0.8. The solid green line shows  $\mathcal{N}_n - \mathcal{N}_{n-1}$  with the dashed line indicating zero.

### 5.3.3 Congestion for Nonzero Tunneling

For non-zero  $\gamma$ , the population of a cell does not switch suddenly. In this case, we must consider a suitable condition for ordering. Previously, it was sufficient that within the region of clocking we had  $\mathcal{N}_{n+1} \leq \mathcal{N}_n$ ; however, we might not necessarily be concerned if a later cell becomes slightly populated. As an example, Fig. 5.10 shows the ground states of the 3-dot inverting wire for different congestion ratios at  $\gamma = E_0^k/10$ , a value often seen in the literature. Beyond  $\xi \approx 0.5$ , cell 3 takes on a slight incorrect polarization associated with the same out-of-order population seen in Fig. 5.9c. However, this effect is initially minimal. We might define a more forgiving in-order metric as something like

$$\mathcal{N}_{n+1} - \mathcal{N}_n \leq \mathcal{N}_* \quad \forall n, \mathcal{C} \quad (5.24)$$

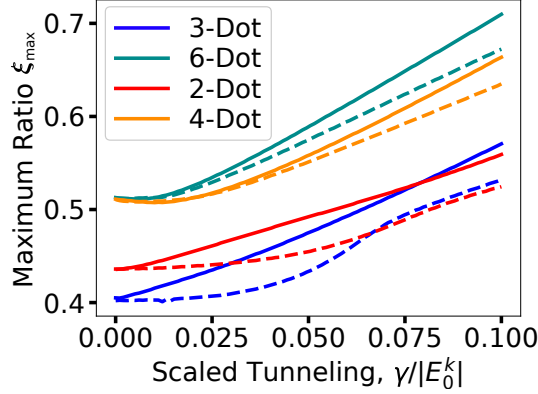


**Figure 5.11:** Maximum congestion ratios for 3 cell wires using devices for varying tunneling rates. The dashed lines show the values for the self-consistent ICHA. Values computed for a wire of length 3. For such a short wire, the  $\gamma = 0$  limit lies between the estimates made by Eqs. (5.22) and (5.23).

for a threshold value  $\mathcal{N}_*$  which is somewhat arbitrary. At  $\xi = 0.6$ , the out-of-order population is relatively clear with an observed maximum value of  $\mathcal{N}_3 - \mathcal{N}_2$  of about 0.33. We take  $\mathcal{N}_* = 0.3$  to be suitable. In Fig. 5.11, we show the maximum values of  $\xi$  which satisfy this criterion for all our considered devices over a range of  $\gamma$ . We compare the trends for the ground state of the full Hamiltonian with those achieved using the ICHA. These are obtained by self-consistently computing the polarizations and populations using Eq. (5.12), initialized with those from the previous clocking fields. Beyond about  $\gamma = 0.075E_0^k$  for inverting and  $\gamma = 0.03E_0^k$  for non-inverting interactions, all the trends are approximately linear. For sufficiently high  $\xi$ , we should expect congestion to dominate. In this case, the ground state would depend primarily on  $\mathcal{D}_0/\gamma = \xi/(\gamma/E_0^k)$  as observed. Note that the arbitrary selection of  $\mathcal{N}_*$  changes the slope of this linear regime.

We conclude this discussion by observing that even without employing wave clocking, correct operation of the 3-dot and 6-dot wires is achievable with modest tunneling rates. In the case of the highest  $\xi$  for 3-dot devices at 1 nm separation, we note that correct operation is possible above  $\gamma \approx 0.15E_0^k$ . For larger separations,  $\gamma = 0.1E_0^k$  is sufficient. The 2-dot and 4-dot SiDB devices, however, would require much higher tunneling rates on the order of  $\gamma \approx 0.5E_0^k$ .

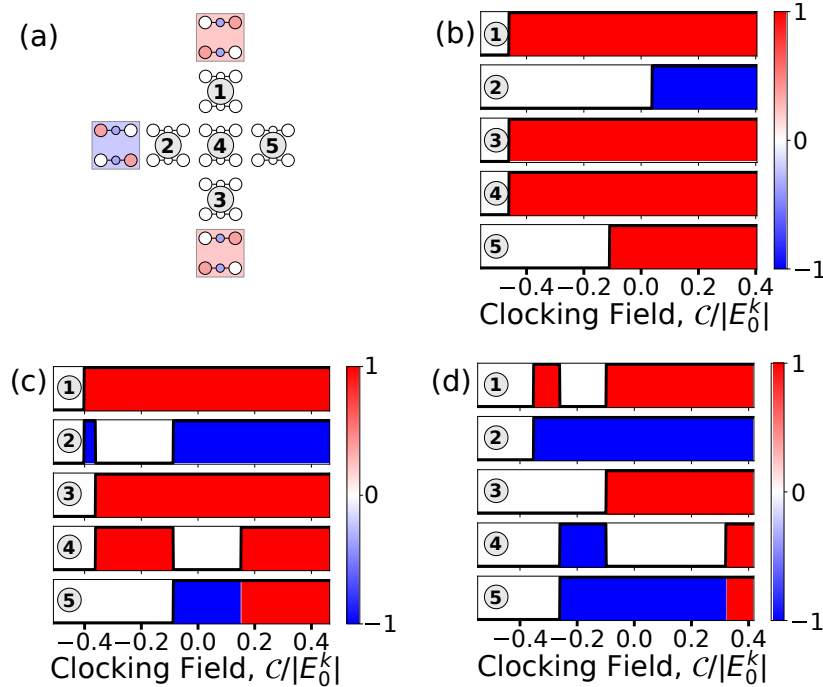


**Figure 5.12:** Ground states of the majority gate shown in (a) with congestion ratios of (b) 0.15, (c) 0.20, and (d) 0.25. The first three cells are adjacent to the inputs, cell 4 experiences the highest congestion at the center of the cross, and cell 5 is the output, expected to take on a polarization of +1. By  $\xi = 0.2$  we already observe undesirable behaviour in the output polarization.

### 5.3.4 The Case of the Majority Gate

Here we consider the case of a majority gate with inputs  $(+1, -1, +1)$ , a challenging case for zone clocking [5]. A schematic of the network as well as the ground states for a number of  $\xi$  values is shown in Fig. 5.12. It is not clear that in-order population should matter here. It is important then that we identify exactly the sort of behaviour that suggests a challenge to clocked operation. In Section 3.1.1, we determined an upper bound on the maximum characteristic rate of the dynamics that relates to transition parameters  $T_n(s) = |\langle \varphi_n | \frac{d}{ds} \hat{\mathcal{H}} | \varphi_0 \rangle| / (E_n - E_0)^2$ . In Fig. 5.13, we show the ground states, energy gaps, and transition parameters for the majority gate using two different  $\gamma$  values. Here  $\frac{d}{ds} \hat{\mathcal{H}}(s) = -\sum_i \frac{d}{ds} C_i(s) (\hat{\mathcal{N}}_i - \hat{I}) = -\frac{d}{ds} C(s) \sum_i (\hat{\mathcal{N}}_i - \hat{I})$  for zone clocking. We assume a trapezoidal clocking profile,

which gives  $\frac{d}{ds}\mathcal{C} = 4\Delta\mathcal{C}$ . We will expand on the application of this transition picture in the next chapter. It suffices here to note that the characteristic rate of the dynamics for adiabatic evolution is limited by the inverse of the maximum  $T_n(s)$ .

When tunneling is weak, each change in the ground state that occurs as the clocking field is swept produces a local minimum in the energy gap. If  $\gamma$  is sufficiently small the avoided level crossings are hyperbolic and well approximated by a Landau-Zener model: see for example Ref. [91]. The values of the minima can be roughly categorized based on the number of population-depopulation events they involve. For example, the population or depopulation of a single cell would produce a gap of roughly  $2\gamma$  as in Fig. 5.5(b). The first minima in Fig. 5.13(b) corresponds to the simultaneous population of two cells, and has a gap smaller than  $2\gamma$ . The remaining three minima can each be seen to describe three simultaneous events: a single depopulation and two populations. As we have assumed no tunneling between the upper sites, we decompose the change of the polarization of cell 5 as a depopulation immediately followed by a population. As we increase  $\gamma$ , it is these polarization-flip transitions which yield the smallest gaps and most strongly constrain the dynamics. We can see this in the transition parameter results, where the final transition dominates. We see also that the value of  $\gamma$  will have a significant effect on the potential operating speed of the 3-state devices. Increasing  $\gamma$  from  $0.02E_0^k$  to  $0.05E_0^k$  yielded a three order of magnitude reduction in the diabatic transition rates. Accounting then for non-zero tunneling, we define the majority gate to display poor behaviour when the ground state contains a change in cell polarization after first achieving an incorrect polarization of magnitude  $|\mathcal{P}| \geq 0.3$ , keeping with our earlier defined  $\mathcal{N}_*$ .

Returning then to Fig. 5.12, we see that at  $\xi = 0.15$  the ground state is well behaved; however, even at  $\xi = 0.20$  we observe undesirable behaviour of cell 5, the output. It is an interesting exercise justifying the order of events here. For example, in Fig. 5.12(c), the ground state is correct until  $\mathcal{C} \approx -0.1E_0^k$ . At this point, we have cells 1, 3, and 4 in the correct polarization. As soon as cell 2 is populated there is too much congestion at cell 4, which depopulates in favour of the output cell; however, the output cell is now under inverting diagonal interactions from the populated cells 1 and 3 and takes on the wrong polarization. A different sequence of populations occurs at  $\xi = 0.25$ . The inclusion of non-zero tunneling for the ma-

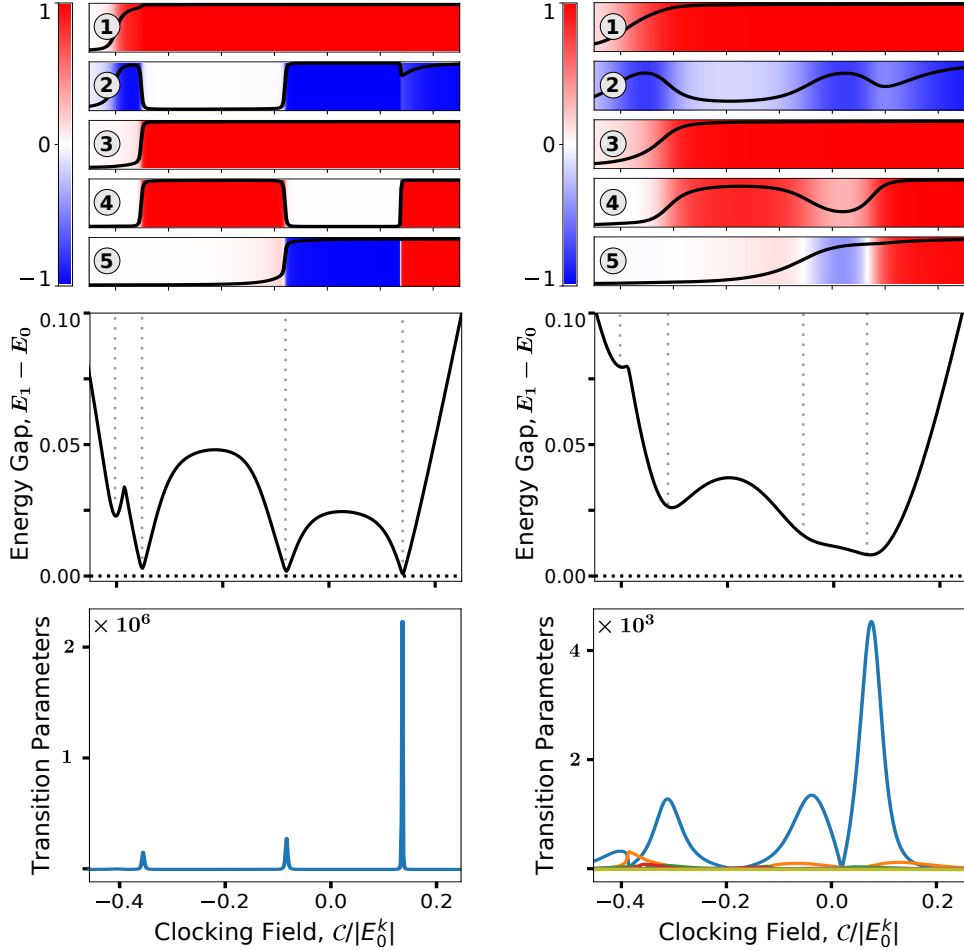


**Figure 5.13:** Ground states, energy gaps, and transition parameters for the majority gate in Fig. 5.12(a) for  $\xi = 0.20$  and non-zero tunneling. In the **left** column, we show the case for weak tunneling,  $\gamma = 0.02E_0^k$ , where each change in the ground state produces a clear hyperbolic gap. For the stronger tunneling,  $\gamma = 0.05E_0^k$ , on the **right**, we see that the gaps corresponding to simple changes in cell population increase significantly, leaving the most crucial gap corresponding to the change in polarization of cell 5. Vertical dotted lines are added to help correlate the minima to features in the ground states. We see in the transition parameters that the final change in the ground state is critical, and that the value of  $\gamma$  will significantly influence the maximum rate of the dynamics.

majority gate does not increase  $\xi$  as much as for the wire. At  $\gamma = E_0^k/10$ , the onset of poor ground state behaviour increases from  $\xi = 0.18$  to  $\xi = 0.23$ . To operate the majority gate using 6-dot devices, we require either a larger value of  $\gamma$  or a smaller value of  $v$ . For example, using  $\gamma = 0.1E_0^k$  requires that we satisfy  $v < 0.3d$ . Alternatively, using  $v = 0.5d$ , we require  $\gamma > 0.92E_0^k$ . For net-negative 4-dot devices, a zone clocked majority gate of this form requires  $\gamma > 0.85E_0^k$ . Large  $\gamma/E_0^k$  can be realised by increasing the device separation but may cause other complications due to the resulting weak  $E_0^k$ . Note that the OR gate design in Ref. [28] and additional gates in Ref. [2] demonstrate that alternate gate designs involving fewer charges are possible. If we cannot otherwise mitigate these congestion interactions, we should take this result as inspiration to consider such alternatives for SiDB devices.

## 5.4 Wave Clocking of Wires

By applying a spatially varying clocking field, we can overcome some of the challenges observed in zone clocking. The discussion is most easily understood for wires. From the perspective of activation energies, the effect of wave clocking is relatively simple. By populating a wire under a clocking gradient, the condition for in-order population becomes

$$C_{n+1}^a < C_n^a + (C_{n+1} - C_n) \approx C_n^a + \nabla C_n \Delta x_n \quad (5.25)$$

for clocking field gradient  $\nabla C_n$  at site  $n$  and cell separation  $\Delta x_n$ . In the weak tunneling limit, the result is to increase the constraint on  $\xi$  by an amount

$$\Delta \xi = \min_n \frac{-\partial_x C_n \Delta x_n}{\tilde{\mu}_{n+1} - \tilde{\mu}_n}. \quad (5.26)$$

For a trapezoidal clocking wave, and assuming a wire has populated in-order, this becomes

$$\Delta \xi = 4 \frac{\Delta C}{E_0^k} \frac{s_0}{\lambda}. \quad (5.27)$$

For a sinusoidal clocking wave it depends on the gradient of the clock when the cell is populating. We can, however, set an upper bound given by the maximum

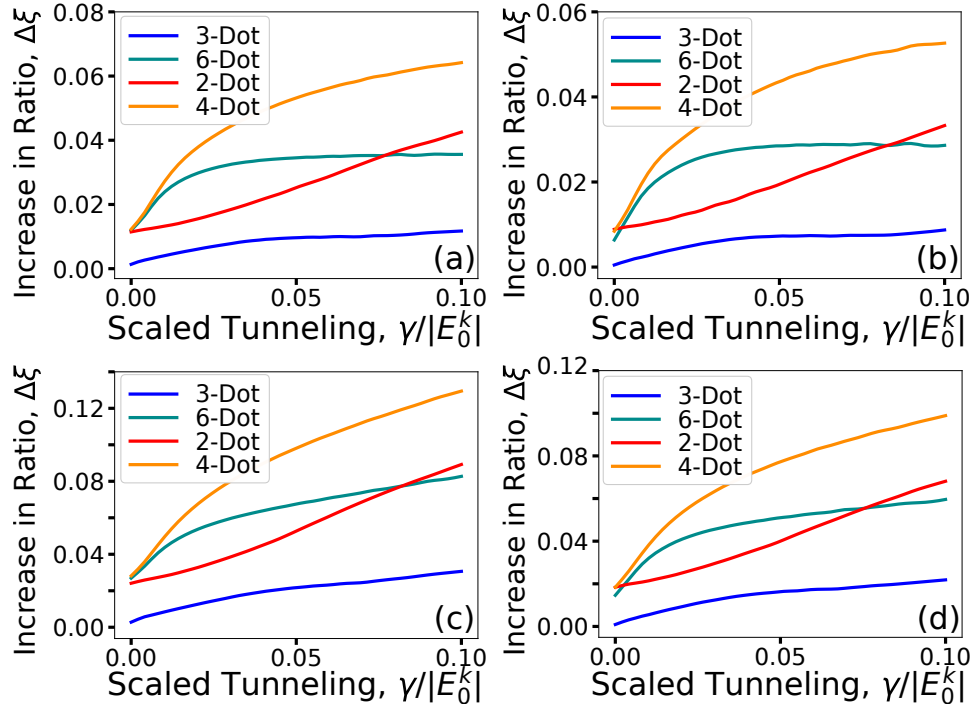


**Figure 5.14:** Increases in the maximum congestion ratios of 3 cell wires for wave clocking at various tunneling rates: **(a)** and **(b)** respectively show results for a trapezoidal and sinusoidal wave with  $\lambda = 200\text{nm}$ ; **(c)** and **(d)** show results for  $\lambda = 100\text{nm}$ . Minimum device separations are used.

gradient

$$\Delta\xi \leq \pi \frac{\Delta\mathcal{C}}{E_0^k} \frac{s_0}{\lambda}. \quad (5.28)$$

We will begin this discussion first in the absence of any adjustment in  $\Delta\mathcal{C}$ , an approach discussed in Section 5.4.2.

#### 5.4.1 Dependence on Device Dimensions

In Fig. 5.14, we show  $\Delta\xi$  for each of our devices as a function of the tunneling rate using the minimum  $\Delta\mathcal{C}$  from our zone clocking considerations. As discussed, clocking wavelengths below 200 nm are currently a challenge. Values for  $\lambda = 100\text{nm}$  are shown simply to demonstrate that the  $\Delta\xi$  would approximately double

as expected. We see also that the sinusoidal wave results are approximately  $\pi/4$  times those of the trapezoidal wave, indicating that the cells happen to populate when the clocking gradient is strongest. Perhaps most importantly, we see that  $\Delta\xi$  is small for  $\lambda = 200\text{nm}$ . This should not be surprising, as for nanoscale devices  $s_0/\lambda$  is on the order of  $10^{-2}$  and our zone clocking  $\Delta C/E_0^k$  is of order 1. To enable SiDB wire operation we need an order of magnitude further increase of  $\Delta\xi$ . One potential approach is to increase  $s_0/\lambda$  either by decreasing  $\lambda$  or increasing  $s_0$ . The former we know to be effective. The applicability of changing  $s_0$  is more involved.

We see in Figs. 5.2 and 5.3, that increasing  $s_0$  decreases  $E_0^k$  and may significantly increase  $\xi$ . Decreasing  $E_0^k$  has a number of consequence. First, the limiting frequency scale of clocking is approximately proportional to the energy scale of the system [5]. By decreasing  $E_0^k$  we likely decrease the operating speed of our devices. Secondly, we risk thermal excitations out of the ground state if the energy scale of the system approaches the thermal energy. For the 1 nm scale MVM devices, separations greater than  $\sim 3\text{nm}$  decrease  $E_0^k$  to below the room temperature thermal energy. For SiDB devices at liquid helium temperatures, the thermal energy scale is reached at 5.1 nm and 5.4 nm separations for the 2 and 4-dot devices respectively. At room temperature and ignoring other necessary alterations, the thermal energy is achieved at around 1.6 nm and 2.6 nm. These consideration limit how high we can set  $s_0$ . The most significant consequence, however, comes from the relative increase in the strength of  $\gamma/E_0^k$  which grows faster than  $\xi$ . The approximations in Section 5.2 suggest  $(\gamma/E_0^k)/\xi$  is proportional to  $s_0^3$  for MVM devices and  $s_0$  for SiDB devices. We know also from Fig. 5.11 that the maximum  $\xi/E_0^k$  for zone clocking is linear in  $\gamma$ . As an example, for 2-dot devices and some fixed  $\gamma$ , doubling  $s_0$  will increase  $\xi$  by a factor of 4,  $\gamma/E_0^k$  by a factor of 8, and thus  $\xi_{\text{max}}$  will grow faster than  $\xi$ . This increase tends to be more significant than the  $\Delta\xi$  from wave clocking.

#### 5.4.2 Raising the Maximum Clocking Strength

We are free to increase the clock sweep by increasing the maximum clocking strength: i.e. replacing  $C_{hi}^a$  in Eq. (5.18) with some larger value. As discussed in Section 5.2.3, there are limits to how strong the clocking field can be. For MVM

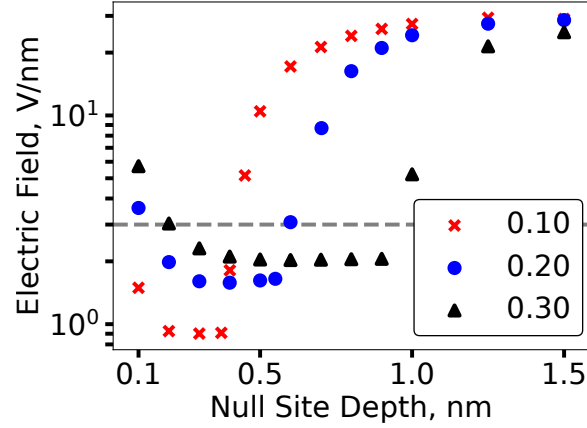


**Figure 5.15:** Dependence of the minimum required clocking fields on the null site depth for a 3-dot wire using a 200 nm trapezoidal wave. Three choices of  $\gamma/E_0^k$  are shown. The horizontal line shows 3 V/nm for reference:  $s_0 = 1$  nm.

devices, the electric fields can be quite large. As an example, for a 3-dot inverting wire with  $s_0 = 1$  nm and  $v = 0.5$  nm using a 200 nm trapezoidal clocking wave, the minimum required clocking field for  $\gamma = 0.2E_0^k$  is about  $C_{hi} = 1.92E_0^k \approx 880$  meV. This corresponds to an electric field strength of  $C_{max}/v = 1.76$  V/nm. The required electric field needed to achieve a given  $\mathcal{C}$  can be reduced by increasing the null site depth,  $v$ . However, for MVM devices,  $\xi$  is proportional to  $v^2$ , increasing the required clocking field for correct device operation. In Fig. 5.15, we show the minimum required electric field needed to operate a 3 cell wire of 3-dot devices in-order as a function of  $v$  for a few different choice of tunneling strength. We see that increasing  $v$  is only a benefit in cases where  $v$  is small. There is an interesting regime over which the required field is independent of the choice in  $v$ , indicating that the required  $\mathcal{C}$  is proportional to  $v$ . We finally note that there is some maximum  $v$  beyond which the required fields quickly increase.

Unfortunately, this approach has limited application for SiDB devices due to the discussed problem of populating additional dangling bonds in our devices. We take the maximum allowable clocking field to be about 200 meV above the largest observed activation energy. As an example, we consider 2-dot devices and set  $\gamma = 6.2$  meV, equal to  $E_0^k/10$  for  $s_0 = 1.15$  nm. For a 200 nm trapezoidal wave, a 3 cell inverting wire correctly operates for maximum clocking fields above  $63E_0^k \approx 3.9$  V,

and the highest observed activation energy is about  $5E_0^k \approx 0.3$  V. This difference is much larger than our allowed 200 meV. We can again reduce the clocking fields by increasing the device separation. At  $s_0 = 1.92$  nm, leaving 4 hydrogen between each SiDB device,  $E_0^k$  is reduced to 14.1 meV and thus  $\gamma = 0.44E_0^k$ . This  $\gamma$  is nearly large enough to allow operation under zone clocking, yet it still requires a clocking field 350 meV above the largest activation energy. At the next possible device separation of  $s_0 = 2.30$  nm, we no longer need to increase the clocking field above the zone clocking estimate with  $E_0^k = 7.8$  meV and a large  $\gamma$  value of  $0.8E_0^k$ . Similar results are observed for larger values of  $\gamma$ : the constraints on the maximum clocking field simply do not easily allow a significant increase in the clock sweep without operating in a regime in which  $E_0^k$  is small and  $\gamma/E_0^k$  is large. We should not necessarily exclude the possibility that wires can still function within the rising edge of the clock despite overpopulation elsewhere. In this case, it may be acceptable to allow higher clocking fields. Further investigation into the dynamic behaviour of the SiDB devices in a more complete charge basis is required. If we must avoid overpopulation, these results suggest that SiDB based QCA may not significantly benefit from wave clocking unless  $\lambda$  can be further reduced or a relatively high  $\gamma/E_0^k$  is realisable.

## 5.5 Summary

The observed prominence of congestion interactions in SiDB devices raises questions about the feasibility of certain higher density arrangements such as logic gates or even simple QCA devices. These interactions are relatively easily overcome for molecular QCA devices such as zwitterionic nido carborane by employing dynamic wave clocking with an increased maximum clocking field. We have investigated the role of these congestion interactions in 3-state QCA, identifying limits for the amount of congestion allowable before the ground state displays undesirable behaviour, both for zone clocking as well as wave clocking. For zone clocking, we find reasonable parameter ranges for molecular QCA which enable both wire and majority gate operation. We find that the high congestion energies of net-negative SiDB structures makes even wire operation under zone clocking challenging unless the inter-dot tunneling rate is allowed to be quite large: roughly half the kink

energy or more. Such large values may pose other challenges. For majority gate operation, it may be necessary to employ architecture specific gates, such as those presented in Ref. [28] and Ref. [2], rather than the common 5 cell cross usually considered in QCA design. We argue that the capacity for overpopulation of these SiDB devices limits the extent to which wave clocking can mitigate congestion interactions for current constraints on clocking wavelengths. These large congestion energies emerge due to the use of net-negative SiDB devices. If a net-neutral variant could be demonstrated, the congestion energies would decay similarly to those of molecular QCA devices and SiDB-based QCA operation would be more easily achieved.

## Chapter 6

# Limits of Adiabatic Clocking for 2-State QCA Networks

We will now look more closely at the link between QCA clocking and quantum annealing introduced in Chapter 3. It was established that zone clocking in 2-state QCA could be understood as quantum annealing with a transverse field Ising model. We will use this understanding to investigate the adiabaticity and maximum clocking frequency of a subset of the basic building blocks of QCA networks. In particular, we consider the frequency below which a QCA logic gate gives the correct output with at least 99% likelihood. The selection of building blocks, with the relevant naming schemes, are shown in Fig. 1.2. The analysis is divided into three contributions. In Section 6.1, we discuss how the choice in clocking schedule influences overall performance, including how basic knowledge about the low energy spectrum can inform a better choice in schedule. In Section 6.2, we study the performance of our building blocks in the coherent limit, excluding any environmental interactions. Finally, in Section 6.3, we incorporate a simple model of thermal dissipation, and discuss the extent to which dissipation changes the performance estimates.

It is necessary to emphasize the distinction between two different rates that will be included in this discussion. The operation in QCA zone clocking which parallels quantum annealing corresponds to the switching phase in Fig. 1.3. It is natural to restrict our normalized time  $s$  to this phase, which represents only a quarter of

the clocking period. As a consequence, the characteristic rate of the dynamics as defined in Section 2.2 does not directly correspond to the actual clocking frequency of the network. This *clocking frequency*, expressed relative to the  $f_0$ , can be obtained as  $\tilde{f}_c = f/4f_0 = \pi\tilde{f}/2$  where the frequency scale  $f$  should be understood to be the inverse of the switching period.

## 6.1 Choosing a Clocking Schedule

The choice of annealing schedule has a significant effect on the ultimate performance of a quantum annealing process: see, for example, [92]. From Section 3.2 and Eq. (3.14), the Hamiltonian of interest for 2-state zone clocking is

$$\hat{\mathcal{H}}(s) = -\frac{1}{2}A(s)\sum_i\hat{\sigma}_x^i + \frac{1}{2}B(s)\left[\sum_i h_i\hat{\sigma}_z^i - \sum_{\langle ij\rangle} E_{ij}^k\hat{\sigma}_z^i\hat{\sigma}_z^j\right]. \quad (6.1)$$

For now we allow  $B(s)$  to be time dependent and define the initial *transverse* and *classical* Hamiltonians  $\hat{\mathcal{H}}_X = -\sum_i\hat{\sigma}_x^i$  and  $\hat{\mathcal{H}}_{\text{cl}} = \sum_i h_i\hat{\sigma}_z^i - \sum_{\langle ij\rangle} E_{ij}^k\hat{\sigma}_z^i\hat{\sigma}_z^j$ . We will use the term *clocking schedule* to describe the profile of  $A(s)$  used for a given clock zone. QCADesigner, uses a sinusoidal schedule which is approximately linear over the switching regime [34]. Linear clocking schedules have also been considered for the 3-state QCA model [93]. In this section, we make some considerations for how details of the shape of the clocking schedule influence the behaviour of the system during clocking.

### 6.1.1 Performance Metrics

The first task is to better establish metrics for QCA performance. As we will be considering dissipation, it is natural to use the density operator,  $\hat{\rho}(s)$ , to define the state of the QCA network, with dynamics calculated with Eq. (2.8). We make the

following definitions, explained in the following discussion:

$$\text{Adiabaticity:} \quad \mathcal{M}_A(s) = \text{Tr} \hat{\rho}(s) \hat{P}_g(s) \quad (6.2a)$$

$$\text{Classical Performance:} \quad \mathcal{M}_{cl} = \text{Tr} \hat{\rho}(1) \hat{P}_{cl} \quad (6.2b)$$

$$\text{Logical Performance:} \quad \mathcal{M}_L = \frac{1}{2^{|\Omega|}} \prod_{i \in \Omega} (1 + \lambda_z^i(1) \mathcal{P}_i^{cl}) \quad (6.2c)$$

For adiabatic clocking, the system should remain near the ground state at all times.  $\mathcal{M}_A(s)$  describes the overlap between the system state and the space of potentially degenerate ground states of  $\hat{\mathcal{H}}(s)$ , given as the expected value of the ground state projection operator  $\hat{P}_g(s) = \sum_d |\psi_g^d\rangle \langle \psi_g^d|$ . Clocking ideally results in the system reaching the ground state of the classical Hamiltonian  $\hat{\mathcal{H}}_{cl}$ . We assume a non-degenerate classical ground state with a projection operator  $\hat{P}_{cl} = |\psi_{cl}\rangle \langle \psi_{cl}|$ .  $\mathcal{M}_{cl}$  describes the overlap with this state. Absent correlations in  $\hat{\rho}(1)$ ,  $\mathcal{M}_{cl}$  simplifies to

$$\tilde{\mathcal{M}}_{cl} \approx \frac{1}{2^N} \prod_{i=1}^N (1 + \lambda_z^i(1) \mathcal{P}_i^{cl}), \quad (6.3)$$

with  $\mathcal{P}_i^{cl} = \text{Tr} \hat{P}_{cl} \hat{\sigma}_z^i$  the polarization of each cell in the classical ground state. In principle, the polarizations of certain output cells may be logically correct even if the state fails to reach the ground state. By restricting the product in Eq. (6.3) to a finite subset,  $\Omega$ , of the cells, we can define a logical performance,  $\mathcal{M}_L$ . In this investigation, we consider a ‘‘high performance’’ target of  $\mathcal{M}_{cl} \geq 0.99$ .

### 6.1.2 Figures of Merit for the Ground State

For typical QCA networks, we will have a non-degenerate ground state. We can therefore use non-degenerate perturbation theory to determine important figures of merit for the initial and final ground states:

$$\mathcal{M}_0 = \langle \hat{P}_X \rangle(0) = 1 - \alpha_0^{-2} F_0 + O(\alpha_0^{-3}), \quad (6.4a)$$

$$\mathcal{M}_1 = \langle \hat{P}_{cl} \rangle(1) = 1 - \alpha_1^2 F_1 + O(\alpha_1^3), \quad (6.4b)$$

where  $\hat{P}_X$  is the projection operator onto the ground state of  $\hat{\mathcal{H}}_X$ , expectation values are taken for the ground state of  $\hat{\mathcal{H}}(s)$ ,  $\alpha_0$  and  $\alpha_1$  are the initial and final values of

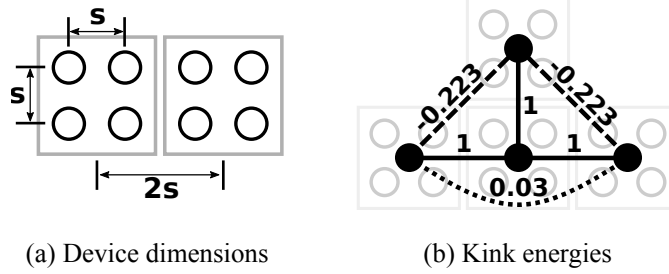


**Figure 6.1:** QCA Device dimensions and computed kink energies relative to  $\mathcal{E}$ . We ignore the 0.03 and weaker interactions.

**Table 6.1:** F-parameters in Eq. (6.4) from Eq. (6.5) for the simulated devices.

Device	Wire-N	Inverter	Maj-111	Maj-101	Maj-110
$F_0$	$\frac{1}{16}(N+3)$	0.581	1.012	1.012	1.012
$F_1$		2.217	1.141	2.259	1.735

the ratio  $\alpha(s) = A(s)/B(s)$ , and  $F_0$  and  $F_1$  are network-specific parameters dependent only on  $(h_i, E_{ij}^k)$ . In the limit of slow clocking,  $\mathcal{M}_{cl}$  approaches  $\mathcal{M}_1$ . It is necessary then to choose  $\alpha_1$  such that  $\mathcal{M}_1 > 0.99$ . For  $\hat{\mathcal{H}}_{cl}$ , we find

$$F_0 = \frac{1}{4} \sum_{i=1}^N |h_i|^2 + \frac{1}{16} \sum_{\langle ij \rangle} |E_{ij}^k|^2, \quad F_1 = \frac{1}{4} \sum_{i=1}^N \frac{1}{\tilde{h}_i^2}, \quad (6.5)$$

with  $\tilde{h}_i = h_i - \sum_{j \neq i} E_{ij}^k \mathcal{P}_i^{cl}$  calculated for the polarizations of the ground state of  $\hat{\mathcal{H}}_{cl}$ . For our performance target, we obtain a necessary constraint on  $\alpha_1$ :

$$\alpha_1^{-1} \geq \max \sqrt{F_1/1 - \mathcal{M}^*}, \quad (6.6)$$

with some  $\mathcal{M}^* > 0.99$ . Schematics of the device interactions are shown in Fig. 6.1 with the computed  $F_0$  and  $F_1$  shown in Table 6.1. Our constraint is approximately  $\alpha_1 \leq 1/15$ . If we can assume that  $\mathcal{M}_A(1)$  is independent of  $\alpha_1$  when  $\alpha_1$  is small, then it can be shown that [5]

$$\mathcal{M}_{cl}(\tilde{f}, \alpha_0, \alpha_1) \approx \mathcal{M}_{cl}(\tilde{f}, \alpha_0, 0) \mathcal{M}_1(\alpha_1). \quad (6.7)$$

We will use QCADesigner's default value of  $\alpha_1 = 1/20$ , giving  $\mathcal{M}^* = .9943$  which satisfies our 0.99 performance constraint.

### 6.1.3 Candidate Clocking schedules

An optimal choice of clocking schedule will depend on details of the environmental interaction and will not be addressed here. Instead, we introduce a schedule which mimics the standard linear schedule used in quantum annealing studies. We assume the following: (1) the kink energies are fixed by the network geometry and hence  $B(s) = 1$ ; (2) the tunneling energies cannot be made infinite or zero; and (3) the rate of change of the eigenstates for the linear schedule is a good choice for quantum annealing. The eigenstates of Eq. (6.1) depend only on the ratio  $\alpha(s)$ . We define our clocking schedules by their initial and final ratios  $\alpha_0$  and  $\alpha_1$ . We consider for comparison an appropriate **Linear** schedule with  $B(1) = 1$ :

$$A_L(s) = 1 - (1 - \alpha_1)s, \quad (6.8a)$$

$$B_L(s) = 1 - (1 - 1/\alpha_0)(1 - s). \quad (6.8b)$$

Imposing  $B(s) = 1$ , we define an analogous schedule with the same eigenstates:  $A_Q(s) = A_L(s)/B_L(s)$ ,

$$A_Q(s) = 1 + (\alpha_0 - 1) \frac{1 - \ell s}{1 + (\alpha_0 - 1)s}, \quad (6.9)$$

which we refer to as the **Quasilinear** schedule, as it is perhaps the closest we can get to the linear schedule under the given constraints. The  $\ell$  here satisfies  $A_L(1/\ell) = B_L(1/\ell)$  and has value  $\ell = 1 + (1 - \alpha_1)/(1 - \alpha_0^{-1})$ . Finally, the **Sinusoidal** schedule in QCADesigner has the form

$$A_S(s) = \frac{\alpha_0 - \alpha_1}{\sqrt{2}} \cos\left(\frac{\pi}{2}(s + 1/2)\right) + \frac{\alpha_0 + \alpha_1}{2}. \quad (6.10)$$

Schematics of these clocking schedules and the corresponding low energy eigen-spectra of an inverter are shown in Fig. 6.2. If we assume a simple Landau-Zener model for the minimum energy gap, we can make a first order performance estimate. The gap was fit to Eq. (3.9), with the Landau-Zener parameters summarized

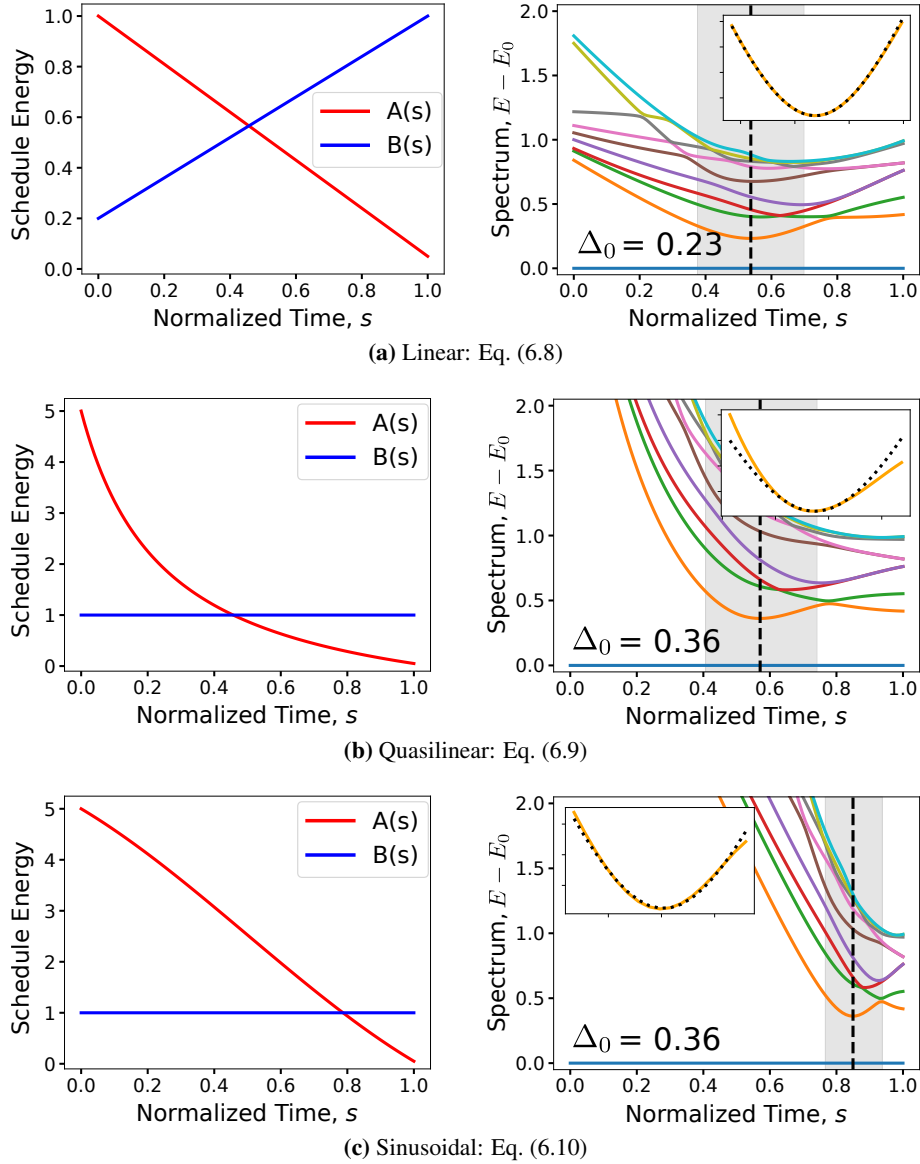


**Figure 6.2:** Schedule energies for the considered clocking schedules with  $\alpha_0 = 0.5$ ,  $\alpha_1 = 1/20$ . Spectra are shown for the QCA inverter, including only the 10 lowest energy eigenvalues with the ground state subtracted. The location and size of the minimum gap is indicated for comparison. The gap was fit using Eq. (3.9) within  $\Delta s = 0.07$  of the minimum gap. The fit is shown in the inset over the shaded region representing  $\pm W$  about the minimum.

**Table 6.2:** Fit parameters for the hyperbolic approximation of the minimum gap of the inverter for the different clocking schedules. Errors indicate  $2\sigma$  estimates from the fit covariance matrix where significant.

Clocking schedule	$\Delta_0$	$W$	$\Delta_0 W$
Linear	0.233	0.162	0.037
Quasilinear	0.362	$0.168 \pm 0.005$	$0.062 \pm 0.002$
Sinusoidal	0.362	$0.087 \pm 0.002$	$0.030 \pm 0.001$

in Table 6.2. If the avoided crossing were well described by the Landau-Zener model we should expect the characteristic rate needed to achieve a given  $\mathcal{M}_{cl}$  to be proportional to  $\Delta_0 W$ ; however, we have not established that the eigenstates involved in the avoided crossing satisfy the conditions inherent to the Landau-Zener approximation. Further, the hyperbolic fit is not particularly convincing for the Quasilinear schedule and we are ignoring other details of the spectrum. Nevertheless, this result suggests that the Quasilinear schedule might outperform both the Linear and Sinusoidal schedules. The classical performance was computed for our simple QCA components using Eq. (2.8) for the different clocking schedules, with the system initialized in the ground state of  $\hat{\mathcal{H}}(0)$ . Performance comparisons are shown in Fig. 6.3, including the maximum characteristic rate at which  $\mathcal{M}_{cl} = 0.99$  was achieved. In all cases, the Quasilinear schedule performed at least as well as the Linear and Sinusoidal schedules; in most cases, it was a significant improvement. Unless stated otherwise, it will be used for all results that follow.

#### 6.1.4 Initial Coherent Oscillations

Even if we initialize the system in the ground state of  $\hat{\mathcal{H}}(0)$ , we will observe oscillations induced by the clocking field. These oscillations manifest in our performance metrics as can be seen in Figs. 6.4 and 6.5. We can approximate the magnitude of oscillations using time dependent perturbation theory for the ground state and first excited state of  $\hat{\mathcal{H}}(0)$ , ignoring degeneracy for this simple analysis. If  $A(s)$  has an initial linear component, we get a transition probability into the excited state for small  $s$  of

$$P_{g \rightarrow e}(s) \propto \frac{|\frac{d}{ds}A(0)|^2}{A_0^4} \left( \frac{\tilde{f}}{A_0} \right) \sin^2 \left( \frac{\omega_r s}{2} \right), \quad (6.11)$$

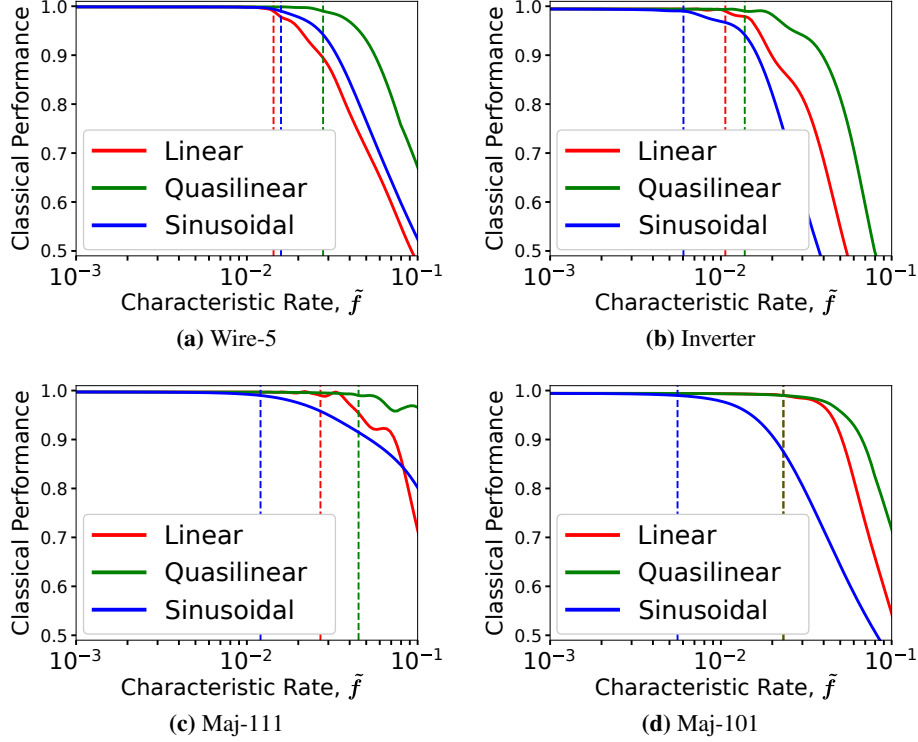


**Figure 6.3:** Comparison of classical performances for the different clocking schedules:  $\alpha_0 = 5$ ,  $\alpha_1 = 1/20$ . Dashed lines mark the maximum characteristic rate, below which  $\mathcal{M}_{cl} \geq 0.99$ . Schedule smoothing employed: see Section 6.1.4.

where  $A_0 = A(0)$  and  $\omega_r \approx A_0/\tilde{f}$ . If  $A(s)$  has no initial linear component, we calculate

$$P_{g \rightarrow e}(s) \propto \frac{|\frac{d^2}{ds^2}A(0)|^2}{A_0^4} \left(\frac{\tilde{f}}{A_0}\right)^3 \sin^2\left(\frac{\omega_r s}{2}\right). \quad (6.12)$$

These oscillations are “Rabi-like” in that they match what we would expect if we replaced the clocking field with a weak oscillation given by the  $\omega_r$  component of its frequency decomposition. Importantly, if  $\tilde{f}/A_0 \ll 1$  we can significantly reduce these initial oscillations by modifying the initial clocking schedule in order to remove any linear component. We employ a smoothing procedure in which we apply the map

$$s' = s\left(1 - e^{-s^2/2\sigma^2}\right). \quad (6.13)$$

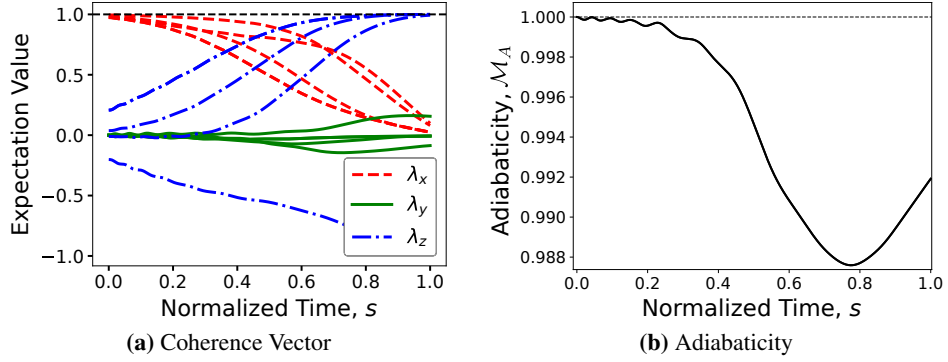


**Figure 6.4:** Coherence vector and adiabaticity for a simulation of Maj-101 using the Quasilinear schedule with  $\tilde{f} = 3 \times 10^{-2}$ ,  $\alpha_0 = 5$ ,  $\alpha_1 = 1/20$ . Initial coherent oscillations arise due to the changing Hamiltonian. These oscillations tend to weaken during clocking; however, a lowered adiabaticity when approaching the critical regime of avoided level crossings can propagate to a reduced final performance.

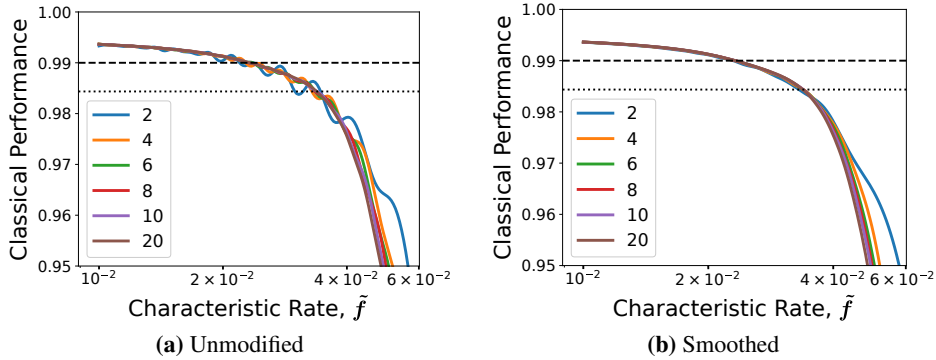


**Figure 6.5:** Classical performance of Maj-101 for different  $\alpha_0$  values (a) before and (b) after initial smoothing. Results use the Quasilinear schedule with  $\alpha_1 = 1/20$ . The dashed line indicates the  $\mathcal{M}_{cl} = 0.99$  performance threshold, with the dotted line the effective threshold for  $\alpha_1 = 0$  using Eq. (6.7). Note the oscillations in (a) are more prominent for small  $\alpha_0$ .

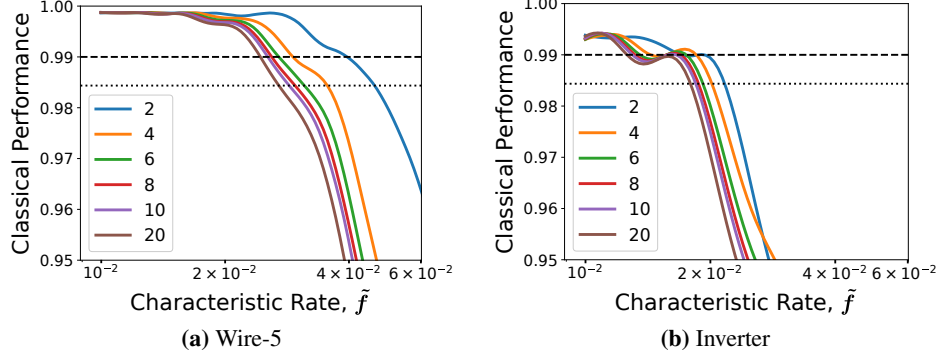


**Figure 6.6:** Classical performance for different  $\alpha_0$  values with  $\alpha_1 = 1/20$ . In cases where there is a clear avoided level crossing in the LES, smaller  $\alpha_0$  values yield higher performance. We use the left-most intercept when defining maximum characteristic rate to account for potential performance oscillations. The lower  $F_0$  value of the wire gives it a higher  $\mathcal{M}_1$  upper bound.

This map has a few useful properties: (1) it leaves the initial value of the schedule unchanged; (2) it cancels the linear component of the initial schedule; and (3), it only affects the schedule over a period of  $\sim 2\sigma$ , meaning we can remove the initial oscillations without affecting the later schedule. We set  $\sigma = 4\pi\tilde{f}/A_0$  to smooth over two periods of the oscillations. The effect is clear in Fig. 6.5b.

### 6.1.5 Choosing the Initial Clocking Field

For Maj-101 in Fig. 6.5, the choice of  $\alpha_0$  did not significantly influence the classical performance. This will not generally be the case. In Fig. 6.6, we see the performance for both the wire and inverter for different initial clocking values. In these cases, the lower the value of  $\alpha_0$ , the higher the performance. If we assume the only important feature of the clock to be a single Landau-Zener-like avoided level crossing, the maximum characteristic rate that allows a given adiabaticity is

$$\tilde{f}_{max} \approx \frac{\pi\Delta_0 W}{-2\ln(1 - \mathcal{M}_A)}, \quad (6.14)$$

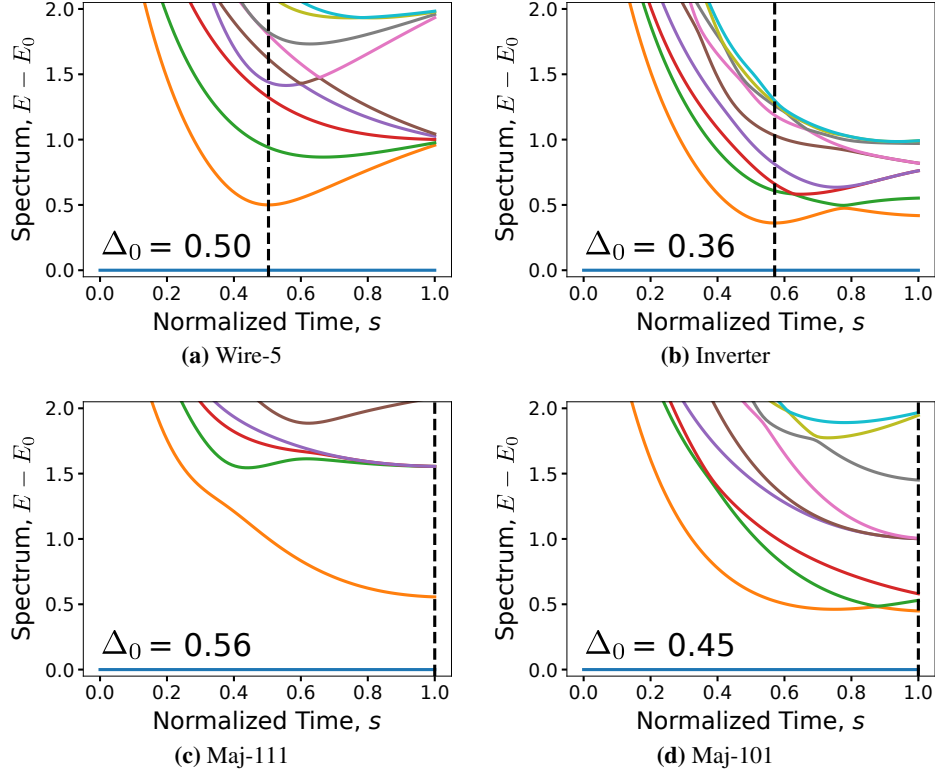


**Figure 6.7:** Low energy spectra of the simulated devices relative to the ground state energy with the location and size of the minimum gap indicated. Only 10 energy levels are shown for the inverter.

where the gap width,  $W$ , is inversely proportional to the slope of the clocking field near the minimum gap. For the Quasilinear schedule, the slope satisfies

$$\frac{d}{ds}A_Q(s) = \frac{\alpha_0^2}{[1 + (\alpha_0 - 1)s]^2} \frac{d}{ds}A_Q(1), \quad (6.15)$$

where  $\frac{d}{ds}A_Q(1) = -(1 - \alpha_1/\alpha_0) \approx -1$  for small  $\alpha_1$ . We then expect  $\tilde{f}_{max}$  to be proportional to  $[s_* + (1 - s_*)/\alpha_0]^2$  with  $s_*$  the location of the minimum gap. The spectra for most of the simulated devices are shown in Fig. 6.7. For majority gates, the minimum gap occurs in the classical limit,  $s_* = 1$ , hence we expect no  $\alpha_0$  dependence. If the minimum gap occurs at some earlier  $s_*$ , we expect  $\tilde{f}_{max}$  to

decrease with increasing  $\alpha_0$  as observed.

QCADesigner uses a value of  $\alpha_0 = 5$  and from these considerations we might naïvely assume we should use an even smaller value of  $\alpha_0$ ; however, we are ignoring some important caveats. We initialize the system near the ground state of  $\hat{\mathcal{H}}(0)$ . If  $\alpha_0$  is small, the initial state already has a significant projection onto the classical ground state. In that sense, much of the work the clocking is supposed to achieve must have been done by whatever process set up the initial state. Indeed from Eq. (6.4) we see that  $\alpha_0 = 5$  gives a projection onto the ground state of  $\hat{\mathcal{H}}_X$  of only  $\mathcal{M}_0 = 0.96$  in the worst case of a majority gate. In addition, the cell polarizations,  $\lambda_z^i$ , will have initial values on the order of  $\alpha_0^{-1}$ , as high as 0.2 in Fig. 6.4, pointing to a second issue: with small  $\alpha_0$ , “deactivated” cells may remain partially polarized, perhaps enough that the next clock zone may bias our outputs. Both of these issues are resolved by using a higher value of  $\alpha_0$ ; however, we see in Fig. 6.6 that there is only minimal decrease in performance beyond  $\alpha_0 = 5$ . We conclude then that we cannot justify using a smaller value of  $\alpha_0$ , nor would we expect using a larger value to influence performance within the scope of our analysis.

## 6.2 Coherent Behaviour of QCA Components

Here we consider the behaviour of our QCA components excluding any dissipation. In all results that follow, we use clocking ratios of  $\alpha_0 = 5$  and  $\alpha_1 = 1/20$ .

### 6.2.1 Analysis of QCA Wires

In Fig. 6.9, we consider the performance of wires of various lengths. For the special case of a left-driven wire as in Fig. 1.2, the Hamiltonian is of the form

$$\hat{\mathcal{H}}_W(s) = -\frac{1}{2}A(s)\sum_{i=1}^N\hat{\sigma}_x^i + \frac{1}{2}B(s)\left[\hat{\sigma}_z^1 - \sum_{\langle ij \rangle}^N\hat{\sigma}_z^i\hat{\sigma}_z^j\right]. \quad (6.16)$$

Using a slight modification to the Jordan-Wigner transform approach used for the unbiased wire [94], we can obtain an analytic description of the low energy spectrum for biased wires in terms of the set of eigenenergies

$$\varepsilon_k = \sqrt{B^2(s)\sin^2(q_k) + [A(s) - B(s)\cos(q_k)]^2}, \quad (6.17)$$

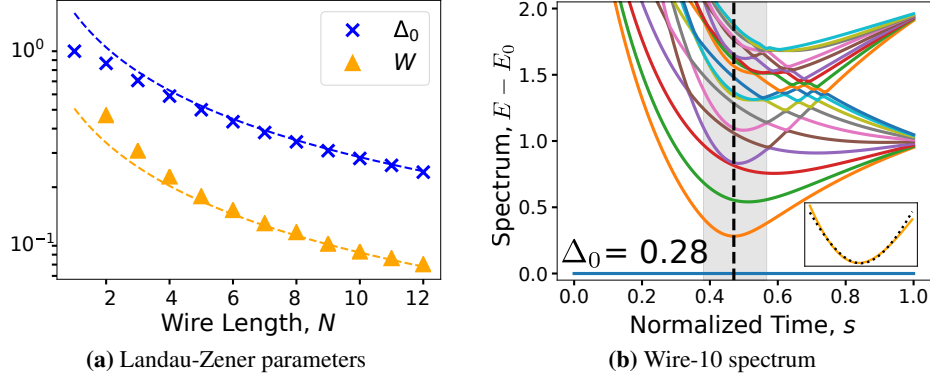


**Figure 6.8:** Landau-Zener parameters as a function of the wire length: **(a)** comparison of Eq. (6.18) to values extract from fitting the lowest energy gap in the spectrum; **(b)** example wire spectrum with a hyperbolic fit of the gap. As the wire length increases, the gap becomes more hyperbolic.

with  $k \in \{1, \dots, N\}$  and pseudo-momenta  $q_k = k\pi/(N+1)$ . Each energy level of  $\hat{\mathcal{H}}_W(s)$  is found by summing over a subset of the eigenenergies  $\varepsilon_k$ . For large  $N$ , each of the  $\varepsilon_k$  can be fit to the hyperbolic form Eq. (3.9) with the minimum occurring for  $A(s_*) = B(s_*)$  and parameters:

$$\Delta_0 \approx B(s_*)q_k, \quad W = \frac{\Delta_0}{\Delta m} \approx \frac{B(s_*)q_k}{\Delta m}, \quad (6.18)$$

where  $\Delta m = \frac{d}{ds}|A - B|(s_*)$  is the difference in schedule rates at the gap. Fig. 6.8 compares Eq. (6.18) with  $\Delta_0$  and  $W$  parameters fit to computed wire spectra. As the wire length increases, the lowest energy gap becomes increasingly hyperbolic and Eq. (6.18) becomes more accurate. For a wire of length  $N$ , both  $\Delta_0$  and  $W$  are approximately proportional to  $q_k \propto (N+1)^{-1}$ . The Landau-Zener approximation then predicts an adiabaticity of

$$\mathcal{M}_A(N, \tilde{f}) \approx 1 - e^{-2\pi\nu/4\tilde{f}(N+1)^2}. \quad (6.19)$$

If there were only one excited state,  $\nu/(N+1)^2$  would correspond to  $\Delta_0 W$  for  $k = 1$  and large  $N$ ; however, we see from Fig. 6.8(b) that there are multiple potentially relevant excited states. We then take  $\nu$  to be some parameter dependent on the

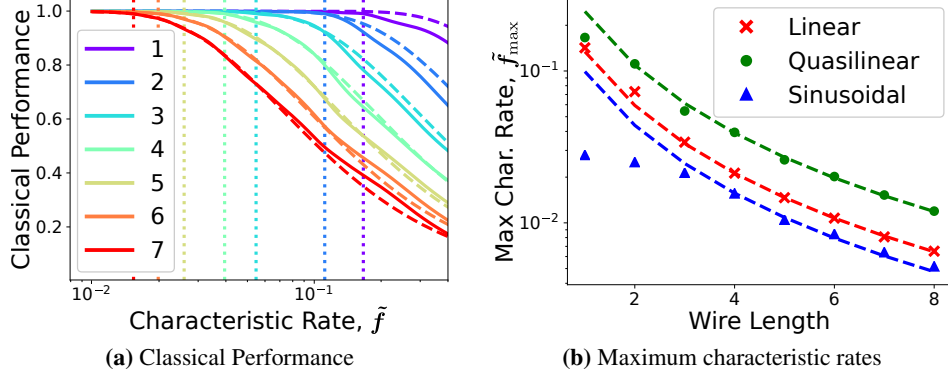


**Figure 6.9:** (a) Performance of wires of different length as a function of the characteristic rate using the Quasilinear schedule. Maximum characteristic rates are indicated by the vertical lines. In (b), we summarize these rates for all clocking schedules. Dashed lines are predictions from Eq. (6.20) using fit  $\nu$ .

clocking schedule. Using Eq. (6.7) and solving Eq. (6.19) for  $\tilde{f}$ , the maximum characteristic rate for 99% classical performance is then

$$\tilde{f}_{\max}(N) \approx -\frac{\pi\nu}{2\log(1 - 0.99/Q_1(N))(N+1)^2}, \quad (6.20)$$

Simulations were run for wires of various lengths and their maximum characteristic rates extracted. The results are shown in Fig. 6.9. These rates were fit with Eq. (6.20) for  $N \geq 4$  to obtain  $\nu_L \approx 1.60$ ,  $\nu_Q \approx 2.93$ , and  $\nu_S \approx 1.18$  for our respective Linear, Quasilinear, and Sinusoidal schedules. It is clear that the Landau-Zener model gives a good estimate of wire performance, at least beyond  $N = 3$ . Using Eq. (6.18) and considering only the first excited state, we can estimate  $\nu \approx \nu_1$ :

$$\nu_1 = (N+1)^2 \Delta_0 W|_{k=1} \approx \frac{\pi^2}{\Delta m} B^2(s_0). \quad (6.21)$$

The other excited states serve as additional channels for diabatic transitions and hence we should expect  $\nu < \nu_1$ . For our schedules, we can find expressions for  $\nu_1$ :

**Table 6.3:** Comparison of fit and analytical estimates of the Landau-Zener  $\nu$  parameter for wires. Errors indicate  $2\sigma$  deviations from the fit covariance matrix.

Clocking schedule	$\nu_{fit}$	$\nu_1$
Linear	$1.60 \pm 0.02$	1.80
Quasilinear	$2.93 \pm 0.07$	3.19
Sinusoidal	$1.18 \pm 0.04$	1.99

$$\nu_1^L = \pi^2 \frac{(1 - \alpha_1/\alpha_0)^2}{[2 - (\alpha_1 + 1/\alpha_0)]^3} = 1.80, \quad (6.22a)$$

$$\nu_1^Q = \pi^2 \frac{\ell + (\alpha_0 - 1)}{\ell^2(\alpha_0 - 1)} = 3.19, \quad (6.22b)$$

$$\nu_1^S = \frac{4\pi}{\sqrt{(\alpha_0 - \alpha_1)^2 + 4(\alpha_0 - 1)(1 - \alpha_1)}} = 1.99. \quad (6.22c)$$

For comparison, the fit  $\nu$  and analytical estimates of  $\nu_1$  are listed in Table 6.3. We see that  $\nu < \nu_1$  as expected. Further, with the exception of the Sinusoidal schedule, the first excited state gives a good estimate for  $\nu$ . We arrive at two important observations: (1) QCA wires seem to adhere to the simple Landau-Zener model for adiabaticity, even considering only the first excited state; and (2), in the absence of additional factors, the  $(N + 1)^{-2}$  scaling of  $\tilde{f}_{max}$  means the maximum characteristic rate of any QCA network under zone-clocking will quickly be limited by the longest wire to be clocked. The Landau-Zener character of wires, in addition to the ease of calculating the energy spectrum, suggests an obvious target for future investigation of an optimised wire clocking schedule.

### 6.2.2 QCA Building Blocks

We consider now the coherent performance of our set of basic QCA components. We transition from using the classical performance to using the logical performance, Eq. (6.2c), for the component output cells. This is perhaps a more meaningful metric for real device performance and will also allow more direct comparison with the ICHA results in the next section. Fig. 6.10 shows all the performance metrics for each device as a function of the characteristic rate. There are a num-

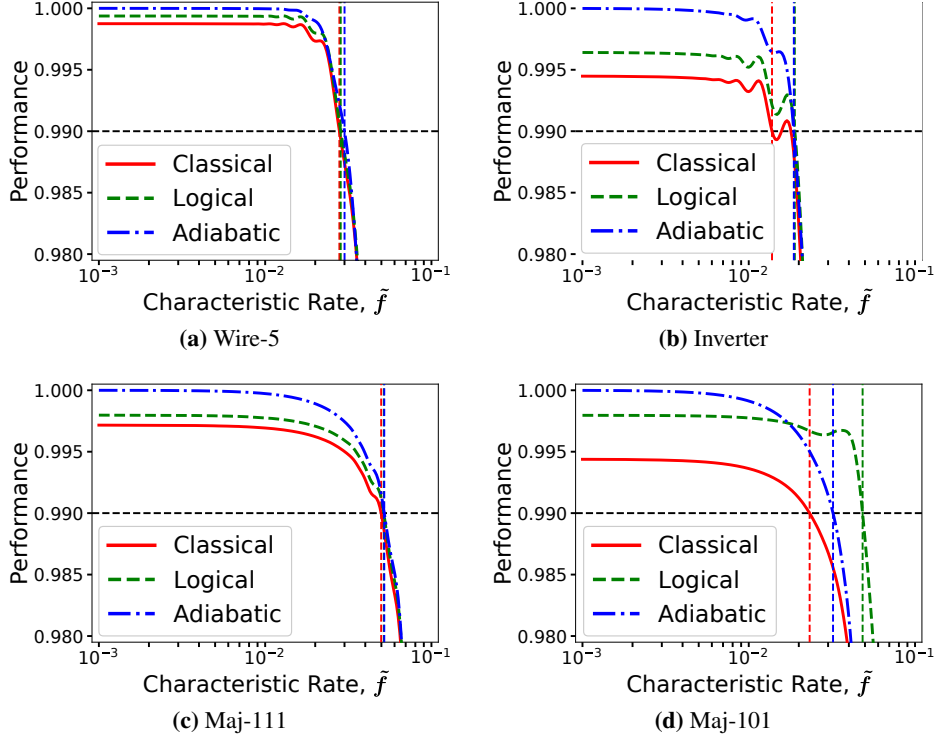
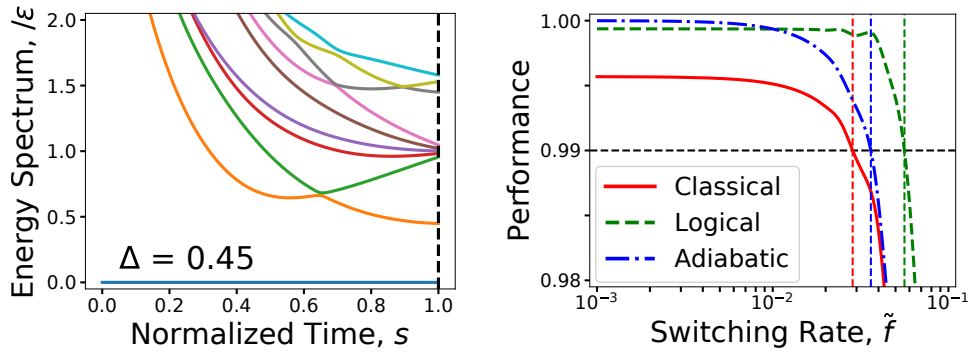


**Figure 6.10:** Performance metrics for the QCA building blocks. 99% thresholds for the different metrics are indicated.

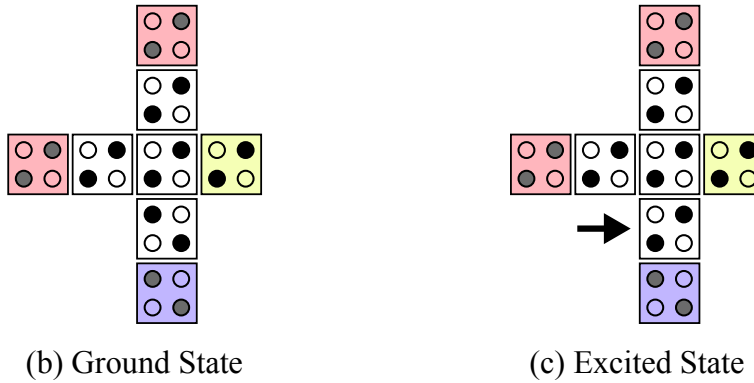
ber of things to note: (1) in the limit of high adiabaticity, or slow  $\tilde{f}$ , the metrics approximately differ only by the ratios determined in Section 6.1.2:

$$\mathcal{M}_{cl}/\mathcal{M}_A \approx \mathcal{M}_1, \quad \mathcal{M}_L/\mathcal{M}_A \approx 1 - \frac{1}{4}\alpha_1^2/|\tilde{h}_n|^2, \quad (6.23)$$

with  $\tilde{h}_n$  the effective bias for the output cell in the classical limit; (2) the remaining features and oscillations in the performance arise later in the simulations and are not a consequence of the initial Rabi oscillations discussed in Section 6.1.4; (3) the predicted maximum characteristic rate for wires doesn't significantly depend on the choice of metric, meaning our discussion in the previous section also applies to the logical performance; and (4), we observe that in certain cases the logical performance gives significantly higher maximum characteristic rates than either of



(a) Maj-110 spectrum and performance metrics



(b) Ground State

(c) Excited State

**Figure 6.11:** (a) and (b) show the low energy spectrum and performances of Maj-110. Both the classical ground state (c) and the first excited state (d) have the same logical output. This results in an increased  $\mathcal{M}_L$  metric over  $\mathcal{M}_{cl}$  and higher characteristic rates. These states differ only where indicated.

the other metrics. Note that a network is logically correct either when in the ground state or when in an excited state which happens to have correct outputs. This is the case for Maj-101 and Maj-110; the latter is illustrated in more detail in Fig. 6.11. A summary of the maximum clocking frequencies for the different devices and metrics is included in Table 6.4. Due to their simplicity, we should expect wires to be the highest performing devices of a given size. Our inverters have an input-to-output path length of 5 cells and maximum clocking frequencies similar but slightly lower than those of Wire-5. Majority gates have a path length of 3 cells from each

**Table 6.4:** Maximum clocking frequencies,  $\pi\tilde{f}_{max}/2$ , relative to  $f_0$ , for our basic QCA circuits based on different metrics. We include also Wire-3 which has a comparable size scale to the majority gates. Minimum gaps are included for reference.

Device	Adiabatic	Classical	Logical	$\Delta_0$
<b>Wire-5</b>	$4.7 \times 10^{-2}$	$4.4 \times 10^{-2}$	$4.5 \times 10^{-2}$	0.500
<b>Inverter</b>	$2.9 \times 10^{-2}$	$2.2 \times 10^{-2}$	$3.0 \times 10^{-2}$	0.362
Wire-3	$9.8 \times 10^{-2}$	$9.4 \times 10^{-2}$	$9.5 \times 10^{-2}$	0.707
<b>Maj-111</b>	$8.8 \times 10^{-2}$	$7.8 \times 10^{-2}$	$8.1 \times 10^{-2}$	0.556
<b>Maj-101</b>	$5.1 \times 10^{-2}$	$3.7 \times 10^{-2}$	$7.6 \times 10^{-2}$	0.449
<b>Maj-110</b>	$5.7 \times 10^{-2}$	$4.5 \times 10^{-2}$	$8.8 \times 10^{-2}$	0.448

input, which we can compare against the results for Wire-3. This suggests our bounds for wires found in the previous section may serve as upper bounds on more complicated components through an effective input-to-output path length. Another necessary observation is that majority gates, unlike wires and inverters, do not have a prominent hyperbolic minimum gap. In such cases, or when there are multiple minima in the spectrum which might significantly contribute, the minimum gap tends not to be a good predictor for performance. A more detailed analysis of the low energy spectrum would yield a better prediction.

### 6.2.3 Estimating Performance from the LES

Here we will use the formulation discussed in Section 3.1.1 to construct efficient methods of investigating adiabaticity either directly from the LES or by simulating dynamics using a reduced subset of the energy eigenstates. We determined that in the limit of small  $\tilde{f}$ , the adiabaticity can be approximated in terms of transition parameters  $T_n = \langle \varphi_n | \frac{d}{ds} \hat{\mathcal{H}} | \varphi_0 \rangle / (E_n - E_0)^2$ . It is possible to use this simple observation to construct a rough estimate of the maximum characteristic rate directly from the  $T_n$ . We take  $P_0(s) = 1 - \sum_{n \neq 0} |c_n(s)|^2$ , and impose our adiabaticity condition:  $P_0(s) \geq 0.99 \forall s$ . Applying our approximation of  $c_n(s)$  from Eq. (3.6), we arrive at

$$\tilde{f}_{max} \approx \sqrt{\frac{1 - 0.99}{\max_s \sum_{n \neq 0} |T_n(s)|^2}}. \quad (6.24)$$

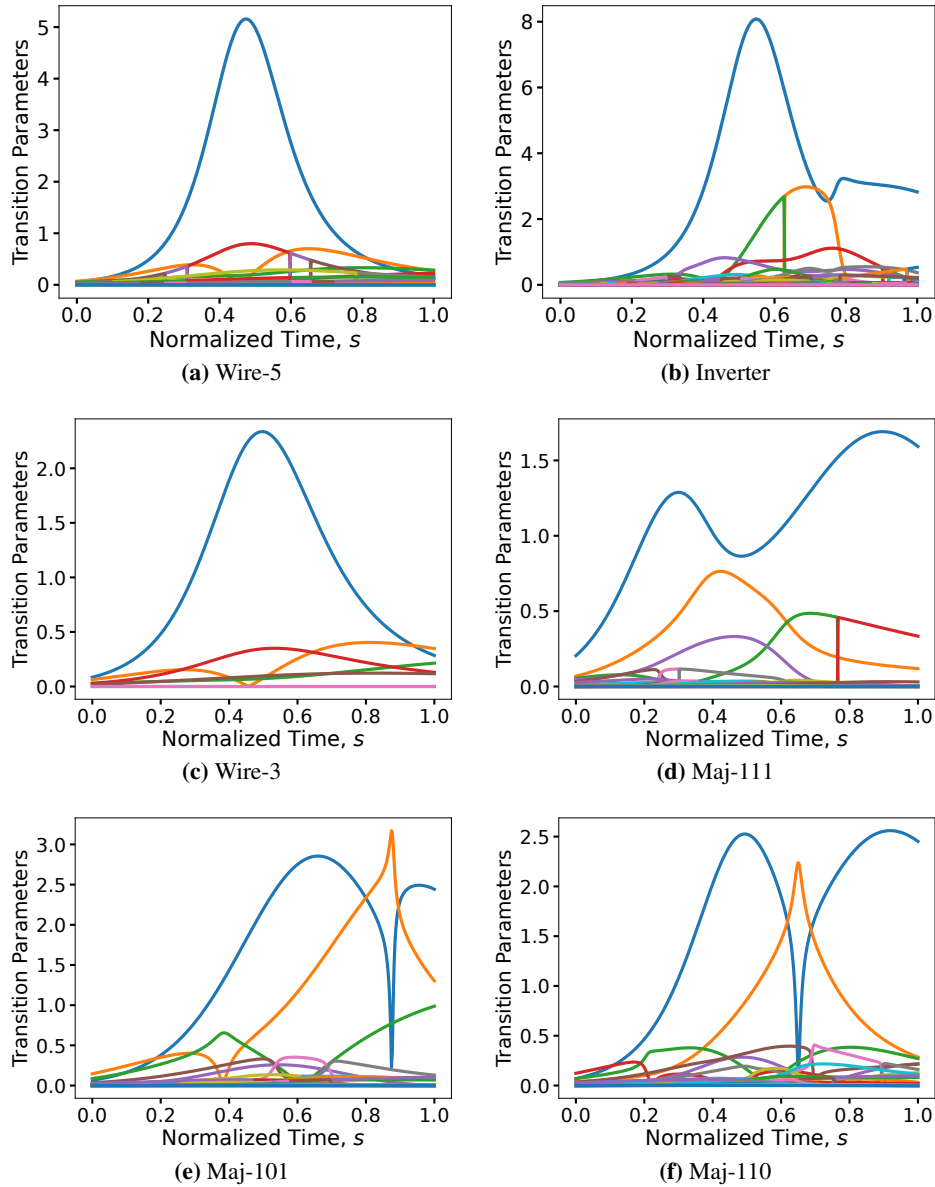


**Figure 6.12:** Transition parameters for all our QCA devices. When there is only one primary peak, there is good agreement between Eq. (3.8) and the measured clocking frequencies. In the case of the majority gates, multiple peaks produce a higher overall diabatic transition probability and hence a lower maximum clocking frequency.

**Table 6.5:** Maximum clocking frequencies computed using different adiabaticity estimation methods. The exact values are taken from Table 6.4. For Eq. (6.25), the number of included excited states is listed.

Device	Table 6.4	Eq. (6.24)	Eq. (6.25)	
			1 Excited	2 Excited
<b>Wire-5</b>	$4.7 \times 10^{-2}$	$2.94 \times 10^{-2}$	$4.84 \times 10^{-2}$	$4.76 \times 10^{-2}$
<b>Inverter</b>	$2.9 \times 10^{-2}$	$1.70 \times 10^{-2}$	$3.07 \times 10^{-2}$	$2.98 \times 10^{-2}$
Wire-3	$9.8 \times 10^{-2}$	$6.50 \times 10^{-2}$	$9.90 \times 10^{-2}$	$9.82 \times 10^{-2}$
<b>Maj-111</b>	$8.8 \times 10^{-2}$	$7.80 \times 10^{-2}$	$9.25 \times 10^{-2}$	$8.79 \times 10^{-2}$
<b>Maj-101</b>	$5.1 \times 10^{-2}$	$3.54 \times 10^{-2}$	$8.48 \times 10^{-2}$	$5.28 \times 10^{-2}$
<b>Maj-110</b>	$5.7 \times 10^{-2}$	$4.47 \times 10^{-2}$	$4.71 \times 10^{-2}$	$5.06 \times 10^{-2}$

There are a number of inaccuracies in this approximation. First, Eq. (3.6) requires that  $\tilde{f}$  be sufficiently small. We are not necessarily in a suitable regime near  $\tilde{f}_{max}$ . Second, we are still ignoring all interactions between excited states. Nevertheless, in Fig. 6.12, we calculate  $|T_n(s)|$  from the LES of all our devices. The resulting maximum clocking frequencies are included in Table 6.5. In this case, Eq. (6.24) always underestimates the maximum clocking frequency of our devices: at a max of about 40% in the case of the inverter. Another potential approach is to directly simulate the dynamics of  $c_n(s)$  through Eq. (3.3). After excluding the  $\langle \varphi_n | \frac{d}{ds} | \varphi_n \rangle$  term, we have

$$\frac{d}{ds} c_n = - \sum_{m \neq 0} c_m \frac{\langle \varphi_n | \frac{d}{ds} \hat{H} | \varphi_m \rangle}{E_m - E_n} e^{-i(\theta_m - \theta_n)/\tilde{f}}, \quad (6.25)$$

with  $c_0(0) = 1$  and  $c_{n \neq 0}(0) = 0$ . The maximum clocking frequency is the lowest  $\pi\tilde{f}/2$  such that  $|c_0(1)|^2 < 0.99$ . In Fig. 6.12, we see that only a few of the eigenstates sufficiently couple to the ground state to be worth including. The simplest model includes only the ground state and a single excited state. The result maximum clocking frequencies are also included in Table 6.5. This model produces good agreement with the exact values for the wires and inverter, a fairly good estimate for Maj-111 and Maj-110, but a poor estimate of Maj-101. Looking again at Fig. 6.12, we can make some justification. Transitions in the wires and inverter are dominated by the first excited state. Additional excited states, primarily the second excited state, are non-negligible for all majority gates, with the contribution actu-

ally overcoming that of the first excited state in Maj-101. Even including just this second excited state, we get much improved accuracy.

### 6.3 Dissipative Behaviour

We will consider two approaches to modelling a simple dissipation mechanism for environmental interactions: *spectral relaxation*, in which the density operator relaxes to some  $\hat{\rho}_{ss}(s)$  dependent only on the eigenspectrum of  $\hat{\mathcal{H}}(s)$  as in [95]; and *mean field relaxation*, where the coherence vectors of each cell relax to a local dissipation vector given by the instantaneous state of the network [45]. For spectral relaxation, we consider three different potential steady states:

$$\text{Boltzmann [95] :} \quad \hat{\rho}_{ss}^{\beta}(s) = \frac{1}{\mathcal{Z}_{\beta}} e^{-\beta \hat{\mathcal{H}}(s)} \quad (6.26a)$$

$$\text{Ground :} \quad \hat{\rho}_{ss}^{\text{G}}(s) = \frac{1}{\mathcal{Z}_{\text{g}}} \hat{P}_{\text{g}}(s) \quad (6.26b)$$

$$\text{Classical [96] :} \quad \hat{\rho}_{ss}^{\text{C}}(s) = \frac{1}{\mathcal{Z}_{\text{c}}} \hat{P}_{\text{cl}} \quad (6.26c)$$

where the  $\mathcal{Z}$  are appropriate normalization constants such that  $\text{Tr} \hat{\rho}_{ss}(s) = 1$ . Each of these spectral steady states has a local dissipation vector:

$$\eta_a^i = \text{Tr} \hat{\rho}_{ss} \hat{\sigma}_a^i. \quad (6.27)$$

For the ICHA, a mean field steady state is usually employed of the form [29],

$$\eta_a^i = -\tanh\left(\frac{\beta}{2} |\mathbf{\Gamma}_i|\right) \frac{\Gamma_a^i}{|\mathbf{\Gamma}_i|}, \quad (6.28)$$

with  $\mathbf{\Gamma}_i$  as in Eq. (2.11). While it is possible to construct a steady state density operator from the local dissipation vectors by defining the higher order steady state elements [45], we have found this process to be prohibitively slow. We will present results for mean field relaxation only via the ICHA. All performance results are now in terms of the logical performance. Dynamics using  $\hat{\rho}(s)$  are computed using Eq. (2.8), while ICHA results use Eq. (2.11).

### 6.3.1 Spectral Relaxation of the Density Operator

We consider the steady states specified in Eq. (6.26) that depend only on the energy eigenspectrum. As an example, Fig. 6.13 shows the logical performance for Maj-101 over a range of both the characteristic rate,  $\tilde{f}$ , and the relaxation rate,  $\tilde{\xi}$ . There are three regimes of interest illustrated in Fig. 6.14. If the characteristic rate is large with respect to the relaxation rate,  $\tilde{f} \gtrsim 10\tilde{\xi}$ , then the dynamics are approximately coherent. In this regime, the choice of steady state does not significantly affect the performance. If the relaxation rate is large with respect to the characteristic rate,  $\tilde{\xi} \gtrsim 10\tilde{f}$ , then the system tracks the steady state and the performance is entirely governed by whether the steady state has the correct logic. For small  $\alpha_1$ , both the ground state and classical steady states give the correct logic and thus have high performing relaxed regimes. For a Boltzmann distribution the behaviour is more complicated. The logical performance in the relaxed regime has a lower bound approximately defined by the first excited state with incorrect output logic. To first order for sufficiently small thermal energies,

$$\mathcal{M}_L > 1 - d_1 e^{-\beta\Delta_1}, \quad (6.29)$$

with  $\Delta_1$  the gap between the ground state and the lowest energy incorrect state and  $d_1$  its degeneracy. We should expect a region of high performance in the relaxed regime for  $\beta$  above approximately

$$\beta^* \approx [\log(d_1) - \log(1 - 0.99)]/\Delta_1. \quad (6.30)$$

For Maj-101 we get  $\Delta_1 = 0.554$ ,  $d_1 = 2$ , and an estimated transition at  $\beta^* \approx 9.6$ . In Fig. 6.13(c-f) we observe a domain with  $\mathcal{M}_L$  above 0.99 emerge somewhere between  $\beta = 5$  and 20. The transition actually occurs just above  $\beta = 10.0$  (see Fig. 6.13(e)) which is fairly close to our estimate. The exact value of  $\mathcal{M}_L$  in the limit of infinite  $\tilde{\xi}$  for a Boltzmann steady state is obtained as

$$\mathcal{M}_L(\beta) = \frac{1}{2}(1 + |\text{Tr} \hat{\rho}_{ss}^\beta(1) \hat{\sigma}_z^n|) \quad (6.31)$$

for output cell  $n$ . In Fig. 6.15, we show  $\mathcal{M}_L(\beta)$  for all the QCA components. Table 6.6 compares the  $\beta^*$  estimates using Eq. (6.30) with the values from Fig. 6.15.

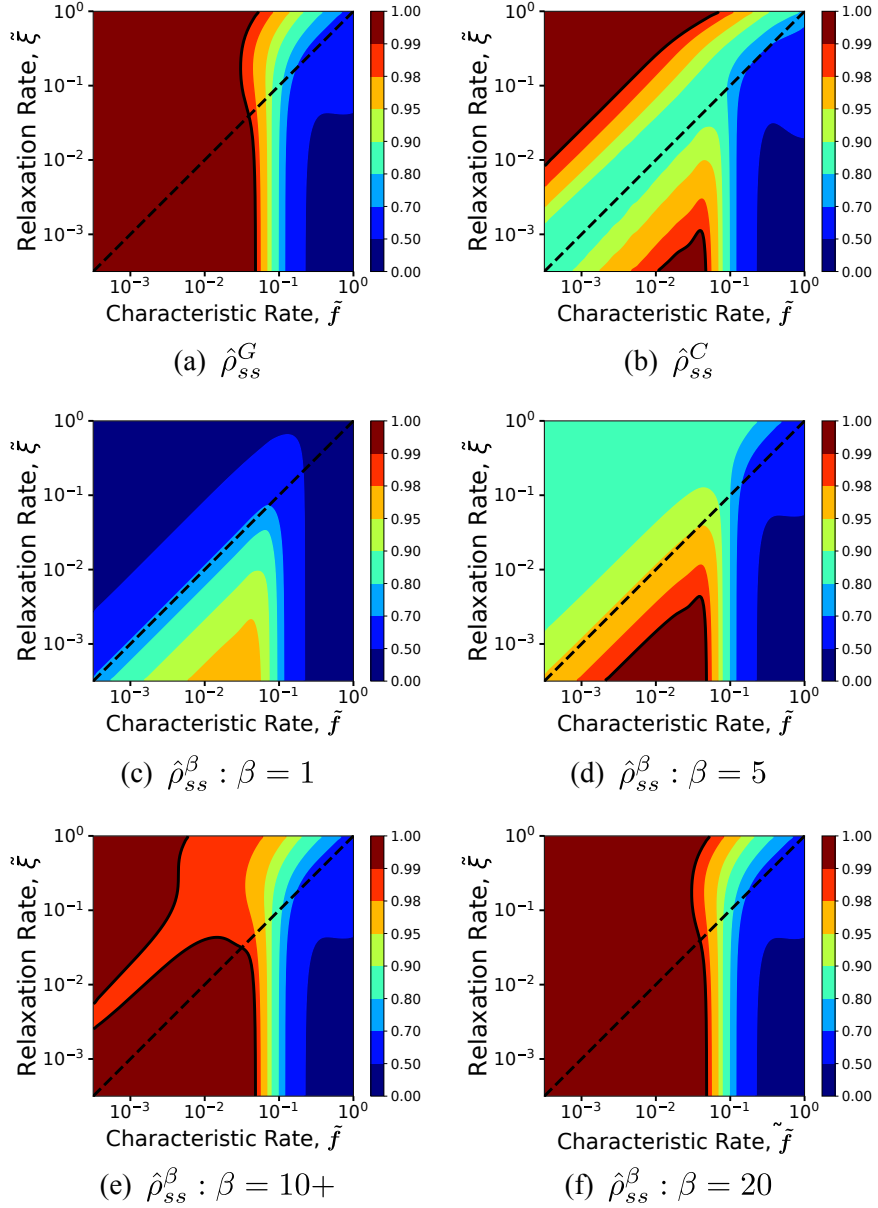


**Figure 6.13:** Logical performance of Maj-101 for different spectral steady states: (a)  $\hat{\rho}_{ss}^G$ ; (b)  $\hat{\rho}_{ss}^C$ ; (c-f)  $\hat{\rho}_{ss}^\beta$  for  $\beta = 1, 5, 10+, 20$ . The dashed line represents equal characteristic and relaxation rates and the solid contour represents a performance of 0.99. (e) shows the behaviour immediately after the critical inverse temperature:  $10+ = 10.1$

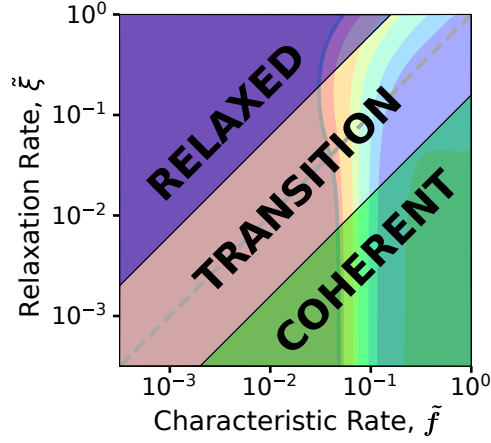


**Figure 6.14:** There are three regions of interest: the **coherent** regime, in which the system is governed by coherent dynamics; the **relaxed** regime, in which the system closely tracks the steady state; and the **transition** between these two regimes.

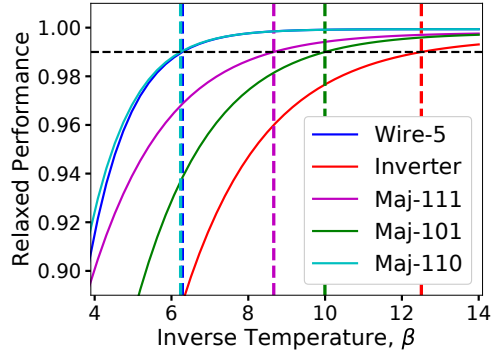


**Figure 6.15:** Logical performance in the relaxed regime for QCA components with the Boltzmann distribution steady state.  $\mathcal{M}_L = 0.99$  thresholds are indicated.

The most significant difference occurs for the inverter, which has a second incorrect excited state with a slightly higher energy gap of 0.554. The contribution of this state is ignored in our estimate. If the characteristic and relaxation rates are of the same order, the behaviour depends on the interplay between the coherent dynamics and the relaxation. Of the steady states considered, the most interesting behaviour occurs for  $\hat{\rho}_{ss}^C$ , with a band of low performance along  $\tilde{\xi} \approx \tilde{f}$ . This result is easily explained by observing that the classical ground state will generally be a high energy configuration of  $\hat{\mathcal{H}}(0)$  and very near the ground state of  $\hat{\mathcal{H}}(1)$ . Ini-

**Table 6.6:** Threshold  $\beta$  value for high performance in the relaxed regime. Parameters for Eq. (6.30) are estimated from the spectrum of  $\frac{1}{2}\hat{\mathcal{H}}_{cl}$

Device	$d_1$	$\Delta_1$	Eq. (6.30)	Fig. 6.15
Wire-5	5	1	6.2	6.3
Inverter	1	0.416	11.1	12.5
Maj-111	1	0.554	8.3	8.7
Maj-101	2	0.554	9.6	10.0
Maj-110	5	1	6.2	6.2

tially, the dissipation acts to excite the network out of the ground state; later in the clock, the dissipation acts to help drive the network back down in energy. Increasing  $\tilde{\xi}$  initially hurts performance until the relaxation is strong enough to overcome these initial excitations.

We summarize the performance for each QCA component by extracting the maximum clocking frequency as a function of  $\tilde{\xi}$  for each choice of steady state. The results are shown in Fig. 6.16. Each set of data is obtained by first finding  $\tilde{f}_{max}$  in the coherent limit and then tracking the  $\mathcal{M}_L = 0.99$  contour as  $\tilde{\xi}$  is increased. We first mention a few unsurprising results: (1) the clocking frequency is approximately independent of the choice of steady state in the coherent limit; (2) the trends become parallel to  $\tilde{f} = \tilde{\xi}$  in the relaxed regime, meaning performance is guaranteed as long as  $\tilde{\xi}/\tilde{f}$  is sufficiently large; and (3), for Boltzmann steady states the performance is improved as the temperature is decreased. There are apparent discontinuities in some of the trends. These correspond to cases like Fig. 6.13(e), where we observe two regions of high performance. Interestingly, unless  $\tilde{\xi}$  is sufficiently large, we observe a decrease in maximum clocking frequency for any of our spectral steady states.

### 6.3.2 Spectral Relaxation with the ICHA

In Fig. 6.17 we repeat the analysis using the ICHA. The behaviour in the relaxed regime matches what we observe in Fig. 6.16. On inspection, the limits in the coherent regime differ slightly, with the maximum clocking frequency slightly higher for wires and inverters and lower for majority gates. In the transition regime, however, we observe significantly different results, particularly for Wire-5 and

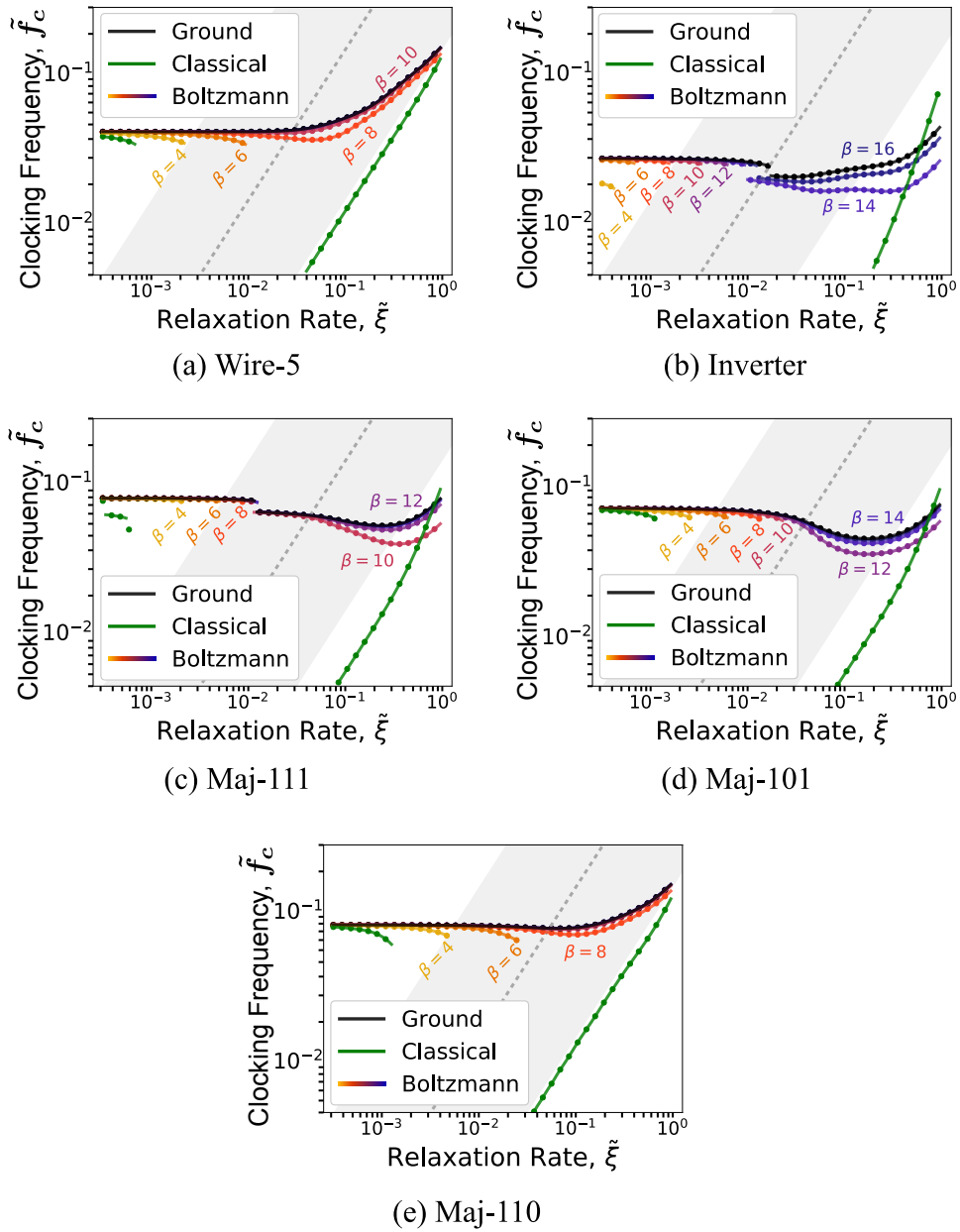


**Figure 6.16:** Maximum clocking frequencies relative to  $f_0$  for different spectral steady states. A sample set of  $\beta$  values are indicated for the Boltzmann distribution. Classical steady state results are cropped for ease of view. The shaded region and dashed line indicate the approximate edges of the transition regime.

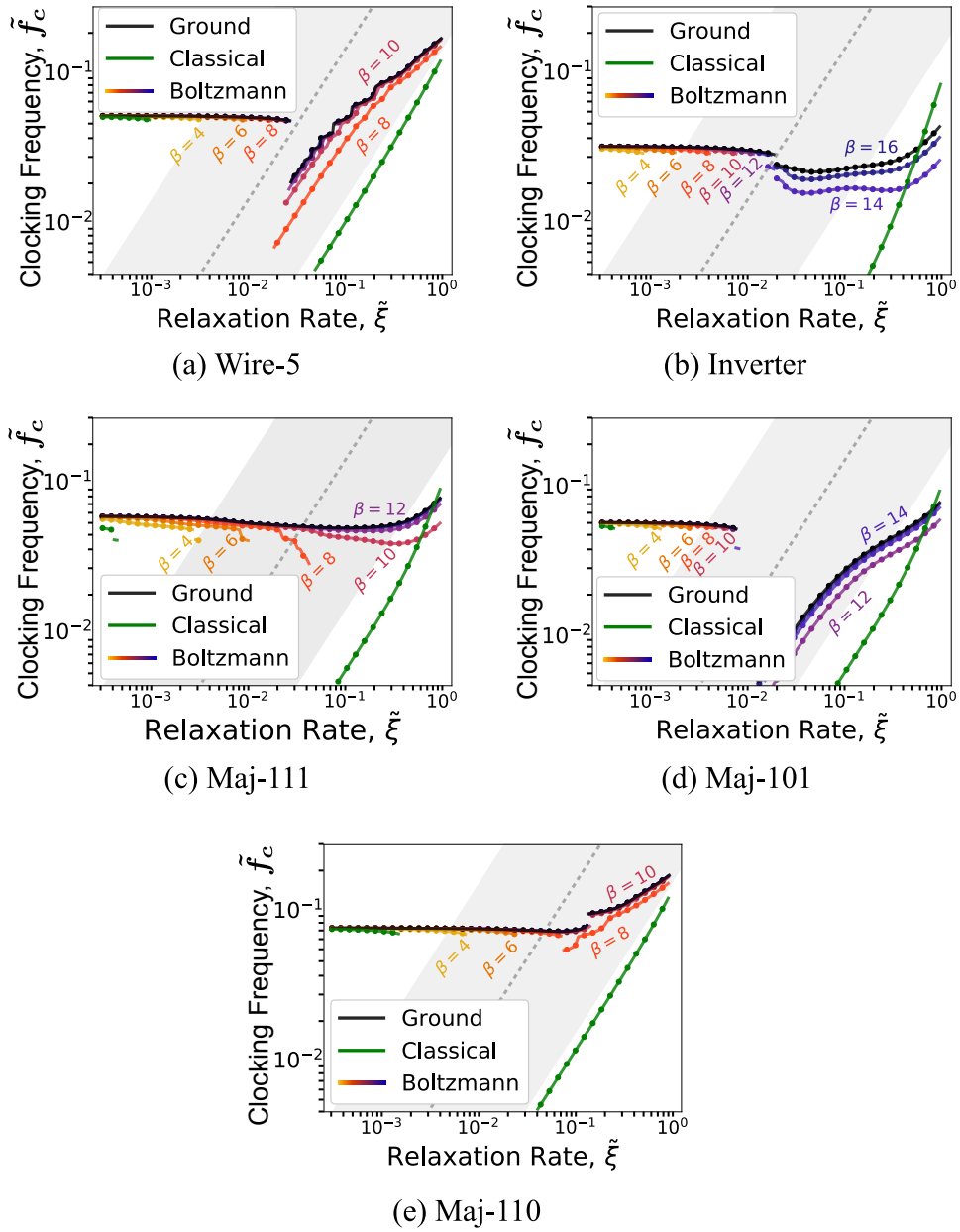


**Figure 6.17:** ICHA: Maximum clocking frequencies relative to  $f_0$  for the different spectral steady states. A sample set of  $\beta$  values are indicated for the Boltzmann distribution.

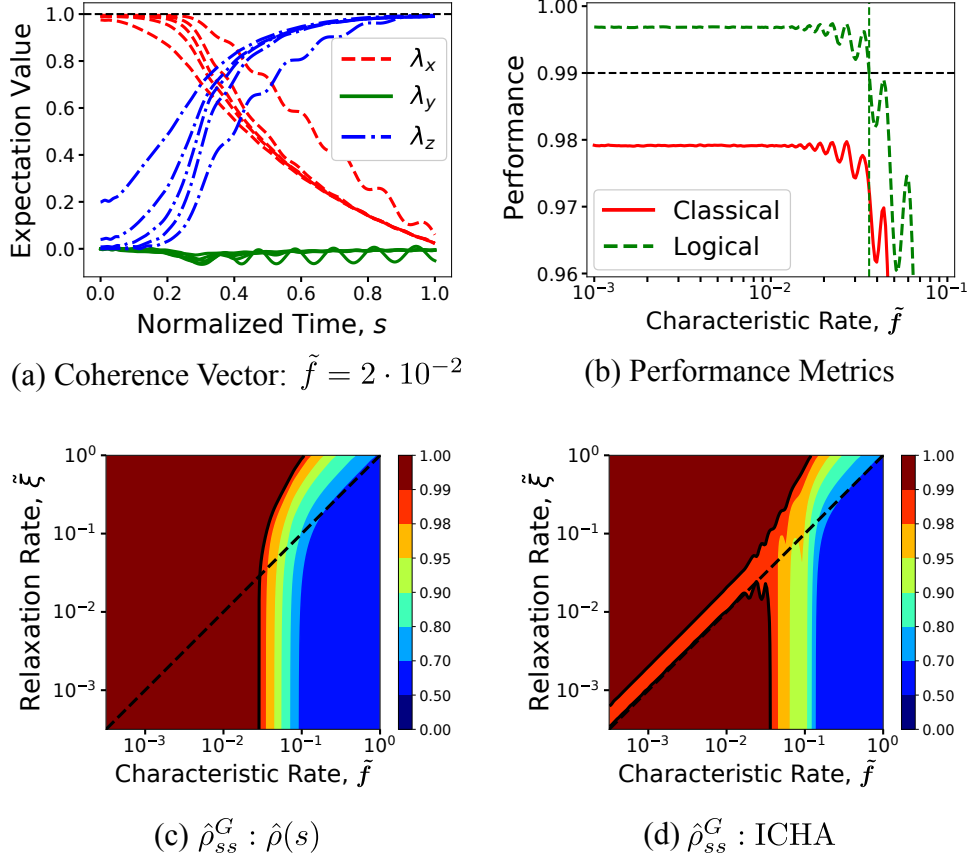


**Figure 6.18:** (a) Oscillations in the ICHA simulation of Wire-5:  $\tilde{f} = 2 \times 10^{-2}$ . These oscillations manifest in the coherent performance metrics (b) and produce interesting features in the logical performance contours. We compare the ground state relaxation using the density operator (c) and ICHA (d).

Maj-101. To understand this behaviour, we need to consider the dynamic equations of the ICHA. Absent any dissipation, Eq. (2.11) is stationary only if  $\lambda_i \propto \Gamma_i$ ; otherwise, coherent oscillations occur as has been previously studied [95]. This can be seen by taking the derivative of the  $\lambda_y^i$  equation in Eq. (2.11):

$$\tilde{f}^2 \frac{d^2}{ds^2} \lambda_y^i = -(\tilde{h}_i^2 + \gamma_i^2) \lambda_y^i + O(\gamma_n \lambda_y^n), \quad (6.32)$$

where the remaining terms tend to be small near the end of the switching phase. For sufficiently fast  $\tilde{f}$ , the  $\lambda_y^i$  can remain non-zero and will then oscillate with angular frequencies  $\nu_i^2 = (\tilde{h}_i^2 + \gamma_i^2)/\tilde{f}^2$ . The  $\lambda_x^i$  and  $\lambda_z^i$  are driven to oscillate by the remaining equations:

$$\tilde{f} \frac{d}{ds} \lambda_x^i = -\tilde{h}_i \lambda_y^i, \quad \tilde{f} \frac{d}{ds} \lambda_z^i = -\gamma_i \lambda_y^i. \quad (6.33)$$

Fig. 6.18 shows the coherence vector for Wire-5 using the ICHA for a particular choice of  $\tilde{f}$ . In this case, these coherent oscillations are clear. From Eq. (6.32), we can predict an oscillation frequency for Wire-5 in non-dimensional units:

$$f_{osc} = \frac{1}{2\pi\tilde{f}} [|\lambda_z^4|^2 + \alpha_1^2]^{1/2}. \quad (6.34)$$

Taking  $|\lambda_z^4| \approx 1$ , we get  $f_{osc} \approx 8.0$  which matches the observed oscillation. This leads to oscillations in the performance both in the coherent limit (Fig. 6.18(b)) as well as when dissipation is added (Fig. 6.18(d)). In Fig. 6.18(d), we see also a band of slightly lower performance along  $\tilde{\xi} \approx \tilde{f}$ . That this effect appears significant is entirely a consequence of our arbitrary choice of the 0.99 threshold. This region of lower performance also exists in Fig. 6.18(c); however, we observe slightly higher  $\mathcal{M}_L$  values in the low  $\tilde{f}$  regime when using the density operator approach, keeping this region above 0.99.

### 6.3.3 Mean Field Relaxation with the ICHA

We conclude by considering the commonly used mean field method: Eq. (6.28). As this method is  $\beta$  dependent it is natural to compare it with our analysis of the Boltzmann steady state. We can determine the  $\beta^*$  sufficient to guarantee a high performing relaxed regime by making two observations: (1) in the limit of high  $\tilde{\xi}$  we have  $\lambda_z^n = \eta_z^n$  and hence  $\mathcal{M}_L = \frac{1}{2}(1 + |\eta_z^n|)$  for output cell  $n$ ; and (2), in this limit the  $\mathbf{\Gamma}_i$  in Eq. (6.28) becomes a function of the vector  $\boldsymbol{\eta}_z$  of all the  $\eta_z^i$  values. We can then obtain  $\boldsymbol{\eta}_z$  as a fixed point of Eq. (6.28) by iteration starting with the ground state polarizations of  $\hat{\mathcal{H}}(1)$ . The results of this process are shown in Fig. 6.19 with a comparison of the extracted  $\beta^*$  to those of the Boltzmann steady state shown in Table 6.7. With the exception of Maj-111, we get lower  $\beta^*$  values

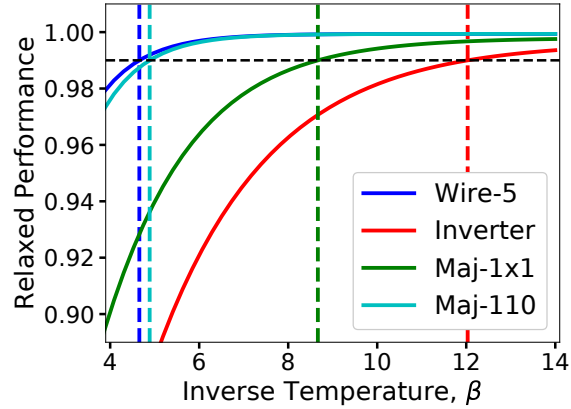


**Figure 6.19:** Logical performance in the relaxed regime for the mean field relaxation with the ICHA. Maj-101 and Maj-111 are indistinguishable for sufficiently large  $\beta$ .

**Table 6.7:** Comparison of  $\beta^*$  values for the two temperature dependent steady states.

Device	Wire-5	Inverter	Maj-111	Maj-101	Maj-110
Boltzmann	6.3	12.5	8.7	10.0	6.2
Mean Field	4.7	12.0	8.7	8.7	4.9

using the mean field.

In Fig. 6.20, we show the maximum clocking frequencies for the mean field steady state. We use spectral relaxation to the ground state as reference. Qualitatively, there is much in common with the Boltzmann steady state, keeping in mind the slightly different  $\beta^*$  transitions. One significant feature that was not observed in our previous results is that the mean field can give maximum clocking frequencies higher than what can be achieved using spectral relaxation to the true ground state. This is likely a result of the tendency for the mean field to reinforce the polarizations of cells, increasing the output cell polarization and hence  $\mathcal{M}_L$ . See, for example, the cell response in Ref. [41].

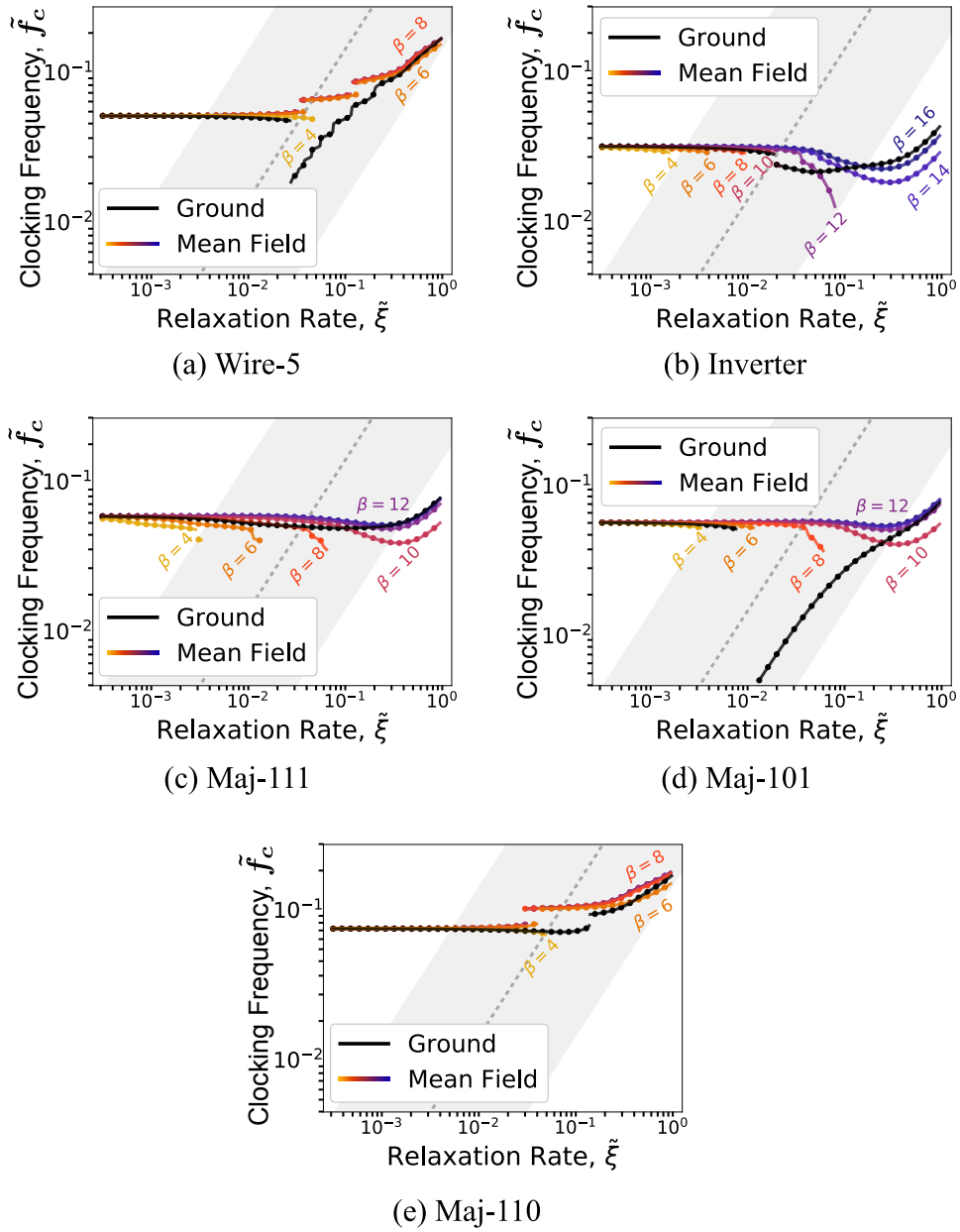


**Figure 6.20:** Maximum clocking frequencies relative to  $f_0$  for mean field relaxation using the ICHA. The results for the ground state are shown for reference and comparison to Fig. 6.17.

## 6.4 Summary

By interpreting QCA clocking as quantum annealing, we arrived at an understanding of some of the mechanisms by which properties of the low energy spectrum influence dynamics and, ultimately, clocking performance. We identified criteria for choosing a clocking schedule, and arrived at an improved schedule allowing for high performance, defined as a 99% likelihood of observing the correct ground state, at higher clocking frequencies. In the case of wires, this new schedule can be operated roughly 2.5 times faster than the existing schedule in QCADesigner. In the coherent limit, we observed upper bounds on the clocking frequency 1-2 orders of magnitude below the intrinsic frequency  $f_0 = \mathcal{E}/h$ . Earlier work by Timler *et al.* established similar bounds at 1-3 orders of magnitude below  $f_0$  [29]. Their analysis was based on constraining the expected amount of power dissipated by device operation in a given area. This suggests that while considerations of power are important for evaluating QCA implementations, we should carefully consider the conditions under which QCA networks can be expected to produce correct outputs.

Using an analytical solution for driven wires, we determined that they are well approximated by a simple Landau-Zener model for adiabaticity, having a maximum clocking frequency that falls off with the square of the wire length. This suggests an unforgiving trade-off between operational frequency and maximum clock zone size unless alternative decoherence mechanisms can be invoked [97]. We also observed for this small dataset that wires present an upper bound for more complicated networks through an effective longest input-to-output length. Further work would be needed to determine whether this is of general use.

We investigated a simple thermal bath relaxation model for decoherence. While the choice in steady state does influence performance, the effect is relatively small unless the system is operated in a regime where the rate of relaxation dominates. Outside of this regime, we observe either of two cases. If the steady state has the correct logic in the relaxed regime, then we observe at worst an approximate factor of 2 decrease in maximum clocking frequency compared to the coherent limit; otherwise, there is a maximum allowable relaxation rate beyond which high performance is not achievable. The bounds in this near-coherent regime are therefore within a factor of 2 of those in the coherent limit.

## Chapter 7

# Simulating 2-State QCA on Quantum Annealing Hardware

In the previous chapter, it was demonstrated that through understanding QCA clocking as a QA process, information about the LES could be used both to characterize the choice in clocking schedule as well as predict clocking performance. Without further development, this method is practical only for small networks where the LES can be easily computed; however, the link to QA suggests that additional insight might be gained by investigating an analogous QA hardware architecture, in which numerical simulation is not a limitation. Work by D-Wave Systems Inc. in Burnaby, Canada, to realize a large scale quantum annealing platform has made it possible to explore physical quantum annealing in real-world applications including large numbers of variables [67, 98]. Most of the discussion in this chapter focusses on the previous D-Wave 2000Q QPU, which offers 2048 potential physical superconducting flux qubits in a  $16 \times 16$  grid of 8-qubit tiles. One challenge to running the QPU on a given problem lies in the sparse connectivity between qubits. The 2000Q uses the “Chimera” topology, summarized in Fig. 7.1, with each qubit connected to at most six neighbours. The more recent Advantage QPU offers more than 5000 qubits and uses a higher connectivity topology, termed “Pegasus” [99, 100]. Pegasus introduces four additional couplers within each tile, shown in Fig. 7.2, as well as additional inter-tile couplings. Each qubit in the Pegasus topology is connected to at most 15 qubits. Details on the tile connections

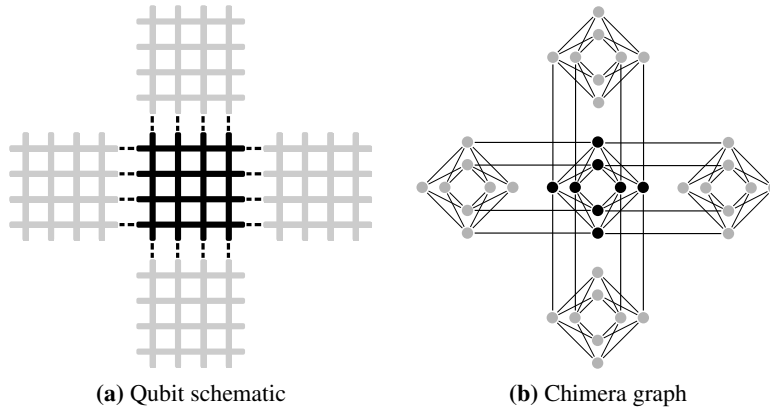


**Figure 7.1:** Qubit layout for one tile of the QPU. There are 4 vertical and 4 horizontal qubits with couplers at the intersections. Couplers between tiles are indicated by the dashed lines. In the graph representation qubits are represented by nodes and couplers by the connecting edges. Each qubit has at most 6 adjacent qubits.

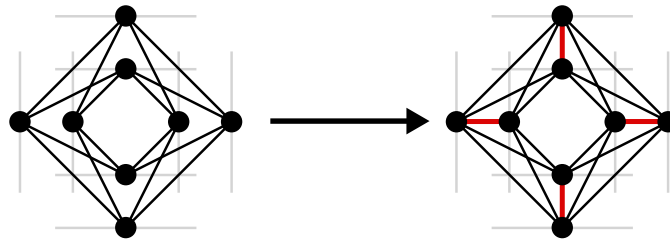


**Figure 7.2:** The Pegasus topology adds 4 internal couplers within each 8-qubit tile. This enables the mapping of 3-cycles, allowing for more compact embeddings.

are given in Appendix C.1. This connectivity constraint ultimately means that it is not possible to embed a given QCA network onto the QPU using a one-to-one mapping between individual QCA cells and qubits. Additional qubits are needed to facilitate all interactions, with multiple qubits representing a single QCA cell. The choice of these multi-qubit groups defines the *embedding* of a QCA circuit. In this chapter, we discuss the challenge of embedding and the steps necessary for simulating QCA networks on the D-Wave QPU.

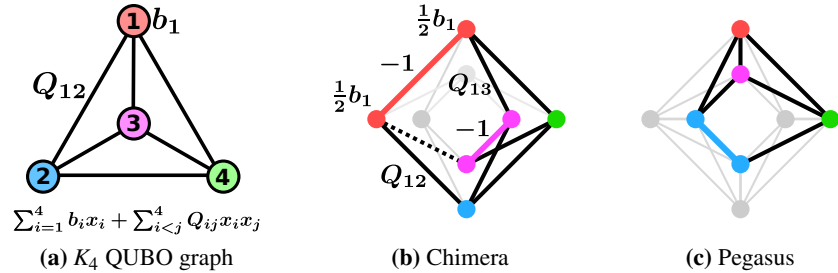


**Figure 7.3:** Minimal embeddings for  $K_4$  on the Chimera and Pegasus topologies. Colours show the corresponding node in the  $K_4$  problem graph. Coloured edges are internal to the vertex model with  $J = -1$ . Dashed edges are optional. The embeddings are not unique; in Chimera for example, any horizontal qubit in a tile can be swapped with any other, and similarly for the vertical qubits.

## 7.1 Embedding Problems on the QPU

In general, any QUBO or equivalent problem can be mapped to the D-Wave QPU. To avoid confusion between the  $h_i$  and  $J_{ij}$  terms of an Ising model and those of the QPU, we will use the  $b_i$  and  $Q_{ij}$  notation from QUBO. We can represent a given problem by a *problem graph*, with the  $b_i$  values mapped to node weights, and the coupling terms,  $Q_{ij}$ , to edge weights. Similarly, we can understand the potential qubits and couplers on the QPU as a *hardware connectivity graph*, where each qubit is a node, and each coupler an edge between the corresponding qubit nodes. A single tile of the Chimera graph is shown in Fig. 7.1(b). In the literature, nodes in the problem graph tend to be called *logical qubits* and nodes in the hardware graph are called *physical qubits*. Ideally, each logical qubit would be mapped to a single physical qubit; however, the edges in the hardware graph are limited by the QPU connectivity. The solution is to map each logical qubit to a set  $\Omega$ , called a *vertex model*, of physical qubits. This task is known as minor embedding [101]. As an example, embeddings for the complete graph of 4 nodes,  $K_4$ , which use the fewest number of physical qubits are shown in Fig. 7.3. There are a few rules for assigning parameters to physical qubits in vertex models [102]:

- Couplers between physical qubits in a vertex model should attempt to force the qubits to be of the same spin in the ground state. As parameter ranges on

the QPU are constrained to  $|h_i|, |J_{ij}| \leq 1$ , this translates to  $J_{ij} = -1$  within the vertex model.

- Edges and the corresponding  $Q_{ij}$  between logical qubits must map to edges between the corresponding vertex models. If multiple edges are available between two vertex models, the edges must satisfy  $\sum_{n \in \Omega_i} \sum_{m \in \Omega_j} J_{nm} = Q_{ij}$ . In this work, we set one of the  $J_{ij}$  to  $Q_{ij}$  and leave the rest disabled.
- Node weights within a vertex model must satisfy  $\sum_{n \in \Omega_i} h_n = b_i$ . We choose to set  $h_n = b_i / |\Omega_i| \forall n \in \Omega_i$ .

For a real QPU, some of the qubits or couplers may be disabled due to issues in fabrication or calibration [103]. This does not fundamentally change the task, only further restrict the hardware connectivity graph. Finding efficient embeddings is known to be NP-hard [101], with deterministic algorithms having complexity exponential in the size of problem graph [104]. Fortunately, polynomial time heuristic algorithms exist for attempting to find graph minors [104, 105]. Results for embedding larger problems will be summarized in Section 7.1.3; however, we first need to establish the problem graph structure of 2-state QCA networks.

### 7.1.1 QCA Connectivity Graph Representations

It is natural to discuss the interactions between QCA cells in terms of a connectivity graph. There are two species of 2-state QCA cell often considered in the literature: the 4-dot cell with quadrupole-quadrupole like interactions; and the 2-dot cell with dipole-dipole interactions. Typical device geometries, polarization states, and  $J_{ij}$  terms are shown in Figs. 7.4 and 7.5. Importantly, we can consider each cell as a vertex in a connectivity graph, with edge weights given by  $J_{ij}$ . Due to the rapid fall-off of cell interactions, we can ignore most interactions, and thus the degree of such graphs is often relatively small. A few important examples are shown in Fig. 7.6. The 4-dot majority gate and inverter often represent the highest density of cells in 4-dot networks, and have degrees of only 4 and 5 respectively. The somewhat more complicated 2-dot majority gate has a higher degree of either 10 or 12 depending on the choice of included interactions. This is representative of the highest device density typically observed in 2-dot networks. Higher density

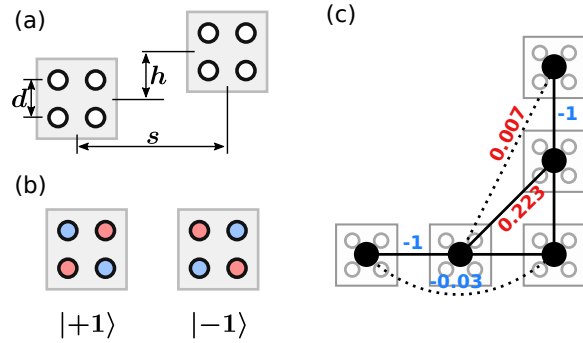


**Figure 7.4:** Schematic of the 4-dot cell. Intra- and inter-cell distances are defined in (a). In (b), we define the two polarization states given by antipodal charge occupation of the dots; here each cell has two holes (red) and two electrons (blue). In (c), we show computed  $J_{ij}$  parameters for different cell separations, scaled to the strongest observed interaction. The colours aid in identifying the sign of  $J_{ij}$  with dotted lines showing weak interactions which are usually ignored. Values shown for  $d = 1$  nm and  $s = h = 2$  nm.

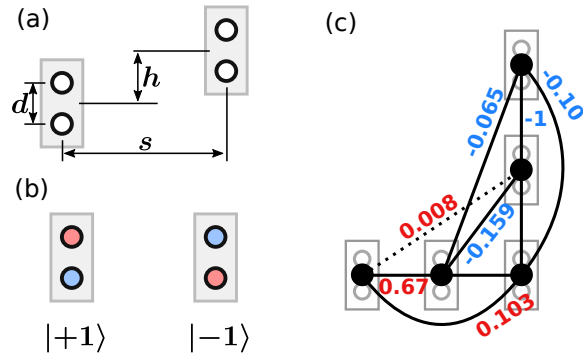


**Figure 7.5:** Schematic of the 2-dot cell: (a) intra- and inter-cell distances; (b), polarization states; (c), scaled  $J_{ij}$  parameters. Here the next-to-nearest interactions are sufficiently strong that their contribution cannot necessarily be ignored. Values shown for  $d = 1$  nm,  $s = 1.5$  nm, and  $h = 2$  nm.

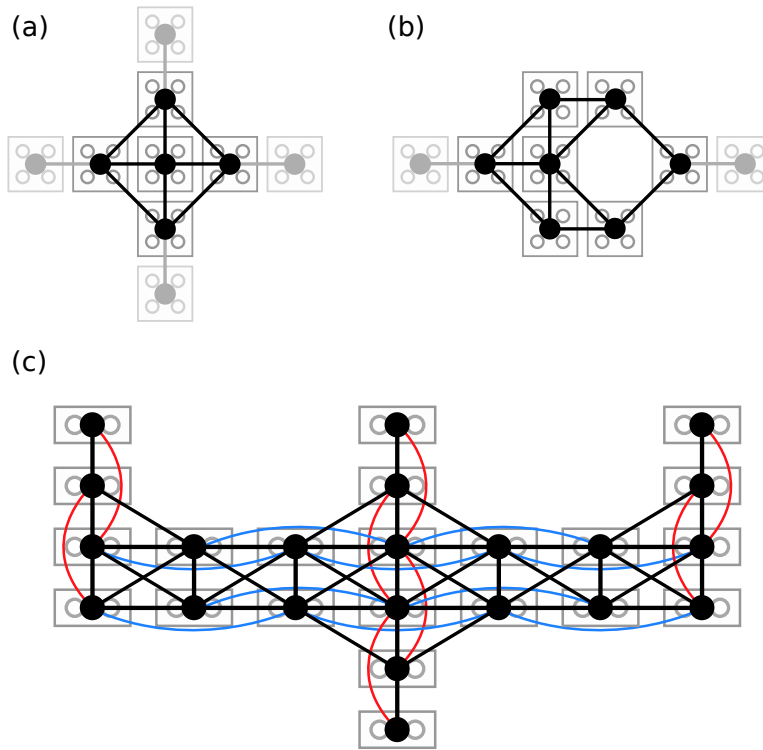


**Figure 7.6:** Connectivity graph representations of basic components in QCA networks: **(a)** 4-dot majority gate, **(b)** 4-dot inverter, and **(c)** 2-dot majority gate. The colored edges in **(c)** are added to remove clutter and highlight slightly weaker interactions. The weaker  $-0.065$  interaction is neglected for simplicity.

devices can be speculated, such as multi-wide wires [106, 107] or 5-input majority gates [108]; however, these are not currently common in QCA design. Larger QCA networks are usually sparsely connected arrangements of these or similar relatively dense sub-networks. Embeddings for the majority gate and inverter are shown in Figs. 7.7 and 7.8.

### 7.1.2 Summary of Embedding Algorithms

Early embedding experiments were targeted for the 512 qubit D-Wave Two hardware graph. Due to the sparsity of QCA connectivity graphs, an in-house algorithm was developed for comparison against D-Wave’s heuristic *minorminer* [105]. A

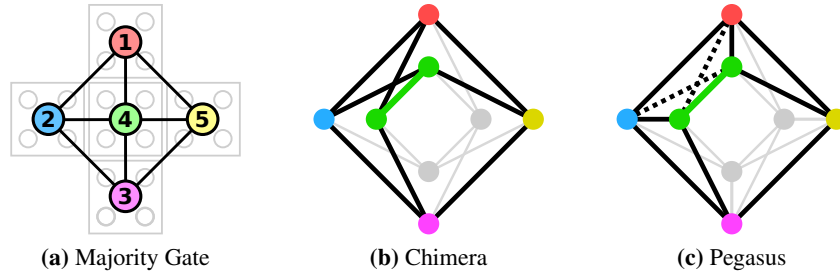


**Figure 7.7:** Minimal embeddings for the majority gate. The extra intra-tile couplers in the Pegasus topology do not reduce the number of required physical qubits; however, they do offer additional choices for edges, which is potentially useful if some couplers/qubits are not functional on the QPU.

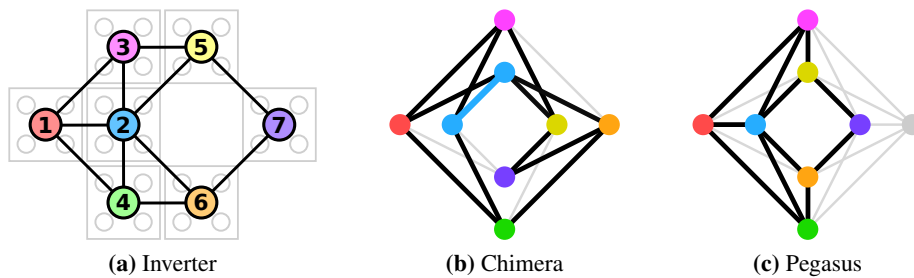


**Figure 7.8:** Minimal embeddings for the inverter. In this case, a perfect embedding is possible in the Pegasus topology.

brief overview of the two algorithms is given here for comparison.

### Dense Placement Algorithm

The Dense Placement (DP) algorithm uses a simultaneous “place-and-route” approach commonly used in field-programmable gate array (FPGA) design [109]. It attempts to place every logical qubit onto a single corresponding *assigned* physical qubit. Chains of physical qubits are routed between the assigned qubits if no edge exists. A number of strategies are used for selection and assignment of the first logical qubit, order of logical qubits to embed, maintenance and reservation of available neighbours for future routings, and recovery when no neighbours are available. If an embedding is found, a linear programming approach is used to

convert this “assigned qubit and interaction chain model” into an equivalent set of vertex models. Details regarding the DP algorithm can be found in Appendix A.2 or in published work [6, 7].

### **D-Wave’s Heuristic Algorithm: Minorminer**

For each node in the problem graph, assign an initial vertex model as follows. If none of the current node’s neighbours have been assigned a vertex model, randomly select a physical qubit as the vertex model. Otherwise, find the qubit with the smallest total path cost to all of the adjacent vertex models and assign this qubit as the root of the vertex model. Initially, the same qubit can be used by multiple paths at a high cost. Paths to the adjacent vertex models are distributed between vertex models to minimize the largest vertex model size. After initial placement, iteratively loop through each problem node, forget the previously assigned vertex model and try to find a better one. The metrics for improvement are defined as the number of times a single qubit is used in the set of all vertex models (must be no more than once for a successful embedding), the sum of vertex model sizes, and the largest vertex model size. A detailed discussion on minorminer can be found in Ref. [105].

### **Recent Advancements**

Since our initial investigation, more recent efforts by Pinilla and Wilton [110] have introduced layout aware embedding of QCA networks. In some cases, this approach has been shown to produce embeddings requiring fewer physical qubits than either the DP algorithm or minorminer. In addition, minorminer has undergone a number of revisions, improving performance. We include here a limited sample of the original embedding results in order to demonstrate general trends.

#### **7.1.3 Embedding Results**

We consider 4-dot QCA using two potential levels of connectivity: *Full Adjacency*, where we include both nearest neighbour ( $J_{ij} = -1$ ) as well as diagonal ( $J_{ij} = 0.233$ ) interactions; and *Limited Adjacency*, where we exclude diagonal interactions except those on the output of an inverter. Refer to Fig. 7.4, for context.

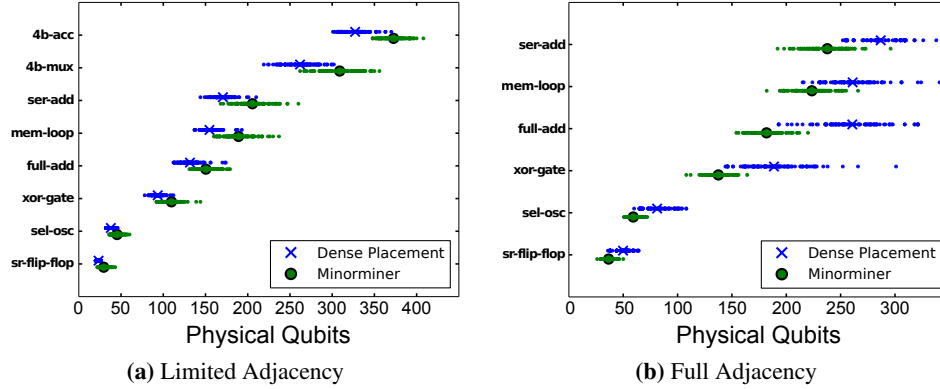


**Figure 7.9:** Number of physical qubits used for each benchmark circuit. Smaller dots are individuals embeddings, with 100 attempts per circuit. The large markers show the average. The 4 bit 2-1 multiplexer and accumulator could not be embedded onto the 512 qubit QPU using full adjacency.

**Table 7.1:** Benchmark circuits and the number of non-driver cells

Circuit	Cells	Circuit	Cells
SR Flip Flop	20	Memory Loop	120
Selectable Oscillator	31	Serial Adder	126
XOR Gate	73	4 Bit 2-1 MUX	192
Full Adder	98	4 Bit Accumulator	273

Both algorithms were run on two categories of QCA networks: a set of benchmark circuits of differing complexity and number of cells, and randomly generated QCA connectivity graphs. We assume here a Chimera topology without any disabled qubits or couplers. For performance of the algorithms with disabled qubits, see Appendix C.2.3.

#### 7.1.4 Benchmark Circuits

The list of considered benchmark circuits and the corresponding number of cells is included in Table 7.1. For each benchmark, we attempted 100 embeddings using both algorithms and adjacency types. The results are summarized in Fig. 7.9. The DP algorithm required fewer physical qubits for limited adjacency, with minorminer requiring fewer for full adjacency. In Fig. 7.10, we compare the average

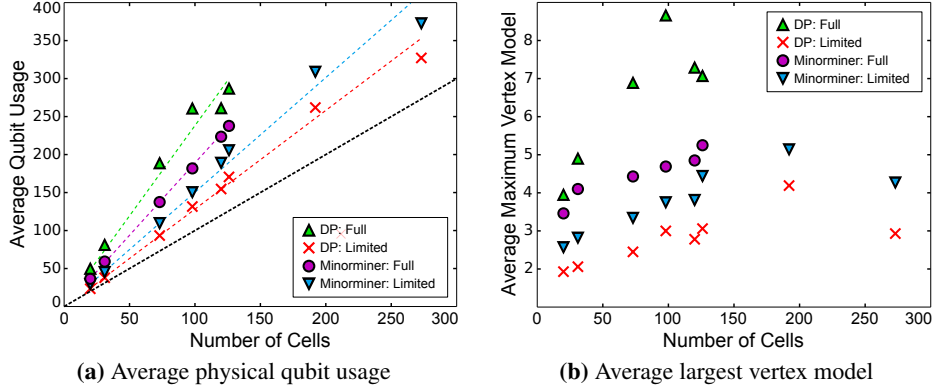


**Figure 7.10:** Comparison of physical qubit usage and vertex models sizes for both algorithms and adjacencies. In (a), we show the averages from Fig. 7.9, with the black line indicating a one-to-one embedding, and coloured lines showing linear fits. The average largest vertex model sizes are shown in (b).

physical qubit usage and maximum vertex model size for all cases. We see that the number of required qubits is approximately proportional to the number of cells. There is less of a trend for the vertex model sizes, which likely depend more on the circuit complexity.

### 7.1.5 Generated Circuits

A stochastic circuit generator was implemented to investigate the range of QCA circuits that can be embedded onto the QPU. Each generated circuit connectivity graph is comprised of a random set of QCA components: inverters, majority gates, fixed polarization inputs. These components are *wired* together by generating random trees from the component outputs to random sets of available inputs. We generated 2000 circuits in both adjacencies and attempted to find embeddings. For each circuit, ten attempts were made with a maximum allowed runtime of 30 seconds, after which the embedding was assumed to have failed. The average required physical qubits for all successfully embedded circuits are shown in Fig. 7.11. We see similar trends to what was observed for the benchmark circuits. In Fig. 7.12, we show the single trial success probabilities as a function of the number of cells. These values correspond to the number of generated circuits of a given size which

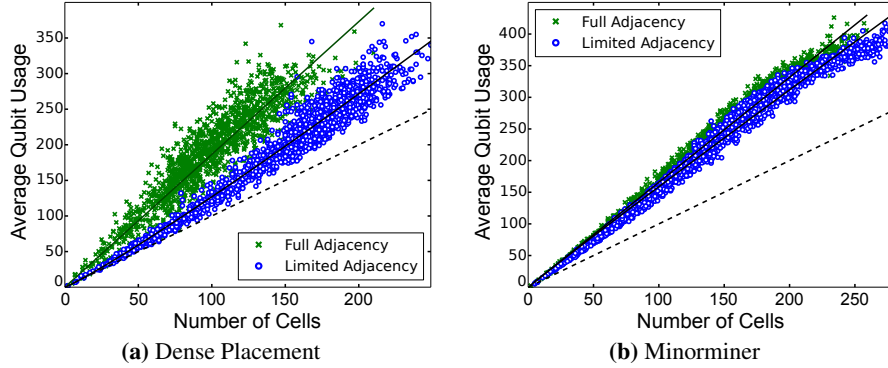


**Figure 7.11:** Average number of physical qubits needed to embed generated QCA circuits of different sizes. The solid black lines show power function fits which are approximately linear.

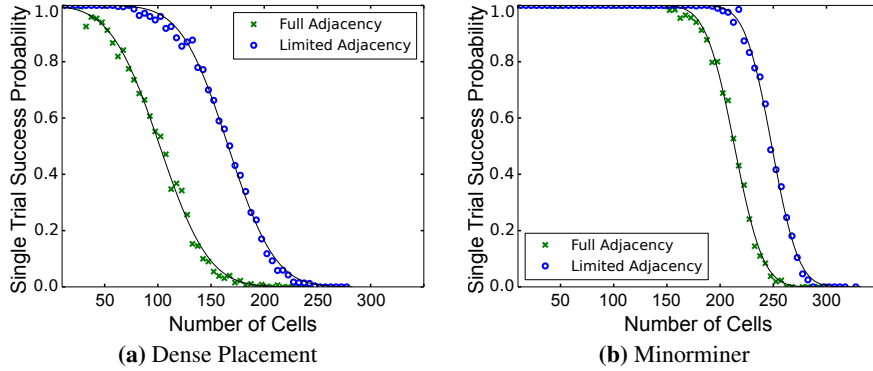


**Figure 7.12:** Average single trial embedding success probabilities using both algorithms. Points are obtained by counting the number of generated circuits with sizes in bins of 5 cells that were successfully embedded. Sigmoid fits are shown.

were successfully embedded within ten trials. We see that minorminer is much more likely to succeed in a given embedding attempt.

Further embedding results can be found in Appendix C.2, including average run times for finding embeddings of generated circuits, characteristic run times for larger QPUs, and results when random sets of disabled qubits are considered.

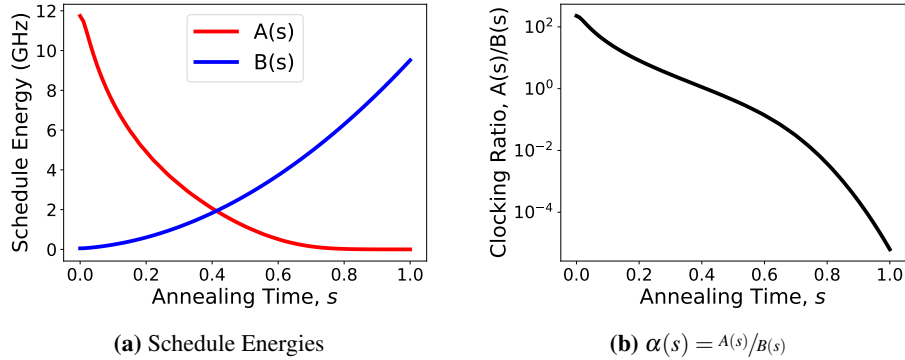


**Figure 7.13:** Annealing schedule for the D-Wave 2X, used in all presented annealing results and calculations. For reference,  $1 \text{ GHz} \equiv 4.1356 \mu\text{eV}$

## 7.2 Annealing Results

Here we present a number of results run on the 1152 qubit D-Wave 2X. The annealing schedule for the QPU is shown in Fig. 7.13. The energy scale on the QPU is comfortably expressed in GHz. This conversion relates to the energy of a photon with a given frequency  $f$ :  $E = hf$ , for the Planck constant  $h = 4.1356 \mu\text{eV}/\text{GHz}$ . When running problems on the QPU, users have control of a number of parameters. Relevant here are the *number of annealing trials* per gauge transformation, an arbitrary redefinition of the spin conventions of the qubits, and the *annealing time*,  $t_a$ , which defines our characteristic rate:  $\tilde{f} = 10^{-3} \text{ GHz} \cdot \mu\text{s}/\mathcal{E} \cdot t_a$ . Staying consistent with the framework in Chapter 6, we set  $\mathcal{E} = B(1) \approx 9.5 \text{ GHz}$ . The anneal times are typically on the order of  $10^1 \mu\text{s}$  to  $10^3 \mu\text{s}$ , meaning our characteristic frequency is on the order of  $10^{-5}$  to  $10^{-7}$ . These are much slower than the  $10^{-1}$  to  $10^{-2}$  sufficient for adiabatic evolution as determined in Chapter 6. This poses a potential issue for investigating the performance of small QCA devices if the goal is to study diabatic transitions near the coherent limit. At such relatively slow annealing speeds we should expect all our devices to run adiabatically. Any diabatic transitions likely arise due to other details of the evolution or QPU implementation, such as thermally assisted excitations [103, 111, 112].

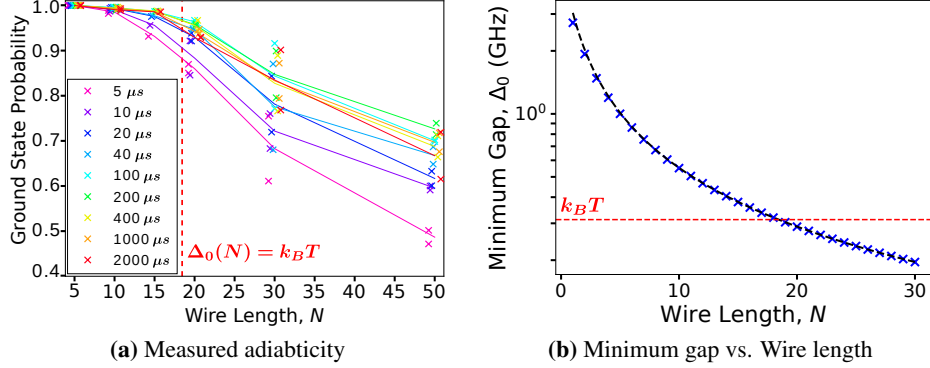


**Figure 7.14:** Annealing results for wires of different lengths with various annealing times. In (a), we show the proportional of trials returning the correct ground state. Each mark represents an annealing run of 50,000 trials. Two wires of each length were embedded using different sets of qubits. The lines pass through the average. Lengths of 5, 10, 15, 20, 30, and 50 were used; the markers are staggered for ease of view. The wire length at which the minimum gap falls below the thermal energy at 15 mK is indicated:  $N \sim 18.45$ . In (b), we present the minimum energy gap as a function of the wire length. The black dashed line gives the approximation from Eq. (6.18):  $\Delta_0(N) \approx B(s^*)\pi/(N+1)$ , with  $A(s^*) = B(s^*) = 1.934\text{GHz}$  at  $s^* = 0.413$ .

### 7.2.1 Adiabaticity of Wires

An important test for the QPU behaviour is simple wires of various lengths. They have both an analytical spectrum, Eq. (6.17), as well as a guaranteed one-to-one embedding. In Fig. 7.14, we present the measured adiabaticity, approximated by the number of annealing trials which return the correct ground state, for a selection of wires. We saw in Section 6.2.1 that long QCA wires are well approximated by a simple Landau-Zener model; however, the results here fall off far too quickly. Using Eqs. (6.18) and (6.20), we can calculate that the largest wire we should be able to run for a given adiabaticity,  $P_A$ , should be  $N_{max} \approx \sqrt{-20.2\text{GHz} \cdot t_a / \ln(1 - P_A)}$ . Even for the shortest annealing time,  $t_a = 5\mu s$ , we should have an adiabaticity of 0.99 at  $N_{max} \approx 147$ . This approximation ignores both environmental interactions as well as any additional details of the qubit behaviour. We see in Fig. 7.14 that the minimum energy gap of the wire becomes smaller than the thermal energy be-

tween  $N = 18$  and  $N = 19$ . This roughly corresponds to the start of the fall-off in the adiabaticity curves. This raises the possibility that what we are seeing is the result of thermal excitations.

### 7.2.2 Changes in the Spectrum after Embedding

Before looking more closely at the dependence on the annealing time,  $t_a$ , it is necessary to discuss a potential issue. While our choice in embedding and parameter assignment guarantees that the ground states in the classical limit ( $s = 1$ ) before and after embedding correspond, we have not yet considered what happens to the rest of the spectrum during annealing. In Fig. 7.15, we present the low energy spectra for a few simple QCA components that require only one additional physical qubit for embedding. In the case of the adapter, which connects normal 4-dot QCA cells to a rotated variant, we see barely any change to the spectrum after embedding, with the exception of some of the higher energy states and a slight decrease in the minimum gap. For Maj-101, we again see a slight decrease in the minimum gap but also significant change among the first three excited states. The most prominent change occurs for the inverter, with a large decrease in the minimum gap. In fact, at  $s = 1$  the first excited state for the embedded inverter has a kink within the vertex model, describing a state which has no analog in the original network. It would be possible to avoid this new state by increasing the relative strength of the  $J_{ij}$  within the vertex models, achieved by decreasing all other  $h_i$  and  $J_{ij}$  by some scaling factor; however, this would effectively increase the thermal energy, making thermal excitations more likely.

### 7.2.3 Transition Parameters

It is informative to look at the transition parameters associated with these spectra, shown in Fig. 7.16. Unlike previous cases, we are not expressing our spectra in dimensionless units. The transition parameters are then given in units of inverse energy:  $\text{GHz}^{-1}$ . We will primarily focus our analysis on the first excited state. For the adapter, we observed a 21.7% decrease in the minimum gap. If only the eigenenergies have changed, we should expect the transition parameter  $T_1$ , inversely proportional to the gap squared, to have increased by 63%. We observe

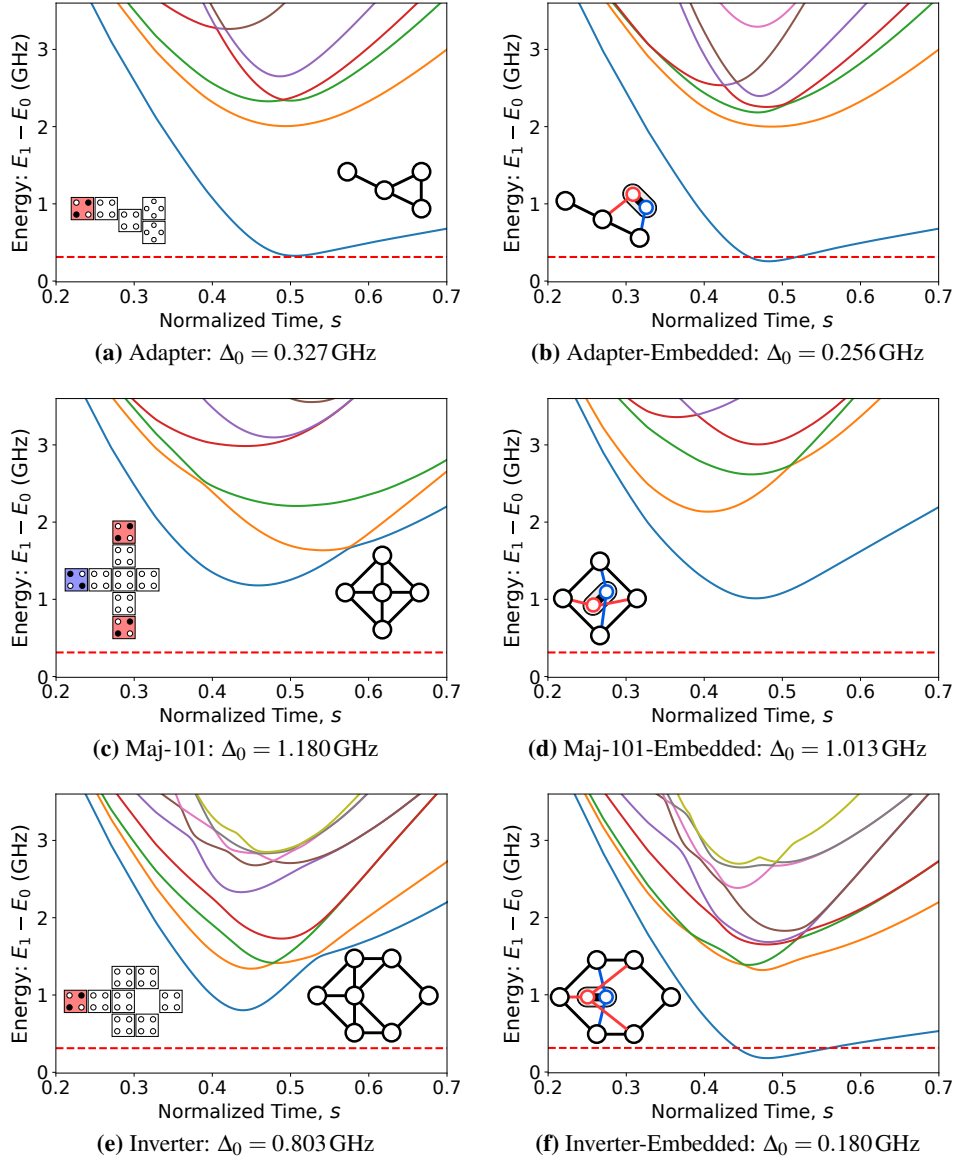


**Figure 7.15:** Change in the spectrum for the most efficient embeddings. Depending on the device and the embedding, the low energy spectrum can be significantly effected, as with the inverter, or barely affected at all. Minimum gaps are included in the sub-figure captions. The thermal energy at 15 mK is indicated by the red dashed line.

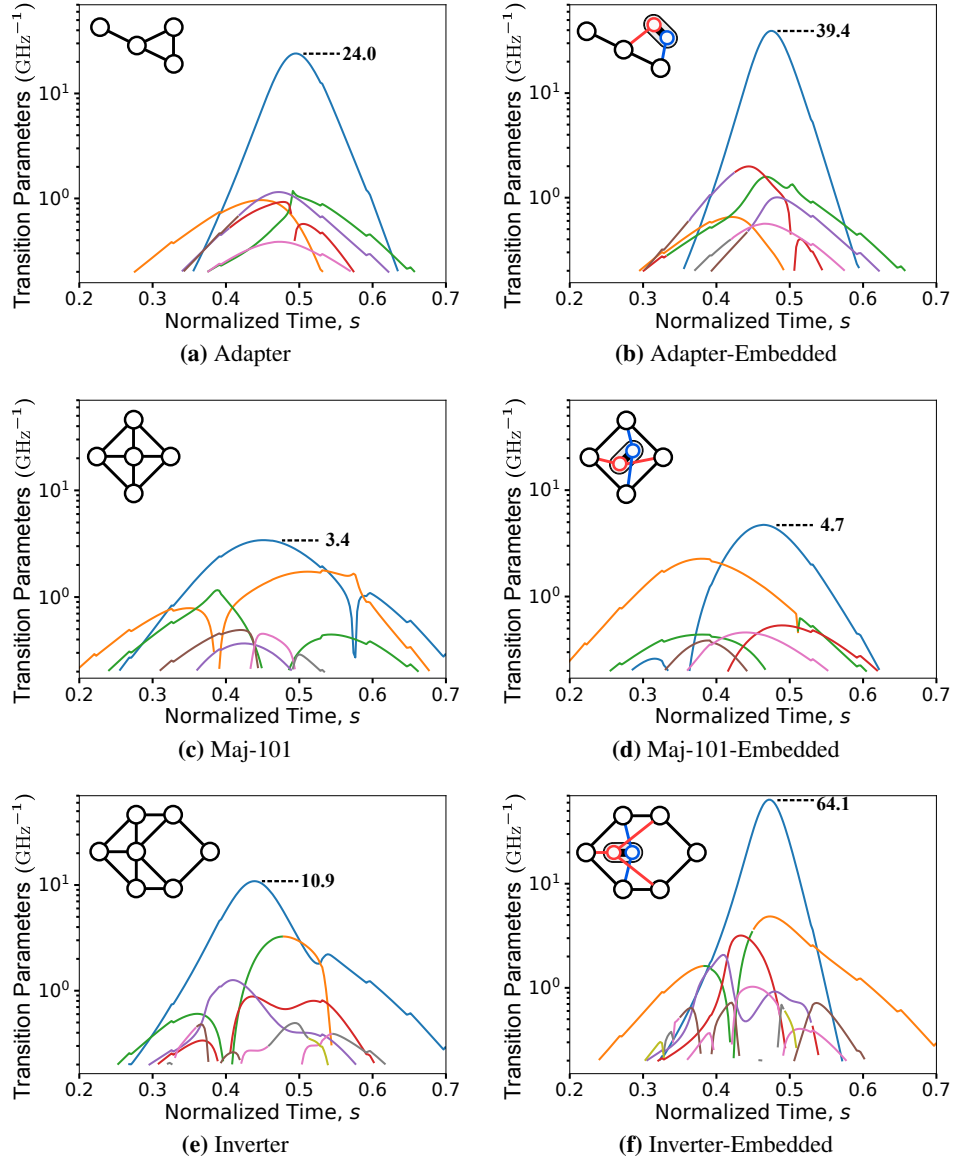


**Figure 7.16:** Transition parameters for the spectra in Fig. 7.15. The vertical scale is the same for all plots to help with comparison. The slight jaggedness is due to very small steps in the  $B$  schedule which causes spikes in  $\frac{d}{ds}B(s)$  and hence  $\frac{d}{ds}\hat{\mathcal{H}}$ . The values of the maximum peaks are given.

an increase of 64%. Similarly for Maj-101, we should expect an increase in  $T_1$  of about 36%, and we observe 38%. We infer from this that the embedding did not significantly change  $\langle \varphi_1 | \frac{d}{ds} \hat{\mathcal{H}} | \varphi_0 \rangle$ . It might in principle be possible then to correct for this increase in  $T_1$  by reducing the annealing speed near the minimum gap, decrease the transition rate and thereby recover some estimate of the dynamics of the original network, at least if we anneal slow enough that the rest of the eigenstates can be ignored. The same argument does not apply for the inverter. For a 77.5% reduction in the gap, we should expect  $T_1$  to increase by nearly  $20\times$ , yet we observed only about  $6\times$ . This means that  $\langle \varphi_1 | \frac{d}{ds} \hat{\mathcal{H}} | \varphi_0 \rangle$  is significantly different near the minimum gap. This is consistent with our observation that the first excited state at  $s = 1$  is incompatible with any state in the original system. Interestingly, we see that despite having a much smaller gap, the second excited state ends up having a higher transition parameter near the end of the anneal, suggesting a much stronger coupling if not for the larger gap. This second excited state ends up corresponding to the original first excited state, which can be seen in the spectra.

#### 7.2.4 Dependence on the Annealing Time

In Fig. 7.17, we show the ground state probabilities as a function of the annealing time for both a subset of the wires as well as the adapter, majority gate, and inverter. Unlike in the Landau-Zener model, where running things slower always improves adiabaticity, here we see an optimum annealing time for each given embedding. That time differs even for the same problem embedded using different qubits. The decline in performance with the increase in annealing time has been attributed to coupling to the environment [111, 112]. It is argued that for fast annealing, the dynamics are similar to diabatic transitions seen in the Landau-Zener model, or perhaps other descriptions of closed system phase transitions (see Ref. [112]). Such transitions are inverse to the annealing time. Due to the presence of thermal noise, excitations into energy levels with gaps on the order of the thermal energy are possible [111]. The longer the system spends near the minimum gap, where such transitions are easiest, the more likely it is for the system to be excited out of the ground state.

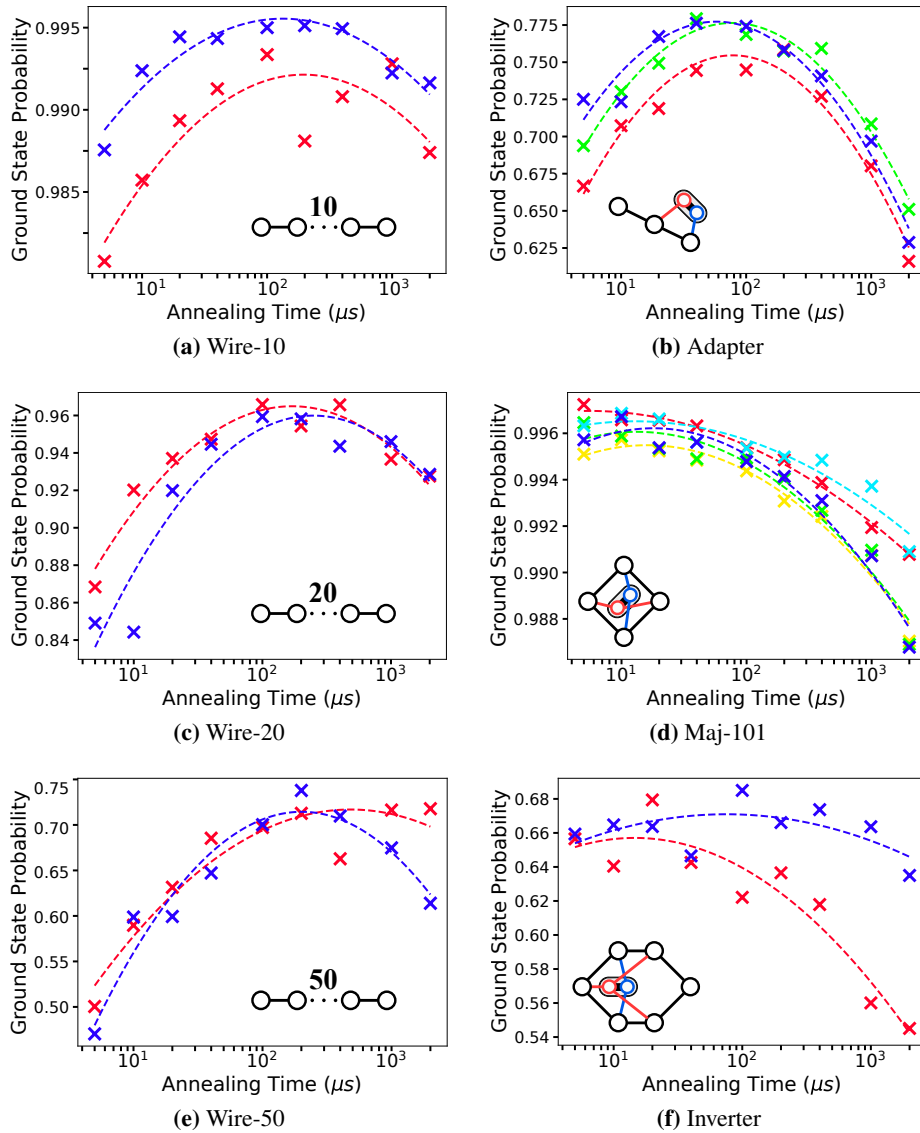


**Figure 7.17:** Proportion of annealing results which produce the ground state for our sample embeddings as a function of the annealing time. The colours indicate different embeddings for each network, with 50,000 annealing trials for each marker. The dashed lines show a simple quadratic fit for each embedding.

### 7.3 Summary

In this chapter, we have discussed the potential for applying a physical implementation of quantum annealing as a means of investigating the dynamic behaviour of QCA networks, in particular the QPU developed by D-Wave Systems Inc. For the particular qubit connectivity available in the Chimera or Pegasus topology, it is not possible to map all QCA networks to the QPU without the use of additional qubits. Schemes for embedding a given QCA network onto the QPU were discussed, where each QCA cell is mapped to a connected set of physical qubits called a vertex model. We found that the use of these additional qubits results in a difference between the spectra of the original and embedded networks. In the simple case, we observe a slight decrease in the minimum gap without any significant change in  $\langle \varphi_1 | \frac{d}{ds} \hat{\mathcal{H}} | \varphi_0 \rangle$ . The embedding of an inverter introduced a new first excited state which did not correspond to a polarization state. For this embedding, it is questionable whether any meaningful estimate of performance could be extracted. For larger networks, not only is it a challenge to determine the spectrum in order to check the consequences of the embedding, but we typically end up having multiple vertex models containing more than two physical qubits. This suggests that additional work would be needed in order to better understand how to map the annealing results back to performance estimates of the original system.

We saw from the annealing results that there are two competing mechanisms for diabatic transitions on the QPU. For fast annealing rates, transitions consistent with closed system dynamics dominate. These transitions decrease as the annealing time is increased. As the annealing time is increased further, transitions associated with coupling to the environment become prominent. This results in an optimum annealing time which produces the largest adiabaticity. It is not clear how these transition mechanisms on the QPU map to those of any particular QCA implementation.

## Chapter 8

# Eigenspectrum Decomposition of QCA Networks

In Chapter 6, we concluded that the low energy spectrum was a powerful tool for understanding QCA performance, but that its applicability was limited by the intractable diagonalization of the  $N$ -cell Hamiltonian for larger QCA networks. In the previous chapter, we noted that extracting performance metrics for larger QCA networks embedded on the QPU would require a better understanding of how embedding effects the spectrum. We will conclude by addressing two ideas related to QCA spectra. First, we investigate a means to decompose larger QCA networks into meaningful subcomponents, and how important features in the low energy spectrum of the full network can be attributed to those components. Secondly, we discuss how to estimate the spectrum for large QCA networks. In Section 8.1, we discuss how the system Hamiltonian in the 2-state approximation can be decomposed into meaningful sub-Hamiltonians given some partition or decomposition of a QCA network into components. These sub-Hamiltonians give estimates of the reduced density operators of each component. In Section 8.2, we establish an objective function which gives a measure of how well a given decomposition captures the low energy characteristics of the full network. Using this metric, we identify the problem of network decomposition as a graph partitioning problem with signed edge weights. Strategies for finding the optimal network decomposition for smaller QCA networks with exactly solvable ground states are discussed. We show how

the low energy spectra of the component Hamiltonians describe features of the full spectrum. In Section 8.3, we introduce a heuristic method based on the component Hamiltonian construction which allows for the study of larger networks. In Section 8.4, we discuss the computation of transition parameters. In Section 8.5, we demonstrate one potential application of this formalism, the meaningful comparison of alternate variations of network components. Finally, in Section 8.6, we give a few additional details relating to extensions of the component model to 3-state QCA and for dynamic wave clocking.

## 8.1 Decomposing the QCA Network Hamiltonian

When designing QCA networks, it is practical to conceptually decompose the network into smaller interconnected components, typically logic gates. It is meaningful then to ask whether it is possible to understand properties such as the performance of a given QCA network in terms of contributions from subsets of the network. The first step is in understanding how to decompose the Hamiltonian. We can define a network *partition*  $\{\mathcal{S}_\ell\}$  to be any set of non-empty components, where each QCA cell belongs to exact one of the components  $\mathcal{S}_\ell$ . Note that for our models of QCA, the Hamiltonian only ever contains operators that affect at most two cells. Then for a given partition, we can always decompose  $\hat{H}$  as

$$\hat{H} = \sum_{\ell} \hat{H}_\ell + \sum_{\langle \ell \ell' \rangle} \hat{\mathcal{M}}_{\ell \ell'}, \quad (8.1)$$

where  $\hat{H}_\ell$  only contains terms within  $\mathcal{S}_\ell$  and  $\hat{\mathcal{M}}_{\ell \ell'}$  contains all the terms between components  $\mathcal{S}_\ell$  and  $\mathcal{S}_{\ell'}$ . A good choice for the  $\hat{H}_\ell$  and  $\hat{\mathcal{M}}_{\ell \ell'}$  will be discussed later. In QCA, we are mostly interested in quantities that relate to either individual cells or pairs of cells. If we assume the system is in thermal equilibrium, then the expectation value of any operator  $\hat{O}_\ell$  that influences only cells within  $\mathcal{S}_\ell$  can be expressed as

$$\langle \hat{O}_\ell \rangle = \text{Tr} \hat{O}_\ell \hat{\rho} = \frac{1}{\mathcal{Z}} \text{Tr} \hat{O}_\ell e^{-\beta \hat{H}}, \quad (8.2)$$

with inverse temperature  $\beta = 1/k_B T$  and normalization constant  $\mathcal{Z} = \text{Tr} e^{-\beta \hat{H}}$ . As  $\hat{O}_\ell$  depends only on  $\mathcal{S}_\ell$ , we can take the trace over the complement of  $\mathcal{S}_\ell$  to obtain

the reduced density operator  $\hat{\rho}_k = \text{Tr}_k^c \hat{\rho}$  and get

$$\langle \hat{O}_k \rangle = \text{Tr}_k \hat{O}_k \hat{\rho}_k \quad (8.3)$$

### 8.1.1 The Ideal Component Hamiltonian

For any finite temperature and reduced density operator  $\hat{\rho}_k$ , there always exists a Hamiltonian  $\hat{H}_k$  that captures the physics of all operators  $\hat{O}_k$ . In particular, we express  $\hat{\rho}_k$  in two forms: (1) its own eigenbasis  $(W_k^\alpha, |u_k^\alpha\rangle)$  with  $W_k^\alpha \geq 0$ ; and (2), a Boltzmann distribution:

$$\hat{\rho}_k = \sum_{\alpha} W_k^\alpha |u_k^\alpha\rangle \langle u_k^\alpha| = \frac{1}{\mathcal{Z}_k} e^{-\beta \hat{H}_k}. \quad (8.4)$$

Every eigenstate  $|u_k^\alpha\rangle$  is also an eigenstate of  $\hat{H}_k$  with eigenvalue  $\mathcal{E}_\alpha = -\beta^{-1} \log W_k^\alpha - \beta^{-1} \log \mathcal{Z}_k$ . We can write

$$\hat{H}_k = -\beta^{-1} \sum_{\alpha} \log W_k^\alpha |u_k^\alpha\rangle \langle u_k^\alpha| - \beta^{-1} \log \mathcal{Z}_k \hat{I}. \quad (8.5)$$

Ideally, we would equate these  $\hat{H}_k$  to those in Eq. (8.1); unfortunately, computing  $\hat{H}_k$  in this way requires knowledge of the full system density operator and is thus not practical for larger networks. Instead, we will employ mean-field theory to attempt to estimate  $\hat{H}_k$ .

### 8.1.2 Mean-Field Theory Approximation

The approach here is to estimate properties of the reduced density operators in the absence of correlation terms between the components. We begin with the Callen-Suzuki identity [113]:

$$\langle \hat{O}_k \rangle \approx \frac{1}{\mathcal{Z}} \text{Tr} \hat{E}_k(\hat{O}_k) e^{-\beta \hat{H}}, \quad (8.6)$$

where

$$\hat{E}_k(\hat{O}_k) = \frac{\text{Tr}_k \hat{O}_k e^{-\beta \bar{\mathcal{H}}_k}}{\text{Tr}_k e^{-\beta \bar{\mathcal{H}}_k}}, \quad (8.7)$$

is an operator on the complement of  $\mathcal{S}_\ell$  for the expected value of  $\hat{O}_\ell$  over the degrees of freedom of  $\mathcal{S}_\ell$ . The Hamiltonian  $\tilde{\mathcal{H}}_\ell$  here contains all terms of  $\hat{H}$  that affect  $\mathcal{S}_\ell$ . In particular, for the terms defined in Eq. (8.1),

$$\tilde{\mathcal{H}}_\ell = \hat{H}_\ell + \sum_{\ell \neq \ell} \hat{\mathcal{M}}_{\ell\ell} \quad (8.8)$$

We will use the 2-state approximation as a specific case study. From Eq. (2.3), we can write  $\tilde{\mathcal{H}}_\ell$  explicitly as

$$\tilde{\mathcal{H}}_\ell = -\frac{1}{2} \sum_{i \in \mathcal{S}_\ell} \gamma_i \hat{\sigma}_x^i + \frac{1}{2} \left[ \sum_{i \in \mathcal{S}_\ell} \hat{h}_i \hat{\sigma}_z^i - \sum_{\langle ij \rangle \in \mathcal{S}_\ell} E_{ij}^k \hat{\sigma}_z^i \hat{\sigma}_z^j \right] \quad (8.9)$$

where  $\hat{h}_i = h_i \hat{I} - \sum_{\ell \neq \ell} \sum_{j \in \mathcal{S}_\ell} E_{ij}^k \hat{\sigma}_j^z$  is a biasing operator containing all interactions involving site  $i$  excluding those internal to  $\mathcal{S}_\ell$ . We make the ansatz that, for  $i$  and  $j$  in different components, we can exchange the  $\hat{\sigma}_j^z$  term with some constant  $m_j$ : i.e.  $\hat{\sigma}_z^j \hat{\sigma}_z^i \rightarrow m_j \hat{\sigma}_z^i$ . These  $m_i$  would typically be called *magnetisations*; however, we will simply call them the *mean fields*. Then  $\tilde{\mathcal{H}}_\ell$  represents an Ising spin-glass model on  $\mathcal{S}_\ell$  with  $\hat{h}_i \approx \tilde{h}_i \hat{I}$  for a constant:

$$\tilde{h}_i = h_i - \sum_{\ell \neq \ell} \sum_{j \in \mathcal{S}_\ell} E_{ij}^k m_j. \quad (8.10)$$

As this form of  $\tilde{\mathcal{H}}_\ell$  satisfies  $[\tilde{\mathcal{H}}_\ell, \hat{H} - \tilde{\mathcal{H}}_\ell] = 0$ , it follows that this approximation is equivalent to assuming a decomposable density operator given by the Kronecker product of the reduced density operators:  $\hat{\rho} = \otimes_\ell \hat{\rho}_\ell$ . Here we again assume  $\hat{\rho}$  is given by a Boltzmann distribution. Conventional mean field theory tells us we should use [113]

$$m_i = \text{Tr}_\ell \hat{\sigma}_z^i \hat{\rho}_\ell = \frac{1}{\mathcal{Z}_\ell} \text{Tr}_\ell \hat{\sigma}_z^i e^{-\beta \tilde{\mathcal{H}}_\ell}. \quad (8.11)$$

We can now define our estimate of the terms in Eq. (8.1):

$$\hat{H}_\ell = -\frac{1}{2} \sum_{i \in \mathcal{S}_\ell} \gamma_i \hat{\sigma}_x^i + \frac{1}{2} \left[ \sum_{i \in \mathcal{S}_\ell} \tilde{h}_i \hat{\sigma}_z^i - \sum_{\langle ij \rangle \in \mathcal{S}_\ell} E_{ij}^k \hat{\sigma}_z^i \hat{\sigma}_z^j \right] \quad (8.12a)$$

$$\hat{\mathcal{M}}_{\ell\ell} = -\frac{1}{2} \sum_{i \in \mathcal{S}_\ell} \sum_{j \in \mathcal{S}_\ell} E_{ij}^k (\hat{\sigma}_z^i - m_i) (\hat{\sigma}_z^j - m_j) + \mathcal{E}_{\ell\ell} \quad (8.12b)$$

where  $\mathcal{E}_{\ell\ell} = \frac{1}{2} \sum_{i \in \mathcal{S}_\ell} \sum_{j \in \mathcal{S}_\ell} E_{ij}^k m_i m_j$  is just a constant. The necessary identity operators that accompany all constants are suppressed for conciseness. In practice, we need to compute  $\hat{H}_\ell$  self-consistently with  $m_i$  via Eq. (8.11).

## 8.2 System Energy-Based Decomposition

When operating near the adiabatic limit, the low energy eigenstates of a QCA network produce important information about network performance [5]. We consider the relevant case of determining the energy of a QCA network. Observe that in the limit of zero thermal energy,  $\hat{\rho}$  becomes equal to the ground state of  $\hat{H}$ . In this case, the  $m_i$  are analogous to the instantaneous ground state polarizations used in the multi-cell ICHA discussed in Section 2.2.4. If the thermal energy is on the order of the energy gap between the ground and first excited states, then  $\hat{\rho}$  and the  $\hat{\rho}_\ell$  contain contributions only from a few of the lowest energy eigenstates. If we want to estimate the energy of the system, we have

$$E = \langle \hat{H} \rangle = \sum_{\ell} \langle \hat{H}_\ell \rangle + \sum_{\ell \neq \ell'} \langle \hat{\mathcal{M}}_{\ell\ell'} \rangle. \quad (8.13)$$

We define  $\langle \hat{A} \rangle_r$  as our estimate of the expected value of  $\hat{A}$  using only the reduced density operators, and  $\Delta(\hat{A}) = \langle \hat{A} \rangle_r - \langle \hat{A} \rangle$ . We can then split the error in our estimate of the system energy into two components: the error internal to each component, arising from any inaccuracy in the estimation of  $\hat{\rho}_\ell$ , and the error in estimating inter-component interactions. If we used the exact  $\hat{\rho}_\ell$  defined in Eq. (8.4), the former would be exactly zero; however, for our mean field approximation we are left with an error:

$$\Delta E_{\text{int}} = -\frac{1}{2} \sum_i \gamma_i \Delta(\hat{\sigma}_x^i) + \frac{1}{2} \left[ \sum_i h_i \Delta(\hat{\sigma}_z^i) - \sum_{\ell} \sum_{\langle ij \rangle \in \mathcal{S}_\ell} E_{ij}^k \Delta(\hat{\sigma}_z^i \hat{\sigma}_z^j) \right]. \quad (8.14)$$

The error arising from inter-component couplings is given by

$$\Delta E_{\text{ext}} = -\frac{1}{2} \sum_{\langle \ell\ell' \rangle} \sum_{i \in \mathcal{S}_\ell} \sum_{j \in \mathcal{S}_{\ell'}} E_{ij}^k \Delta(\hat{\sigma}_z^i \hat{\sigma}_z^j). \quad (8.15)$$

As discussed, our definition of the mean fields,  $m_i$ , produces a density operator of the form  $\hat{\rho} = \otimes_{\ell} \hat{\rho}_{\ell}$ . It follows that the  $\Delta(\hat{\sigma}_z^i \hat{\sigma}_z^j)$  terms in Eq. (8.15) are given by

$$\Delta(\hat{\sigma}_z^i \hat{\sigma}_z^j) = -M_{zz}^{ij} + \Delta(\hat{\sigma}_z^i) \langle \hat{\sigma}_z^j \rangle + \langle \hat{\sigma}_z^i \rangle \Delta(\hat{\sigma}_z^j) \quad (8.16)$$

plus an additional term  $\Delta(\hat{\sigma}_z^i) \Delta(\hat{\sigma}_z^j)$  taken to be small. The correlation proper  $M_{zz}^{ij} = \langle \hat{\sigma}_z^i \hat{\sigma}_z^j \rangle - \langle \hat{\sigma}_z^i \rangle \langle \hat{\sigma}_z^j \rangle$  is a measure of the loss of information about the coupling between sites  $i$  and  $j$  due to neglecting inter-component correlations [36, 42]. The latter two terms can be absorbed into Eq. (8.14) by subtracting  $E_{ij}^k \langle \hat{\sigma}_z^j \rangle$  terms from the  $h_i$ . This leaves

$$\Delta E = \Delta E_{\text{int}}(\{m_i\}) + \frac{1}{2} \sum_{\langle \ell \ell' \rangle} \sum_{i \in \mathcal{S}_{\ell}} \sum_{j \in \mathcal{S}_{\ell'}} E_{ij}^k M_{zz}^{ij}. \quad (8.17)$$

Here  $\Delta E_{\text{int}}$  is now a function of the  $\langle \hat{\sigma}_z^i \rangle$ , or equivalently the mean fields. By definition, a good approximation of the reduced density operators produces small  $\Delta$  terms for operators internal to the components. We assume then that  $\Delta E_{\text{int}}$  will be small relative to the second term in Eq. (8.17). We are tempted at this point to identify the decomposition of QCA networks as a graph partitioning problem.

### 8.2.1 Energy-Optimal Component Decomposition

If our goal is to identify a decomposition which best reproduces the reduced density operators when the system operates nearly adiabatically, i.e. to capture information about the lowest energy eigenstates of the approximate sub-Hamiltonians, we see that the best choice of components in a decomposition should minimize the error term in Eq. (8.17) arising from the correlation proper. That is, we should minimize a cost function of the form

$$C(\{\mathcal{S}_{\ell}\}) = \left| \sum_{\langle \ell \ell' \rangle} \sum_{i \in \mathcal{S}_{\ell}} \sum_{j \in \mathcal{S}_{\ell'}} E_{ij}^k M_{zz}^{ij} \right|. \quad (8.18)$$

We assume for now that the correlation proper are known from the ground state of the full system. In Section 8.3, we discuss an approach for approximating these values for systems too large to solve exactly. Using the connectivity graph structure

defined in Section 7.1.1, we see that QCA network decomposition becomes a graph partitioning problem with signed edge weights and an objective function  $C$ . In particular, the partitioning takes the form of a minimum k-cut problem [114, 115]. There are two challenges here. First, common graph partitioning libraries employ an objective function given as a linear combination of edge weights. To address this, we could define two objective functions  $C_+$  and  $C_-$ :

$$C_{\pm}(\{\mathcal{S}_{\ell}\}) = \sum_{\langle \ell \ell \rangle} \sum_{i \in \mathcal{S}_{\ell}} \sum_{j \in \mathcal{S}_{\ell}} \pm E_{ij}^k M_{zz}^{ij}. \quad (8.19)$$

We can then find the optimal partitions,  $\{\mathcal{S}_{\ell}\}_{\pm}$ , for both of these objective functions. Whichever produces the smallest absolute value of their corresponding  $C_{\pm}$  optimises  $C$ . The second challenge is due to the signed edge weights  $w_{ij} = E_{ij}^k M_{zz}^{ij}$ . Available solvers require non-negative, typically integer-valued, edge weights. We will not attempt to solve the signed partitioning problem in this work. Instead, the results we present are achieved in two steps. We first consider an upper bound on Eq. (8.18):

$$C(\{\mathcal{S}_{\ell}\}) \leq \tilde{C}(\{\mathcal{S}_{\ell}\}) = \sum_{\langle \ell \ell \rangle} \sum_{i \in \mathcal{S}_{\ell}} \sum_{j \in \mathcal{S}_{\ell}} |E_{ij}^k M_{zz}^{ij}|. \quad (8.20)$$

This objective can be optimized using a standard solver such as METIS [116] with edge weights  $w_{ij} = |E_{ij}^k M_{zz}^{ij}|$ . Where integer weights are required, simple quantization is used. We take the resulting partition as an initial guess of the true optimum. Local adjustments are then made manually in order to further reduce the values of Eq. (8.18). This refinement process could be automated in future.

## 8.2.2 Decompositions for Clocked Networks

Network clocking manifests as some time varying parameter in the Hamiltonian. The decomposition which optimizes Eq. (8.18) then may vary with time. This is not particularly appropriate for our purposes. We instead consider a different objective function. In particular, we define the optimal decomposition as that which minimizes the highest observed value of  $C$  over a set of sample times,  $\{t_n\}$ . We

define the dynamic objective function

$$C_d(\{\mathcal{S}_\ell\}) = \max_{t_n} \left| \sum_{\langle \ell \ell' \rangle} \sum_{i \in \mathcal{S}_\ell} \sum_{j \in \mathcal{S}_{\ell'}} E_{ij}^k(t_n) M_{zz}^{ij}(t_n) \right|. \quad (8.21)$$

Again, we can find an initial partition using the upper bounded variant with edge weights  $w_{ij} = \max_{t_n} |E_{ij}^k(t_n) M_{zz}^{ij}(t_n)|$ . Of interest during QCA clocking are the intervals over which the gap between the ground and first excited state is minimum [5]. We use these minima as our  $t_n$ .

### 8.2.3 Decomposition of a Solvable System

Let us consider the 2-dot majority gate in Fig. 7.6(c) where we fix the inputs to have respective polarizations of  $(+1, -1, +1)$  or binary 101. The Hamiltonian of this 19 cell network is too large for exact eigenvalue decomposition in a reasonable time; however, using sparse matrix methods we can successfully employ Lanczos iteration to reliably approximate the spectrum [44]. In Fig. 8.1 we show a few possible decompositions of the majority gate and the resulting energy eigenspectra. These spectra are achieved as follows. First we find the  $k$  lowest eigenpairs of the full system Hamiltonian  $\hat{H}(\gamma)$  using a Python wrapper of the ARPACK package [117, 118]. It is assumed that all cells share a clock:  $\gamma_i = \gamma$ . Using the computed ground states, we construct the low-temperature mean fields  $m_i(\gamma) = \langle \hat{\sigma}_z^i \rangle$ . We compute the component Hamiltonians using the instantaneous effective biases  $\tilde{h}_i(\gamma)$  from Eq. (8.10), and then the lowest energy eigenstates in the component spectra. We can make a few interesting observations: (1) the best choice of network decomposition is not typically the one which evenly divides the network into equally sized components; (2), when the components are chosen well, the component spectra seem to reproduce important features of the full spectrum; and (3), even a slight deviation from the optimal decomposition can drastically change the component spectra and result in a failure to predict important features. Any decomposition that splits up the two high density columns fails to reproduce the first minima in the component spectra.

It is worth considering what the component spectra actually describe. We consider the basis of product states of the eigenstates of the component Hamiltonians.

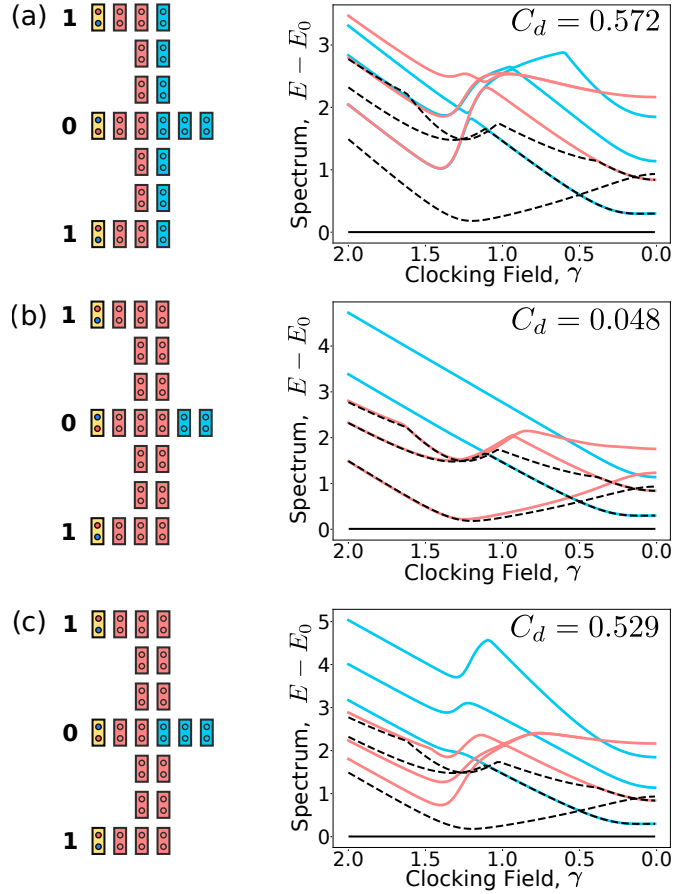


**Figure 8.1:** Sample decomposition of the 2-dot majority gate with binary inputs 101. The orange shaded devices have fixed polarization and simply provide  $h$  biases to their neighbours. In this case, the network is decomposed into 2 components indicated with red and blue. The corresponding energy eigenspectra are shown as the clocking parameter,  $\gamma$ , is swept. Ground state energies are subtracted to highlight features in the spectra. Here the black dashed line shows the spectrum of the full system. The colored spectra are obtained from the component Hamiltonians given by Eq. (8.12a) with the mean fields given by the polarization of the full system ground state. In (a), we use a naïve balanced decomposition, where we simply split the network in half. The decomposition based on our dynamic objective function, Eq. (8.21), is shown in (b). We see that the component spectra closely reproduce the features of the true spectrum. In (c), we see that a slight deviation from the optimal decomposition can drastically change the component spectra, which fail to predict the first minimum. Only the few lowest energy excited states are shown. Values of  $C_d$  are shown for the set  $\gamma \in \{1.196, 0.11\}$ .

By subtracting the ground state energies, a given component spectrum describes product states where all other components are in their ground state. This follows from the observation that for our definition of the mean fields and given that only one component is excited, at least one of  $\hat{\sigma}_z^i - m_i$  and  $\hat{\sigma}_z^j - m_j$  will have an expected value of 0 for  $i$  and  $j$  in different components. If a feature in the true spectrum matches one of the component spectra, this suggests that both the ground state and the corresponding excited state must be approximately such product states. This holds for the ground state when the instantaneous value of Eq. (8.18) is small, and thus the ground state energy is approximated by the component ground states. Our choice of decomposition does not directly consider whether this is true for the excited states; however, by choosing our sample times  $\{t_n\}$  to correspond to the minima in the energy gap, we attempt to guarantee at least one of the necessary criterion for the full and component spectra to agree.

#### 8.2.4 Additional Details on Finding Partitions

In Fig. 8.1, we can get a decomposition with a slightly lower cost than our presented optimal if we simply use the cell adjacent to the 0 input as the first component. For the given inputs, that cell has very little influence on the rest of the network and does not significantly contribute. This decomposition gives  $C_d = 0.043$ . The component spectrum of the rest of the network is effectively that of the full network. Such decompositions, however, are not particularly informative as they do not attribute features in the spectrum to individual network components. There are a number of ways we might avoid this scenario. Firstly, we have said nothing about how many components should be used in a decomposition. We are free to increase this number to attempt to force the partitioning algorithm to identify non-trivial components. Additionally, solvers like METIS attempt to minimise the objective function, in our case the so-called edge-cut function, while trying to keep the component sizes balanced. A constant  $\varepsilon$  is defined such that for  $K$  components, the largest component contains at most a fraction  $(1 + \varepsilon)/K$  of the cells. For all results presented in this work, initial partitioning was done using METIS 5.1.0 set for  $k$ -way multilevel partitioning using the “cut” objective type and set to force contiguous partitions. The value of  $\varepsilon$ , through the “ufactor” parameter, was set to 0.3

by default but adjusted for each network if unsuitable components were produced.

### 8.3 Heuristic Solver for Large Networks

When the true ground state of the system is known, we can determine the  $M_{zz}^{ij}$  exactly and attempt to find an optimal decomposition. However, the size of the Hilbert space for 2-state networks scales as  $2^N$  for  $N$  cells, meaning the complexity of exact eigenvalue decomposition is at least as hard as  $O(4^N)$ . This is solvable for practical hardware and time scales for only a dozen or so cells. Using sparse heuristic solvers which employ methods such as Lanczos iteration [44, 119], we can extend this to 20 or so cells. Beyond this limit, we must begin to make approximations. One approach would be to employ something like density matrix renormalization groups (DMRG) [120]. Interestingly, the component decomposition approach we have established introduces a potential related solution. In identifying the optimal decomposition, we used information about the ground state to construct mean fields which produce useful component Hamiltonians. We can consider the inverse problem. Given an approximation of the component Hamiltonians, we attempt to efficiently produce an estimate of the ground state, or indeed additional states, of the full system. We will employ a variational procedure based on basis reduction, similar in concept to DMRG. This approach will be referred to as the Component Mode (CM) solver.

#### 8.3.1 Component Mode Formulation

We suppose we are given some initial partition and a guess of the mean fields. We assume for now that each component is small enough to be solved exactly:  $|\mathcal{S}_\ell| \lesssim 20$ . We can now construct our estimates of each of the component Hamiltonians, Eq. (8.12a). Recall that our mean field approximation was equivalent to assuming a density operator of the form  $\hat{\rho} = \bigotimes_{\ell} \hat{\rho}_{\ell}$ . If this were truly the case, the ground state of the full system would be the product state of the ground states of each of our component Hamiltonians. We observe that we must assume a number of inaccuracies: (1) the initial decomposition will generally be sub-optimal; (2), the given mean fields may be inaccurate; and (3), the mean-field model itself is imperfect. For simplicity we assume there are only two components. From Eq. (8.12),

the Hamiltonian of the full system can be expressed up to a constant as

$$\hat{H} = \hat{H}_1 \oplus \hat{H}_2 - \frac{1}{2} \sum_{i \in \mathcal{S}_1} \sum_{j \in \mathcal{S}_2} E_{ij}^k (\hat{\sigma}_z^i - m_i) \otimes (\hat{\sigma}_z^j - m_j), \quad (8.22)$$

Where here we understand the  $\hat{H}_n$  and  $\hat{\sigma}_z^i$  to be of dimension  $2^{|\mathcal{S}_n|}$  and explicitly denote the Kronecker sum and product. Our approach will be to select a subset of the eigenstates of each of the component Hamiltonians. In DMRG, we would find the dominant eigenpairs of the reduced density operators, those with the largest eigenvalues [121]. As we have assumed our reduced density operators to be Boltzmann distributions, these dominant eigenstates are exactly the lowest energy eigenstates of the component Hamiltonians. For each component, we select some number,  $d_n$ , of the lowest energy eigenstates. We call these states the *component modes*, which form the columns of the transformation operators  $U_n \in \mathbb{C}^{2^{|\mathcal{S}_n|} \times d_n}$ . We then obtain reduced basis representations of the relevant component operators of size  $d_n \times d_n$ :

$$\mathbf{H}_n = U_n^\dagger \hat{H}_n U_n, \quad \boldsymbol{\sigma}_z^i = U_n^\dagger \hat{\sigma}_z^i U_n. \quad (8.23)$$

The reduced basis representation of the full system Hamiltonian is then constructed simply as

$$\mathbf{H} = \mathbf{H}_1 \oplus \mathbf{H}_2 - \frac{1}{2} \sum_{i \in \mathcal{S}_1} \sum_{j \in \mathcal{S}_2} E_{ij}^k (\boldsymbol{\sigma}_z^i - m_i) \otimes (\boldsymbol{\sigma}_z^j - m_j), \quad (8.24)$$

with a dimension of  $\mathbf{d} = \prod_n d_n$ . For decomposition into  $K$  components we make two adjustments: (1) we replace  $\hat{H}_1 \oplus \hat{H}_2$  with  $\bigoplus_n \hat{H}_n$ , the Kronecker sum over all component Hamiltonians; and (2), we have a coupling term for each pair of components, made easier by first constructing the  $\mathbf{d} \times \mathbf{d}$  representations of the  $\boldsymbol{\sigma}_z^i$ . We can then estimate the ground state of  $\mathbf{H}$ ,  $|\boldsymbol{\varphi}_0\rangle$ , or even additional low energy eigenstates. Using the reduced basis representation of  $\hat{\sigma}_z^i$ , we can get new estimates of the mean fields and correlation properers:

$$m_i = \langle \boldsymbol{\varphi}_0 | \boldsymbol{\sigma}_z^i | \boldsymbol{\varphi}_0 \rangle, \quad M_{zz}^{ij} = \langle \boldsymbol{\varphi}_0 | \boldsymbol{\sigma}_z^i \boldsymbol{\sigma}_z^j | \boldsymbol{\varphi}_0 \rangle - m_i m_j, \quad (8.25)$$

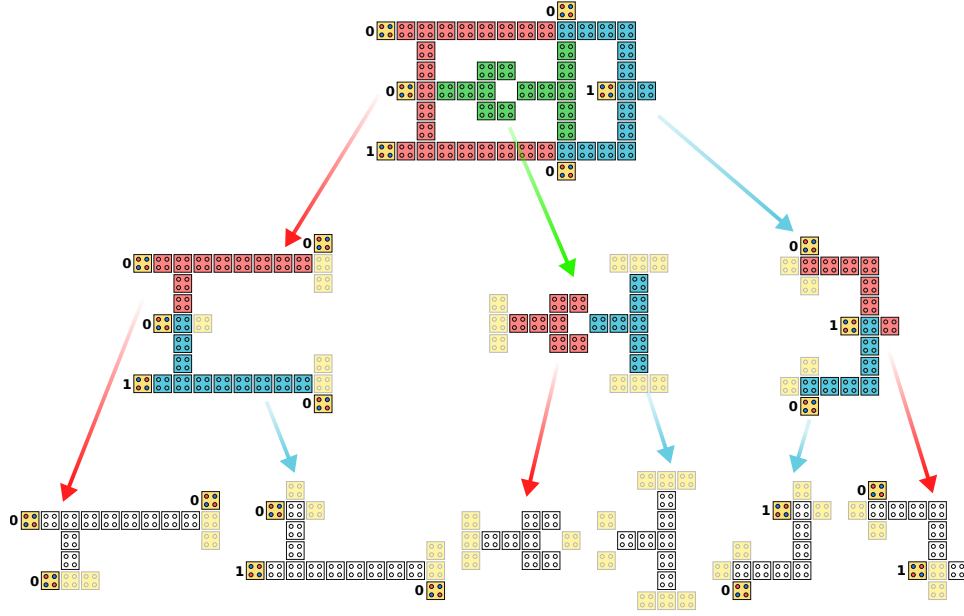


**Figure 8.2:** Example decomposition tree of a large QCA network. The cell colours indicate the components at that level of the decomposition. Orange cells have fixed polarization and belong to either of two classes. Dark orange cells indicate fixed inputs in the full network. Faded orange cells indicate representative biases arising from inter-component interactions. These should be understood as cells with fixed polarizations defined by the current mean field estimates. Note that the fixed polarization cells do not get split between the components. They are copied to all components which they influence.

again using the full  $d \times d$  dimensional version of  $\sigma_z^i$ . The  $m_i$  can then be fed back into Eq. (8.22) after updating the  $\hat{H}_n$  and the ground state solved self-consistently. In addition to estimating the low energy spectrum of the full system, note that this method necessarily produces the component spectra in finding the reduced basis.

### 8.3.2 Larger Networks

If the components themselves are too large for exact diagonalization, we can employ this heuristic method recursively. We observe that the component formulation produces a useful reduced basis representation of the system Hamiltonian. Note

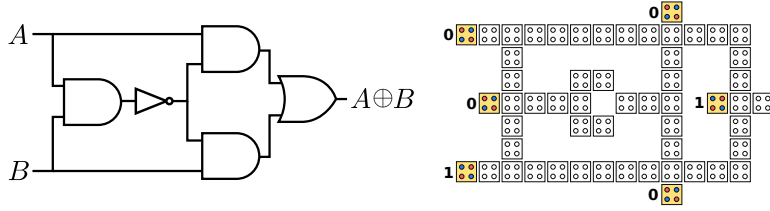


**Figure 8.3:** Circuit diagram and the equivalent 4-dot QCA network for the considered 49 cell XOR gate, not counting fixed input cells.

also that there is nothing in Eq. (8.22) that requires  $\hat{H}_n$  or  $\hat{\sigma}_z^i$  to be in their full representations, only that the  $\hat{\sigma}_z^i$  be in the same representation as their corresponding  $\hat{H}_n$ . Then for each component, we either apply exact diagonalization if the component is sufficiently small, or recursively call the CM solver to construct an appropriate reduced basis representation. This requires two additions to the CM solver: First, we must now provide both the component spectra as well as the reduced representations of the  $\hat{\sigma}_z^i$  as computed in Eq. (8.23). Second, we now require a tree of decompositions which inform the solver of how each component is further broken down into sub-components. An example of such a tree is shown in Fig. 8.2. We can apply our existing understanding of identifying decompositions here, either automatically using Eq. (8.20), or by manually specifying the decomposition. Details on the implementation of the CM solver are discussed in Appendix A.3.

### 8.3.3 Example Network

Of primary interest are relatively compact QCA networks, 10-20 cells across and perhaps 40-100 cells in total, that can be fit within a single clock zone. Most larger networks are typically just sparsely wired together combinations of such networks. As an example, we consider the 49 cell exclusive-or gate shown in Fig. 8.3 with inputs 0 and 1. Even though simple, this network is beyond exact diagonalization and of sufficient complexity for our purposes. In Fig. 8.4, we show a selection of decompositions and the corresponding low-energy spectra and objective costs. We compare against the energy gap between the ground and first excited states as computed using the DMRG implementation in ITensor v3.1.3, an open-source tensor network library [122]. For each value of  $\gamma$ , the ground and excited state were

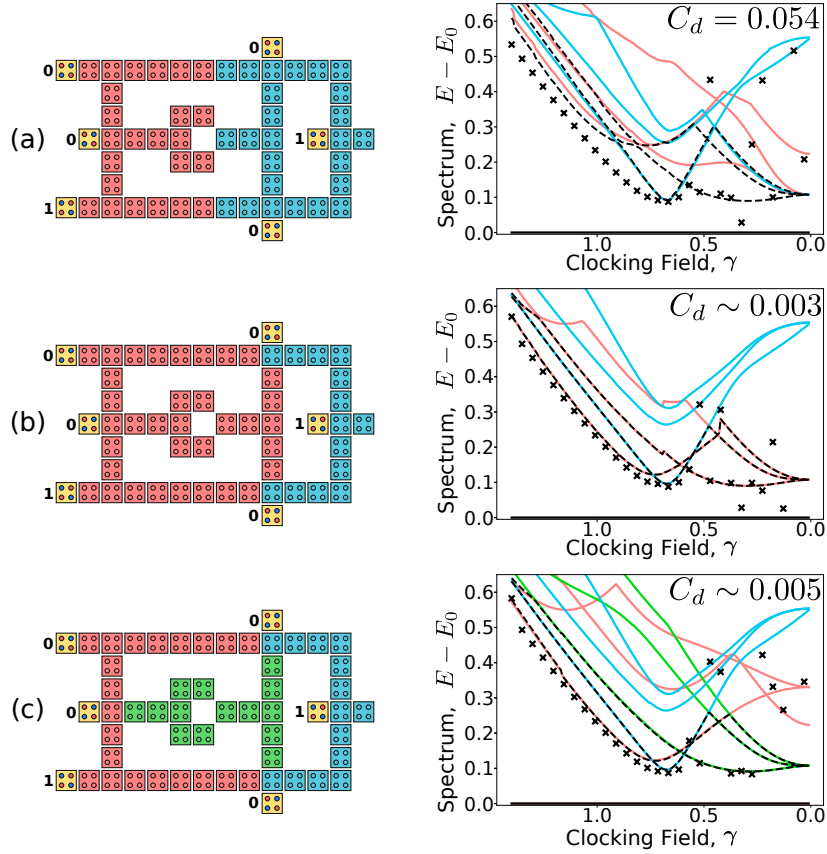


**Figure 8.4:** Sample decompositions of the XOR gate. Colours indicate both component cells and the corresponding spectra. The low energy spectrum computed using the CM solver is indicated by the dashed lines. The crosses show the first excited state as computed using a DMRG. The first 2-component decomposition in **(a)** is achieved purely using the kink energies as weights:  $w_{ij} = |E_{ij}^k|$ . The blue component fairly accurately predicts the location and value of the lowest minima. A second minima is seen in the full spectrum but is not obviously associated with either component. The ground states at the minima,  $\gamma_n \in \{0.673, 0.295\}$ , were used to compute  $C_d$ , from which we achieved the optimal 2-component decomposition shown in **(b)**. We see that the adjusted red component contributes two features: the  $\gamma \rightarrow 0$  limit, as well as part of the first minima observed in the DMRG results. This motivates a search for a 3-component decomposition. The optimum is shown in **(c)**. The particular choice of DMRG accuracy parameters used were often unable to correctly track the ground state for small  $\gamma$ , leading to the scattered values. A self-consistency limit of 0.001 was used for the CM solver, hence values of  $M_{zz}^{ij}$  and thus  $C_d$  are only reliable to that order.

retained to initialise the DMRG at the next instance. Instability in the DMRG results is apparent near the  $\gamma \rightarrow 0$  limit; however, we will see that the second lower  $\gamma$  minimum gap is expected to contribute far less towards transitions in the dynamics than the higher  $\gamma$  minimum. Verification against the DMRG results in this regime is therefore less critical. Further refining of the accuracy parameters may have resolved the instability. We observe that even using the simplest 2-component decomposition shown in Fig. 8.4(a), much of the features of the first excited state are captured assuming the DMRG results to be accurate. That being said, it is not clear that the red component spectrum predicts anything of interest. Outside of the noted instability, the ground states for both methods agreed to two decimal places. Using the minima from the CM solver as not to bias the choice in  $\gamma_n$  using the DMRG results, we identified the optimal 2-component decomposition shown in Fig. 8.4(b). The predicted minima did not change. The two observed minima in the red component spectrum motivates an optimized 3-component decomposition shown in Fig. 8.4(c). Not only do we observe close agreement between the predicted features and the DMRG results, we see clearly how each component contributes to the spectrum.

## 8.4 Estimating Transitions in the Component Mode Basis

The CM solver produces estimates of a limited subset of the low energy eigenstates. It is natural then to consider whether it possible to compute the transition parameters in order to get some idea of clocking performance. The  $T_n(s)$  require that we evaluate both  $\langle \varphi_n | \frac{d}{ds} \hat{H} | \varphi_0 \rangle$  as well as the energy gaps,  $E_n - E_0$ , for each state. While we can produce both an estimate of the eigenvalues of the system as well as the corresponding eigenstates, these eigenstates are expressed in a somewhat non-intuitive basis: a recursively defined product space of component eigenstates. It would be very useful if we could express  $\frac{d}{ds} \hat{H}$  in this same basis. Fortunately, the component mode construction both allows and requires that we maintain representations of  $\hat{\sigma}_z^i$  in the component basis. It is trivial, to keep track of  $\hat{\sigma}_x^i$  as well. The

component basis representation of  $\frac{d}{ds}\hat{H}$  is given by :

$$\frac{d}{ds}\mathbf{H} = -\frac{1}{2}\sum_i \frac{d}{ds}\gamma_i \boldsymbol{\sigma}_x^i + \frac{1}{2}\left[\sum_i \frac{d}{ds}h_i \boldsymbol{\sigma}_z^i - \sum_{\langle ij \rangle} \frac{d}{ds}E_{ij}^k \boldsymbol{\sigma}_z^i \boldsymbol{\sigma}_z^j\right]. \quad (8.26)$$

If we assume clocking via  $\gamma_i(s)$  only, then we have the simple expression

$$\langle \boldsymbol{\varphi}_m | \frac{d}{ds}\hat{H} | \boldsymbol{\varphi}_n \rangle = -\frac{1}{2}\sum_i \frac{d}{ds}\gamma_i(s) \langle \boldsymbol{\varphi}_m | \boldsymbol{\sigma}_x^i | \boldsymbol{\varphi}_n \rangle. \quad (8.27)$$

The computed transition parameters are shown in Fig. 8.5. We can also consider transitions from the perspective of the component Hamiltonians.

$$T_n^{\ell}(s) = \frac{\langle \boldsymbol{\varphi}_n^{\ell} | \frac{d}{ds}\hat{H}_{\ell} | \boldsymbol{\varphi}_0^{\ell} \rangle}{(E_n^{\ell} - E_0^{\ell})^2} \quad (8.28)$$

where  $\hat{H}_{\ell} | \boldsymbol{\varphi}_n^{\ell} \rangle = E_n^{\ell} | \boldsymbol{\varphi}_n^{\ell} \rangle$  for the  $n$ 'th eigenstate of the  $\ell$ 'th component Hamiltonian, and  $\langle \boldsymbol{\varphi}_n^{\ell} | \frac{d}{ds}\hat{H}_{\ell} | \boldsymbol{\varphi}_0^{\ell} \rangle \approx -\frac{1}{2}\sum_{i \in \mathcal{S}_{\ell}} \frac{d}{ds}\gamma_i(s) \langle \boldsymbol{\varphi}_n^{\ell} | \boldsymbol{\sigma}_x^i | \boldsymbol{\varphi}_0^{\ell} \rangle$ . The results are included in Fig. 8.5(b). We see that the transition parameters computed using the component spectra almost perfectly reproduce those of the full spectrum. This should not be surprising as we have chosen our decomposition such that the first excited state is approximately a product state with all but one of the components in the ground state. Transitions from the ground state to the excited state should exactly correspond to transition from the ground state of that component to its excited state. The only exceptions occur near crossings between the component spectra, in which case the full system eigenstates tend to be superpositions of the crossing states.

We do not include dynamics calculations here; however, it is possible also to directly compute the dynamics using the reduced basis approach used in Section 6.2.3. In the component mode basis, we have

$$\frac{d}{ds}c_n \approx -\sum_{m \neq n} c_m \frac{\langle \boldsymbol{\varphi}_n | \frac{d}{ds}\mathbf{H} | \boldsymbol{\varphi}_m \rangle}{E_m - E_n} e^{-i(\theta_m - \theta_n)/\bar{J}} \quad (8.29)$$

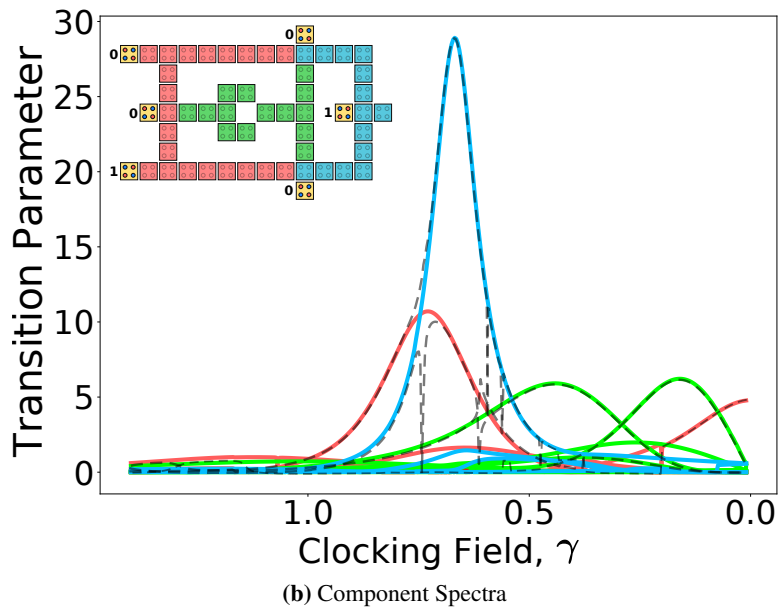
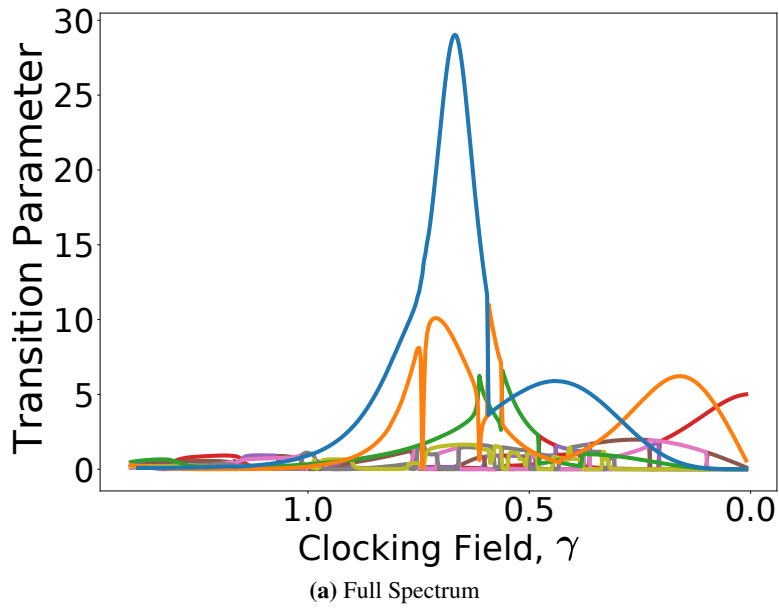


**Figure 8.5:** Estimates of the transition parameters for the 49 cell XOR gate. Assumes a linear schedule with  $\frac{1}{2} \frac{d}{ds} \gamma_i(s) = -1$ . The multiple crossings among higher energy states in the full spectrum lead to rapid changes in some of the parameters. In (b), we consider the transition parameters computed using only the component spectra. Values for the lowest energy states in (a) are overlaid for comparison.

## 8.5 Component Substitution

For a given network decomposition, we can consider the effect of altering the design of one of the components. As an example, suppose we substituted the inverter component in the XOR gate with another symmetric variant, as in Fig. 8.6(a). There are a few points to consider here. Firstly, if the component substitution does not significantly change the mean fields of the cells at the component interfaces throughout the full range of clocking parameters, then the component spectra of all other components should remain approximately unchanged. Secondly, if the decomposition remains of high quality, having a small value of  $C_d$ , after the substitution, then any changes to the component spectrum for the new inverter should correspond to changes in the full spectrum. We can see both of these effects in the computed spectra in Fig. 8.6(b), with the transition parameters computed in Fig. 8.6(c). This simple observation suggests a potential strategy for targeting weaknesses in designs and making systematic improvements.

## 8.6 Application to Alternate QCA Models

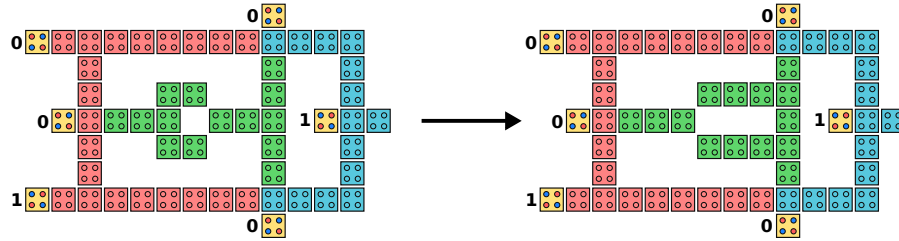
The effectiveness of the decomposition method and heuristic solver arise due to the sparsity of the network connectivity graphs and expected limited correlations. There is nothing special about our focus on 2-state QCA or even our use of zone clocking. Here we briefly discuss the other common model for QCA devices, the 3-state QCA, as well as an important consideration for dynamic wave clocking.

### 8.6.1 Modifications for 3-State QCA

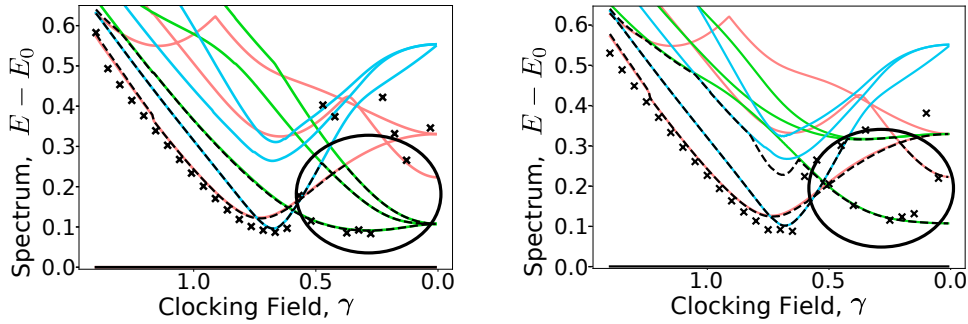
For the  $N$  device Hamiltonian in the 3-state approximation, Section 5.1, a similar analysis to Section 8.1 will reveal that we should replace  $h_i$  and  $\mu_i$  in the component Hamiltonians with effective parameters

$$\tilde{h}_i = h_i - \sum_{\ell \neq i} \sum_{j \in \mathcal{S}_\ell} E_{ij}^k \mathcal{P}_j, \quad (8.30a)$$

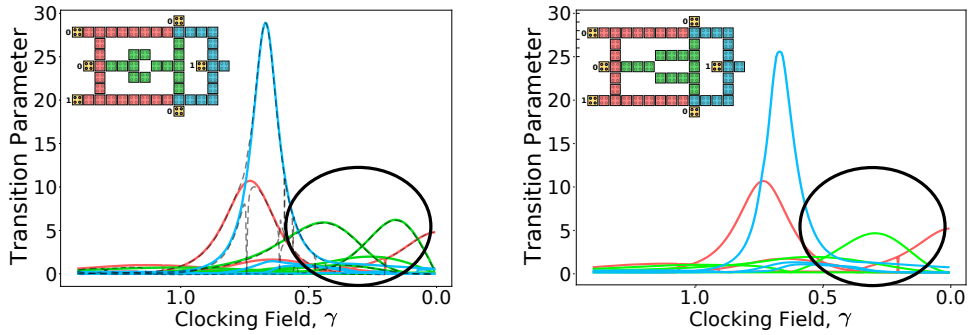
$$\tilde{\mu}_i = \mu_i + \sum_{\ell \neq i} \sum_{j \in \mathcal{S}_\ell} \mathcal{D}_{ij} \mathcal{N}_j, \quad (8.30b)$$



(a) Substitution of the inverting component in the XOR gate.



(b) Resulting change in the low energy spectrum and component spectra.



(c) Change in the transition parameters

**Figure 8.6:** Change in the low energy spectra and transition parameters associated with substituting the inverting element in the green component with an alternate variant. Regions of interest are highlighted. In this particular case, there is a slight increase in the minimum gap associated with the blue component. This results in a decrease in the corresponding transition peak.

where  $\mathcal{P}_i = \langle \hat{\mathcal{P}}_i \rangle$  and  $\mathcal{N}_i = \langle \hat{\mathcal{N}}_i \rangle$  are the mean fields. The component coupling operators are just

$$\begin{aligned} \hat{\mathcal{M}}_{\mathcal{R}\ell} = & -\frac{1}{2} \sum_{i \in \mathcal{S}_{\mathcal{R}}} \sum_{j \in \mathcal{S}_{\ell}} E_{ij}^k (\hat{\mathcal{P}}_i - \mathcal{P}_i) (\hat{\mathcal{P}}_j - \mathcal{P}_j) \\ & + \sum_{i \in \mathcal{S}_{\mathcal{R}}} \sum_{j \in \mathcal{S}_{\ell}} \mathcal{D}_{ij} (\hat{\mathcal{N}}_i - \mathcal{N}_i) (\hat{\mathcal{N}}_j - \mathcal{N}_j) + \text{const.} \end{aligned} \quad (8.31)$$

For component decomposition, the appropriate objective function is

$$C(\{\mathcal{S}_{\mathcal{R}}\}) = \left| \sum_{\langle \mathcal{R}\ell \rangle} \sum_{i \in \mathcal{S}_{\mathcal{R}}} \sum_{j \in \mathcal{S}_{\ell}} \left( E_{ij}^k M_{PP}^{ij} - 2\mathcal{D}_{ij} M_{NN}^{ij} \right) \right|, \quad (8.32)$$

with  $M_{PP}^{ij} = \langle \hat{\mathcal{P}}_i \hat{\mathcal{P}}_j \rangle - \mathcal{P}_i \mathcal{P}_j$  and  $M_{NN}^{ij} = \langle \hat{\mathcal{N}}_i \hat{\mathcal{N}}_j \rangle - \mathcal{N}_i \mathcal{N}_j$ . The details of network decomposition and the heuristic method are otherwise analogous.

## 8.6.2 Dynamic Wave Clocking

The dynamic objective function Eq. (8.21) applies perfectly well in the case where the clocking fields are cell specific. The primary challenge here is that wave clocking does not employ clock zones, and importantly lacks the discrete boundaries between those zones. In zone clocking, we can limit the set of cells to be considered to those within a single clock zone. Cells in adjacent zones either experience relatively high or relatively low clocking fields, and thus do not significantly change their state as the current zone is clocked. As a result, they are effectively just biases. Neither the CM solver nor DMRG will cope well with potentially thousands of cells in the entire QCA network for some of the larger designs. For wave clocking, we can still keep the idea of a finite set of relevant cells; however, that set evolves as the clocking wave travels. Efficiently computing the spectra then likely requires a strategy that tracks the set of cells within the rising edge of the clocking wave that cannot be assumed to serve only as biases. One simple approach would be to include cells once their clocking fields surpass some threshold value, and set them as biases once their polarization in the estimated ground state surpasses some magnitude. Further investigation would be needed.

## 8.7 Summary

In this chapter, we have produced two significant results. The main goal of our investigation was to demonstrate that important features of the low energy spectrum can be attributed to individual components of the network. We established one way to identify these critical components when the spectrum is known. This form of decomposition is useful from a design perspective as it allows us to directly link overall weaknesses in the network performance with individual choices in components. Future research may provide new design rules based on selecting components which optimize features in the spectrum. The second result was the formulation of the CM solver, which naturally emerges from the component decomposition. It has proved promising for approximating the low energy spectrum of larger networks, where exact diagonalization of the system Hamiltonian is infeasible. We were able to extract the necessary parameters,  $\langle \varphi_n | \frac{d}{ds} \hat{\mathcal{H}} | \varphi_m \rangle$ , for estimating diabatic transitions efficiently in the component mode basis. This potentially allows estimation of clocking performance for large QCA networks.

## Chapter 9

# Conclusion and Future Work

Nanoscale implementations of QCA offer the potential for high frequency, low power computation beyond the limits of conventional CMOS. However, at such small dimensions, additional challenges emerge. One such challenge is the need to simulate the behaviour of large numbers of devices. In the limit of full coherence, this can mean manipulating quantum states with exponentially many variables, seemingly possible only for small networks. The contributions of this thesis can be broadly split into two related categories: (1) modelling the behaviour of clocked SiDB arrangements and investigating their suitability as a platform for nanoscale QCA, and (2), a study of QCA clocking from the perspective of quantum annealing, ultimately determining how details about the low energy eigenspectrum during clocking relate to QCA performance.

### 9.1 SiDBs as a Platform for Nanoscale QCA

In Chapter 4, we discussed simple models which reproduce observed behaviour in fabricated SiDBs. This included an understanding of the preferred charge states taken on by arrangements of SiDBs as a constrained energy optimization problem, as well as a hopping model for the slow dynamics observed when charges are shared between degenerate sites. SiQAD, a CAD tool for designing and simulating SiDB arrangements, emerged as an attempt both to understand existing experimental results, as well as to predict and study new designs, such as potential

SiDB-based QCA implementations. This tool was made open source with the aim to promote efforts in exploring the design space, as well as to develop additional simulation engines and design tools. Using clocking electrodes, the electric potential at the surface can be manipulated, producing controllable band-bending in regions of SiDBs. This allows for a population-based clocking scheme, where SiDB devices are deactivated by inducing upward band-bending. When this method was applied to SiDB-based QCA wires, a complicated trajectory of preferred configurations was revealed, with devices populating out-of-order.

In Chapter 5, we studied this out-of-order population from the familiar terrain of 3-state QCA, with preferred charge configurations becoming ground states of a 3-state Hamiltonian with strong congestion interactions. In this framework, a change in the preferred configuration translates to an avoided level crossing between the current ground and first excited states. We ultimately determined that if we assume SiDB-based QCA devices to be net-negative when activated, and only consider tunneling between the SiDBs and null sites (bulk), then even wire operation may be a challenge. Familiar designs for logic gates such as majority gates would likely need to be replaced with SiDB-specific arrangements. If, in the future, it is demonstrated that net-neutral SiDB devices can be implemented, potentially using both DB- and DB+ states, then SiDB-based QCA may be more feasible. Inclusion of a tunneling energy between the SiDBs may also be of interest.

## **9.2 Estimating QCA Performance using the Low Energy Spectrum**

Much progress has been previously made in understanding the dynamics of QCA networks. Use of the ICHA, though computationally efficient, results in an approach to QCA design and clock zone selection which is not practical for the relative dimensions of clocking electrodes in nanoscale QCA. Intermediate models including additional inter-cell correlations have shown some success in more closely reproducing the behaviour of the full quantum treatment; however, there remain challenges which have yet to be resolved. In this thesis we took a different approach by establishing the importance of the low energy spectrum in understanding the behaviour of QCA networks. Previously, the spectrum has been used to

justify reduced basis approximations [43], and more recently in discussing adiabatic switching of individual QCA cells [93]. This work aims to position the study of the energy spectrum as an essential tool for assessing the behaviour of QCA designs.

Chapter 6 served as a demonstration for some useful applications of the spectrum for small QCA networks. First, we established criteria for the shape of the clocking profile in order to increase adiabaticity. These ideas were based on properties of the resulting ground state and early dynamics. An analytical model for biased QCA wires in the 2-state approximation was presented and used to demonstrate that zone-clocked QCA wires beyond a few cells adhere to a simple Landau-Zener model. We compared estimates of threshold clocking frequencies beyond which performance suffered. Merely looking at the eigenenergies was not sufficient to accurately predict performance with the exception of the wire; however, by incorporating the values of  $\langle \phi_m | \frac{d}{ds} \hat{\mathcal{H}} | \phi_n \rangle$ , we achieved high accuracy using only the lowest few energy eigenstates. This demonstrates that once the spectrum is known, the dynamics can be efficiently simulated. This left the challenge of efficiently computing the spectrum.

The parallels between QCA zone clocking and quantum annealing on the QPU developed by D-Wave Systems Inc. presented an obvious potential method for directly studying the performance of clocked QCA without being limited by computational resources; however, a number of as yet unresolved challenges became clear. The main obstacle is in understanding how the particular choice of embedding changes the spectrum, and ultimate the effective dynamics of the original QCA network. In the cases where this change was minimal, we observe evidence of diabatic transitions likely resulting from coupling with the environment. This highlights an important point which should be addressed. The claim is often made in the QCA literature that as the nearest-neighbour kink energies for nanoscale QCA lie above 25 meV, operation at room temperature should be possible without suffering from thermal excitations. There are a couple of contentions we see from the experimental annealing results. First, the kink energies may give a measure of the gap between the ground and first excited states in the classical limit, but we see from the spectra that the actual minimum gap during clocking can easily be an order of magnitude smaller. Further, even in the case where the minimum

gaps lie above the thermal energy, as is the case for the embedded majority gate in Fig. 7.15, as the annealing time is increased we still see evidence of weak but non-negligible thermal excitations. More work is needed, both in order to improve the agreement between the spectra of the original and embedded network but also in order to determine if there is any mapping between the diabatic mechanisms exhibited by the QPU and those in any particular implementation of QCA.

The final contribution was in attempting to address the need for understanding the spectra of large QCA networks. This investigation simultaneously touched on the question of how we might study the behaviour of large QCA circuits through knowledge of individual components. We established a method for decomposing the system Hamiltonian into contributions from a given set of components, and a means to identify components which contribute important features to the spectrum. This result is primarily significant in that it will allow researchers to identify important sub-circuits which significantly impact performance. This may stimulate research into design rules which optimize these critical components. The component formulation naturally led to a heuristic approach for estimating the low energy spectrum of large QCA networks, particularly in such a way that the terms needed for estimating dynamics using a limited subset of the energy eigenstates are efficient to compute. There are a number of open questions here. First, the current implementation leaves the decomposition only semi-automated, still requiring some familiarity and guesswork in order to converge on the optimal decomposition. A more robust method is needed, potentially also addressing the necessary challenge of signed graph partitioning. Dynamic wave clocking remains a conceptual challenge from the perspective of analysing the low energy spectrum. It is clear that only a relatively small subset of the network contributes to the dynamics at any give time; however, the exact approach to efficiently implement either the component mode solver or the decomposition method is not immediately clear.

# Bibliography

- [1] M. Rashidi, W. Vine, T. Dienel, L. Livadaru, J. Retallick, T. Huff, K. Walus, and R. A. Wolkow, “Initiating and monitoring the evolution of single electrons within atom-defined structures,” *Phys. Rev. Lett.*, vol. 121, p. 166801, Oct 2018.
- [2] S. S. H. Ng, J. Retallick, H. N. Chiu, R. Lupoiu, L. Livadaru, T. Huff, M. Rashidi, W. Vine, T. Dienel, R. A. Wolkow, and K. Walus, “SiQAD: A design and simulation tool for atomic silicon quantum dot circuits,” *IEEE Transactions on Nanotechnology*, vol. 19, pp. 137–146, 2020.
- [3] H. N. Chiu, S. S. H. Ng, J. Retallick, and K. Walus, “PoisSolver: a tool for modelling silicon dangling bond clocking networks,” in *2020 IEEE 20th International Conference on Nanotechnology (IEEE-NANO)*. IEEE, Jul. 2020, pp. 134–139.
- [4] J. Retallick and K. Walus, “Population congestion in 3-state quantum-dot cellular automata,” *Journal of Applied Physics*, vol. 127, no. 24, p. 244301, 2020.
- [5] J. Retallick and K. Walus, “Limits of adiabatic clocking in quantum-dot cellular automata,” *Journal of Applied Physics*, vol. 127, no. 5, p. 054502, 2020.
- [6] J. Retallick, M. Babcock, M. Aroca-Ouellette, S. McNamara, S. Wilton, A. Roy, M. Johnson, and K. Walus, “Embedding of quantum-dot cellular automata circuits onto a quantum annealing processor,” in *2014 Conference on Optoelectronic and Microelectronic Materials & Devices*. IEEE, Dec. 2014.
- [7] J. Retallick, M. Babcock, M. Aroca-Ouellette, S. McNamara, S. Wilton, A. Roy, M. Johnson, and K. Walus, “Algorithms for embedding quantum-dot cellular automata networks onto a quantum annealing processor,” 2017.

- [8] J. Retallick and K. Walus, “Investigation of quantum-dot cellular automata networks using a quantum annealing processor,” Presented at the 253rd ACS National Meeting, San Francisco, USA, Apr. 2017.
- [9] J. Retallick and K. Walus, “Low-energy eigenspectrum decomposition (LEED) of quantum-dot cellular automata networks,” *submitted for publication*, 2020.
- [10] A. Nourbakhsh, A. Zubair, R. N. Sajjad, A. Tavakkoli K. G., W. Chen, S. Fang, X. Ling, J. Kong, M. S. Dresselhaus, E. Kaxiras, K. K. Berggren, D. Antoniadis, and T. Palacios, “MoS<sub>2</sub> field-effect transistor with sub-10 nm channel length,” *Nano Letters*, vol. 16, no. 12, pp. 7798–7806, Dec 2016.
- [11] C. Qiu, Z. Zhang, M. Xiao, Y. Yang, D. Zhong, and L.-M. Peng, “Scaling carbon nanotube complementary transistors to 5-nm gate lengths,” *Science*, vol. 355, no. 6322, pp. 271–276, 2017.
- [12] D. Bhowmik, L. You, and S. Salahuddin, “Spin hall effect clocking of nanomagnetic logic without a magnetic field,” *Nature Nanotechnology*, vol. 9, pp. 59 EP –, Nov 2013.
- [13] X. Fong, Y. Kim, K. Yogendra, D. Fan, A. Sengupta, A. Raghunathan, and K. Roy, “Spin-transfer torque devices for logic and memory: Prospects and perspectives,” *IEEE Transactions on Computer-Aided Design of Integrated Circuits and Systems*, vol. 35, no. 1, pp. 1–22, Jan 2016.
- [14] R. A. Wolkow, L. Livadaru, J. Pitters, M. Taucer, P. Piva, M. Salomons, M. Cloutier, and B. V. C. Martins, *Silicon Atomic Quantum Dots Enable Beyond-CMOS Electronics*. Berlin, Heidelberg: Springer Berlin Heidelberg, 2014, pp. 33–58.
- [15] C. S. Lent, P. D. Tougaw, W. Porod, and G. H. Bernstein, “Quantum cellular automata,” *Nanotechnology*, vol. 4, no. 1, pp. 49–57, Jan 1993.
- [16] P. D. Tougaw and C. S. Lent, “Logical devices implemented using quantum cellular automata,” *Journal of Applied Physics*, vol. 75, no. 3, pp. 1818–1825, 1994.
- [17] I. Amlani, A. O. Orlov, G. Toth, G. H. Bernstein, C. S. Lent, and G. L. Snider, “Digital logic gate using quantum-dot cellular automata,” *Science*, vol. 284, no. 5412, pp. 289–291, 1999.

- [18] A. O. Orlov, I. Amlani, G. H. Bernstein, C. S. Lent, and G. L. Snider, "Realization of a functional cell for quantum-dot cellular automata," *Science*, vol. 277, no. 5328, pp. 928–930, 1997.
- [19] G. L. Snider, A. O. Orlov, I. Amlani, G. H. Bernstein, C. S. Lent, J. L. Merz, and W. Porod, "Quantum-dot cellular automata: Line and majority logic gate," *Japanese Journal of Applied Physics*, vol. 38, no. Part 1, No. 12B, pp. 7227–7229, Dec. 1999.
- [20] G. Tóth and C. S. Lent, "Quasiadiabatic switching for metal-island quantum-dot cellular automata," *Journal of Applied Physics*, vol. 85, no. 5, pp. 2977–2984, 1999.
- [21] A. O. Orlov, R. Kumamuru, R. Ramasubramaniam, C. S. Lent, G. H. Bernstein, and G. L. Snider, "Clocked quantum-dot cellular automata shift register," *Surface Science*, vol. 532–535, pp. 1193–1198, Jun. 2003.
- [22] R. P. Cowburn, "Room temperature magnetic quantum cellular automata," *Science*, vol. 287, no. 5457, pp. 1466–1468, Feb. 2000.
- [23] G. Csaba, A. Imre, G. Bernstein, W. Porod, and V. Metlushko, "Nanocomputing by field-coupled nanomagnets," *IEEE Transactions on Nanotechnology*, vol. 1, no. 4, pp. 209–213, Dec. 2002.
- [24] A. Imre, "Majority logic gate for magnetic quantum-dot cellular automata," *Science*, vol. 311, no. 5758, pp. 205–208, Jan. 2006.
- [25] C. S. Lent, B. Isaksen, and M. Lieberman, "Molecular quantum-dot cellular automata," *Journal of the American Chemical Society*, vol. 125, no. 4, pp. 1056–1063, 2003, pMID: 12537505.
- [26] J. A. Christie, R. P. Forrest, S. A. Corcelli, N. A. Wasio, R. C. Quardokus, R. Brown, S. A. Kandel, Y. Lu, C. S. Lent, and K. W. Henderson, "Synthesis of a neutral mixed-valence diferrocenyl carborane for molecular quantum-dot cellular automata applications," *Angewandte Chemie International Edition*, vol. 54, no. 51, pp. 15 448–15 451, 2015.
- [27] M. B. Haider, J. L. Pitters, G. A. DiLabio, L. Livadaru, J. Y. Mutus, and R. A. Wolkow, "Controlled coupling and occupation of silicon atomic quantum dots at room temperature," *Phys. Rev. Lett.*, vol. 102, p. 046805, Jan 2009.

- [28] T. Huff, H. Labidi, M. Rashidi, L. Livadaru, T. Diemel, R. Achal, W. Vine, J. Pitters, and R. A. Wolkow, “Binary atomic silicon logic,” *Nature Electronics*, vol. 1, no. 12, pp. 636–643, 2018.
- [29] J. Timler and C. S. Lent, “Power gain and dissipation in quantum-dot cellular automata,” *Journal of Applied Physics*, vol. 91, no. 2, pp. 823–831, 2002.
- [30] C. S. Lent, M. Liu, and Y. Lu, “Bennett clocking of quantum-dot cellular automata and the limits to binary logic scaling,” *Nanotechnology*, vol. 17, no. 16, pp. 4240–4251, aug 2006.
- [31] D. Abedi, G. Jaberipur, and M. Sangsefidi, “Coplanar full adder in quantum-dot cellular automata via clock-zone-based crossover,” *IEEE Transactions on Nanotechnology*, vol. 14, no. 3, pp. 497–504, May 2015.
- [32] C. A. T. Campos, A. L. Marciano, O. P. Vilela Neto, and F. S. Torres, “USE: A universal, scalable, and efficient clocking scheme for qca,” *IEEE Transactions on Computer-Aided Design of Integrated Circuits and Systems*, vol. 35, no. 3, pp. 513–517, March 2016.
- [33] E. Blair and C. Lent, “Clock topologies for molecular quantum-dot cellular automata,” *Journal of Low Power Electronics and Applications*, vol. 8, no. 3, 2018.
- [34] K. Walus, T. J. Dysart, G. A. Jullien, and R. A. Budiman, “QCADesigner: a rapid design and simulation tool for quantum-dot cellular automata,” *IEEE Transactions on Nanotechnology*, vol. 3, no. 1, pp. 26–31, March 2004.
- [35] C. S. Lent and P. D. Tougaw, “Lines of interacting quantum-dot cells: A binary wire,” *Journal of Applied Physics*, vol. 74, no. 10, pp. 6227–6233, 1993.
- [36] G. Tóth and C. S. Lent, “Role of correlation in the operation of quantum-dot cellular automata,” *Journal of Applied Physics*, vol. 89, no. 12, pp. 7943–7953, 2001.
- [37] K. Hennessy and C. S. Lent, “Clocking of molecular quantum-dot cellular automata,” *Journal of Vacuum Science & Technology B: Microelectronics and Nanometer Structures Processing, Measurement, and Phenomena*, vol. 19, no. 5, pp. 1752–1755, 2001.

- [38] V. Vankamamidi, M. Ottavi, and F. Lombardi, “Two-dimensional schemes for clocking/timing of QCA circuits,” *IEEE Transactions on Computer-Aided Design of Integrated Circuits and Systems*, vol. 27, no. 1, pp. 34–44, Jan. 2008.
- [39] E. Sicard, “Introducing 14-nm FinFET technology in Microwind,” Jun. 2017.
- [40] G. Tóth, “Correlation and coherence in quantum-dot cellular automata,” Ph.D. dissertation, 2000, copyright - Database copyright ProQuest LLC; ProQuest does not claim copyright in the individual underlying works; Last updated - 2019-10-17.
- [41] F. Karim, “Investigation of the correlated dynamics of quantum-dot cellular automata circuits and systems,” Ph.D. dissertation, University of British Columbia, 2014.
- [42] F. Karim and K. Walus, “Efficient simulation of correlated dynamics in quantum-dot cellular automata (qca),” *IEEE Transactions on Nanotechnology*, vol. 13, no. 2, pp. 294–307, March 2014.
- [43] P. D. Tougaw and C. S. Lent, “Dynamic behavior of quantum cellular automata,” *Journal of Applied Physics*, vol. 80, no. 8, pp. 4722–4736, 1996.
- [44] C. Lanczos, “An iteration method for the solution of the eigenvalue problem of linear differential and integral operators,” *Journal of Research of the National Bureau of Standards*, vol. 45, no. 3, pp. 255–282, 10 1950.
- [45] G. Mahler and V. A. Weberruß, *Quantum Networks*. Springer Berlin Heidelberg, 1998.
- [46] E. Farhi, J. Goldstone, S. Gutmann, J. Lapan, A. Lundgren, and D. Preda, “A quantum adiabatic evolution algorithm applied to random instances of an NP-complete problem,” *Science*, vol. 292, no. 5516, pp. 472–475, Apr. 2001.
- [47] E. Farhi, J. Goldstone, S. Gutmann, and M. Sipser, “Quantum computation by adiabatic evolution,” 2000.
- [48] M. Born and V. Fock, “Beweis des adiabatsatzes,” *Zeitschrift für Physik*, vol. 51, no. 3, pp. 165–180, Mar 1928.
- [49] W. Vinci and D. A. Lidar, “Non-stoquastic hamiltonians in quantum annealing via geometric phases,” *npj Quantum Information*, vol. 3, no. 1, Sep. 2017.

- [50] T. Kadowaki and H. Nishimori, “Quantum annealing in the transverse ising model,” *Physical Review E*, vol. 58, no. 5, pp. 5355–5363, Nov. 1998.
- [51] G. E. Santoro, R. Martoňák, E. Tosatti, and R. Car, “Theory of quantum annealing of an ising spin glass,” *Science*, vol. 295, no. 5564, pp. 2427–2430, 2002.
- [52] A. Das and B. K. Chakrabarti, “Colloquium: Quantum annealing and analog quantum computation,” *Rev. Mod. Phys.*, vol. 80, pp. 1061–1081, Sep 2008.
- [53] J. Brooke, T. F. Rosenbaum, and G. Aeppli, “Tunable quantum tunnelling of magnetic domain walls,” *Nature*, vol. 413, no. 6856, pp. 610–613, Oct. 2001.
- [54] M. W. Johnson, M. H. S. Amin, S. Gildert, T. Lanting, F. Hamze, N. Dickson, R. Harris, A. J. Berkley, J. Johansson, P. Bunyk, E. M. Chapple, C. Enderud, J. P. Hilton, K. Karimi, E. Ladizinsky, N. Ladizinsky, T. Oh, I. Perminov, C. Rich, M. C. Thom, E. Tolkacheva, C. J. S. Truncik, S. Uchaikin, J. Wang, B. Wilson, and G. Rose, “Quantum annealing with manufactured spins,” *Nature*, vol. 473, no. 7346, pp. 194–198, May 2011.
- [55] S. Morita and H. Nishimori, “Mathematical foundation of quantum annealing,” *Journal of Mathematical Physics*, vol. 49, no. 12, p. 125210, Dec. 2008.
- [56] W. van Dam, M. Mosca, and U. Vazirani, “How powerful is adiabatic quantum computation?” in *Proceedings 42nd IEEE Symposium on Foundations of Computer Science*. IEEE, 2001.
- [57] L. D. Landau, “Zur theorie der energieübertragung. II,” *Physikalische Zeitschrift der Sowjetunion*, vol. 2, pp. 46–51, 1932.
- [58] C. Zener and R. H. Fowler, “Non-adiabatic crossing of energy levels,” *Proceedings of the Royal Society of London. Series A, Containing Papers of a Mathematical and Physical Character*, vol. 137, no. 833, pp. 696–702, 1932.
- [59] G. A. Kochenberger, F. Glover, B. Alidaee, and C. Rego, “An unconstrained quadratic binary programming approach to the vertex coloring problem,” *Annals of Operations Research*, vol. 139, no. 1, pp. 229–241, Oct. 2005.
- [60] R. Martoňák, G. E. Santoro, and E. Tosatti, “Quantum annealing of the traveling-salesman problem,” *Physical Review E*, vol. 70, no. 5, Nov. 2004.

- [61] A. Perdomo-Ortiz, N. Dickson, M. Drew-Brook, G. Rose, and A. Aspuru-Guzik, “Finding low-energy conformations of lattice protein models by quantum annealing,” 2012.
- [62] A. Lucas, “Ising formulations of many NP problems,” *Frontiers in Physics*, vol. 2, 2014.
- [63] S. Jiang, K. A. Britt, A. J. McCaskey, T. S. Humble, and S. Kais, “Quantum annealing for prime factorization,” *Scientific Reports*, vol. 8, no. 1, Dec. 2018.
- [64] G. Kochenberger, J.-K. Hao, F. Glover, M. Lewis, Z. Lü, H. Wang, and Y. Wang, “The unconstrained binary quadratic programming problem: a survey,” *Journal of Combinatorial Optimization*, vol. 28, no. 1, pp. 58–81, Apr. 2014.
- [65] M. Anthony, E. Boros, Y. Crama, and A. Gruber, “Quadratic reformulations of nonlinear binary optimization problems,” *Mathematical Programming*, vol. 162, no. 1-2, pp. 115–144, Jun. 2016.
- [66] R. B. Stinchcombe, “Ising model in a transverse field. i. basic theory,” *Journal of Physics C: Solid State Physics*, vol. 6, no. 15, pp. 2459–2483, aug 1973.
- [67] M. W. Johnson, P. Bunyk, F. Maibaum, E. Tolkacheva, A. J. Berkley, E. M. Chapple, R. Harris, J. Johansson, T. Lanting, I. Perminov, E. Ladizinsky, T. Oh, and G. Rose, “A scalable control system for a superconducting adiabatic quantum optimization processor,” *Superconductor Science and Technology*, vol. 23, no. 6, p. 065004, Apr. 2010.
- [68] T. R. Huff, H. Labidi, M. Rashidi, M. Koleini, R. Achal, M. H. Salomons, and R. A. Wolkow, “Atomic white-out: Enabling atomic circuitry through mechanically induced bonding of single hydrogen atoms to a silicon surface,” *ACS Nano*, vol. 11, no. 9, pp. 8636–8642, Jul. 2017.
- [69] N. Pavliček, Z. Majzik, G. Meyer, and L. Gross, “Tip-induced passivation of dangling bonds on hydrogenated si(100)-2 × 1,” *Applied Physics Letters*, vol. 111, no. 5, p. 053104, Jul. 2017.
- [70] R. Achal, M. Rashidi, J. Croshaw, D. Churchill, M. Taucer, T. Huff, M. Cloutier, J. Pitters, and R. A. Wolkow, “Lithography for robust and editable atomic-scale silicon devices and memories,” *Nature Communications*, vol. 9, no. 1, Jul. 2018.

- [71] J. W. Lyding, T.-C. Shen, J. S. Hubacek, J. R. Tucker, and G. C. Abeln, “Nanoscale patterning and oxidation of h-passivated si(100)-2×1 surfaces with an ultrahigh vacuum scanning tunneling microscope,” *Applied Physics Letters*, vol. 64, no. 15, pp. 2010–2012, Apr. 1994.
- [72] T. C. Shen, C. Wang, G. C. Abeln, J. R. Tucker, J. W. Lyding, P. Avouris, and R. E. Walkup, “Atomic-scale desorption through electronic and vibrational excitation mechanisms,” *Science*, vol. 268, no. 5217, pp. 1590–1592, Jun. 1995.
- [73] E. T. Foley, A. F. Kam, J. W. Lyding, and P. Avouris, “Cryogenic UHV-STM study of hydrogen and deuterium desorption from si(100),” *Physical Review Letters*, vol. 80, no. 6, pp. 1336–1339, Feb. 1998.
- [74] M. Smeu, H. Guo, W. Ji, and R. A. Wolkow, “Electronic properties of si(111)-7 × 7 and related reconstructions: Density functional theory calculations,” *Phys. Rev. B*, vol. 85, p. 195315, May 2012.
- [75] P. Scherpelz and G. Galli, “Optimizing surface defects for atomic-scale electronics: Si dangling bonds,” *Phys. Rev. Materials*, vol. 1, p. 021602, Jul 2017.
- [76] M. Rashidi, E. Lloyd, T. R. Huff, R. Achal, M. Taucer, J. J. Croshaw, and R. A. Wolkow, “Resolving and tuning carrier capture rates at a single silicon atom gap state,” *ACS Nano*, vol. 11, no. 11, pp. 11 732–11 738, Nov. 2017.
- [77] H. Labidi, M. Taucer, M. Rashidi, M. Koleini, L. Livadaru, J. Pitters, M. Cloutier, M. Salomons, and R. A. Wolkow, “Scanning tunneling spectroscopy reveals a silicon dangling bond charge state transition,” *New Journal of Physics*, vol. 17, no. 7, p. 073023, jul 2015.
- [78] T. R. Huff, T. Dienel, M. Rashidi, R. Achal, L. Livadaru, J. Croshaw, and R. A. Wolkow, “Electrostatic landscape of a hydrogen-terminated silicon surface probed by a moveable quantum dot,” *ACS Nano*, vol. 13, no. 9, pp. 10 566–10 575, 2019, PMID: 31386340.
- [79] L. Livadaru, P. Xue, Z. Shaterzadeh-Yazdi, G. A. DiLabio, J. Mutus, J. L. Pitters, B. C. Sanders, and R. A. Wolkow, “Corrigendum: Dangling-bond charge qubit on a silicon surface (2010 new j. phys. 12 083018),” *New Journal of Physics*, vol. 19, no. 11, p. 119501, Nov. 2017.
- [80] Z. Shaterzadeh-Yazdi, “Coherence of coupled dangling-bond pairs on the silicon surface,” Ph.D. dissertation, University of Calgary, 2014.

- [81] M. Rashidi, J. A. J. Burgess, M. Taucer, R. Achal, J. L. Pitters, S. Loth, and R. A. Wolkow, “Time-resolved single dopant charge dynamics in silicon,” *Nature Communications*, vol. 7, no. 1, Oct. 2016.
- [82] S. S. H. Ng, “Computer-aided design of atomic silicon quantum dots and computational applications,” Master’s thesis, University of British Columbia, 2020.
- [83] J. L. Pitters, I. A. Dogel, and R. A. Wolkow, “Charge control of surface dangling bonds using nanoscale schottky contacts,” *ACS Nano*, vol. 5, no. 3, pp. 1984–1989, Feb. 2011.
- [84] N. Apsley and H. P. Hughes, “Temperature-and field-dependence of hopping conduction in disordered systems,” *Philosophical Magazine*, vol. 30, no. 5, pp. 963–972, Nov. 1974.
- [85] R. A. Marcus, “Electron transfer reactions in chemistry. theory and experiment,” *Reviews of Modern Physics*, vol. 65, no. 3, pp. 599–610, Jul. 1993.
- [86] Qt C++ framework. The Qt Company. <https://www.qt.io>.
- [87] E. P. Blair, M. Liu, and C. S. Lent, “Signal energy in quantum-dot cellular automata bit packets,” *Journal of Computational and Theoretical Nanoscience*, vol. 8, no. 6, pp. 972–982, 2011.
- [88] Y. Lu, M. Liu, and C. Lent, “Molecular quantum-dot cellular automata: From molecular structure to circuit dynamics,” *Journal of applied physics*, vol. 102, no. 3, p. 034311, 2007.
- [89] E. Blair, “Electric-field inputs for molecular quantum-dot cellular automata circuits,” *IEEE Trans. Nanotechnol.*, vol. 18, p. 453–460, May 2019.
- [90] F. Karim, K. Walus, and A. Ivanov, “Analysis of field-driven clocking for molecular quantum-dot cellular automata based circuits,” *Journal of computational electronics*, vol. 9, no. 1, pp. 16–30, 2010.
- [91] S. S. Pidaparathi and C. S. Lent, “Exponentially adiabatic switching in quantum-dot cellular automata,” *Journal of Low Power Electronics and Applications*, vol. 8, no. 3, 2018.
- [92] S. Morita, “Faster annealing schedules for quantum annealing,” *Journal of the Physical Society of Japan*, vol. 76, no. 10, p. 104001, Oct. 2007.

- [93] S. S. Pidaparathi and C. S. Lent, “Exponentially adiabatic switching in quantum-dot cellular automata,” *Journal of Low Power Electronics and Applications*, vol. 8, no. 3, 2018.
- [94] J. Dziarmaga, “Dynamics of a quantum phase transition: exact solution of the quantum ising model.” *Physical Review Letters*, vol. 95 24, p. 245701, 2005.
- [95] M. Taucer, F. Karim, K. Walus, and R. A. Wolkow, “Consequences of many-cell correlations in clocked quantum-dot cellular automata,” *IEEE Transactions on Nanotechnology*, vol. 14, no. 4, pp. 638–647, July 2015.
- [96] F. Karim and K. Walus, “Calculating the steady-state polarizations of quantum cellular automata (qca) circuits,” *Journal of Computational Electronics*, vol. 13, no. 3, pp. 569–584, Sep 2014.
- [97] E. P. Blair and C. S. Lent, “Environmental decoherence stabilizes quantum-dot cellular automata,” *Journal of Applied Physics*, vol. 113, no. 12, p. 124302, 2013.
- [98] R. Harris, M. W. Johnson, T. Lanting, A. J. Berkley, J. Johansson, P. Bunyk, E. Tolkacheva, E. Ladizinsky, N. Ladizinsky, T. Oh, F. Cioata, I. Perminov, P. Spear, C. Enderud, C. Rich, S. Uchaikin, M. C. Thom, E. M. Chapple, J. Wang, B. Wilson, M. H. S. Amin, N. Dickson, K. Karimi, B. Macready, C. J. S. Truncik, and G. Rose, “Experimental investigation of an eight-qubit unit cell in a superconducting optimization processor,” *Physical Review B*, vol. 82, no. 2, Jul. 2010.
- [99] N. Dattani, S. Szalay, and N. Chancellor, “Pegasus: The second connectivity graph for large-scale quantum annealing hardware,” 2019.
- [100] K. Boothby, P. Bunyk, J. Raymond, and A. Roy, “Next-generation topology of d-wave quantum processors,” 2020.
- [101] N. Robertson and P. Seymour, “Graph minors .XIII. the disjoint paths problem,” *Journal of Combinatorial Theory, Series B*, vol. 63, no. 1, pp. 65–110, Jan. 1995.
- [102] V. Choi, “Minor-embedding in adiabatic quantum computation: I. the parameter setting problem,” *Quantum Information Processing*, vol. 7, no. 5, pp. 193–209, Sep. 2008.

- [103] J. Marshall, E. G. Rieffel, and I. Hen, “Thermalization, freeze-out, and noise: Deciphering experimental quantum annealers,” *Physical Review Applied*, vol. 8, no. 6, Dec. 2017.
- [104] V. Choi, “Minor-embedding in adiabatic quantum computation: II. minor-universal graph design,” *Quantum Information Processing*, vol. 10, no. 3, pp. 343–353, Oct. 2010.
- [105] J. Cai, W. G. Macready, and A. Roy, “A practical heuristic for finding graph minors,” 2014.
- [106] A. Fijany and B. N. Toomarian, “New design for quantum dots cellular automata to obtain fault tolerant logic gates,” *Journal of Nanoparticle Research*, vol. 3, no. 1, pp. 27–37, 2001.
- [107] C. S. Lent, K. W. Henderson, S. A. Kandel, S. A. Corcelli, G. L. Snider, A. O. Orlov, P. M. Kogge, M. T. Niemier, R. C. Brown, J. A. Christie, N. A. Wasio, R. C. Quardokus, R. P. Forrest, J. P. Peterson, A. Silski, D. A. Turner, E. P. Blair, and Y. Lu, “Molecular cellular networks: A non von neumann architecture for molecular electronics,” in *2016 IEEE International Conference on Rebooting Computing (ICRC)*. IEEE, Oct. 2016.
- [108] M. Balali, A. Rezai, H. Balali, F. Rabiei, and S. Emadi, “A novel design of 5-input majority gate in quantum-dot cellular automata technology,” in *2017 IEEE Symposium on Computer Applications Industrial Electronics (ISCAIE)*, 2017, pp. 13–16.
- [109] L. McMurchie and C. Ebeling, “PathFinder,” in *Proceedings of the 1995 ACM third international symposium on Field-programmable gate arrays - FPGA '95*. ACM Press, 1995.
- [110] J. P. Pinilla and S. J. E. Wilton, “Layout-aware embedding for quantum annealing processors,” in *High Performance Computing*, M. Weiland, G. Juckeland, C. Trinitis, and P. Sadayappan, Eds. Cham: Springer International Publishing, 2019, pp. 121–139.
- [111] N. G. Dickson, M. W. Johnson, M. H. Amin, R. Harris, F. Altomare, A. J. Berkley, P. Bunyk, J. Cai, E. M. Chapple, P. Chavez, F. Cioata, T. Cirip, P. deBuen, M. Drew-Brook, C. Enderud, S. Gildert, F. Hamze, J. P. Hilton, E. Hoskinson, K. Karimi, E. Ladizinsky, N. Ladizinsky, T. Lanting, T. Mahon, R. Neufeld, T. Oh, I. Perminov, C. Petroff, A. Przybysz, C. Rich, P. Spear, A. Tcaciuc, M. C. Thom, E. Tolkacheva, S. Uchaikin, J. Wang,

- A. B. Wilson, Z. Merali, and G. Rose, “Thermally assisted quantum annealing of a 16-qubit problem,” *Nature Communications*, vol. 4, no. 1, May 2013.
- [112] P. Weinberg, M. Tylutki, J. M. Rönkkö, J. Westerholm, J. A. Åström, P. Maninen, P. Törmä, and A. W. Sandvik, “Scaling and diabatic effects in quantum annealing with a d-wave device,” *Physical Review Letters*, vol. 124, no. 9, Mar. 2020.
- [113] J. Strecka and M. Jaščur, “A brief account of the ising and ising-like models: Mean-field, effective-field and exact results,” *Acta Physica Slovaca*, vol. 65, p. 235, 08 2015.
- [114] O. Goldschmidt and D. S. Hochbaum, “A polynomial algorithm for the k-cut problem for fixed k,” *Mathematics of Operations Research*, vol. 19, no. 1, pp. 24–37, 1994.
- [115] R. G. Downey, V. Estivill-Castro, M. Fellows, E. Prieto, and F. A. Rosamund, “Cutting up is hard to do: The parameterised complexity of k-cut and related problems,” *Electronic Notes in Theoretical Computer Science*, vol. 78, pp. 209 – 222, 2003, CATS’03, Computing: the Australasian Theory Symposium.
- [116] G. Karypis and V. Kumar, “A fast and high quality multilevel scheme for partitioning irregular graphs,” *SIAM Journal on scientific Computing*, vol. 20, no. 1, pp. 359–392, 1998.
- [117] P. Virtanen, R. Gommers, T. E. Oliphant, M. Haberland, T. Reddy, D. Cournapeau, E. Burovski, P. Peterson, W. Weckesser, J. Bright, S. J. van der Walt, M. Brett, J. Wilson, K. Jarrod Millman, N. Mayorov, A. R. J. Nelson, E. Jones, R. Kern, E. Larson, C. Carey, Í. Polat, Y. Feng, E. W. Moore, J. Vand erPlas, D. Laxalde, J. Perktold, R. Cimrman, I. Henriksen, E. A. Quintero, C. R. Harris, A. M. Archibald, A. H. Ribeiro, F. Pedregosa, P. van Mulbregt, and SciPy 1.0 Contributors, “SciPy 1.0: Fundamental Algorithms for Scientific Computing in Python,” *Nature Methods*, 2020.
- [118] R. B. Lehoucq, D. C. Sorensen, and C. Yang, *ARPACK: Solution of Large Scale Eigenvalue Problems by Implicitly Restarted Arnoldi Methods*, Available from netlib@ornl.gov, 1997.
- [119] I. Ojalvo and M. Newman, “Vibration modes of large structures by an automatic matrix-reduction method,” *Aiaa Journal - AIAA J*, vol. 8, pp. 1234–1239, July 1970.

- [120] S. R. White, “Density matrix formulation for quantum renormalization groups,” *Physical Review Letters*, vol. 69, no. 19, p. 2863, 1992.
- [121] S. R. White, “Density-matrix algorithms for quantum renormalization groups,” *Phys. Rev. B*, vol. 48, pp. 10 345–10 356, Oct 1993.
- [122] *ITensor Library (version 3.1.3)* <http://itensor.org>.

# Appendix A

## Algorithm Details

### A.1 SiDB HoppingDynamics Engine

The in-text discussion for HoppingDynamics related the dynamics to hopping rates,  $v_{ij}$ . In practise, it can be inefficient to run simulations by time-stepping using the rate equations: in some cases the rates can be unchanged for relatively large periods of time; in others, multiple hopping events can occur within a single time step and it can be tricky to determine the correct final state. Here we will discuss a more appropriate interpretation of the hopping model, as well as some additional details on limiting complexity.

#### A.1.1 Hopping Intervals

Rather than calculating hopping probabilities in time steps  $p_{ij}(t; dt) = v_{ij}(t)dt$ , we can reinterpret the hopping model in terms of *hopping intervals*,  $\tau_i$ . These intervals define the amount of time before an electron at a DB- site performs a hop, and satisfy  $P(\tau_i \leq t) = 1 - \exp(-\int_0^t \bar{v}_i(t')dt')$ , where  $\bar{v}_i(t) = \sum_{j \neq i} v_{ij}(t) + v_{i,B}(t)$  is the net outgoing hopping rate. Here we include only SiDB-SiDB rates and the surface-bulk hopping; however, any additional channels can be included. It is not sensible to generate a hopping interval as a random variable whose distribution depends on future values of the tunneling rates. To resolve this, we generate a simple exponential random variable  $\bar{\tau}_i \sim \text{Exp}(\lambda = 1)$  which satisfies  $P(\bar{\tau}_i \leq t) = 1 - \exp(-t)$ , define a *depletion rate*  $\frac{d}{dt} \bar{\tau}_i(t) = -\bar{v}_i(t)$ , and set the hopping interval

$\tau_i$  as the time for  $\bar{\tau}_i$  to reach 0. Then  $\bar{\tau}_i = \int_0^{\tau_i} \bar{v}_i(t') dt'$  and  $P(\tau_i \leq t) \equiv P(\bar{\tau}_i \leq \int_0^t \bar{v}_i(t') dt') = 1 - \exp(-\int_0^t \bar{v}_i(t') dt')$  as required. This is a useful trick, as we can generate  $\bar{\tau}_i$  every time a charge arrives at a new site, and  $\bar{\tau}_i$  will reach zero over a hopping interval consistent with the future rates.

This approach is particularly useful when there are no time-varying external fields  $V_i^{\text{ext}}(t)$ . In this case, the hopping rates only change when there is a reconfiguration of charge in the surface, or a surface-bulk hop. The next event that will happen will occur in  $\Delta\tau = \min_i \bar{\tau}_i / \bar{v}_i$  seconds. We can advance the system by this amount, decrement the  $\bar{\tau}_i$  by  $\bar{v}_i \Delta\tau$ , determine and perform the appropriate hopping event (see next section), update the  $v_{ij}$ , and continue. In generating Fig. 4.7, we do not time step over the full 18 minutes of simulated hopping events, we simply calculate all hopping events that will occur over that interval, compare that list against the times when the tip will be over the SiDBs, and read off the charge states. If dynamic fields are used, we step time in increments of  $\Delta t$  over which we assume the fields to be constant. Within each increment, we compute all hopping events.

### A.1.2 Event Selection

After  $\tau_i$  seconds, the charge at site  $i$  hops to some target  $j$ . We set the probability of a given target being selected to be proportional to the corresponding tunneling rate:  $P_{i \rightarrow j}(t) = v_{ij}(t) / \bar{v}_i(t)$ . The target  $j$  here can also be the bulk for a depopulation event.

### A.1.3 Cohopping

In certain circumstances, lower energy configurations exist which, if only single charge hops are allowed, would require passing through a higher energy configuration to reach. In this case, it may be justified to allow for cohopping, where two charges hop simultaneously. An example and schematic of cohopping is shown in Fig. A.1. In the current version of HoppingDynamics, cohopping is used primarily as a mechanism for escaping high energy metastable configurations, rather than taken as physically justified. For a cohopping event from sites  $(i, j)$  to  $(k, l)$ , we assign a rate

$$v_{ij \rightarrow kl} = v_0 e^{-\alpha_{CH} r_{ij}} \chi_{ij \rightarrow kl} \eta(\Delta G_{ij \rightarrow kl}) \quad (\text{A.1})$$

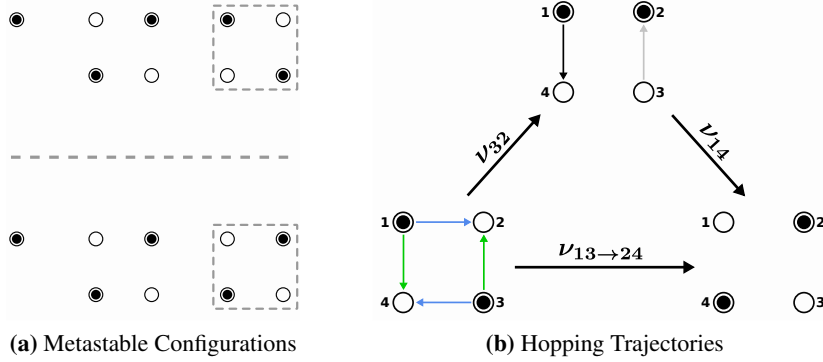


**Figure A.1:** Cohopping schematic. In (a), we show two metastable configurations for a biased pair of SiDB QCA cells. In order to reach the lower energy state on the bottom, both of the charges in the right cell must hop. Using only single hopping events, the least expensive way trajectory is to first hop the rightmost charge at site 3. Due to the repulsion from the other charge, this would increase the system energy. If cohopping is enabled, we can hop both charges simultaneously without having to overcome the temporary barriers.

where  $v_0$  is the calibrated pre-factor from Eq. (4.6),  $\alpha_{CH}$  is a cohopping spatial attenuation factor which restricts cohopping to nearby sites,  $\chi_{ij \rightarrow kl}$  describes the dependence on the distances between the involved sites, and  $\eta$  defines the energy dependence for the chosen hopping model with  $\Delta G_{ij \rightarrow kl} = \Delta E_{ij \rightarrow kl} + \rho_i + \rho_j$ . We define  $\chi_{ij \rightarrow kl}$  in terms of the spatial components of the single charge hopping rates:  $\chi_{ij}$  where  $v_{ij} = v_0 \chi_{ij} \eta(\Delta G_{ij})$ :

$$\chi_{ij \rightarrow kl} = \frac{1}{2} (\chi_{ik} \chi_{jl} + \chi_{il} \chi_{jk}), \quad (\text{A.2})$$

We can understand a cohopping event from  $ij \rightarrow kl$  as either of two trajectories:  $i \rightarrow k$  and  $j \rightarrow l$ , or  $i \rightarrow l$  and  $j \rightarrow k$ . If we assume two hopping events to be simultaneous but independent, the probability would satisfy  $p_{i \rightarrow k, j \rightarrow l}(t; dt) = v_{ik} v_{jl} dt dt$  with a spatial component  $\chi_{ik} \chi_{jl}$ . Our choice in Eq. (A.2) is simply the average over both trajectories.

### A.1.4 Restricted Range Hopping

There are potentially  $O(N^2)$  possible  $v_{ij}$  and  $O(N^4)$  possible  $v_{ij \rightarrow kl}$ . Realistically, hopping events between sufficiently distant SiDBs are unlikely to ever contribute. Similarly for cohopping, two charges which are far apart are unlikely to be sufficiently correlated to justify them as candidates for cohopping. We define two distance bounds: the maximum hopping distance  $R_{hop}$ , and a maximum cohopping pair separation  $R_{CH}$ . For each *DB*– site  $i$ , we only keep track of  $v_{ij}$  for DB0 sites  $j$  within a radius of  $R_{hop}$ . For each *DB*– pair  $(i, j)$  with  $r_{ij} < R_{CH}$  we track  $v_{ij \rightarrow kl}$  for DB0 sites satisfying  $r_{ik} < R_{hop}$  and  $r_{jl} < R_{hop}$ . For all results shown, we use  $R_{hop} = R_{CH} = 5$  nm.

## A.2 Dense Placement Algorithm

The Dense Placement algorithm uses a simultaneous “place-and-route” approach commonly used in FPGA design [109]. It attempts to place every node in the QCA connectivity graph onto a corresponding *assigned qubit* in the Chimera graph. Interactions between cells are facilitated either by direct coupling or by chains of qubits routed between these assigned qubits.

### Initial Seed

We begin by selecting an initial seed, the first QCA cell and its corresponding qubit, as follows. We select QCA cell  $i$  with probability proportional to  $A_i^p$  where  $A_i$  is the number of neighbours of the cell and  $p$  is a constant. In this paper,  $p$  was selected to be 3 to prioritize high adjacency cells but still allow some chance for lower adjacency cells. To select the seed qubit, we first select a tile according to a Gaussian distribution about the center of the QPU with width  $\sigma$ . The qubits of that tile are then randomly ordered and iterated through until a qubit is found with enough neighbours to facilitate the interactions of the selected seed cell. If no such qubit is found, a new tile is selected. In this work,  $\sigma$  was chosen to be 1 to strongly bias initial placement near the center of the Chimera graph.

## Cell Placement

Building from the initial seed, for each iteration of the main loop we look at the set of unplaced cells adjacent to the set of placed cells and sort by decreasing number of unplaced connections. For each cell to be placed, we aim to select a qubit with sufficiently many available neighbouring qubits to facilitate all interactions. Such a qubit is referred to as *suitable*. The chosen qubit is that which is both suitable and yields the shortest total path to all qubits assigned to adjacent cells. This is achieved by simultaneously running a lowest-cost-path search from each such qubit until a suitable qubit is reached by all search trees. The cost of each edge in the search contains two components: a contribution from the type of coupling to the new node (internal or external to a tile), and an edge proximity contribution which weighs nodes in tiles closer to the edge of the processor more strongly. For dense placement, internal tile placements are preferred so internal couplers have lower cost than external couplers. The external coupler cost was chosen to be 1.9 times the internal coupler cost such that one external coupler was preferable to two internal couplers. The edge proximity cost increases linearly as the minimum distance to the processor edge decreases. An increase in cost of 0.5 per tile was used. The chosen parameters tightly pack long chains of low adjacency cells and reduce the risk of running out of room for embedding.

## Routing

The routing algorithm is based on negotiated congestion, a well-established path finding technique used in mapping netlists to FPGAs [109]. This method aims to minimize the path length for each route by use of a cost scheme that penalizes the using a qubit for more than one path.

## Seam Opening

In the case that there is no suitable qubit available, the translational symmetry of the Chimera graph allows an avenue of qubits and couplers to be “opened” by shifting all qubits after or before a row or column. We interpret this as opening a seam between two rows or columns. As specific qubits or couplers may be inactive due to manufacturing yield, some shifted qubits may require remapping. Such qubits

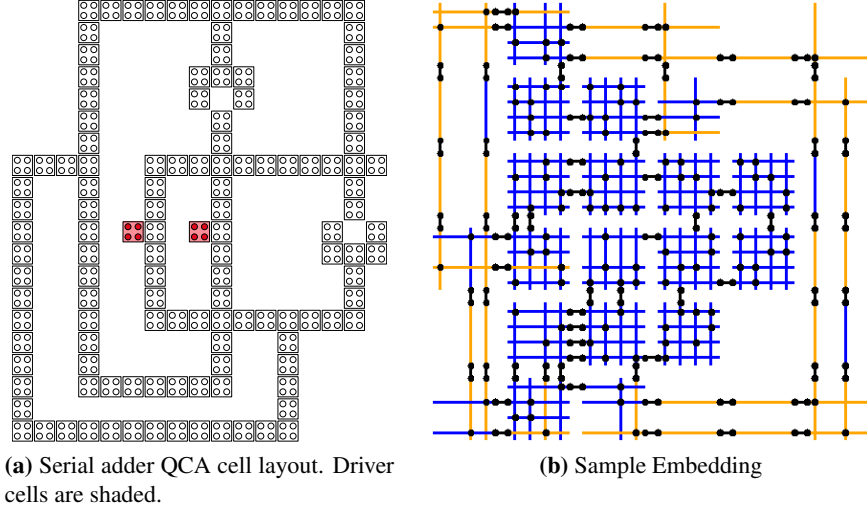


**Figure A.2:** Example embedding of a serial adder QCA circuit. Here qubits are represented by line segments with active couplers shown by black circles. Darker shaded qubits indicate those assigned to QCA cells with lighter shaded qubits indicating virtual qubits. Only tiles with used qubits are shown.

are said to “conflict.” Following such a shift, remapping is achieved by finding new placements for cells with conflicting assigned qubits and rerouting conflicting paths. The new cell placements can result in recursive calls to seam opening and remapping. We select the seam to open according to a simple metric. For the cell being placed, we consider all seams adjacent to assigned qubits of the cell’s placed neighbours. For each of these seams and each opening direction, we check that there is a free row or column to shift into. If so, we assign to that seam a cost,  $C$ , given by

$$C = c_q n_q + c_p n_p + c_d d, \quad (\text{A.3})$$

where  $n_q$  and  $n_p$  are the number of conflicting assigned qubits and paths,  $d$  is the seam distance defined as the minimum distance between the seam and the mean location of all assigned qubits, and  $c_q$ ,  $c_p$ , and  $c_d$  are the relevant cost factors. In this work, the cost factors were chosen as  $c_q = 3$ ,  $c_p = 4$ , and  $c_d = 3$ . Typically, fewer qubits were needed for replacing a small number of qubits than rerouting a number of paths.

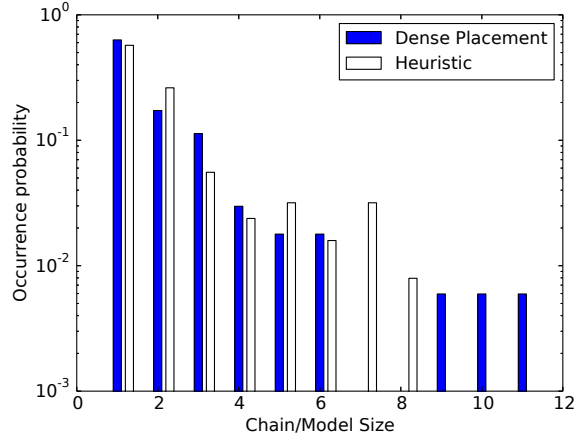


**Figure A.3:** Occurrence probability of qubit chain lengths and vertex-model sizes for the Dense Placement and Heuristic algorithms respectively for a sample trial of the serial adder with full adjacency. Chain lengths are measured by the number of couplers used with models measured by the number of qubits. Due to the different interpretations of embedding used by the two algorithms, the distributions represent how each model allocates virtual qubits. Note the occurrence of long qubit chains for the Dense Placement algorithm.

The Dense Placement algorithm is good at keeping most routes between mapped qubits to only one or two couplers. However, as the placement builds outwards from the center and does not currently account for how the final cells to be placed are connected, there are often long chains of ten or more qubits about the perimeter of the embedding needed to facilitate the final connections. The QCA cell layout and a sample embedding for a serial adder are shown in Fig. A.2 with the distribution of qubit chain lengths shown in Fig. A.3. Note the long chains that are around the perimeter as discussed.

### A.2.1 Parameter Assignment and Model Conversion

Between each pair of qubits assigned to adjacent QCA cells there can exist a chain of virtual qubits. The interaction term  $J_{ij}$  between the two cells can be assigned to any coupler along this chain without changing the effective interaction between the assigned qubits, given that all other connectors are assigned  $J_c = -1$ . Parameter assignment then takes the form of finding an effective vertex model for each cell by

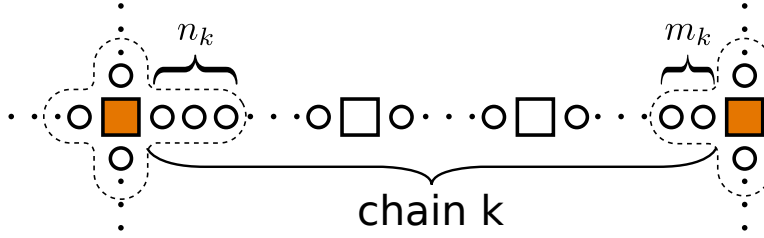


**Figure A.4:** Schematic of a chain between two end nodes. Squares and circles represent assigned and virtual qubits respectively. The filled squares are the end nodes terminating chain  $k$  and the unfilled squares are internal nodes within chain  $k$ . Dotted boundaries indicate the end-node vertex models.

deciding where along each virtual qubit chain to assign the interaction term. Once the vertex models are found, we can proceed as above to assign bias and interaction parameters.

In [6], we argue that the energy of the first excited state in a system of two interaction wire, serving as analogs for vertex models, is maximized if the wires are of similar size. We assume then that we should aim to minimize the largest vertex model in our embedding. One can formulate the allocation of virtual qubits with the aim to minimize the maximum of all vertex-model sizes as a linear optimization problem. First, to maintain the correct number of connectors between vertex models observe that any cell with greater or less than 2 neighbours must contain in its vertex model its assigned qubit. It is then useful to reinterpret the QCA circuit connectivity graph as a set of “end node” ( $A_i \neq 2$ ) cells connected by chains of “internal node” ( $A_i = 2$ ) cells. The Dense Placement algorithm then effectively constructs chains containing virtual and internal nodes between the end nodes. One such chain is illustrated in Fig. A.4. Note that the internal nodes could be placed anywhere along these chains without changing the embedding as long as their order is maintained. Qubit allocation then reduces to determining the number of qubits at the end of each chain assigned to the vertex models of the end nodes. The remaining qubits of each chain are divided evenly between the internal-node cells. Only chains containing virtual qubits need to be considered.

The  $k^{\text{th}}$  chain contains  $N_k$  internal nodes and total of  $M_k$  qubits, excluding the end nodes. Of these qubits,  $n_k$  and  $m_k$  qubits are assigned to the vertex models of

the end nodes at the beginning and end of the chain respectively. Then the  $k^{\text{th}}$  chain has an average internal-node vertex-model size,  $\bar{s}_k$ , of

$$\bar{s}_k = \frac{M_k - n_k - m_k}{N_k}. \quad (\text{A.4})$$

If  $S_\ell$  is the sum of all  $n_i, m_j$  associated with the  $\ell^{\text{th}}$  end node, then each end node has a vertex-model size,  $s_\ell$  of

$$s_\ell = 1 + S_\ell. \quad (\text{A.5})$$

The linear programming problem is then given as minimizing the maximum of the set of all  $\bar{s}_k$  and  $s_\ell$  with constraints  $n_i, m_i \geq 0 \forall i$  and  $n_i + m_i \leq M_i - N_i \forall i$ . This is an integer programming problem and hence is potentially computationally intensive; however, the number and allowed range of parameters is typically small so this was not a concern. If necessary, linear programming (LP) relaxation can be used, removing the integer constraint on  $n_i$  and  $m_i$ , with some consideration to rounding in post-processing. This method optimizes the maximum vertex-model size but does not consider the distribution of the remaining vertex models. Better results could be obtained from a nonlinear optimization which considers all vertex-model sizes.

### A.3 Component Mode Solver

Here we discuss a number of details relevant to the implementation and application of the CM solver for the results in this work.

#### Initial Conditions

As a variation approach, the CM solver cannot guarantee convergence to the optimal ground state from some arbitrary initial condition. The solver is best applied as a means of tracking the low energy spectrum of a QCA network as some parameter is continuously changed. This is appropriate for studying QCA clocking, in which the mean fields in the depolarized regime are simple:  $m_i \approx 0$ . Assuming that the  $m_i$  change sufficiently continuously as the clocking fields are adjusted, the solver is provided with a good estimate.

### Selecting the Reduced Basis

In general, the reduced basis representations of the  $\hat{\sigma}_z^i$  are dense, and thus we need to keep  $\mathbf{d}$ , the dimension of  $\mathbf{H}$ , reasonable if we want to have fast diagonalization. In particular, we define a maximum dimension,  $d_{\text{thresh}}$ , allowed for  $\mathbf{H}$ , chosen based on constraints on available resources and the desired trade-off between accuracy and speed. We then require that  $\mathbf{d} = \prod_n d_n \leq d_{\text{thresh}}$ . The remaining question is choosing how many states from each component to included. We employ an approach which effectively translates  $d_{\text{thresh}}$  to a temperature constraint. If the density operator is taken to be a Boltzmann distribution, the energy eigenstates contribute with weight  $p_n \propto e^{-\beta(E_n - E_0)}$ . We might consider the *important* eigenstates to be those which satisfy  $p_n \geq p^*$  or equivalently  $E_n - E_0 \leq k_B T^*$  for some temperature bound  $T^*$ . We add component eigenstates to the basis in order of increasing energy after subtracting off the component ground state energies. States are added until the next addition would push  $\mathbf{d}$  beyond  $d_{\text{thresh}}$ . For all results shown, a value of  $d_{\text{thresh}} = 5000$  was used.

### Order of Mean Field Updates

There are a number of schemes that could be considered for when to update the mean fields during the self-consistency and recursive steps. In the case where recursion is not necessary, we update the mean fields upon a new estimate of the full system ground state. However, when each component is solved during recursion we obtain a new and potentially better estimate of the fields for that component. We could self-consistently solve each component before constructing its reduced basis; however, this makes the self-consistency loop potentially exponential in the depth of the decomposition tree. In addition, despite a significant increase in runtime, we have not observed an cases where this method gave different results than simply waiting for the full system ground state. In this work, convergence was achieved when  $\max_i |\Delta m_i| \leq 0.001$  and typically only one or two iterations were required at each value of  $\gamma$ .

### **Sub-Decomposition**

Further decompositions of the components were done automatically using METIS with weights  $w_{ij} = |E_{ij}^k|$ . At each level of the decomposition tree, components larger than 16 cells were split into two connected sub-components with the larger containing at most  $2/3$  of the cells:  $\epsilon = 1/3$ .

### **Decomposition Updates**

Optimal decomposition is a question both of identifying the set of minima used in the dynamic objective function as well as accurately computing the  $M_{zz}^{ij}$ . In experimenting with the CM solver, we found that the accuracy of the first excited state is largely dependent on the choice of decomposition. Roughly speaking, the poorer the choice in components, the more component modes are needed and thus either the slower or less accurate the result. However, unless the initial choice is particularly poor, the ground state itself can be computed with speed and accuracy comparable to DMRG. In addition, even a rough estimate of the locations of the minima seems to be suitable for identifying good decompositions.

### **Note on Complexity**

For a given choice of accuracy parameters, both the CM solver and DMRG require  $O(N)$  diagonalization steps per iteration. We should expect then that both have runtime complexity which scale comparably with the number of devices. The challenge in characterizing complexity comes from understanding how the needed accuracy parameters depend on the complexity of the network. Further investigation is needed to address this. As an example, the considered XOR gate results included 200  $\gamma$  values, and took about 2-3 minutes for both the CM solver and the DMRG implementation on a single core: roughly one second per update. Neither our Python implementation of the CM solver nor our choice in parameters for ITensor's DMRG were particularly optimized.

## Appendix B

# Additional Derivations

### B.1 Analytical Estimate of the 3-State QCA Cell Ground State Energy

We give exact expressions for the population and polarization of a 3-state QCA cell in Eq. (5.12) given the ground state energy  $E_0$  of the form

$$E_0 = \frac{1}{2}(\mathcal{C} - |h|) - \frac{1}{2}\sqrt{\alpha^2 + (\mathcal{C} + |h|)^2}$$

We solve the for the ground state exactly in a few limits:

$$E_0(\gamma, 0, \mathcal{C}) = \frac{1}{2}\mathcal{C} - \frac{1}{2}\sqrt{8\gamma^2 + \mathcal{C}^2} \quad (\text{B.1a})$$

$$E_0(\gamma, h, 0) = -\sqrt{2\gamma^2 + h^2} \quad (\text{B.1b})$$

$$\lim_{|h| \rightarrow \infty} E_0(\gamma, h, \mathcal{C}) = \frac{1}{2}(\mathcal{C} - |h|) - \frac{1}{2}\sqrt{4\gamma^2 + (\mathcal{C} + |h|)^2} \quad (\text{B.1c})$$

from which we obtain a suitable form for  $\alpha$ :

$$\alpha^2(\gamma, h, \mathcal{C}) = 4\gamma \left[ 2 + u^2 - u\sqrt{2 + u^2} \right]$$

with  $u(\gamma, h, 0) = |h|/\gamma$ . After numerical experimentation, we obtain a better approximation by noting that  $u(\gamma, h, C)$  nearly satisfies

$$u(\gamma, h, C) = u(\gamma, h, 0)/f(C/\gamma) \quad (\text{B.2})$$

where  $f(x)$  is approximately the hyperbola  $\sqrt{1+x^2/9} - x/3$ .

## B.2 Clocking Field Range for 3-State QCA Wires

In a completely depopulated wire, the first device to populate is adjacent to the fully polarized driver cell and has an activation energy of

$$\frac{C_{to}^a}{E_0^k} = \xi - \frac{1}{2} \quad (\text{B.3})$$

This defines a lower limit on the clocking field. For a fully populated wire, taken to be infinite, a cell in the middle experiences maximum congestion and has an activation energy of

$$\frac{C_{hi}^a}{E_0^k} = \begin{cases} 2\xi \cdot \zeta(q, \alpha_s) - (1 - 1/2^{p-1})\zeta(p), & \text{Inverting} \\ 2\xi \cdot \zeta(q, \alpha_s) - \zeta(p), & \text{Non-Inverting} \end{cases} \quad (\text{B.4})$$

where  $\zeta(q, \alpha) = \alpha^{-1} \text{Li}_q(\alpha)$  with  $\text{Li}_q(\alpha) = \sum_k \alpha^k / k^q$  the polylogarithm function which satisfies  $\text{Li}_q(1) = \zeta(q)$  and  $\text{Li}_1(\alpha) = -\ln(1 - \alpha)$ . Note that the activation energy is slightly higher for an inverting wire as the contributions to the polarization bias do not all add. If  $\xi$  is sufficiently small, it is possible for the polarization bias to have a larger contribution to the activation energy than the congestion, resulting in a negative activation energy. We observe in this case that the last cell in the wire experiences half of the congestion and polarization bias of a cell in the middle, and hence has half the activation energy. In this special case, we should increase the negative  $C_{hi}^a$  to half of its value. These cases account for all results shown in this work.

### B.3 Y Spin Invariance in the 2-State Approximation

In the 2-state approximation, we are free to choose the “up” conventions for each of our spin directions. In particular, we are free to select which of the eigenspinors  $\frac{1}{\sqrt{2}} \begin{bmatrix} 1 \\ -i \end{bmatrix}$  and  $\frac{1}{\sqrt{2}} \begin{bmatrix} 1 \\ i \end{bmatrix}$  in the z-spin basis correspond to  $|+y\rangle$ . Swapping between the two y-spin conventions corresponds to taking the complex conjugate of all spin operators:  $(\hat{\sigma}_x, \hat{\sigma}_y, \hat{\sigma}_z) \rightarrow (\hat{\sigma}_x, -\hat{\sigma}_y, \hat{\sigma}_z)$ . Further, any state  $|\psi\rangle$  in one convention becomes its conjugate  $|\psi\rangle^*$  in the other. From these results, we make two important observations. (1) As there are no  $\hat{\sigma}_y$  terms in the Hamiltonian,  $\hat{H}$  given in Eq. (2.3), an energy eigenpair  $(E, |\psi\rangle)$  of  $\hat{H}$  is also an eigenpair of  $\hat{H}^*$ . It follows that in the z-spin basis all energy eigenstates have real coefficients:  $|\psi\rangle = |\psi\rangle^*$ . (2) For any product  $\hat{O}$  of  $\hat{\sigma}_\mu^i$  operators,  $\langle \psi | \hat{O} | \psi \rangle = (-1)^{n_y} \langle \psi^* | \hat{O} | \psi^* \rangle$  with  $n_y$  the number of  $\hat{\sigma}_y^i$  terms. For energy eigenstates, we then have  $\langle \hat{O} \rangle = (-1)^{n_y} \langle \hat{O} \rangle$ . The expected value of any product of Pauli spin operators with any energy eigenstate is zero if there are an number of  $\hat{\sigma}_y$  terms. All out considered steady states are of the form:

$$\langle \hat{O} \rangle_{ss} = \text{Tr} \hat{\rho}_{ss} \hat{O} = \sum_k r_k \langle \phi_k | \hat{O} | \phi_k \rangle \quad (\text{B.5})$$

for real  $r_k$  and energy eigenstates  $|\phi_k\rangle$ . Hence  $\langle \hat{O} \rangle_{ss} = 0$  for all  $\hat{O}$  containing an odd number of  $\hat{\sigma}_y$  terms.

## Appendix C

# Supplemental Details

### C.1 Pegasus Topology

The Pegasus topology is effectively three nested Chimera graphs with added edges. Four additional couplers are added within each 8-qubit tile, shown in Fig. 7.2. In Fig. C.1, we show how the tiles in Pegasus are connected. Tiles within a Chimera sub-graph have the same connections as in Chimera. We can call this *intra-Chimera* coupling. Tiles in different sub-graphs are connected in a triangular lattice. This we call *inter-Chimera* coupling. In Fig. C.2, we show the specific inter-Chimera couplings between qubits in each tile. In total, each qubit has 5 internal couplers within each tile, 2 intra-Chimera couplers, and 8 inter-Chimera couplers.

### C.2 Additional Embedding Results

#### C.2.1 Embedding Time

For such a specific class of embedding problems, it is not meaningful to discuss theoretical worst-cases for time complexity. Instead, we consider only a best-fit to the average run times for the generated circuits. More specifically, we quantize the algorithm run times by the value of the fitted model at the size  $\mu$  where the single trial embedding success probability is 50%: see Fig. 7.12. In Fig. C.3, we show the

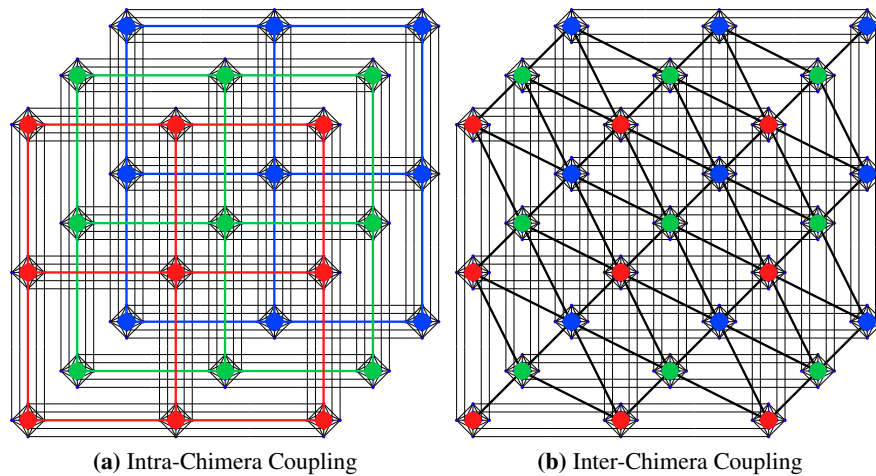


**Figure C.1:** Tile connectivity of the Pegasus topology. The tiles can be divided into three nested Chimera graphs, indicated by the colors. All the Chimera-like couplers between tiles in each Chimera sub-graph still exist. Coupling between sub-graphs can be described by a triangular lattice.

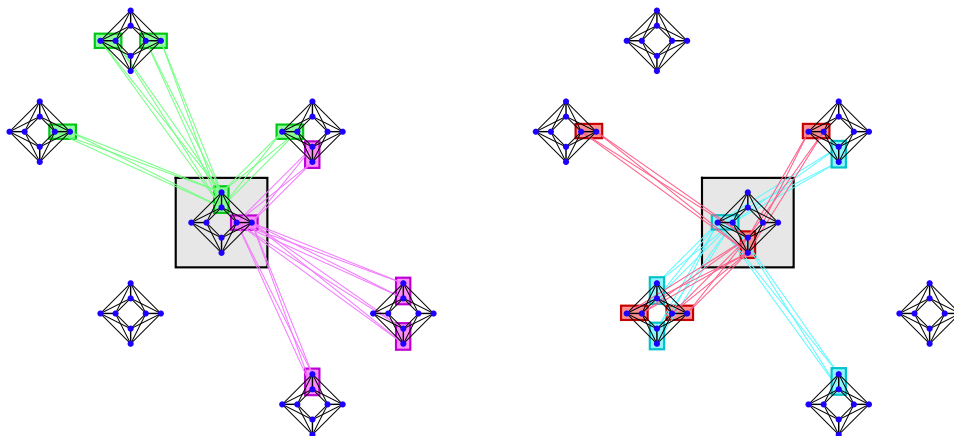


**Figure C.2:** Connectivity between qubits in different Chimera sub-graphs. Though each qubit has 8 inter-Chimera couplings, the distribution depends on the choice of qubit in the tile.

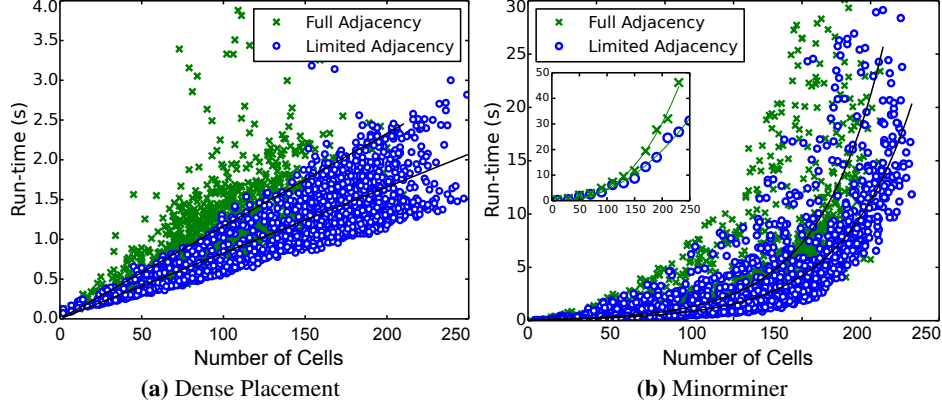


**Figure C.3:** Average run times for generated circuits on the 512 qubit processor for both algorithms with best fits. The inset of **(b)** shows the maximum run times for bins of 20 cells with a power fit.

average run times for the generated circuits for both algorithms and both adjacency types. Run times for the Dense Placement algorithm are approximately linear with the circuit size due to the local nature of cell placement. For minorminer, run times were best fit by an exponential. Note the significant difference in time scale between the two algorithms, particularly for large circuits. Minorminer is reported in [105] to have a worst case time complexity of  $O(n_H n_G e_H (e_G + n_G \log(n_G)))$  with  $n$  and  $e$  the number of nodes and edges in the source graph,  $H$ , and the target graph,  $G$ . In our case  $H$  is the QCA circuit connectivity graph and  $G$  the Chimera graph. Depending on the complexity of a circuit of  $N_{cells}$  cells and the range of included interactions, the number of edges in  $H$  is between  $N_{cells} - 1$  and  $\frac{1}{2}N_{cells}(N_{cells} - 1)$ . Hence the worst case time complexity of minorminer should be between  $O(N_{cells}^2 N_{qbits}^2 \log(N_{qbits}))$  and  $O(N_{cells}^3 N_{qbits}^2 \log(N_{qbits}))$  for a processor containing  $N_{qbits}$  qubits. For a given processor, we should then expect the run times to have an upper bound of the form  $t_{max}(N) \propto N^\alpha$  with  $2 \leq \alpha \leq 3$ . The inset in Fig. C.3b shows the maximum run times within bins of 20 cells and the associated power law fits. The trends for limited and full adjacency were found to have powers of  $2.21 \pm .16$  and  $2.73 \pm .21$ , which lie within expected values. All embeddings were done using a single core of an Intel Core i7-2670QM processor.

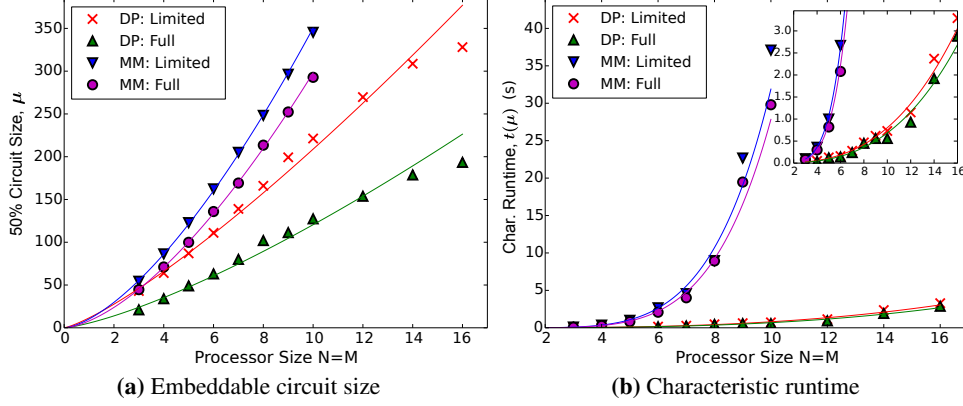


**Figure C.4:** Metrics for the 50% circuit size and characteristic run time for both algorithms and adjacencies as a function of the processor size.

**Table C.1:** Power law fit parameters for the characteristic circuit size,  $\mu$ , and run time  $t(\mu)$ .

Method	$A_\mu$ (cells)	$b_\mu$	$A_t$ (ms)	$b_t$
DP-L	$11.6 \pm 1.0$	$1.26 \pm 0.04$	$1.15 \pm 0.20$	$2.85 \pm 0.08$
DP-F	$5.5 \pm 0.6$	$1.34 \pm 0.06$	$0.84 \pm 0.19$	$2.91 \pm 0.11$
MM-L	$10.3 \pm 0.2$	$1.53 \pm 0.01$	$0.41 \pm 0.11$	$4.89 \pm 0.14$
MM-F	$8.0 \pm 0.2$	$1.57 \pm 0.02$	$0.31 \pm 0.06$	$4.95 \pm 0.11$

## C.2.2 Scaling Performance

Here we investigate the trend of the 50P circuit size,  $\mu(N)$ , and the characteristic run time,  $t(\mu, N)$ , of both algorithms over a range of processor sizes. We consider only square processors. That is, we assume there are  $N$  rows and  $M = N$  columns of 8 qubit tiles. Due to its exponential run-time performance, we only tested minorminer up to processors of size  $N = 10$ . The Dense Placement algorithm was tested on processors up to size  $N = 16$ . The estimated values of  $\mu(N)$  and associated run times  $t(\mu, N)$  are shown in Fig. C.4 with power law fits. The fit parameters are included in Table C.1 where  $\mu(N) = A_\mu N^{b_\mu}$  and  $t(\mu, N) = A_t N^{b_t}$ . The inset in Fig. C.4b has the y-range expanded to better see the Dense Placement algorithm performance. While the power law fits for  $\mu(N)$  appear accurate up to  $N = 10$ , there is a notable fall-off for the Dense Placement algorithm for larger processor

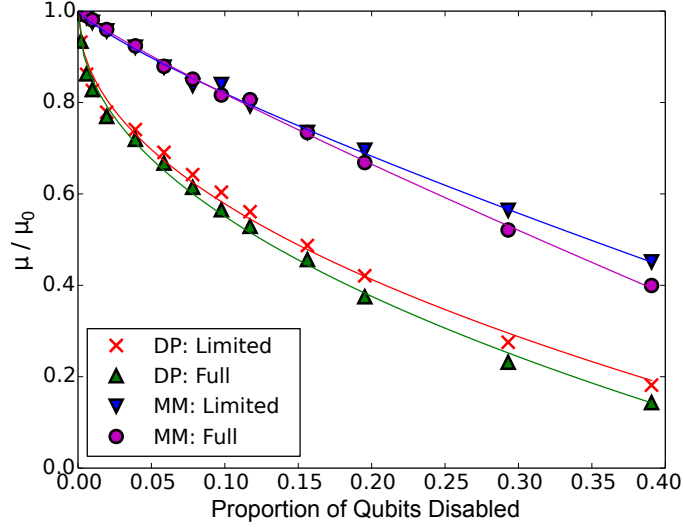


**Figure C.5:** Relative decrease in the embeddable circuit size as a function of the proportion of qubits disabled. Fits are shown.

sizes, likely due to the need to coordinate the discussed long chains for the final cell placements.

### C.2.3 Resilience to Processor Yield

So far, we have assumed all of the qubits and couplers in the processor to be available. Here we investigate the performance of both algorithms for generated circuits with different percentages of the available qubits disabled. A new set of disabled qubits is uniformly generated for each embedding trial for each circuit. Fig. C.5 shows the relative  $\mu$  values for different percentages of disabled qubits on a 512 qubit processor. Here  $\mu_0$  indicates the value of  $\mu$  when no qubits are disabled. We fit a model of the form

$$\mu(n_{dis}) = \mu_0 \left[ 1 - \alpha n_{dis}^\beta \right] \quad (\text{C.1})$$

where  $0 \leq n_{dis} \leq 1$  is the proportion of qubits disabled. As typical values of  $n_{dis}$  are small ( $\sim 0.05$ ), of importance is the observation that  $\mu(n_{dis})$  for the Dense Placement algorithm falls off quickly with  $n_{dis}$ . In contrast, minorminer seems to be much more resilient to yield.

## Appendix D

# Equations

### D.1 Gell-Mann Matrices

$$\begin{aligned}\hat{\lambda}_1 &= \begin{pmatrix} 0 & 1 & 0 \\ 1 & 0 & 0 \\ 0 & 0 & 0 \end{pmatrix} & \hat{\lambda}_2 &= \begin{pmatrix} 0 & -i & 0 \\ i & 0 & 0 \\ 0 & 0 & 0 \end{pmatrix} & \hat{\lambda}_3 &= \begin{pmatrix} 1 & 0 & 0 \\ 0 & -1 & 0 \\ 0 & 0 & 0 \end{pmatrix} \\ \hat{\lambda}_4 &= \begin{pmatrix} 0 & 0 & 1 \\ 0 & 0 & 0 \\ 1 & 0 & 0 \end{pmatrix} & \hat{\lambda}_5 &= \begin{pmatrix} 0 & 0 & -i \\ 0 & 0 & 0 \\ i & 0 & 0 \end{pmatrix} & & \\ \hat{\lambda}_6 &= \begin{pmatrix} 0 & 0 & 0 \\ 0 & 0 & 1 \\ 0 & 1 & 0 \end{pmatrix} & \hat{\lambda}_7 &= \begin{pmatrix} 0 & 0 & 0 \\ 0 & 0 & -i \\ 0 & i & 0 \end{pmatrix} & \hat{\lambda}_8 &= \frac{1}{\sqrt{3}} \begin{pmatrix} 1 & 0 & 0 \\ 0 & 1 & 0 \\ 0 & 0 & -2 \end{pmatrix}\end{aligned}$$

### D.2 Equations for All Single and Two Point Correlations

For completeness, we include here the  $i\langle[\hat{\mathcal{H}}, \hat{\Lambda}] \rangle$  components of the dynamics equation up to two-point correlations. The single-point correlations are easily obtained

as

$$\lambda_x^i : -h_i \lambda_y^i + \sum_{n \neq i} E_{ni}^k K_{yz}^{in} \quad (\text{D.1a})$$

$$\lambda_y^i : \gamma_i \lambda_z^i + h_i \lambda_x^i - \sum_{n \neq i} E_{ni}^k K_{xz}^{in} \quad (\text{D.1b})$$

$$\lambda_z^i : -\gamma_i \lambda_y^i \quad (\text{D.1c})$$

Making use of the equality,  $K_{ab}^{ij} = K_{ba}^{ji}$ , we obtain six two-point correlations with equations

$$K_{xx}^{ij} : -h_i K_{xy}^{ji} - h_j K_{xy}^{ij} + \sum_{n \notin \{ij\}} \left[ E_{ni}^k K_{xyz}^{jin} + E_{nj}^k K_{xyz}^{ijn} \right] \quad (\text{D.2a})$$

$$K_{xy}^{ij} : \gamma_j K_{xz}^{ij} - h_i K_{yy}^{ij} + h_j K_{xx}^{ij} + \sum_{n \notin \{ij\}} \left[ E_{ni}^k K_{yyz}^{ijn} - E_{nj}^k K_{xxz}^{ijn} \right] \quad (\text{D.2b})$$

$$K_{xz}^{ij} : -\gamma_j K_{xy}^{ij} - h_i K_{yz}^{ij} + E_{ij}^k \lambda_y^i + \sum_{n \notin \{ij\}} E_{ni}^k K_{yzz}^{ijn} \quad (\text{D.2c})$$

$$K_{yy}^{ij} : \gamma_i K_{yz}^{ji} + \gamma_j K_{yz}^{ij} + h_i K_{xy}^{ij} + h_j K_{xy}^{ji} - \sum_{n \notin \{ij\}} \left[ E_{ni}^k K_{xyz}^{ijn} + E_{nj}^k K_{xyz}^{jin} \right] \quad (\text{D.2d})$$

$$K_{yz}^{ij} : \gamma_i K_{zz}^{ij} - \gamma_j K_{yy}^{ij} + h_i K_{xz}^{ij} - E_{ij}^k \lambda_x^i - \sum_{n \notin \{ij\}} E_{ni}^k K_{xzz}^{ijn} \quad (\text{D.2e})$$

$$K_{zz}^{ij} : -\gamma_i K_{yz}^{ij} - \gamma_j K_{yz}^{ji} \quad (\text{D.2f})$$